The Dynamics of White Dwarfs, Black Holes and Stellar Cusps

Thesis by

Christopher Wegg

In Partial Fulfillment of the Requirements

for the Degree of

Doctor of Philosophy

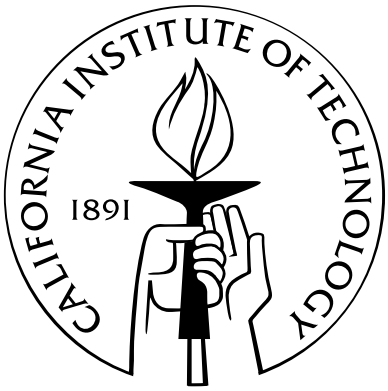

California Institute of Technology

Pasadena, California

2013

(Defended July 19th, 2012)

Abstract

This thesis contains topics related mostly to the dynamics of white dwarfs (chapter 2), the dynamics of stars around binary super massive black holes (chapters 4, 5 and 6) and dynamics in the singular isothermal sphere (chapter 7).

In chapter 2 the kinematics of young ($< 3 \times 10^8$ yr) galactic white dwarfs are investigated. A relationship between the mass and kinematics of white dwarfs is demonstrated, whereby high-mass white dwarfs have low velocity dispersion. This is the result of less scattering during the shorter lifetime of their more massive precursors. The kinematics of the highest-mass white dwarfs ($> 0.95\,M_\odot$) are also investigated, and it is shown that they are consistent with the majority being formed via single-star evolution from massive progenitor stars.

In chapter 3 it is shown that the coolest, oldest white dwarfs can be identified photometrically from their unique colors, and five new ultracool white dwarfs are spectroscopically confirmed.

In chapter 4 it is shown that close binary supermassive black holes (SMBHs) should produce a burst of tidal disruptions of up to $0.1\,\mathrm{yr}^{-1}$ as they form. The quiescent rate is $\sim 10^{-5}\,\mathrm{yr}^{-1}$ per galaxy, and it is therefore shown that binary SMBHs can potentially be identified via multiple tidal disruptions from the same system.

In chapter 5 we perform more extensive simulations of the dynamics of stars around binary SMBHs to better quantify and understand the stellar dynamics. By incorporating general relativistic corrections, we also investigate the processes undergone by compact remnants orbiting the binary SMBHs, analyzing both objects that plunge directly into the SMBHs, and those that undergo extreme mass ratio inspirals (EMRIs). The potential used to mimic general relativistic precession in these simulations is novel, and more accurate for the type of nearly parabolic orbits considered in this work: It is described in chapter 6.

In chapter 7 an analytic solution to the manner in which stars diffuse in the background of a singular isothermal sphere is developed. It is shown a self-similar solution should exist, and this solution is found.

Contents

List of Figures

List of Tables

1 Introduction

1.1 Overview

In this chapter the background needed to understand the importance of the remainder of the thesis is introduced. While the chapters in this thesis are somewhat disparate they all relate to galactic dynamics (chapters 4, 5, 6, and 7), white dwarfs (chapter 3) or both (chapter 2). In addition we (attempt to) apply the analytic work in chapter 7 to white dwarfs to provide an example of its use, and calculate the kinematics of the white dwarfs in chapter 3. This is summarized in the Venn diagram in figure 1.1.

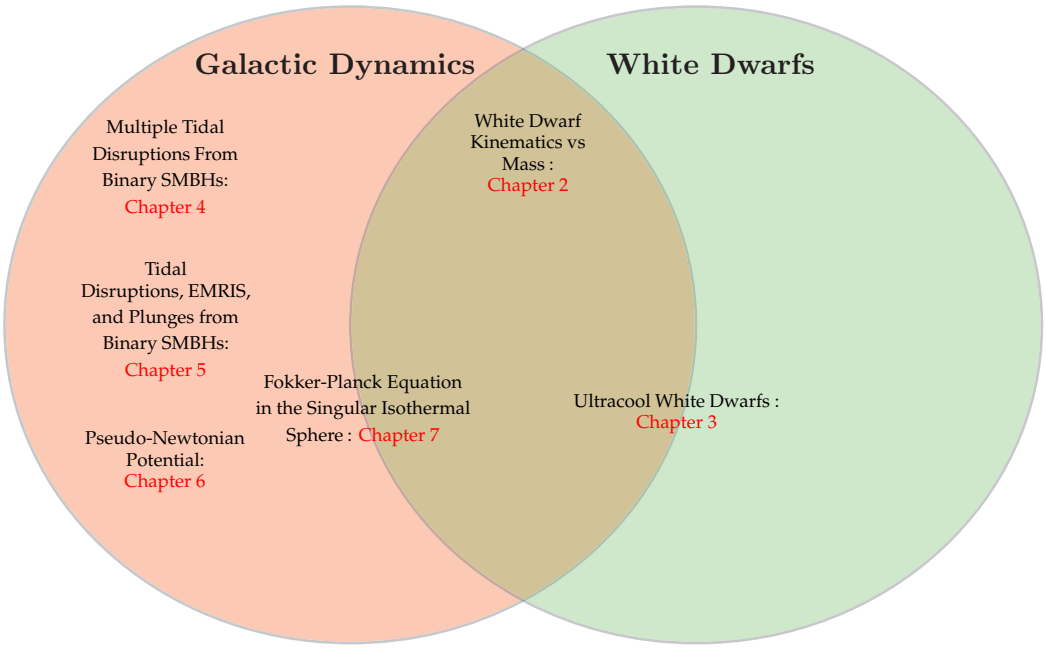

Figure 1.1 Diagrammatic overview of thesis. Chapter 3 contains only a small amount of galactic dynamics: checking the kinematics of the discovered ultracool white dwarfs. Chapter 7 contains only a small amount of white dwarf work: applying the analytic solution of the Fokker-Planck to the dynamics of white dwarfs in globular clusters.

As background to chapters 2 and 3, methods of identifying white dwarfs are introduced in section 1.2, and the kinematics of stars in the solar neighborhood in section 1.3. In chapters 4, 5 and 6 the dynamics of stars around supermassive black hole (SMBH) binaries are investigated. The relevant introductory material is contained in section 1.4, where the relevant scales are discussed in section 1.4.1, and background on SMBH binaries is contained in section 1.4.2. Chapter 7 contains an astrophysically motivated analytic solution to the Fokker-Planck equation, for which few analytic solutions are known. This chapter is more pedagogical, and the necessary background material is contained within the introduction (section 7.1).

1.2 White Dwarfs

White dwarfs are the ultimate end state of any star less massive than $\sim 8\,M_{\odot}$ and as such are ubiquitous. Despite this they can be difficult to identify, particularly the cool objects that are the focus in chapter 3. White dwarfs are simplest to identify in clusters where, owing to the common distance, they are identifiable as being sub-luminous in comparison to their pre-evolved stellar counterparts. A striking example of this is shown in figure 1.2.

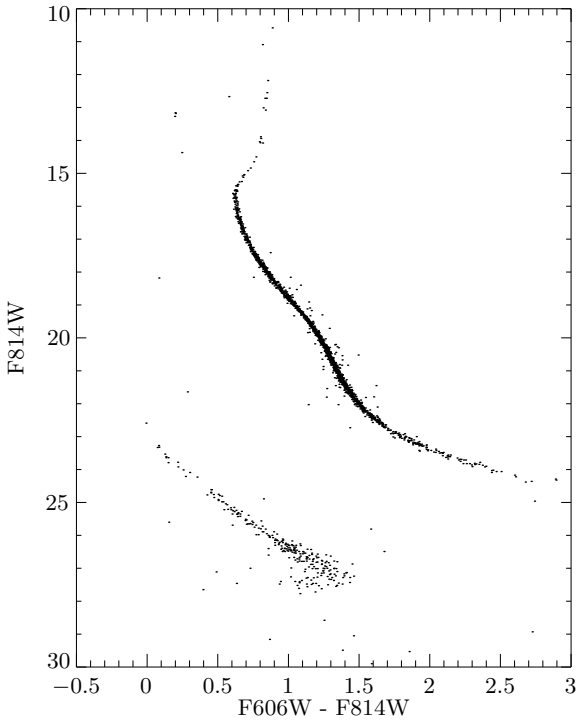

Figure 1.2 A color-magnitude plot of NGC 6397 imaged using the Advanced Camera for Surveys (ACS) on the Hubble Space Telescope (HST). The white dwarf cooling sequence is clearly visible as the sequence of objects ~ 5 mag fainter than the main sequence. Data taken from Richer et al. (2007). The cooling sequence in this cluster was examined in detail in Hansen et al. (2007) and the age of the cluster found to be 11.5 ± 0.5 Gyr (95% confidence limit).

In the field white dwarfs are more challenging to identify. We consider young, hot white dwarfs in chapter 2, which were identified via their blue colors and so targeted by SDSS for spectroscopic follow up. However after approximately 1 Gyr (for white dwarf mass $M_{\rm WD} = 0.6\,M_{\odot}$) white dwarfs cool below $\sim 8000\,K$ and their colors become indistinguishable from the stellar locus of field stars. This is demonstrated in figure 1.3.

Instead, when the white dwarfs have colors indistinguishable from the stellar locus, the reduced proper motion has often been utilized to select probable low luminosity objects and therefore

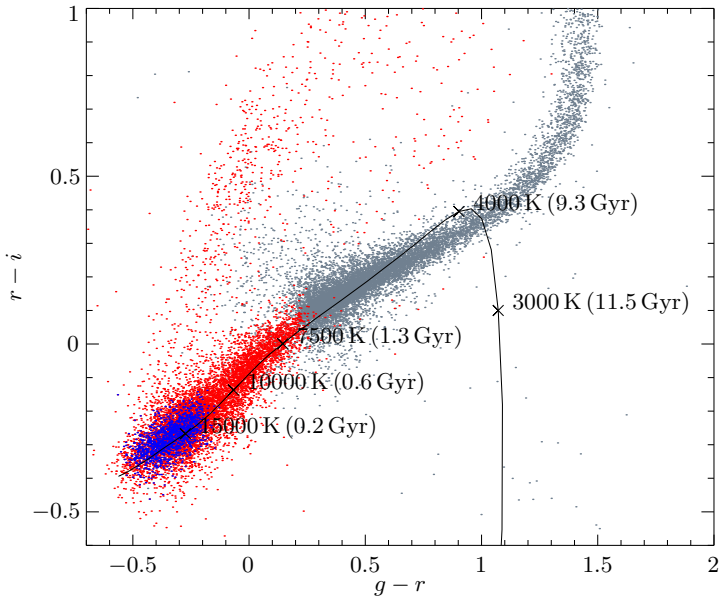

Figure 1.3 Demonstration of selection of hot white dwarfs in color-color space. In grey are all stellar objects with from SDSS in a 4 deg^2 area of sky that have a shape consistent with the PSF and 'good' photometry (see section 3.2). In red are all white dwarfs identified in SDSS DR4 (Eisenstein et al., 2006). In blue are the sample of DA white dwarfs with $T_{\rm eff} > 13000$ K whose kinematics were analyzed in chapter 2. The black line shows the WD atmospheric and cooling model of Bergeron[1] for a white dwarf with mass $0.6\,M_\odot$.

possible white dwarfs. The reduced proper motion is defined as

$$\mathrm{H} \equiv m + 5\log\mu + 5 \tag{1.1}$$

$$= M + 5\log v_\perp - 3.38\,, \tag{1.2}$$

where m and M are the apparent and absolute magnitudes, respectively, μ is the proper motion in arc-seconds per year, and $v_\perp$ is the transverse velocity in km s^{-1}. For groups of stars with the same kinematics the reduced proper motion therefore acts as a proxy, at least statistically, for the absolute magnitude. A cut is then made in the resulting color-reduced proper motion plot so as to best exclude the main stellar locus, and the remaining WD candidates targeted for spectroscopy. The disadvantage of this method is that there is little separation between low-velocity white dwarfs and high-velocity sub-dwarfs. This can result either in inefficient selection, or a highly biased sample of high-velocity white dwarfs. This is illustrated in figure 1.4, which shows there is considerable overlap between high reduced proper motion objects confirmed as white dwarfs, and those that were instead sub-dwarfs. Finally, attempts have been made to use narrow filters to eliminate this

[1] Available from http://www.astro.umontreal.ca/~bergeron/CoolingModels/, uses results from from Holberg and Bergeron (2006), Kowalski and Saumon (2006), Tremblay et al. (2011) and Bergeron et al. (2011)

contamination, however they have not yet been successful (Kilic et al., 2004).

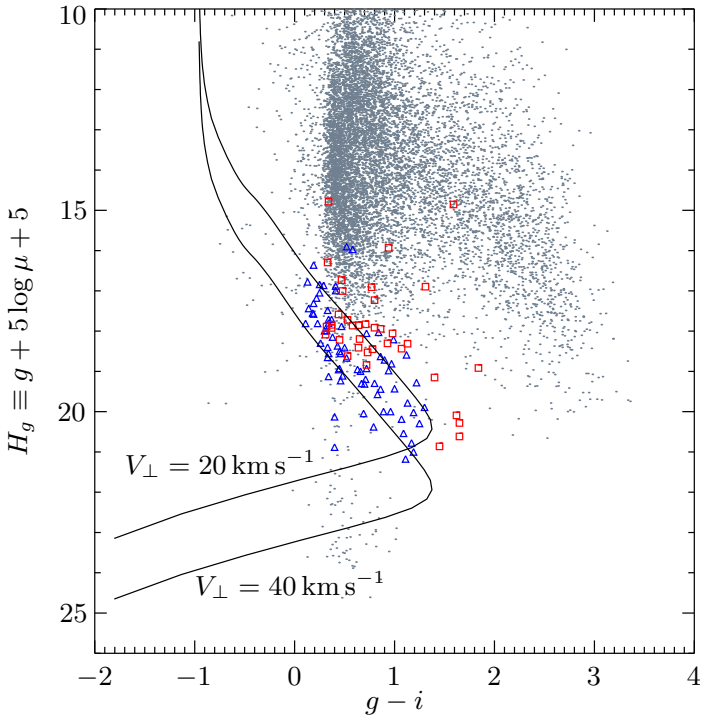

Figure 1.4 Demonstration of selection of hot white dwarfs via reduced proper motion. Blue triangles are objects selected via their high reduced proper motion and identified as white dwarfs by Kilic et al. (2006). Red square are were also selected via their high reduced proper motion but are subdwarfs. The black lines shows the WD atmospheric model of Bergeron for a $0.6\,M_\odot$ white dwarf at transverse velocities of 20 km s^{-1} and 40 km s^{-1}. In grey are all stellar objects with from SDSS in a 4 deg^2 area of sky that have a shape consistent with the PSF and 'good' photometry (see section 3.2).

The interest in the coolest white dwarfs are that they represent the remnants of the earliest populations, for all stars with initial mass $0.8\,M_\odot \lesssim M \lesssim 8\,M_\odot$. Work has been performed on the luminosity function of white dwarfs, and the age of the disk estimated from luminosity of the faintest coolest white dwarfs (e.g., Leggett et al., 1998, find 8.5 ± 1.5 Gyr for the age of the disk). In addition they represent remnants of a large fraction of stars, both by number and stellar mass. Their detection and presence in the halo[2] could therefore shed light on the low-mass end of early stellar populations.

In chapter 3 we show that the coolest, oldest white dwarfs can be identified purely photometrically via their unique colors. This can anticipated by the white dwarf models moving out of the stellar locus as the white dwarf cools below ~ 4000 K in figure 1.3.

[2]In addition Oppenheimer et al. (2001) found what appeared to be an excess of cool white dwarfs showing Halo kinematics. It was claimed that this could represent significant component of the galactic dark matter budget which briefly ignited great interest.

1.3 Local Kinematics

In chapter 2 we investigate the relationship between the kinematics of white dwarfs and their mass. The samples of white dwarfs we investigate are all in the solar neighborhood. Therefore here we briefly introduce the kinematics of stars in the local neighborhood. In figure 1.5 we plot the mean velocity and dispersion of stars in the solar neighborhood as a function of age.

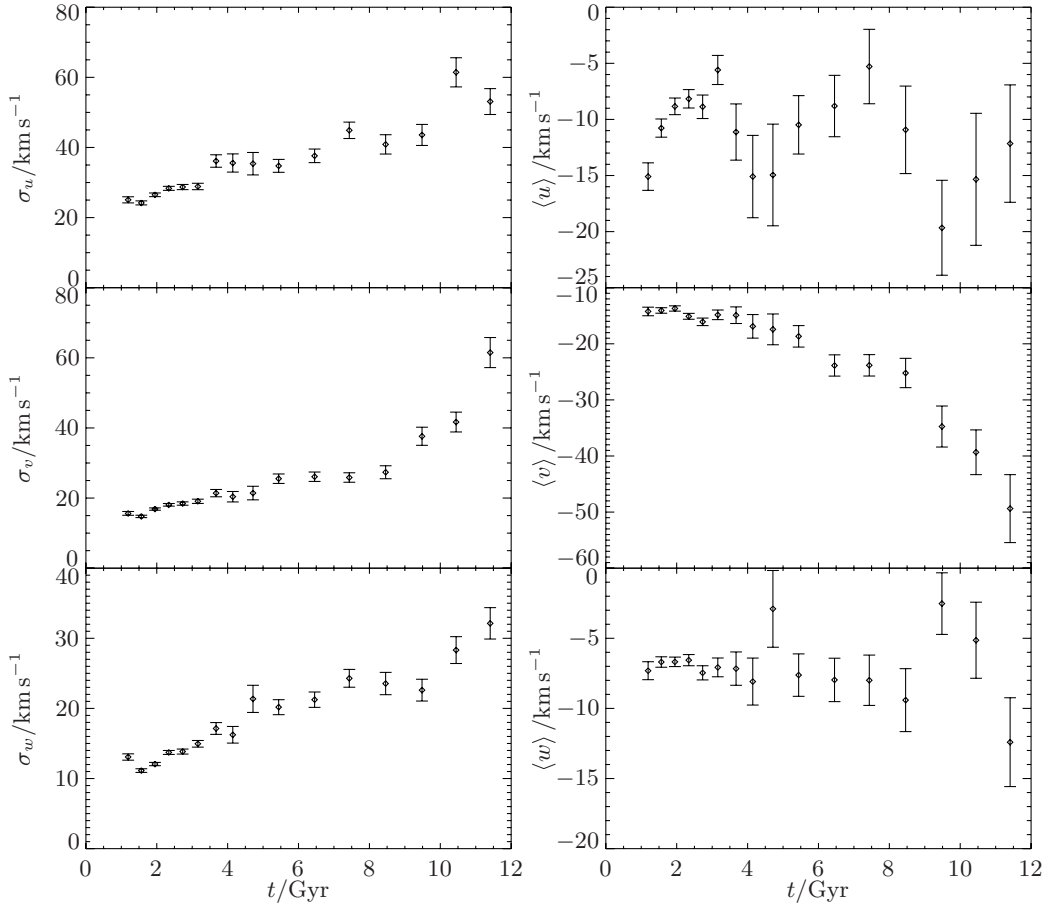

Figure 1.5 Dispersion (left panels) and mean velocity (right panels) of stars in the solar neighborhood as a function of age. U is in the direction of rotation about the galactic center, V is directed towards the galactic center, and W is towards the north galactic pole. Data is taken from the recalibrated Geneva Copenhagen survey of nearby F and G dwarf stars (Holmberg et al., 2007; Nordstrom et al., 2004). Only those stars whose ages are reliably determined, with formal error less than 20 per cent, are plotted.

In the local neighborhood the vast majority of stars are members of the disk, as is the Sun. As a result the majority of local stars have velocities around the galactic center close to the circular velocity of ~ 200 km s^{-1}. The sun has a peculiar velocity of $(U_\odot, V_\odot, W_\odot) = (10.0 \pm 0.4, 5.3 \pm 0.6, 7.2 \pm 0.4)$ km s^{-1} (Dehnen and Binney, 1998). The U and W solar motions are visible as the mean $\langle U \rangle$ and $\langle W \rangle$ in figure 1.5. Measurement of $V_\odot$ is complicated by asymmetric drift.

Detailed quantitative understanding of asymmetric drift can be found from the Jeans Equation

in cylindrical coordinates (e.g., Binney and Tremaine, 2008). However the majority of the effect can be simply understood: As the velocity dispersion is increased from zero, stars in the solar neighborhood have orbits with increasing eccentricities. However, because the density of stars increases inward, stars in the solar neighborhood are more likely to be close to apoapsis than periapsis. A star close to apoapsis will have lower velocity in the direction of galactic rotation than the Solar velocity, which has an orbit close to a circular. Therefore a group of stars with increased velocity dispersion has more negative $\langle V \rangle$. Empirically this relationship is (Dehnen and Binney, 1998)

$$\langle V \rangle = -\frac{\sigma_U^2}{(80 \pm 5)\ \mathrm{km\,s^{-1}}}\ . \tag{1.3}$$

The asymmetric drift can clearly be seen in middle right panel of figure 1.5. Extrapolating $\langle V \rangle$ to zero dispersion gives the solar velocity $V_\odot = (5.3 \pm 0.6)\ \mathrm{km\,s^{-1}}$ (Dehnen and Binney, 1998).

Also shown in figure 1.5 is the increase in velocity dispersion over time, known as disk heating. Stars are initially formed with dispersion of $\sim 10\ \mathrm{km\,s^{-1}}$, and are scattered over their lifetime to higher velocities. These scattering mechanisms may include molecular clouds, spiral arms, merging satellite galaxies, dark matter substructure or some combination of these (Binney and Tremaine, 2008).

In chapter 2 we investigate the relationship between the local kinematics of newly formed white dwarfs and their mass. We find that the dispersion increases with decreasing white mass. This can be understood to be as a result of their increased precursor lifetime from their lower-mass precursor stars.

In chapter 3 we find that all the ultracool white dwarfs discovered are consistent with thick disk kinematics. There is however one previously discovered white dwarf whose kinematics is not consistent with being a disk object, and is instead most likely a halo remnant. Halo stars have more isotropic velocity distribution, and as a result their mean velocity is $\langle V \rangle \sim -220\ \mathrm{km\,s^{-1}}$.

1.4 Supermassive Black Holes

There is now overwhelming evidence that most galactic nuclei harbor supermassive black holes (SMBHs) with mass $\gtrsim 10^6\ M_\odot$ in their centers[3]. This evidence includes (e.g., the review by Ferrarese and Ford, 2005):

- The stellar orbits which have been monitored (known as S-stars Ghez et al., 2005; Schödel et al., 2002) around the *extremely* compact (Doeleman et al., 2008) radio source Sgr A* in the center of our galaxy.

[3]Not all galaxies harbor a SMBH however: There is not one in the nearby bulgeless disk galaxy M33 (Gebhardt et al., 2001).

- Hypervelocity ($v > 275\,\mathrm{km\,s^{-1}}$) stars ejected by dynamical interactions with the SMBH in the galactic center (e.g., Brown et al., 2007; Yu and Tremaine, 2003).
- The Keplerian nature of MASER emission from the centers of a handful of nearby galaxies imply a large mass in a small region (e.g., Miyoshi et al., 1995).
- When the sphere of influence of the black hole is resolved (see equation 1.4), the stellar and gas velocity dispersion rises in the very center of many galaxies. Kinematic modeling of this indicates the presence of a massive compact object (e.g., Gebhardt et al., 2003; Sargent et al., 1978).
- The energy liberated by accretion onto a massive compact object is the only feasible model for emission from AGN due to their rapid variability and high luminosity (e.g., Ferrarese and Ford, 2005).

In chapters 4, 5, and 6 we consider the dynamics of stars around *binary* supermassive black holes (SMBHs). However first, in section 1.4.1, we introduce the relevant processes around isolated SMBHs and the scales relevant to the problem. In section 1.4.2 we extend this to SMBH binaries.

1.4.1 Supermassive Black Hole Scales

Stars whose orbits lie within the sphere of influence of the black hole have orbits whose motion is dominated by the influence of the black hole. The radius of the sphere of influence is given by

$$r_{\mathrm{inf}} \equiv \frac{GM_{\mathrm{BH}}}{\sigma^2} = 11.2\left(\frac{M_{\mathrm{BH}}}{10^8\,M_\odot}\right)\left(\frac{\sigma}{200\,\mathrm{km\,s^{-1}}}\right)^{-2}\ \mathrm{pc}\,. \tag{1.4}$$

The stars considered in chapters 4, 5, and 6 are drawn from those initially bound to the SMBH, i.e., largely inside equation (1.4).

The smallest characteristic scale of the SMBH is the Schwarzschild radius

$$r_s \equiv \frac{2GM_{\mathrm{BH}}}{c^2} = 9.6\times10^{-6}\left(\frac{M_{\mathrm{BH}}}{10^8\,M_\odot}\right)\ \mathrm{pc}\,. \tag{1.5}$$

Since the stars considered in chapters 4 and 5 have typical initial semi-major axis r_{inf}, which is much larger than r_s, stars that closely approach the SMBH normally have very high eccentricity. In chapter 6 we develop pseudo-Newtonian potentials tailored to this case. In this chapter the refer to the orbits as being 'nearly parabolic' meaning that the orbital energy of the particle is small compared to c^2. This is equivalent to having semi-major axes much larger than r_s. The usual pseudo-Newtonian potentials, and the potential of Paczyński and Wiita (1980) in particular, are tailored to particles in nearly circular orbits and accretion disks. The potentials of chapter 6 however much more

accurately trace the trajectories considered in this work, and indeed the trajectory of any 'nearly parabolic' orbit.

Stars whose orbits take them closer than the tidal disruption radius will be torn apart by tidal forces. In chapters 4 and 5 we calculate rates of tidal disruptions around SMBH *binaries*. To order of magnitude, the tidal disruption radius can be estimated by comparing the self-gravity and the tidal force experienced by a star of mass $M_\star$, and radius $R_\star$, at a distance r from the black hole. The tidal force will be $\sim R_\star \times GM_{\rm BH}/r^3$, while the stars self gravity is $\sim GM_\star/R_\star^2$. Comparing these forces the tidal disruption radius,$r_{\rm t}$, is

$$r_{\rm t} = 1.0\times10^{-5}\eta\left(\frac{R_\star\, M_\odot}{M_\star r_\odot^3}\right)^{1/3}\left(\frac{M_{\rm BH}}{10^8\, M_\odot}\right)^{1/3}\ {\rm pc} \tag{1.6}$$

$$= 1.2 r_s \eta\left(\frac{R_\star\, M_\odot}{M_\star r_\odot^3}\right)^{1/3}\left(\frac{M_{\rm BH}}{10^8\, M_\odot}\right)^{-2/3}, \tag{1.7}$$

where r_s is the Schwarzschild radius, and η is an order unity factor which depends on the structure of the star. Therefore for sun-like stars when $M_{\rm BH} > 1.2\times10^8\, M_\odot$ the tidal disruption radius lies within the Schwarzschild radius, and the star silently 'plunges' across the event horizon, adding only to the mass of the black hole with no observational consequences. higher-mass black holes can disrupt stars if the spinning and the orientation is prograde. For maximal spin, SMBHs with mass up to $\sim 8\times10^8\, M_\odot$ are able to disrupt with the correct orientation (Beloborodov et al., 1992; Kesden, 2012). The typical eccentricities of the particles of interest in chapters 4 and 5 (i.e., those that plunge, become an EMRI) or are tidally disrupted will be $1-e\sim r_s/r_h$ and $1-e\sim r_s/r_t$ which is of order 10^{-5}. It is important therefore that the integrator used is able to accurately integrate these highly eccentric orbits. For this reason we use the adaptive symplectic integrator of Preto and Tremaine (1999) whose implementation is described in chapter 5. Since it integrates the paths of orbits in Keplerian potentials *exactly*, it is ideal for the highly eccentric orbits considered.

An important timescale in our simulations is the dynamical timescale, or the time is takes for stars to cross the system. This is given by[4]

$$t_{\rm dyn} \equiv \sqrt{\frac{r^3}{GM_{\rm BH}}} = 1,500\left(\frac{r}{1\ {\rm pc}}\right)^{3/2}\left(\frac{M_{\rm BH}}{10^8\, M_\odot}\right)^{-1/2}\ {\rm yr}\,. \tag{1.8}$$

The other relevant timescale is the relaxation time. This is the characteristic timescale on which the stellar distribution evolves. The relaxation time due to star-star interactions is to order of

[4]Note that by defining $t_{\rm dyn}$ to depend on $M_{\rm BH}$ and not the mass enclosed at radius r, $M(<r)$ this is longer than the orbital timescale when the stars contribute considerably, i.e., close to $r_{\rm inf}$. However most of our interesting events come from stars where this is not the case, and this definition remains constant even as the distribution evolves.

magnitude given by (Binney and Tremaine, 2008)

$$t_{\rm rlx} \sim \frac{0.1N}{\log N}\frac{t_{\rm dyn}}{2\pi} \sim 10^{10}\left(\frac{M_{\rm BH}}{10^8\,M_\odot}\right)^{1/2}\left(\frac{r}{1\ {\rm pc}}\right)^{3/2}\ {\rm yr}\,, \tag{1.9}$$

where N, the number of stars in the system is $\sim M_{\rm BH}/M_\odot$.

Since this timescale is much longer than the ~ 1 Myr simulations in chapters 4 and 5 we ignore star-star scatterings[5] and the problem becomes a parallel series of reduced three-body scatterings.

On timescales longer than the relaxation time, the system is expected to relax to its equilibrium configuration. This single mass systems this is known as a Bahcall-Wolf cusp (Bahcall and Wolf, 1976). To derive this equilibrium solution[6], first assume the power law ansatz, $\rho \propto r^{-\eta}$. More accurate calculations than equation (1.9), of the type performed in chapter 7, find that the local star-star relaxation time is given by (equation 7.106 of Binney and Tremaine, 2008)

$$t_{\rm rlx} \sim \frac{\sigma^3}{G^2 M_\star \rho \log\Lambda}\,. \tag{1.10}$$

where $\log\Lambda$ is the Coulomb logarithm. The velocity dispersion close to the SMBH will rise as $\left\langle v^2\right\rangle = \sigma^2 = GM_{\rm BH}/r$ and therefore $t_{\rm rlx} \propto r^{\eta-3/2}$. A star that is destroyed by the hole via, for example, a tidal disruption, coming from radius r, has energy $E = -GM_{\rm BH}M_\star/r$. If $N(r)$ is the number of stars interior to r, then the flow from radius r will be approximately $N(r)E(r)$ per relaxation time. Since $N(r) \propto r^{3-\eta}$ then the energy flux is approximately $N(r)E(r)/t_{\rm rlx} \propto r^{2-\eta}/r^{\eta-3/2} = r^{7/2-2\eta}$. In steady state the flux must be independent of radius and therefore $\eta = 7/4$. This equilibrium solution, whereby the density of stars forms a cusp with $\rho \propto r^{-7/4}$, is known as a Bahcall-Wolf cusp.

In multimass systems mass segregation complicates the above argument. However, provided that there the highest-mass components are massive enough and not too numerous (Alexander and Hopman, 2009), then the heaviest component forms a $\rho \propto r^{-7/4}$ cusp close the hole, while the lighter components are less centrally concentrated. This has been shown via analytic calculations (Alexander and Hopman, 2009; Bahcall and Wolf, 1977; Keshet et al., 2009) and is born out in numerical simulations (Freitag et al., 2006).

The relaxation timescale in equation (1.9) represents a considerable uncertainty in the processes and dynamics around SMBHs since it is of the same order as the Hubble timescale, as well as the timescale between major mergers which would destroy the equilibrium state. Therefore it is not clear whether the Bahcall-Wolf cusp is realized in the majority of galaxies. Indeed the best resolved cusp is in the center of our galaxy, where the surface density rises consistent with a $\rho \propto r^{-1.5}$ cusp (Genzel et al., 2003). This interpretation however assumes a constant mass-to-light ratio, which

[5] This is not as good an approximation in some cases as it may naively appear: The relaxation time to change the angular momentum by of order unity is is reduced to $(1-e)t_{\rm rlx}$ which can be near to the length of the simulation for some stars.

[6] This argument follows section 7.5.9b of Binney and Tremaine (2008).

would not be the case if there is mass segregation. Around external galaxies the ACS Virgo sample of galaxies (Côté et al., 2004) appears to show that more massive galaxies ($\gtrsim 240\,\mathrm{km\,s^{-1}}$) tend to have less-steep cores than the Bahcall-Wolf cusp (Merritt et al., 2009).

In chapter 5 we also consider the dynamics of compact objects (i.e., stellar mass black holes, neutron stars, white dwarfs) around SMBH binaries. In this case the star is not tidally disrupted on close encounters, and general relativistic corrections can become important.

In the radial direction, the orbits of test particles around a Schwarzschild black hole in General Relativity can be reduced to one-dimensional motion in an effective potential (equation 25.16 of Misner et al., 1973)

$$\left(\frac{dr}{d\tau}\right)^2 = \left(\frac{E}{c^2}+1\right)^2 - V^2(r)\,, \tag{1.11}$$

where $V(r)$ is the effective potential given by

$$V^2(r) = \left(1-\frac{r_s}{r}\right)\left(1+\frac{L^2}{c^2r^2}\right)\,. \tag{1.12}$$

In these equations r is the radial coordinate in the Schwarzschild metric, E and L are the orbital energy and angular momentum, respectively, per unit rest mass of the orbiting particle, and τ is the proper time.

For the orbits of interest $E \ll 1$ and periapsis and apoapsis of the test particle correspond to the roots of

$$\left(1-\frac{r_s}{r_\pm}\right)\left(1+\frac{L^2}{c^2{r_\pm}^2}\right) \approx 1\,, \tag{1.13}$$

where r_+ and r_- are the two largest roots of the quartic and correspond to the apoapsis and periapsis, respectively. However if $L \leq 2r_s c = 4\,GM_{\rm BH}/c$ then a real solution for r_- does not exist and so a particle traveling towards the black hole with angular momentum $L \leq 4\,GM_{\rm BH}/c$ with $dr/dt < 0$ experiences no turning point in dr/dt and 'plunges' across the event horizon. The orbit with $L = 4\,GM_{\rm BH}/c$ is known as the separatrix (Cutler et al., 1994) or the unstable circular orbit (UCO) (Gair et al., 2005).

When gravitational radiation is included finite mass objects with $L > 4GM_{\rm BH}/c$ may still be captured by the SMBH. At each close periapse passage a burst of gravitational radiation is emitted, and the object gradually loses energy and angular momentum inspiraling into the SMBH. This process whereby a stellar mass object inspirals into an SMBH is known as an extreme mass ratio inspiral (EMRI).

Using the approximation of Peters (1964) (whereby the orbit remains Keplerian, and radiation

is calculated to quadrupole order), then the time for an EMRI to inspiral is[7] (Freitag, 2003)

$$t_{\rm emri} = 3.2\times10^9\left(\frac{M_{\rm BH}}{10^8M_\odot}\right)^2\left(\frac{M_\star}{10M_\odot}\right)^{-1}\left(\frac{r_p}{10r_s}\right)^4\left(\frac{1-e}{10^{-5}}\right)^{-1/2}\ {\rm yr}\,. \tag{1.14}$$

In order for an object to inspiral as an EMRI it cannot be perturbed too greatly by scatterings from other stars. The relaxation time $t_{\rm rlx}$ is the time for stars angular momentum to be perturbed by of order the circular angular momentum, $L_{\rm c}$. In the Newtonian limit $L^2 = GMa(1-e^2) = L_{\rm c}^2(1-e^2) \approx 2L_{\rm c}^2(1-e) = 2\,GMr_p$. Since star-star scatterings constitute a random walk then $\Delta L/L_{\rm c} = \sqrt{t/t_{\rm rlx}}$ where ΔL is the change in L. Therefore the time for a potential EMRI to change h, and therefore its periapsis distance, by order unity is $\sim t_{\rm rlx}L^2/L_{\rm c}^2 \sim (1-e)t_{\rm rlx}$. This results in a region of parameter space where $t_{\rm emri}(1-e) < t_{\rm rlx}$. Stars scattered into this region are likely to become EMRIs.

1.4.2 Supermassive Black Hole Binaries

In section 1.4 we described some of the overwhelming evidence that most galaxies harbor a SMBH in their center. In addition galaxies are known to merge regularly, both observationally (Lotz et al., 2011), and from the success of cosmological simulations showing the hierarchical merger of their parent halos (Stewart et al., 2009). However the evidence for the formation, and merger, of binary SMBHs is remarkably limited.

The standard picture by which SMBH binaries form, and merge, is set out in Begelman et al. (1980). Initially the black holes in their parent galaxies are efficiently brought together by dynamical friction with the surrounding stars on a timescale

$$t_{\rm df} = \frac{v^3}{4\pi\log\Lambda\ M_{\rm gal}\,\rho(<v)}\,. \tag{1.15}$$

where $M_{\rm gal}$ is the mass of the less massive galaxy, and $\rho(<v)$ is the local density of stars with velocity less than v. Considering the larger galaxy to be a singular isothermal sphere with $\rho = \sigma_1^2/2\pi Gr^2$, and that the satellite is stripped of stars as it inspirals, truncated at its Hill radius, then the satellite galaxy inspirals on a timescale (Binney and Tremaine, 2008)

$$t_{\rm df} = 2.7\,{\rm Gyr}\frac{1}{\log\Lambda}\left(\frac{\sigma_1}{200\ {\rm km\,s^{-1}}}\right)^2\left(\frac{100\ {\rm km\,s^{-1}}}{\sigma_2}\right)^3\left(\frac{r_i}{30\ {\rm kpc}}\right)\,. \tag{1.16}$$

where σ_1 and σ_2 is the velocity dispersion of the more massive and satellite galaxy, respectively, and r_i is the initial distance between the galaxy centers.

Eventually, provided that the ratio of velocity dispersions is not too great, the SMBHs in their

[7] However in chapter 5 the Peters (1964) expressions are not used for the loss due to gravitational radiation. Instead more accurate expressions for the loss of energy and angular momentum given by Gair et al. (2006b) using semianalytic fits to the Teukolsky equation are used.

centers will form a bound binary system. In chapters 4 and 5 we consider the SMBHs to be surrounded by a cusp of stars. In this case the SMBHs will continue to inspiral rapidly by a combination of dynamical friction (i.e., weak scatterings) and ejections (strong scatterings) until insufficient mass in stars remains. Stars will be ejected from the binary with a specific energy of order $\sim GM_1/R$ where M_1 is the mass of the primary SMBH, and R is their separation. Each subsequent reduction of the semi-major axis by a factor of two in requires that a mass of stars very approximately equal to the secondary SMBH mass, M_2, be ejected. The evolution will therefore stall at a radius $R_{\rm stall}$ given by

$$M_\star(< R_{\rm stall}) \sim M_2 \,, \tag{1.17}$$

where M_1 and M_2 are the masses of the more massive, primary SMBH and the less massive, secondary SMBH, respectively, and C is a numerical coefficient to be found via scattering experiments. Assuming a Bahcall and Wolf (1976) cusp with stellar mass, $M_\star(< r) = 2M_1(r/r_c)^{-3/4}$, and radius r_c, given by equation (4.6) then the stalling radius is

$$R_{\rm stall} \sim (q/2)^{4/5} r_c = 2\,(q/2)^{4/5}(M_1/10^8 M_\odot)^{0.55}\,{\rm pc}\,. \tag{1.18}$$

In chapters 4 and 5 we make use of the simulations of Sesana et al. (2008), who determines $R_{\rm stall}$ for a range of mass ratios to be approximately a factor of 10 smaller than the crude estimate in equation (1.18).

The other manner in which the binary will evolve is via scatterings with stars outside their immediate cusps. However only stars with angular momentum $L \lesssim \sqrt{G(M_1+M_2)R_{\rm stall}}$ will approach and subsequently be ejected, extracting energy from the binary. Stars within this region of angular momentum are referred to as being in the loss cone. Each subsequent reduction of the semi-major axis by a factor of two requires that a mass of stars equal to the secondary SMBH mass be ejected. Therefore the evolution stalls once more when the mass of stars in the loss cone is less than the mass of the secondary. After this the evolution proceeds more slowly, as stars are scattered into the loss cone, on the much longer relaxation timescale.

At sufficiently close separations the evolution is driven by gravitational radiation. A SMBH binary in a circular orbit with separation a will decay in a timescale (Peters, 1964)

$$\begin{aligned} t_{\rm gw} &= \frac{5c^5 a^4}{256 G^3 M_{\rm BH}^3 q(1+q)} \\ &= 58\,\frac{(1+q)^2}{q}\left(\frac{a}{0.1\,{\rm pc}}\right)^4\left(\frac{M_{\rm BH}}{10^8 M_\odot}\right)^{-3}\ {\rm Gyr}\,. \end{aligned} \tag{1.19}$$

An unsolved problem is the manner in which the binary reaches a radius at which $t_{\rm gw}$ becomes less than the age of the universe. The most naive approximation, that stars enter the loss cone

due to star-star scatterings, results in a timescale longer than a Hubble time. Since this occurs at scales of a parsec or less it is often referred to as 'the final parsec problem' (Milosavljević and Merritt, 2003). Many attempts have been made to solve this problem. These include evolution in flattened and triaxial galaxies (Yu, 2002), the Brownian wandering of the binary about the galactic center (Chatterjee et al., 2003), perturbations from a third SMBH and the Kozai mechanism (Blaes et al., 2002), and the evolution to high eccentricity of the SMBH binary (Iwasawa et al., 2011; Khan et al., 2011). In wet mergers (where gas is present) this could also help drive the binary to merger (Armitage and Natarajan 2002; Ivanov et al. 1999, but see also Lodato et al. 2009).

Despite this uncertainty in SMBH binary dynamics two things are more secure: 1. The timescale for evolution of the binary lengthens considerably after the binary has hardened. 2. This timescale appears to empirically be less than a Hubble time in the majority of SMBH binaries since there is little evidence that nearby SMBHs are members of binaries. I.e., it appears Nature has solved the final parsec problem, we are just not sure how she did it.

Based on the theoretical picture outlined above it is expected that many SMBH binary systems should exist, particularly at separations close to the stalling radius. It is therefore surprising that no secure close binary SMBH systems have been found.

At wide, $\sim$ kpc scales many pairs of quasars at the same redshift are visible. While most of these are actually multiple images of the same quasar, at least some are convincingly pairs of black holes (e.g., Komossa, 2003; Mortlock et al., 1999). However, there are no convincing subparsec scale SMBH binaries. One candidate is OJ 287, (Valtonen et al., 2008, 2010) a postulated $1.8\times10^{10}\,M_{\odot}$ black hole within 10,000 years of merging at a redshift of 0.3. A priori such a system is unlikely, however in the coming decade pulsar timing measurements should be able to test the binary nature of OJ 287. In the same way a postulated SMBH binary with period 1.05 years in 3C 66 (Sudou et al., 2003) was ruled rules out by the lack of pulsar timing residuals predicted by gravitational wave emission from the system (Jenet et al., 2004). At present the closest we have come to observing a SMBH binary at its stalling radius is in 0402+379: A pair of radio loud AGN at a projected separation of only 7.3 pc (Rodriguez et al., 2006, 2009). However, despite extensive searches, there is a paucity of observed close SMBH binaries.

In chapter 4 a novel method to identify the elusive close SMBH binaries is proposed, using the greatly increased tidal disruption rate as the SMBH binary stalls.

In chapter 5 the simulations are expanded upon, both explaining the simulations in more detail, and increasing the number of simulated systems. We have also included general relativistic corrections so that the simulations incorporate emission of gravitational waves and precession (which is described in chapter 6). This allows the simulation of EMRIs and plunges from compact objects around SMBH binaries. Detection of the perturbations in the EMRI waveform by low-frequency gravitational wave missions, such as the successors to LISA, would also provide a novel

close SMBH binary detection strategy (Yunes et al., 2011).

1.5 The Fokker-Planck Equation

In chapter 7 we present a new, astrophysically relevant, analytic solution to the Fokker-Planck equation, and introduce the Fokker-Planck Equation as background to that chapter here. The Fokker-Planck equation is often used in astrophysics, particularly in simulations of the evolution of globular clusters (e.g., Cohn, 1979; Cohn and Kulsrud, 1978; Freitag and Benz, 2001; Joshi et al., 2000; Quinlan, 1996) or around supermassive black holes (e.g., Alexander and Hopman, 2009; Hopman, 2009; Hopman and Alexander, 2005; Keshet et al., 2009; Lightman and Shapiro, 1977; Magorrian and Tremaine, 1999; Preto and Amaro-Seoane, 2010). The Fokker-Planck equations utility is that it can be integrated much faster than direct N-body simulations, as well as lending itself more easily to physical understanding of the underlying physical processes.

We begin by deriving the collision-less Boltzmann equation before generalizing to the Fokker-Planck equation. A distribution function $f(\boldsymbol{p}, \boldsymbol{q})$ where $\boldsymbol{q}$ are positions, $\boldsymbol{p}$ their conjugate momenta, specifies the number of stars in a region of phase space, i.e., $dN = f(\boldsymbol{p}, \boldsymbol{q})\, d\boldsymbol{p}\, d\boldsymbol{q}$. As such (ignoring interactions) it must satisfy a continuity equation

$$\frac{\partial f}{\partial t} + \frac{\partial f}{\partial \boldsymbol{p}} \cdot \dot{\boldsymbol{p}} + \frac{\partial f}{\partial \boldsymbol{q}} \cdot \dot{\boldsymbol{q}} = 0 \tag{1.20}$$

which may be more elegantly expressed using Hamilton's equations of motions as

$$\frac{\partial f}{\partial t} + \{f, H\} = 0 \tag{1.21}$$

where $\{\ \cdot\ , H\}$ is the Poisson bracket with the Hamiltonian. Equations (1.20) or (1.21) are known as the collision-less Boltzmann equation. Generally a self-consistent distribution function must also satisfy Poisson's equation:

$$\nabla^2 \Phi = 4\pi G \rho = 4\pi G m \int f\, d\boldsymbol{p} \tag{1.22}$$

where m is the mass of the stars being considered.

Interactions between stars modify the Boltzmann equation. Consider $\Psi(\boldsymbol{w}, \Delta\boldsymbol{w})\, d\Delta\boldsymbol{w}\, dt$ to be the probability that a star in phase space at $\boldsymbol{w} = (\boldsymbol{p}, \boldsymbol{q})$ scatters via interactions to $\boldsymbol{w} + \Delta\boldsymbol{w}$. This modifies the right-hand side of equation (1.21):

$$\begin{aligned} \frac{\partial f}{\partial t} + \{f, H\} = \int d\Delta\boldsymbol{w}\, \big[&\Psi(\boldsymbol{w} - \Delta\boldsymbol{w}, \Delta\boldsymbol{w}) f(\boldsymbol{w} - \Delta\boldsymbol{w}) \\ &- \Psi(\boldsymbol{w}, \Delta\boldsymbol{w}) f(\boldsymbol{w})\big] \end{aligned} \tag{1.23}$$

where the first term in the square brackets is the flux into $\boldsymbol{w}$ from $\boldsymbol{w} - \Delta\boldsymbol{w}$ and the second is the flux out of $\boldsymbol{w}$ into $\boldsymbol{w} + \Delta\boldsymbol{w}$. Equation (1.23) is known as the Master equation.

The Fokker-Planck equation results from the observation that in relaxation or dynamical friction equal decades of impact parameter between stars contribute equally. Since there typically many more decades in a system which result in small perturbational scatterings than large scatterings then the integrand of equation (1.23) can be expanded in a Taylor series. Truncating at second order this gives

$$\begin{aligned}\Psi(\boldsymbol{w} - \Delta\boldsymbol{w}, \Delta\boldsymbol{w}) f(\boldsymbol{w} - \Delta\boldsymbol{w}) - \Psi(\boldsymbol{w}, \Delta\boldsymbol{w}) f(\boldsymbol{w}) = \\ - \sum_i \Delta w_i \Delta w_j \frac{\partial}{\partial w_i} \left[\Psi(\boldsymbol{w}, \Delta\boldsymbol{w}) f(\boldsymbol{w})\right] + \frac{1}{2} \sum_{i,j} \Delta w_i \frac{\partial^2}{\partial w_i \partial_j} \left[\Psi(\boldsymbol{w}, \Delta\boldsymbol{w}) f(\boldsymbol{w})\right]\end{aligned} \tag{1.24}$$

As a result equation (1.23) becomes a diffusion equation known as the Fokker-Planck equation

$$\frac{\partial f}{\partial t} + \{f, H\} = - \sum_i \frac{\partial}{\partial w_i} \left[D_i^1 f(\boldsymbol{w})\right] + \frac{1}{2} \sum_{i,j} \frac{\partial^2}{\partial w_i \partial_j} \left[D_{ij}^2 f(\boldsymbol{w})\right] \tag{1.25}$$

where the diffusion coefficients are given by

$$D_i^1 = \int d\Delta\boldsymbol{w}\, \Psi(\boldsymbol{w}, \Delta\boldsymbol{w}) \Delta w_i \,, \tag{1.26}$$

$$D_{ij}^2 = \int d\Delta\boldsymbol{w}\, \Psi(\boldsymbol{w}, \Delta\boldsymbol{w}) \Delta w_i \Delta w_j \,. \tag{1.27}$$

The Fokker-Planck equation is a second-order partial differential equation (PDE) which admits analytic solutions in only a handful of cases (e.g., Risken, 1989). We present a new, astrophysically motivated, analytic solution in chapter 7.

2

White Dwarf Kinematics vs Mass[1]

Abstract

We have investigated the relationship between the kinematics and mass of young ($< 3 \times 10^8$ years) white dwarfs using proper motions. Our sample is taken from the color-selected catalogues of SDSS (Eisenstein et al., 2006) and the Palomar-Green Survey (Liebert et al., 2005), both of which have spectroscopic temperature and gravity determinations. We find that the dispersion decreases with increasing white dwarf mass. This can be explained as a result of less scattering by objects in the Galactic disk during the shorter lifetime of their more-massive progenitors. A direct result of this is that white dwarfs with high mass have a reduced scale height, and hence their local density is enhanced over their less-massive counterparts. In addition, we have investigated whether the kinematics of the highest-mass white dwarfs ($> 0.95\,M_\odot$) are consistent with the expected relative contributions of single-star evolution and mergers. We find that the kinematics are consistent with the majority of high-mass white dwarfs being formed through single-star evolution.

[1]This chapter is a slight expansion of an article accepted by MNRAS with the authors as: Christopher Wegg and Sterl Phinney in this order, arXiv:1206.1056, (Wegg and Phinney, 2012).

2.1 Introduction

Despite the significant work on both the kinematics and mass distribution of white dwarfs, very little work has addressed their connection.

The kinematics of galactic white dwarfs have been studied on numerous occasions with several motivations. They have proven useful in attempts to unravel the evolutionary history and progenitors of the various classes of white dwarfs (Anselowitz et al., 1999; Sion et al., 1988). Interest in white dwarf kinematics was also prompted by the suggestion that halo white dwarfs could provide a significant contribution to Galactic dark matter (Oppenheimer et al., 2001; Reid, 2005). This effort has concentrated on the identification of halo white dwarfs and estimating the resultant density, which now appears to be a small contribution to the Galactic dark matter budget (Pauli et al., 2006). Moreover, the mass distribution of the most common hydrogen rich (DA) white dwarfs has also been extensively investigated, particularly for white dwarfs with $T \gtrsim 10{,}000\,\mathrm{K}$ which are hot enough for their masses to be deduced spectroscopically from fits to their Balmer lines (Kepler et al., 2007; Liebert et al., 2005; Vennes, 1999). The mass distribution shows a peak at $0.6\,\mathrm{M}_{\odot}$ due to the relative abundance of their lower-mass progenitors with a tail extending to higher-masses formed from more-massive progenitors.

The connection between the galactic kinematics of a group of thin disk objects and their progenitors is largely due to the process of kinematic disk 'heating' (Nordstrom et al., 2004; Wielen, 1977). The hot white dwarfs with short cooling ages we observe in the galactic neighborhood today are formed from a wide range of progenitor masses (~ 0.8–$8\,M_{\odot}$) and hence have a wide range in age. We therefore expect high-mass disk white dwarfs to have a low velocity dispersion in comparison to low-mass disk white dwarfs whose progenitors formed earlier. This connection was suggested in Guseinov et al. (1983) who performed an analysis suggesting that white dwarfs with larger masses have smaller dispersions, however this was re-investigated by Sion et al. (1988) with a larger sample of 78 DA white dwarfs where no evidence for any correlation was found. This paper readdresses the connection between mass and kinematics with a greatly increased sample size.

The outline of the paper is as follows: In section 2.2 we discuss the sample selection and the calculation of distances and proper motions. In section 2.3 we discuss how we estimate the kinematics of the sample without radial velocity information. We use two methods, that of Dehnen and Binney (1998) (section 2.3.1), and a Markov Chain Monte Carlo (MCMC) where we marginalize over the unknown radial velocity (section 2.3.2). In section 2.4 we analyze whether the kinematics are consistent with single-star evolution (SSE) both via analytic methods (section 2.4.1) and simulations (section 2.4.2). In section 2.5 we analyze whether the highest-mass white dwarfs are largely formed through single-star evolution or are the product of the merger of two lower-mass white dwarfs. Finally, we discuss the implications of our findings on the scale height of white dwarfs in section

2.6.

For the reader in a hurry, the primary result of this paper, the relationship between the mass of young white dwarfs and their velocity dispersion, is shown in figure 2.3 and discussed in section 2.3. The implied scale heights, the second key result, are then discussed in section 2.6 and shown in figure 2.18. These results have been checked using a Monte Carlo simulation of the formation and observation of an ensemble of white dwarfs, which is described by flowcharts in figures 2.6–2.8: in figure 2.6 the process of choosing stars is described, in figure 2.7 the process of placing them in the disk is described, and in figure 2.8 the process of determining the observability of the simulated white dwarf is described.

2.2 Sample

We investigate only hydrogen atmosphere (DA) white dwarfs due to the relative simplicity of their spectra and the resultant security of the spectroscopic masses. The sample of DA white dwarfs is taken from two sources, the Palomar-Green (PG) white dwarf survey (Liebert et al., 2005) and the SDSS DR4 white dwarf survey (Eisenstein et al., 2006). The SDSS sample is much larger the the PG sample. The PG sample is included as a demonstration that the results are secure, and not a result of systematics in SDSS, such as the complex selection of targets. For clarity we first discuss which types of white dwarfs we select, then discuss how the SDSS survey is dealt with, and finally how the PG survey was dealt with. The sample and its selection is summarized in table 2.1.

Selected White Dwarfs: Both PG and SDSS are color selected, eliminating the kinematic biases inherent in proper motion based surveys, and contain spectroscopic determinations of surface gravity, $\log g$, and effective temperature, $T_{\rm eff}$, obtained by fitting the profile of the Balmer lines. We restrict the sample to objects whose fitted $T_{\rm eff}$ was between 13,000 K and 40,000 K, since $\log g$ appears to be systematically overestimated at low temperatures and $T_{\rm eff}$ overestimated at higher temperatures (Eisenstein et al., 2006).

The fitted $\log g$ and $T_{\rm eff}$ are converted to masses and ages using the models of the carbon core white dwarf cooling models of Fontaine et al. (2001) below 30,000 K and Wood (1995) with thick hydrogen layers of fractional mass 10^{-4} above 30,000 K [1]. White dwarfs with inferred masses less than 0.47 $M_\odot$ are instead assumed to have helium cores whose masses and ages are calculated from the models of Serenelli et al. (2001). Only objects with cooling ages below 3×10^8 years are included in the sample to avoid significant kinematic heating after white dwarf formation. The requirements of cooling age below 3×10^8 years and $T_{\rm eff}$ above 13,000 K are competing. Above 0.60 $M_\odot$ the WDs cool more slowly and thus the age limit is used, while below 0.60 $M_\odot$ the temperature limit is used.

White dwarfs previously discussed in the literature as known members of binaries were removed from the samples.

SDSS Survey (Eisenstein et al., 2006): Many of the SDSS spectra have low signal-to-noise ratios and hence large errors on their fitted $\log g$ and $T_{\rm eff}$. To ensure accurate masses and photometric distances only objects whose spectra had a signal-to-noise ratio larger than 10 are included. The grid of model atmospheres fitted in the SDSS catalog extends only to $\log g = 9$, and thus, for objects at this limit, the refitted $\log g$ and $T_{\rm eff}$ given in Kepler et al. (2007) were used.

Photometric distances to the white dwarfs in SDSS are calculated by minimizing

$$\chi^2 = \sum_{i=(u,g,r,i,z)} (m_i - [M_i(\log g, T_{\rm eff}) + A_g a_i + 5\log d - 5])^2/\sigma_i^2 \quad (2.1)$$

where m_i and σ_i are the 5 band SDSS photometry and their errors, M_i are the model absolute magnitudes, $A_g a_i$ is the reddening and d the distance in parsecs. The photometric σ_i is the quoted photometric error in SDSS each band added in quadrature to a systematic error of $(u, g, r, i, z) = (0.015, 0.007, 0.007, 0.007, 0.01)$ (Kleinman et al., 2004). Model absolute magnitudes are taken from the atmospheric models provided by Bergeron[2]. $A_g a_i$ is the product of $R_V = 3.1$ extinction in each band of $(a_u, a_g, a_r, a_i, a_z) = (1.36, 1.00, 0.73, 0.55, 0.39)$ and the overall extinction A_g, which is constrained to lie between zero and the value of galactic extinction map of Schlegel et al. (1998) at the position of the object considered.

The resulting distribution of χ^2 values calculated by minimizing equation (2.1) is plotted in figure 2.1. It closely resembles a χ^2 distribution, but with an extended tail. Objects with reduced χ^2 larger than 5 were removed from the sample, most of these objects show an excess towards the redder photometric bands, indicating they are in binaries with a cooler white dwarf companion. Errors in the photometric distance are taken to be the $\Delta\chi^2 = 1$ surface added in quadrature to the distance errors introduced though the uncertainty in $\log g$ and $T_{\rm eff}$.

Proper motions for the SDSS sample are taken from the catalogue of Munn et al. (2008). These proper motions are calculated from the USNO-B1.0 plate positions re-calibrated using nearby galaxies together with the SDSS position so that the proper motions are more accurate and absolute. By measuring the proper motions of quasars Munn et al. (2004) estimates that the 1σ error is 5.6 mas yr^{-1}.

PG Survey: For 132 stars in the PG survey, SDSS photometry was available and the same method was used as for SDSS stars. For the remaining objects the PG catalog photometric distances were used. These were estimated in Liebert et al. (2005) from comparison of the V band magnitude with the predicted M_V from the same models of Holberg and Bergeron (2006). Comparison of the stellar distances given by the two methods gives a standard deviation of 7 per cent. The majority of this

[2]Available from http://www.astro.umontreal.ca/~bergeron/CoolingModels/, uses results from from Holberg and Bergeron (2006), Kowalski and Saumon (2006), Tremblay et al. (2011) and Bergeron et al. (2011)

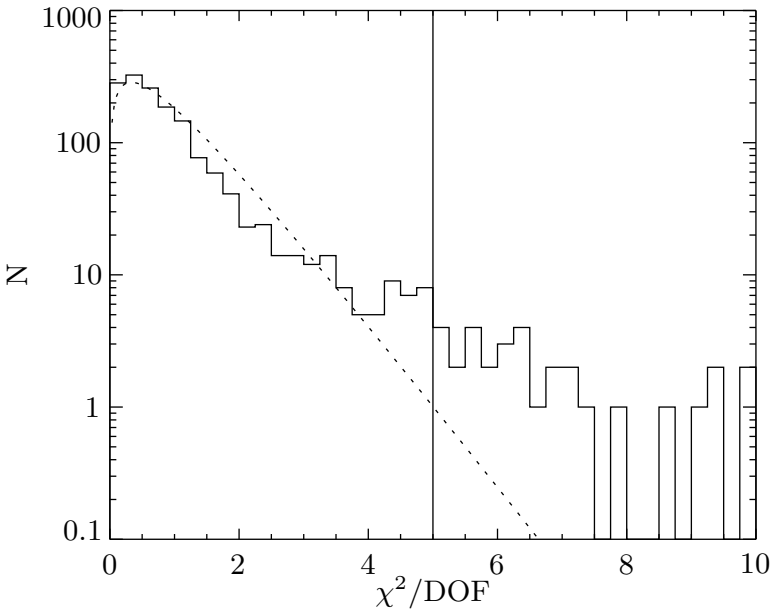

Figure 2.1 χ^2 per degree of freedom (DOF) for the fitted photometric distance of the 1443 SDSS DA white dwarfs considered. A χ^2 function with 3 DOF is plotted as the dotted line. Beyond $\chi^2 = 5$ the white dwarfs are rejected.

error is expected to be in the PG survey distances and hence a conservative 10 per cent error was applied to these.

Proper motions for PG white dwarfs that appear in SDSS are taken from the catalog of Munn et al. (2008). For the remaining objects, the PPMXL proper motion was used where available, which has typical 1σ error of ~ 8 mas yr^{-1} (Roeser et al., 2010).

Finally 4 objects in the PG sample have no reliable PPMXL proper motion, primarily due to a spurious matching of objects between epochs. For these, the proper motion was calculated directly between the scanned Digital Sky Survey-Palomar Observatory Sky Survey (POSS-I Abell, 1955) and POSS-II plates. The proper motion was measured relative to nearby faint stars of similar magnitude corrected for galactic rotation (see section 2.3.1). Typical errors estimated from the proper motions of stars of similar magnitude to be 11 mas yr^{-1}. We emphasize that only 4 of 1491 white dwarfs use this method, and none have mass above 0.95 $M_\odot$ analyzed in more detail in section 2.5.

Final Sample: The resulting sample of 1443 SDSS and 211 PG white dwarfs contains young DA white dwarfs with reliable masses, proper motions and photometric distances. The mass distribution of the samples is shown in figure 2.2. The process of constructing the sample together with numbers of objects is summarized in table 2.1.

	PG	SDSS
Number of DA white dwarfs with good photometry not known to be binaries	299	6926
of these number with signal-to-noise > 10	299	3125
of these number with $13,000\,K < T_{\rm eff} < 40,000\,K$	215	1555
of these number with age $< 3 \times 10^8$ yrs	211	1491
Distance source:		
Liebert et al. (2005)	79	0
SDSS Photometry	132	1491
of these number rejected with $\chi^2 > 5$	0	48
Proper Motion Source:		
Munn et al. (2008)	153	1443
PPMXL	54	0
Manual measurement from POSS I/II	4	0

Table 2.1 Summary of the sample of WDs which passed the cuts described in detail in section 2.2.

2.3 Kinematics Without Radial Velocities

We now turn to calculating the mean velocity and the velocity dispersion for our sample. While radial velocities are required to completely determine the kinematics of an individual object, bulk kinematic properties such as the mean velocity and the velocity dispersion can be determined from only transverse motions.

We use two methods to do so, the frequentist method used in section 2.3.1, and a Markov Chain Monte Carlo in section 2.3.2. Both methods give similar results which are summarized in tabresults.

2.3.1 Method of Dehnen and Binney (1998)

The method used here is adapted from Dehnen and Binney (1998). First the observed proper motions in galactic coordinates, $\mu_\ell^{(\rm obs)}$ and $\mu_b^{(\rm obs)}$, are corrected for Galactic rotation through

$$\begin{aligned} \mu_\ell &= \mu_\ell^{(\rm obs)} - A\cos(2\ell) - B \\ \mu_b &= \mu_b^{(\rm obs)} + A\sin(2\ell)\cos b \sin b. \end{aligned} \tag{2.2}$$

using $A = 14.82\,{\rm km\,s^{-1}\,kpc^{-1}}$ and $B = -12.37\,{\rm km\,s^{-1}\,kpc^{-1}}$ (Feast and Whitelock, 1997). In galactic coordinates where the components are directed towards the galactic center, in the direction of galactic rotation, and towards the north Galactic pole we observe the velocity

$$\mathbf{V}_\perp = 4.74 d \begin{bmatrix} -\mu_\ell \sin\ell \cos b - \mu_b \cos\ell \sin b \\ \mu_\ell \cos\ell \cos b - \mu_b \sin\ell \sin b \\ \mu_b \cos b \end{bmatrix} {\rm km\,s^{-1}} \tag{2.3}$$

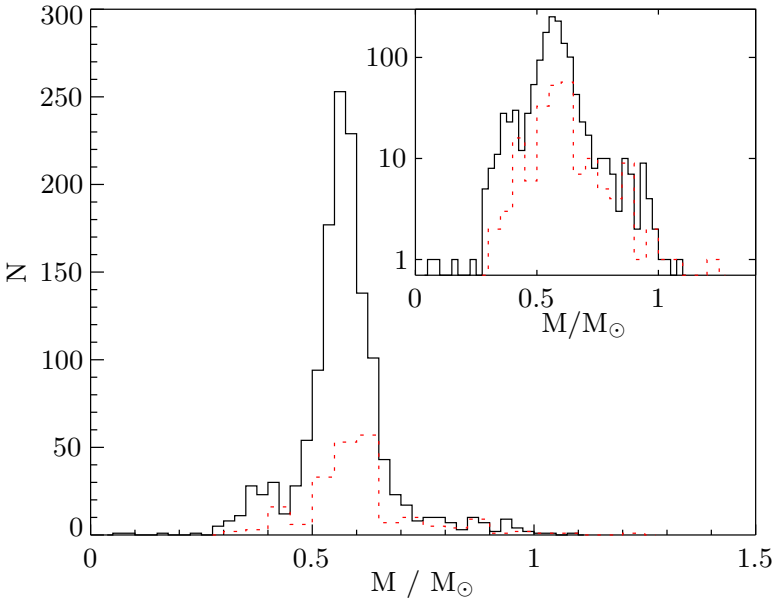

Figure 2.2 Mass distribution of the samples of SDSS (black line) and PG (dashed red line) white dwarfs after the cuts described in section 2.2. Inset graph shows the same data on logarithmic axes.

with d in kpc and proper motions in mas yr^{-1}. This is the projection of the velocity $\mathbf{V}$ onto the sky plane though the projection matrix

$$\mathbf{V}_\perp = \mathbf{A} \cdot \mathbf{V}, \quad \mathbf{A} = \mathbf{I} - \hat{\mathbf{r}} \otimes \hat{\mathbf{r}} \tag{2.4}$$

where $\hat{\mathbf{r}}$ is the unit vector to the star.

Next the quantity S^2 is formed through

$$S^2(\mathbf{V_0}) \equiv \left\langle |\mathbf{V}_\perp - \mathbf{A} \cdot \mathbf{V_0}|^2 \right\rangle. \tag{2.5}$$

Under the assumption that the positions of the observed objects are uncorrelated with the velocity, then the choice of $\mathbf{V_0}$ that minimizes S^2 is the mean velocity. Also S^2 at the minimum is a measure of the dispersion of the group.

Dehnen and Binney (1998) then calculate all independent six elements of the dispersion tensor. Unfortunately, this entails estimating nine parameters which limits its use to samples with large numbers of objects. This would require excessively wide bins for the high-mass region where there are few objects. Instead we choose to make further assumptions about the objects' velocities in order to reduce the number of fitted parameters. The mean velocity of each group towards the galactic center and the north Galactic pole is simply a result of the solar motion and we take these to be 10.00 km s^{-1} and 7.17 km s^{-1} , respectively, (Dehnen and Binney, 1998). The mean velocity in the direction of galactic rotation, V_0, is kept as a free parameter since in addition to the solar

motion this varies between groups due to asymmetric drift. We also assume that the dispersion tensor takes the form

$$\sigma = \sigma_1 \mathrm{diag}\left(1, \frac{1}{1.4}, \frac{1}{2.2}\right) \tag{2.6}$$

which is accurate for main sequence stars in the solar neighborhood (Dehnen and Binney, 1998). This reduces the number of parameters for each group to the asymmetric drift V_0 and the normalization of the dispersion tensor σ_1.

V_0 is calculated by minimizing equation (2.5), and then σ_1 is estimated though a Monte-Carlo simulation: Since S^2 is a measure of the dispersion, an initial estimate of σ_1^2 is taken to be S^2, and a set of simulations is performed where a new velocity is chosen for each white dwarf at its position in the sky from the isothermal distribution with the assumed dispersion tensor and the calculated mean velocity. The error in tangential velocity, assumed to be Gaussian, is added to this. The set of simulations produces a distribution of S^2 values, and σ_1^2 is iterated until the mean S^2 corresponds to the value calculated from observations. S^2 is almost proportional to σ_1^2 when errors in tangential velocity are neglected and so the error in σ_1^2 is estimated from the distribution of S^2 scaled by this proportionality constant.

2.3.2 MCMC Estimate

In addition, a Markov Chain Monte Carlo (MCMC) likelihood-based estimate of the kinematic parameters was obtained. We use uninformative flat priors for the fitted parameters.

We denote the probability that the velocity of the ith object was $\mathbf{V}$ to be $P(\mathbf{V}|\mathbf{D}_i, \sigma_i)$ where $\mathbf{D}_i = (l, b, d, \mu_\ell, \mu_{(\mathrm{b})})$ is the data for the ith object together with the corresponding errors σ_i. μ_ℓ and $\mu_{(\mathrm{b})}$ are the values corrected for galactic rotation by equation (2.2). Under the assumption that positions are uncorrelated with velocity then the distribution function is a function only of velocity: $f(\mathbf{V})$. In addition, in what follows we do not consider the positions, but instead focus on the kinematics through the velocity $\mathbf{V}$. Under these assumptions the overall likelihood for a set of observations of a group of white dwarfs is

$$\mathcal{L} = \prod_i \int d\mathbf{V} f(\mathbf{V}) P(\mathbf{V}|\mathbf{D}_i, \sigma_i) \tag{2.7}$$

$$\Rightarrow \log \mathcal{L} = \sum_i \log \int d\mathbf{V} f(\mathbf{V}) P(\mathbf{V}|\mathbf{D}_i, \sigma_i) \tag{2.8}$$

$$\equiv \sum_i \log \mathcal{L}_i \,. \tag{2.9}$$

In calculating the likelihoods, $\mathcal{L}_i$, we assume a Schwarzschild distribution function, and normally distributed error in proper motion. The unknown radial velocity is integrated over analytically. Explicit expressions for $\mathcal{L}_i$ are given in appendix 2.A.

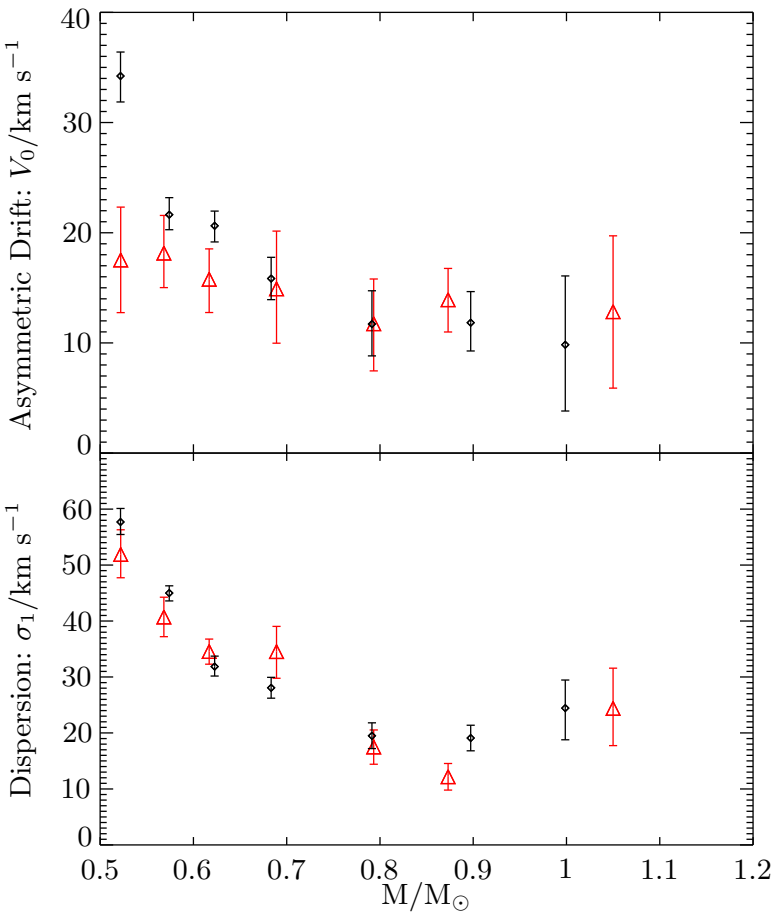

Figure 2.3 Dispersion of SDSS (black) and PG (red) white dwarfs against mass calculated using the using the method described in section 2.3.2. Each bin is plotted at its mean mass.

Again, the dispersion tensor and mean were constrained to reduce the number of parameters. We use flat priors on the dispersion and asymmetric drift. The expression for the likelihood was used to calculate the maximum likelihood estimate of the dispersion tensor, while errors were estimated from a MCMC using Metropolis-Hastings sampling. When the constraints on the dispersion tensor and mean velocity were relaxed this did not substantially alter the results, aside from the larger errors, particularly in the underpopulated bins due to the reduced degrees of freedom. In particular, the results are insensitive to allowing vertex deviation.

The fitting results for the SDSS and PG samples are summarized in table 2.2 and plotted in figure 2.3. In addition, in figure 2.4 the raw transverse velocities measured from the proper motions for three groups of white dwarfs are shown. The lowest-mass white dwarfs, $M < 0.45\,\mathrm{M}_\odot$, are expected to be predominantly formed through binary evolution and have a binary white dwarf partner.This potentially introduces errors into their photometric distances and so we do not consider them beyond simply stating the fitting results in table 2.2.

Table 2.2 Kinematic fitting results from the PG and SDSS samples described in section 2.2 using the methods of sections 2.3.1 and 2.3.2. $M_{\rm low}$ and $M_{\rm high}$ are in units of $M_\odot$, while σ_1 and V are in km s^{-1}. N is the number of white dwarfs in each mass bin.

		PG					SDSS				
$M_{\rm low}$	$M_{\rm high}$	N	Dehnen and Binney (1998)		MCMC		N	Dehnen and Binney (1998)		MCMC	
			σ_1	V	σ_1	V		σ_1	V	σ_1	V
0.30	0.40	5	47 ± 12	22 ± 13	48 ± 10	18 ± 12	70	53 ± 3	33 ± 4	40 ± 3	34 ± 4
0.40	0.47	20	49 ± 6	27 ± 7	49 ± 7	28 ± 6	62	68 ± 4	38 ± 6	70 ± 6	38 ± 6
0.47	0.55	35	47 ± 4	18 ± 6	51 ± 4	17 ± 4	333	56 ± 1	34 ± 2	57 ± 2	34 ± 2
0.55	0.60	53	37 ± 2	17 ± 3	40 ± 3	18 ± 3	482	46 ± 1	20 ± 1	45 ± 1	21 ± 1
0.60	0.65	51	37 ± 2	16 ± 3	34 ± 2	15 ± 2	239	33 ± 1	20 ± 1	31 ± 1	20 ± 1
0.65	0.75	23	33 ± 3	15 ± 4	34 ± 4	14 ± 5	91	26 ± 1	16 ± 2	28 ± 1	15 ± 1
0.75	0.85	9	16 ± 2	11 ± 4	17 ± 3	11 ± 4	30	16 ± 1	11 ± 2	19 ± 2	11 ± 2
0.85	0.95	10	12 ± 2	15 ± 2	12 ± 2	13 ± 2	28	18 ± 1	12 ± 2	19 ± 2	11 ± 2
0.95	1.44	5	22 ± 5	14 ± 7	24 ± 6	12 ± 6	9	19 ± 3	9 ± 5	24 ± 5	9 ± 6

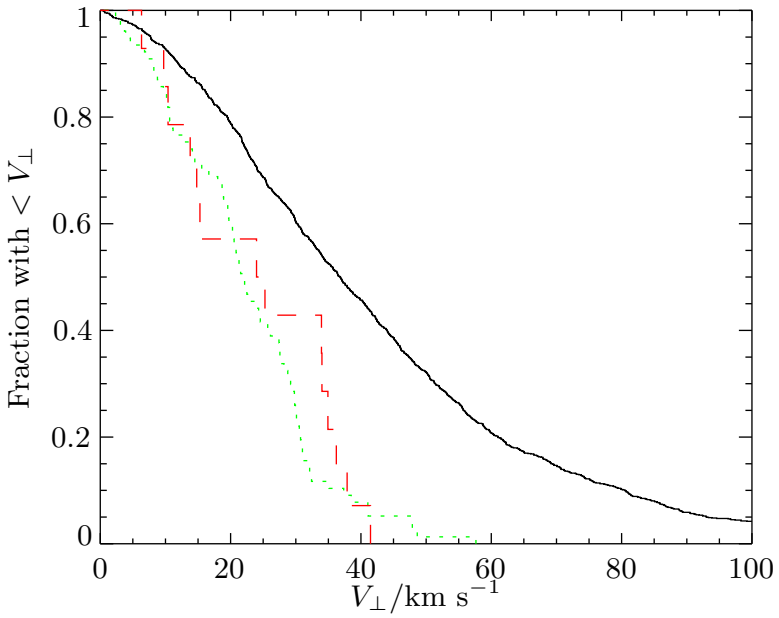

Figure 2.4 Cumulative transverse velocity distribution of the combined SDSS and PG surveys. low-mass white dwarfs ($0.5\,M_\odot \leq M < 0.75\,M_\odot$, with $M = M_1 + M_2$) as solid black, high-mass white dwarfs ($M > 0.95\,M_\odot$) as dashed red, and intermediate mass white dwarfs ($0.75\,M_\odot \leq M < 0.95\,M_\odot$) as dotted green.

2.4 Expectations from Single-Star Evolution

2.4.1 Analytic

In this section we describe the reasons for the relationship WD mass and dispersion within a simple analytic model, before moving onto the more complex Monte Carlo simulations of section 2.4.2.

Within the framework of single-star evolution (SSE) an ensemble of white dwarfs with the same mass would be expected to have a dispersion $\sigma(t_{\rm TOT})$, where $\sigma(t)$ is the disk heating relation, and $t_{\rm TOT}$ is the total age of the white dwarf including its precursor lifetime (i.e., total pre-white dwarf stellar lifetime). Here $t_{\rm TOT}$ will be given by $t_{\rm TOT} = t_{\rm WD} + t_{\rm SSE}(M_{\rm i}(M_{\rm WD}))$ where $t_{\rm WD}$ is the cooling age of the white dwarf and $t_{\rm SSE}(M_{\rm i}(M_{\rm WD}))$ is the total precursor lifetime, which is a function of the white dwarf mass through the initial-final mass relation (IFMR) $M_i(M_f)$. Two components of this prediction are particularly uncertain: the disk heating relation and the IFMR. We discuss these now.

The best constraints on the IFMR come from open clusters. Spectroscopic fits of the masses of white dwarfs give the final mass. The initial mass is estimated using isochrone fitting to the main sequence turnoff to calculate the age of the cluster, which finally allows the corresponding initial mass to be inferred using the precursor lifetime (Catalán et al., 2008). This method has succeeded in producing IFMRs with a typical uncertainty of less than 20%. The strong dependence of the precursor lifetime on mass however makes this a considerable uncertainty in the dispersion

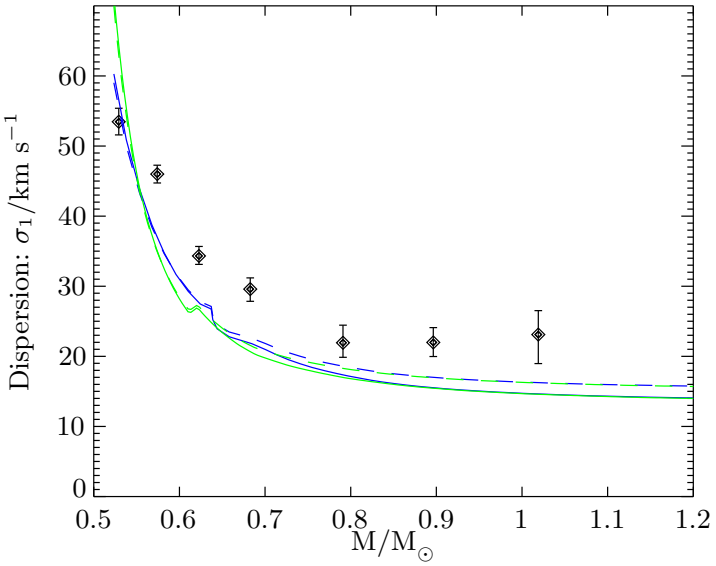

Figure 2.5 Predicted dispersions from models A-D described in table 2.3, as dashed blue, solid blue, dashed green and solid green, respectively. Also plotted are SDSS white dwarfs (black error bars) with the data taken from the MCMC column of table 2.2.

relation.

The most accurate data on the disk heating relation is given in Nordstrom et al. (2004) from an analysis of F and G dwarfs with radial velocities and Hipparcos data, although this data still permits a range of heating models (Seabroke and Gilmore, 2007). However, for consistency, we instead use the disk heating models estimated in Just and Jahreiß (2010), since we also use their companion star formation histories.

The effect of these model uncertainties are shown in figure 2.5 for the models described in table 2.3. Qualitatively the results appear to agree with the predicted relations: for white dwarfs more massive than $0.75\,M_\odot$ the white dwarf progenitors precursor lifetime is short and there is little dependence of the kinematics on mass. Below $0.75\,M_\odot$ the dispersion sharply increases as the progenitor lifetime approached 1 Gyr and longer where the disk heating is significant.

However, while qualitatively the results in figure 2.5 are consistent, there is quantitative disagreement. To assess this disagreement we turn to a more-sophisticated Monte Carlo treatment.

2.4.2 Monte Carlo

As a quantitative check of our results in section 2.4.1 we have performed a Monte Carlo simulation of the production, kinematics, and observation of the white dwarfs in the solar neighborhood, as described in this section. We also describe the simulated selection and observation of these white dwarfs by SDSS and PG. We perform this simulation to assuage fears that our results could be

Table 2.3 Model input parameters for the models of single-star evolution (SSE).

Model	$\sigma(t)$ / km s^{-1}	$M_\mathrm{i}(M_\mathrm{WD})$ / $M_\odot$	$t_\mathrm{SSE}(M_\mathrm{i})$ / Gyr	SFR(t)[a]
A	$66\left(\frac{0.5+t/\mathrm{Gyr}}{0.5+12}\right)^{1/2}$ [b]	From Hurley et al. (2000)	Model from Hurley et al. (2000)	3.25[b]
B	$62\left(\frac{0.32+t/\mathrm{Gyr}}{0.32+10}\right)^{1/2}$ [c]	From Hurley et al. (2000)	Model from Hurley et al. (2000)	$7.68\exp(-t/8\,\mathrm{Gyr})$[c]
C	$66\left(\frac{0.5+t/\mathrm{Gyr}}{0.5+12}\right)^{1/2}$ [b]	$(M_\mathrm{WD}-0.394)/0.109$ [d]	$10^{\left(0.334-\sqrt{1.790-0.2232\times(7.764-\log M_\mathrm{i})}\right)/0.1116}$ [e]	3.25 [b]
D	$62\left(\frac{0.32+t/\mathrm{Gyr}}{0.32+12}\right)^{1/2}$ [c]	$(M_\mathrm{WD}-0.394)/0.109$[d]	$10^{\left(0.334-\sqrt{1.790-0.2232\times(7.764-\log M_\mathrm{i})}\right)/0.1116}$ [e]	$7.68\exp(-t/8\,\mathrm{Gyr})$[c]

[a] In units of $\mathrm{M}_\odot\,\mathrm{pc}^{-2}\,\mathrm{Gyr}^{-1}$. Not used in the analytic SSE simulation of section 2.4.1
[b] Just and Jahreiß (2010) model C
[c] Just and Jahreiß (2010) model D
[d] From Kalirai et al. (2008)
[e] From Padovani and Matteucci (1993)

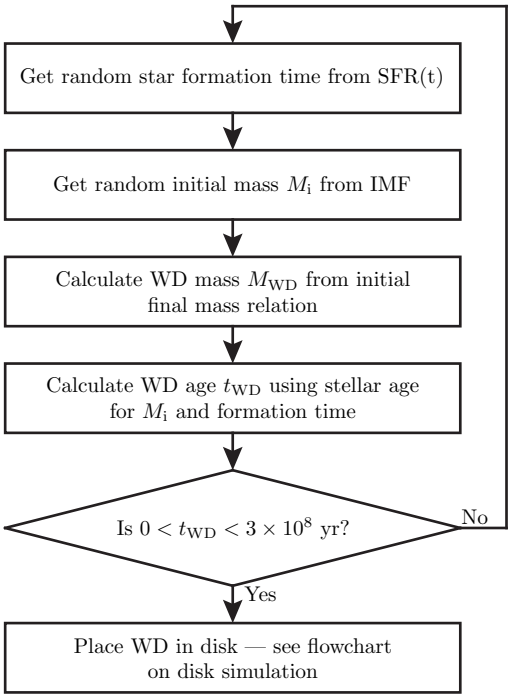

Figure 2.6 Flowchart illustrating the process of simulating white dwarfs formed from single-star evolution (SSE). If a star reaches the final stage, then it is placed in the disk using a process described by the flowchart shown in figure 2.7.

impacted by effects such as selection biases.

This process is somewhat involved, and so for clarity it is summarized in the flow charts in figures 2.6–2.8. The final results of the Monte Carlo simulation are compared with the white dwarf sample in figure 2.10.

Picking Stars: The initial mass was drawn from a Kroupa IMF and one of two star formation histories (Table 2.3). If this resulted in a white dwarf at the present time with an age less than 3×10^8 years, and a temperature between 13,000 K and 40,000 K using the cooling models of Wood (1995) as explained in section 2.2, then it was included in the simulation. See figure 2.6 for synopsis.

Placing Stars in Disk: If a star has been included in the simulation, it is given a velocity dispersion taken from the previously described disk heating models of table 2.3 and axis ratios of the velocity ellipsoid of 1:1/1.4:1/2.2 (Dehnen and Binney, 1998). Its velocity in the disk was drawn from a Gaussian with these widths and it was placed in the plane of the Galaxy using a radial exponential disk with a scale length of 2.5 kpc. Since the furthest $> 0.47\,M_\odot$ WD projected into plane is less than 1 kpc, only WDs placed within this distance are simulated further.

For an isothermal population the vertical position, z, and velocity, v_z, are given by

$$\begin{aligned} f_z(E_z) &\propto \exp(-E_z/\sigma_z^2) \\ &\propto \exp(-v_z^2/2\sigma_z^2)\exp(-\Phi_z(z)/\sigma_z^2)\,, \end{aligned} \tag{2.10}$$

where Φ_z is the gravitational potential. Each star's velocity is thus drawn from a Gaussian with standard deviation given by the previously calculated σ_z, while z is chosen by first drawing $\Phi_z(z)$ from an exponential distribution with scale σ_z^2, and then inverting this to calculate z. We use the mass models of Holmberg and Flynn (2000) for $\Phi_z(z)$.

This process of placing white dwarfs in the local galactic disk is summarized in figure 2.7.

White Dwarf Observability: As a result of this process, each white dwarf has an assigned galactic position and velocity, together with its mass and age. It is then assessed whether it is likely to be observed in either the SDSS or PG survey as follows: First its galactic position is translated to a right ascension, RA, and declination, dec, and, unless this falls on one of the PG plates or the SDSS DR4 spectroscopic plates, the probability of observation is zero.

For white dwarfs in the PG survey the apparent U and B magnitude is calculated from the models of Holberg and Bergeron (2006) with a 0.27 mag error added to each to mimic the photometric errors in PG (Liebert et al., 2005). If it is bluer than $U-B=-0.46$ and brighter than the B band magnitude limit for the PG plate on which it lies then it is considered observed.

For SDSS the spectroscopic targeting is more complex (Kleinman et al., 2004), and the strategy was to construct an empirical observational probability for a star at each magnitude and color. A four-dimensional table of probability of spectroscopic follow up was constructed in $(r, u-g, g-r, r-i)$ grouped in 0.2 mag bins from the SDSS DR4 clean photometry. The expected spectroscopic signal-to-noise was calculated using a quadratic least squares fit to the observed signal-to-noise ratio as a function of g-band magnitude together with normally distributed scatter in signal-to-noise with standard deviation of 1.7. If the signal-to-noise ratio was greater than 10 it was included in the mock sample.

Finally, measurement errors in mass of $0.03\,M_\odot$ and proper motion errors of $5.6\,\mathrm{mas\,yr^{-1}}$are introduced.

The process of assessing if each white dwarf is observed by the PG or SDSS surveys is summarized in figure 2.8. In all simulations we simulate a total of $\sim 2\times10^{11}$ objects.

Monte Carlo Results: The results of this simulation are shown in figure 2.10. As a further check that the simulated white dwarfs have the correct kinematics we plot the distributions in the U, V and W directions (directed towards the Galactic center, in the direction of galactic rotation, and towards the north Galactic pole, respectively) in figure 2.9.

The results of the singe-star evolution (SSE) simulation, described in this section, closely agree

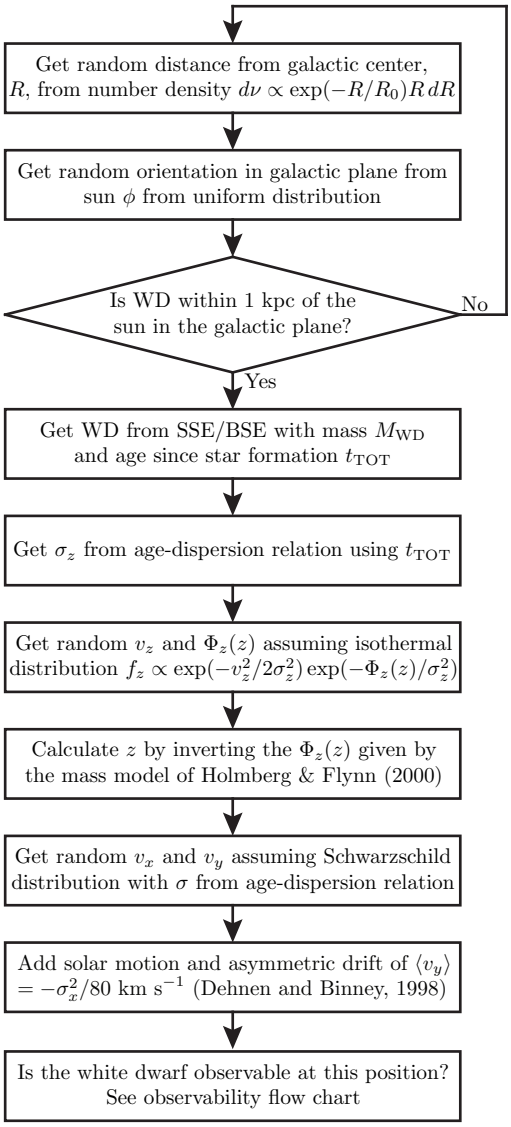

Figure 2.7 Flowchart illustrating the process of placing white dwarfs in the galactic disk and picking their velocity. This process is undertaken if a star reaches the final stage of the flowchart shown in figure 2.7. If a star reaches the final stage of this flowchart, the observability is finally determined using the algorithm described in the flowchart shown in figure 2.8

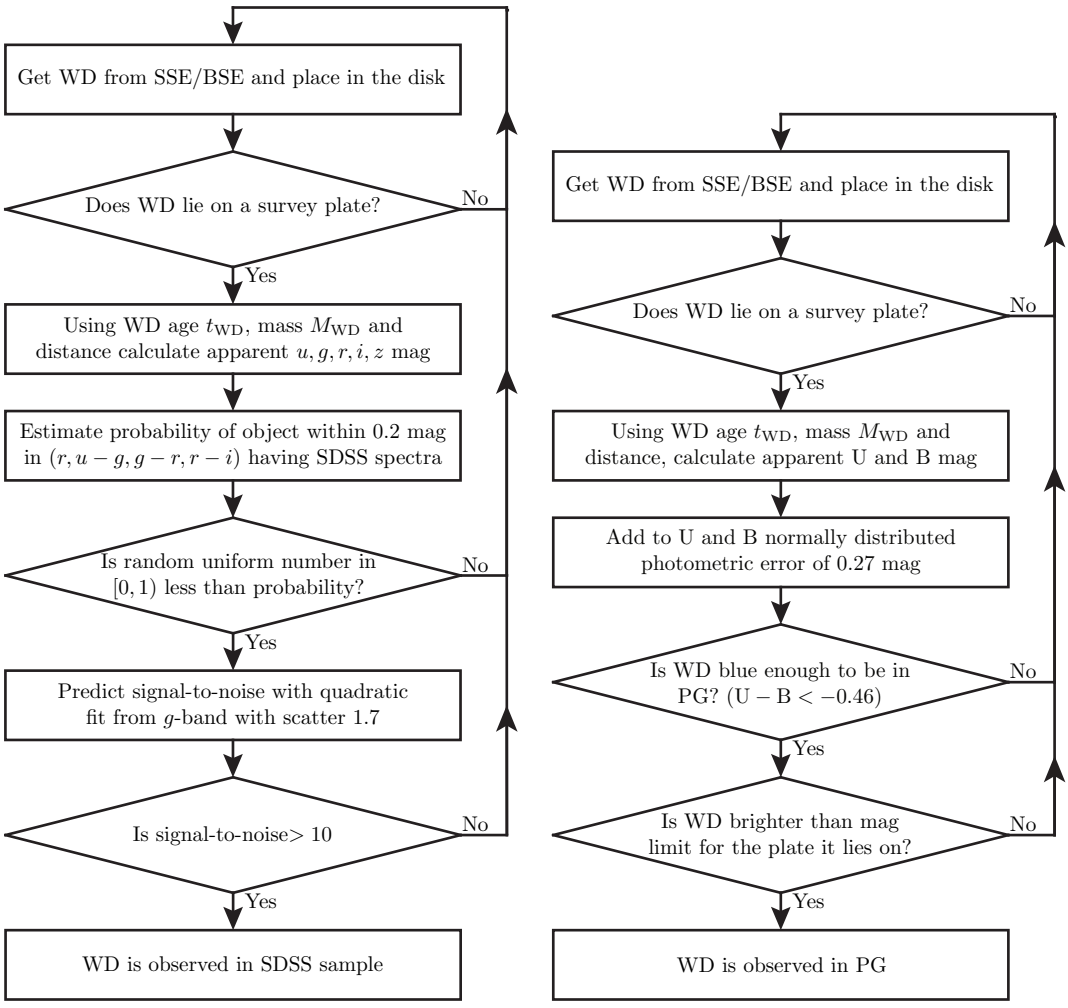

(a) SDSS. (b) Palomar-Green (PG).

Figure 2.8 Flowchart illustrating the process of simulating whether white dwarfs are observed. This process is undertaken if a star has reached the final stage of the flowchart shown in figure 2.7.

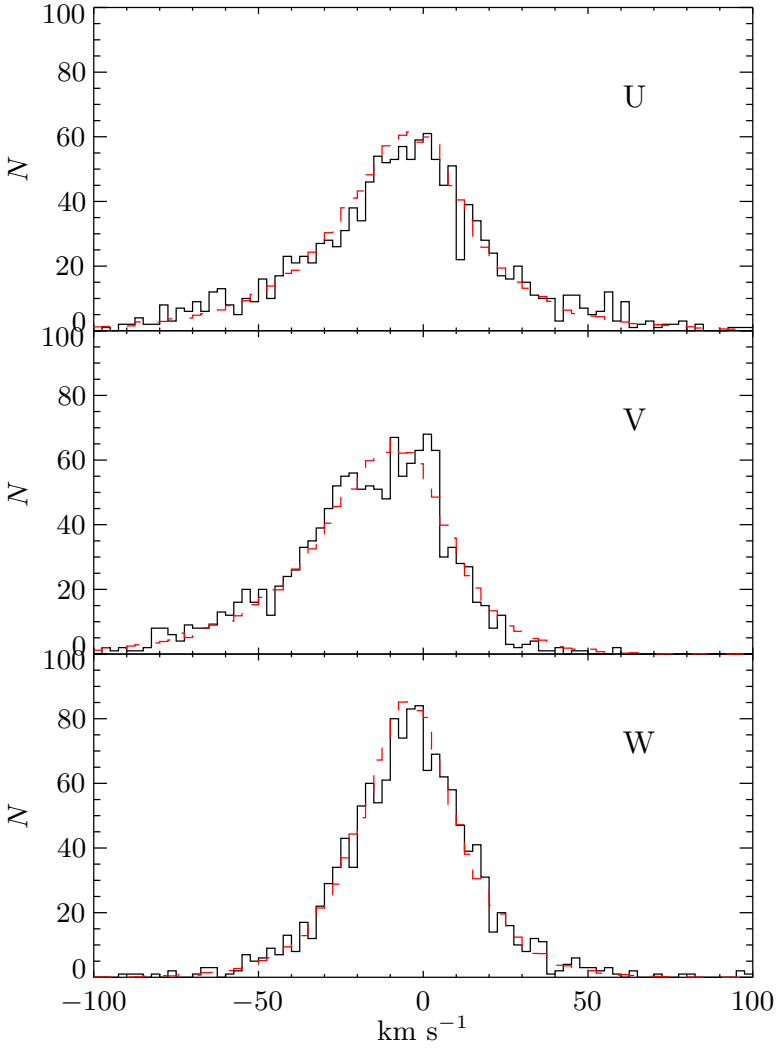

Figure 2.9 Histograms showing the agreement between the observed and simulated velocity distribution in U, V, W directions of SDSS WDs. The black line is the observed distribution, while the dashed red line is the distribution of the SSE simulation for model C. Zero radial velocity is artificially assumed, and number of simulated WDs is normalized to the number observed. U is directed towards the Galactic center, V in the direction of galactic rotation, and W towards the north Galactic pole.

with the observations, modulo the normalization factor. We do not concern ourselves with this overall normalization, however the normalization factor is typically $\lesssim 2$. The simulation also does not produce white dwarfs below $\approx 0.47\,M_\odot$, which are generally expected to form through binary evolution. As may be expected from the analytic models plotted in figure 2.5, the models in table 2.3 all produce white dwarfs that reasonably closely explain the observed samples and their kinematics and so we only plot the results of only one representative model in figure 2.10.

2.5 Expectations from Binary-Star Evolution

It has been suggested that the majority of high-mass white dwarfs were formed from mergers of binary white dwarfs, both on the basis of their number density (Liebert et al., 2005) and a possible peak at $1\,M_\odot$ (Vennes, 1999). To test this hypothesis we use two binary evolution codes (discussed in section 2.5.1) to perform binary population synthesis (described in section 2.5.2), and ultimately what fraction of the sample is likely to have had a binary WD progenitor (section 2.5.4).

2.5.1 Binary Evolution Codes

To address the considerable uncertainties in binary evolution, two binary evolution codes were used. Specifically, the `BSE` code described in Hurley et al. (2000), and the `SeBa` code described in Nelemans et al. (2001). Both codes use the same approach to modeling binary evolution: semi-analytic fits to the structure and evolution of isolated stars are combined with prescriptions for interactions between the stars.

We now turn to the key uncertain physics in binary evolution and describe how it is treated in the two codes.

There are four key initial conditions that govern the evolution of a binary: the initial primary mass $M_{1\mathrm{i}}$, the initial secondary mass $M_{2\mathrm{i}}$ (or equivalently the mass ratio $q_\mathrm{i} = M_{1\mathrm{i}}/M_{2\mathrm{i}}$), the initial binary semi-major axis a_i and the initial eccentricity e_i.

One slice through the four-dimensional space of initial conditions $(M_{1\mathrm{i}}, q_\mathrm{i}, a_\mathrm{i}, e_\mathrm{i})$ showing those conditions, which result in the merger of a pair of white dwarfs is shown in figure 2.11. For those binaries that result in the merger of a pair of white dwarfs there are generally two phases of mass transfer in their evolution. One as each star evolves from the main sequence and expands. Both codes have two distinct channels for forming pairs of white dwarfs. These correspond to the stability of the first phase of mass transfer. The lower branch of figure 2.11 corresponds to binaries where the first phase of mass transfer is stable Roche lobe overflow (RLOF) as the primary evolves off the main sequence and crosses the Hertzsprung gap. For binaries in the upper branch the first phase is dynamically unstable, resulting in a binary in a common envelope (CE). The second phase of mass transfer is always unstable, independent of the branch, resulting in a common envelope

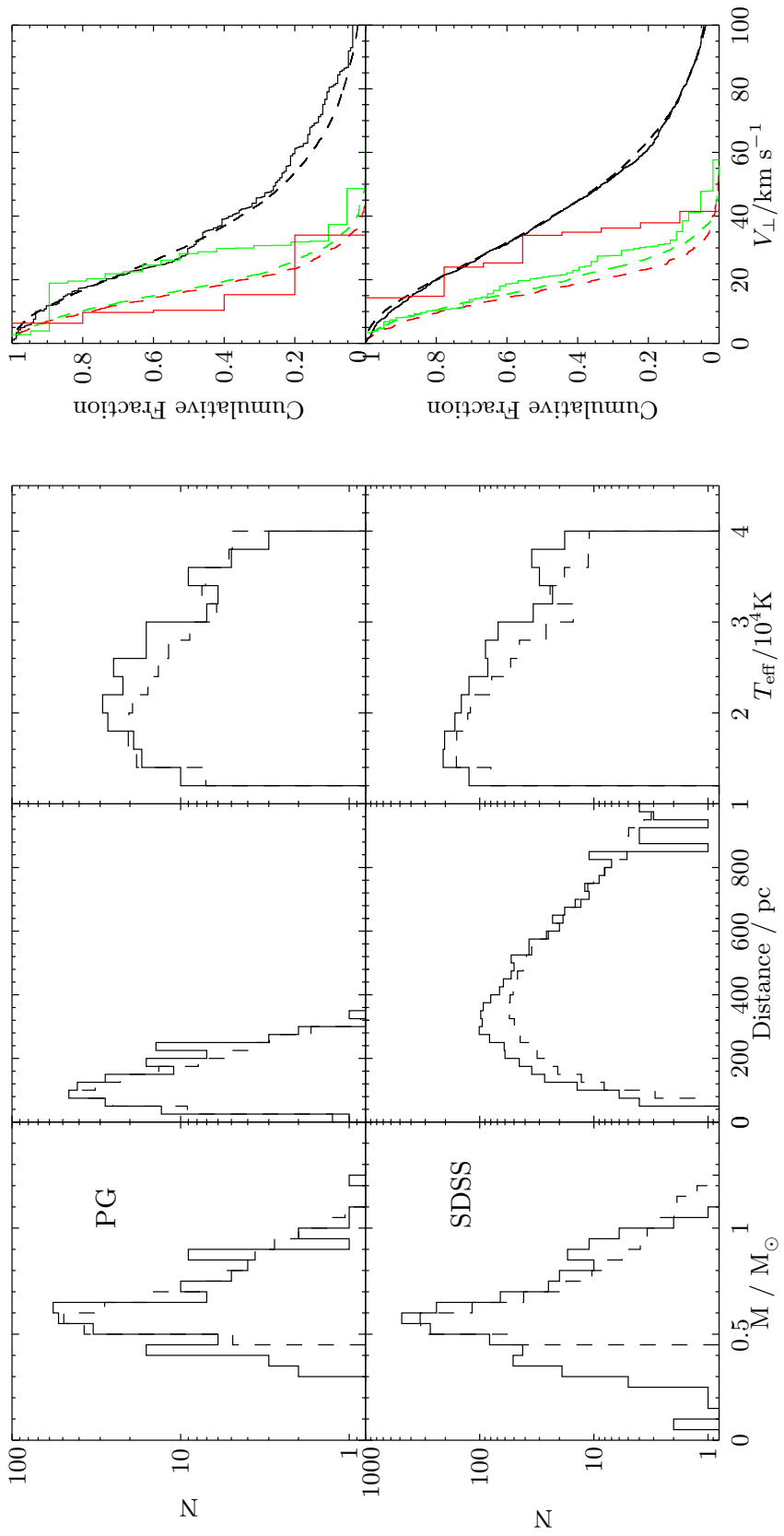

Figure 2.10 Comparison between the observed white dwarfs as the solid lines, and the Monte Carlo simulations of single-star evolution described in section 2.4.2 as the dashed lines. The upper panels show the PG survey and the lower panels the SDSS survey. The rightmost panel shows the cumulative transverse velocity distribution. In this panel colors are as in figure 2.4. Specifically low-mass white dwarfs ($0.5\,M_\odot \le M_1+M_2 < 0.75\,M_\odot$) are plotted in black, high-mass ($M_1 + M_2 > 0.95\,M_\odot$) white dwarfs in red, and intermediate mass white dwarfs ($0.75\,M_\odot \le M_1 + M_2 < 0.95\,M_\odot$) in green. The simulation plotted is model D from table 2.3.

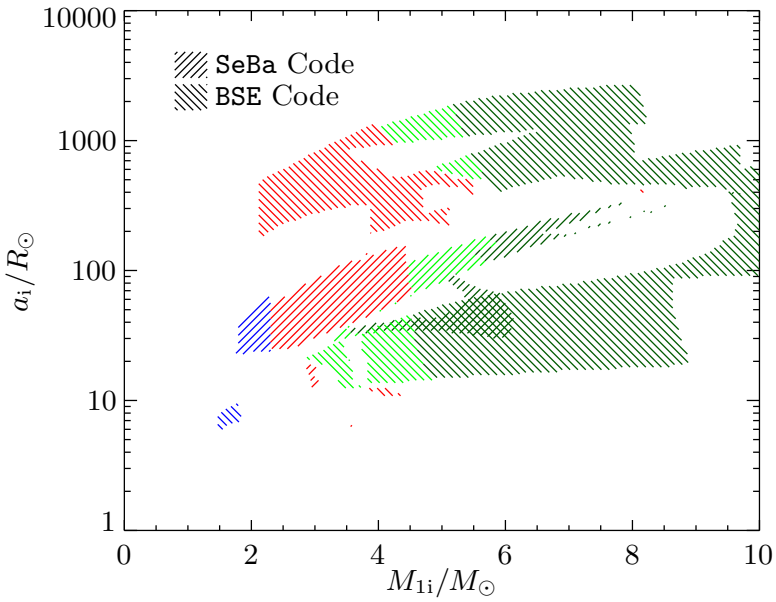

Figure 2.11 Comparison of the WD+WD merger outcomes from the SeBa and BSE codes with their default prescriptions for binary evolution. All simulations use an initial mass ratio of $q_i = 0.5$ and eccentricity of $e_i = 0$. SeBa results are lines 45^0 counterclockwise from vertical and BSE 45^0 clockwise. Green corresponds to CO+CO, red He+CO and blue He+He. The darker green are super-Chandrasekhar ($M_1 + M_2 < 1.4\,M_\odot$) mergers, and the light green sub-Chandrasekhar.

(CE). Following the ejection of this common envelope the two white dwarfs are brought to merger through the emission of gravitational radiation.

The differences between the BSE code and SeBa code in figure 2.11 are striking, and are largely due to the different binary evolution prescriptions, and in particular the treatment of the RLOF and CE phases.

In the RLOF phase mass is transferred on the thermal timescale of the primary as it crosses the Hertzsprung gap. This is shorter than the thermal timescale of the less massive secondary and so it cannot remain in equilibrium. The BSE code treats this by reducing the transfer rate while keeping mass transfer conservative, while SeBa assumes any mass transfer in excess of the thermal timescale of the secondary is ejected from the system with a multiple $n_J = 2.5$ of the angular momentum of the binary. This can be a significant difference for white dwarfs on the lower branch of figure 2.11.

There is also considerable uncertainty in the treatment of the important CE evolution phase. The most fundamental difference is the treatment of the first phase of mass transfer. BSE uses the most commonly used prescription for common envelope evolution known as the α parametrization, for both phases of mass transfer. This is defined through

$$E_{\rm bind} = \alpha_{\rm CE}\Delta E_{\rm orb} \tag{2.11}$$

$$\frac{M_i(M_i - M_f)}{\lambda R} = \alpha_{\rm CE}\left(\frac{M_f m}{2a_f} - \frac{M_i m}{2a_i}\right) \tag{2.12}$$

where the donor mass and radius are denoted M and R, and the accretor mass m. λ is an order unity factor parametrizing the envelope energy of the binary. We have used a constant $\alpha_{\rm CE}\lambda = 2$ for both SeBa and BSE in figure 2.11.

By default SeBa uses a different parametrization for the first phase of mass transfer known as the γ prescription. This treats the common envelope in terms of the angular momentum balance as opposed to the energy balance in the α prescription. Specifically

$$J_{\rm i} - J_{\rm f} = \gamma J_{\rm i} \frac{\Delta M}{M_{\rm tot}} \tag{2.13}$$

where $J_{\rm i}$ and $J_{\rm f}$ are the initial and final orbital angular momenta of the binary, $M_{\rm tot}$ is the total mass of the binary, ΔM is the mass lost, and γ is a parameter taken to be 1.5 in this work.

2.5.2 Binary Population Synthesis

We now describe our method of binary population synthesis.

We use the same distributions in the parameters $(M_{1\rm i}, q_{\rm i}, a_{\rm i}, e_{\rm i})$ as Han (1998) and Nelemans et al. (2001) with the exception of the IMF for which we use a Kroupa (2001) IMF as opposed to a Miller and Scalo (1979) IMF. For reference the probability distributions are:

$$\begin{aligned} P(M_{1\rm i}) &\propto M_{1\rm i}^{-1.35} & 0.8 < M_{1\rm i} \leq 10\,, \\ P(q_{\rm i}) &\propto \text{const.} & 0 < q \leq 1\,, \\ P(\log a_{\rm i}) &\propto \text{const.} & 0 < \log a_{\rm i}/\,R_\odot \leq 5\,, \\ P(e_{\rm i}) &\propto e_{\rm i} & 0 \leq e_{\rm i} < 1\,. \end{aligned} \tag{2.14}$$

Our approach to simulating the results of binary-star evolution is to first produce a 4-dimensional grid of binary simulations in the parameters $(M_{1\rm i}, q_{\rm i}, a_{\rm i}, e_{\rm i})$. Grid points were linearly spaced in $M_{1\rm i}$ between 0.8 and 10 $M_\odot$, linearly spaced in $q_{\rm i}$ between 0 and 1, logarithmically spaced in $a_{\rm i}$ between 1 and 10^4 $R_\odot$, and linearly spaced in $e_{\rm i}^2$ between 0 and 1. The grid size used was a $25 \times 25 \times 50 \times 10$ grid in $(M_{1\rm i}, q_{\rm i}, a_{\rm i}, e_{\rm i})$, respectively. With this choice of grid combined with the distributions in equation (2.14) the population synthesis is particularly simple: an initial primary mass is drawn from the Kroupa (2001) IMF and a random binary from the closest corresponding $(q_{\rm i}, a_{\rm i}, e_{\rm i})$ slice is chosen. In all simulations a total of $\sim 10^{13}$ objects are places in the disk.

The process of simulating stars formed from binary evolution is summarized in figure 2.12.

To assess the uncertainties due to the poorly understood phases of binary evolution we have used four models across the two binary evolution codes: the BSE code with $\alpha_{\rm CE}\lambda = 2$ (model i), the BSE code with $\alpha_{\rm CE}\lambda = 1$ (model ii) the SeBa code using the $\gamma\alpha$ common envelope prescription (model iii) and the SeBa code using the $\alpha\alpha$ prescription (model iv). Both SeBa models (iii and iv)

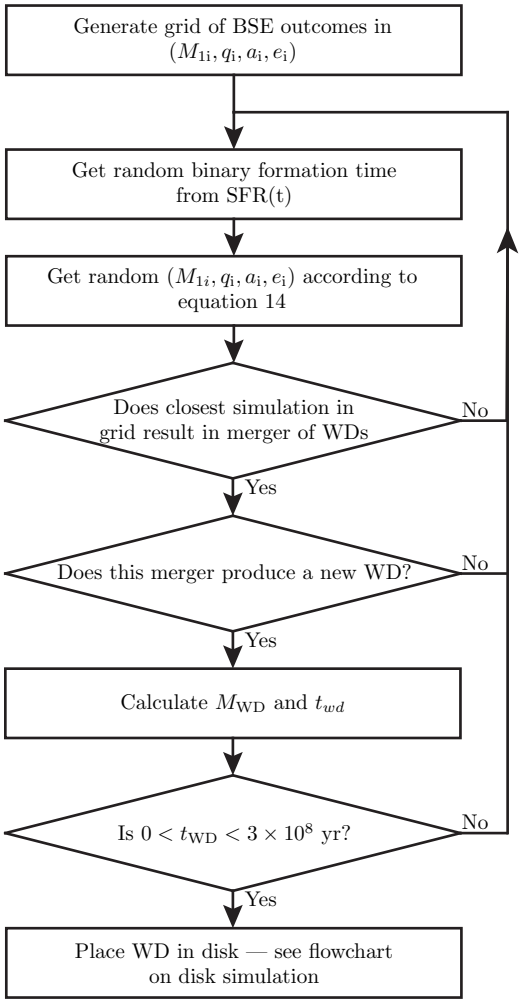

Figure 2.12 Flowchart illustrating the process of simulating white dwarfs formed from binary-star evolution.

Table 2.4 Summary of the four binary evolution models considered. The BSE code is that described by Hurley et al. (2000), and the SeBa code is described in Nelemans et al. (2001). The CE prescription describes how the two phases of common envelope evolution are treated. For example $\gamma\alpha$ describes treatment of the first phase through equation (2.13) and the second through equation (2.12).

Model	Evolution Code	CE Prescription	$\alpha_{\rm CE}\lambda$	γ
i	BSE	$\alpha\alpha$	2	-
ii	BSE	$\alpha\alpha$	1	-
iii	SeBa	$\gamma\alpha$	2	1.5
iv	SeBa	$\alpha\alpha$	2	-

use $\alpha_{\rm CE}\lambda = 2$ and $\gamma = 1.5$. These models are summarized in table 2.4.

2.5.3 White Dwarf Merger Outcomes

We distinguish between four types of white dwarf mergers, the merger of two helium core white dwarfs (He+He), the merger of a helium core white dwarf with a carbon/oxygen core white dwarf (He+CO) and the merger of two carbon/oxygen core white dwarfs (CO+CO) whose total mass is above or below the Chandrasekhar mass.

The highest-mass white dwarfs may have ONeMg cores. White dwarfs with ONeMg cores have not been considered separately from CO white dwarfs in this work. Since they are the highest-mass white dwarfs it is difficult for a pair of white dwarfs with one member an ONeMg white dwarf to merge with total mass below the Chandrasekhar limit.

The Galactic and local merger rates of the various types of white dwarfs for one particular BSE model are shown in figures 2.13 and 2.14, respectively.

In what follows we concern ourselves with the merger of CO+CO white dwarfs, since these are the mergers proposed to result in $\gtrsim 1\,M_\odot$ white dwarfs. Thus, in figure 2.15 we plot the rate at which pairs of white dwarfs with sub-Chandrasekhar total mass merge as calculated from our binary population synthesis of the four models in table 2.4. Note that the overall normalization can be very different. In particular, model ii uses a relatively efficient CE prescription with $\alpha_{\rm CE}\lambda = 1$ for both phases of mass transfer. This in turn results in a smaller range of initial separations that will ultimately result in a gravitational radiation driven WD merger. Despite the differences in overall rate between the models they all display a similar *distribution* of merger times. This is because, apart from at early times, the merger time is dominated by the time to merge by gravitational radiation. This is a strong function of separation, a, specifically $t_{\rm GW} \propto a^4$. As a result, at late times, the merging WDs originally formed a narrow range in separation at WD+WD birth. Approximating this as a power law, $\frac{dN}{da} \propto a^\epsilon$ leads to a merger rate $\frac{dN}{dt} = \frac{dN}{da}\frac{da}{dt} \propto t^{-(3-\epsilon)/4}$, and so for a wide range of ϵ the merger rate declines as $\frac{dN}{dt} \sim t^{-1}$(Maoz et al., 2010).

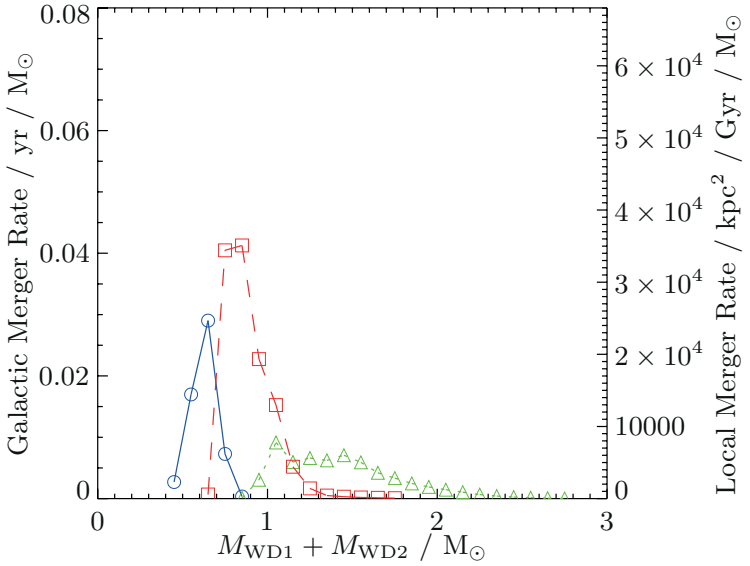

Figure 2.13 Galactic merger rate of pairs of white dwarfs as a function of mass using the BSE model i, the constant $3.25\,M_{\odot}\,{\rm Gyr}^{-1}{\rm pc}^{-2}$ star formation rate of SSE model A, and a 50 per cent binary fraction. The green dotted line corresponds to CO+CO, red dashed line He+CO, and the blue solid line to He+He.

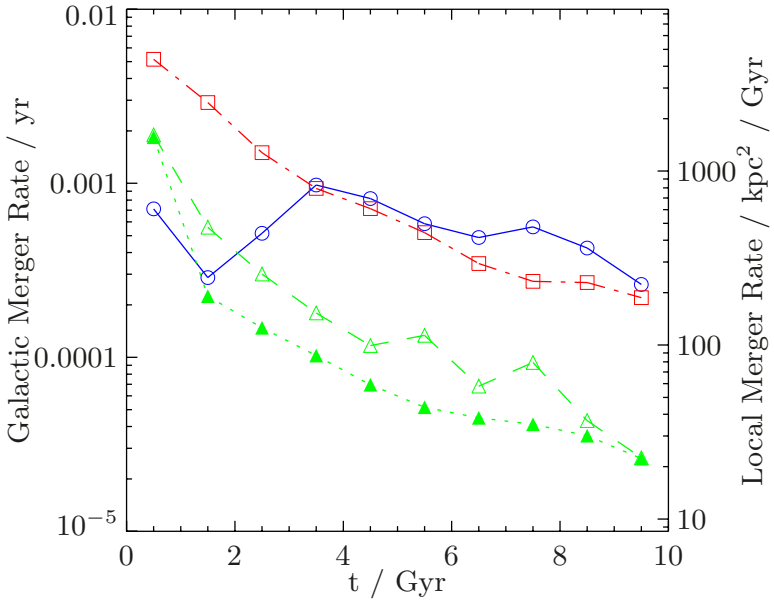

Figure 2.14 As figure 2.13 but as a function of the time since current merging white dwarf binaries formed. For the constant star formation rate considered here this is equivalent to the time to merger since a burst of star formation. The CO+CO mergers are split into super-Chandrasekhar as the dotted green, while the sub-Chandrasekhar are the dashed green.

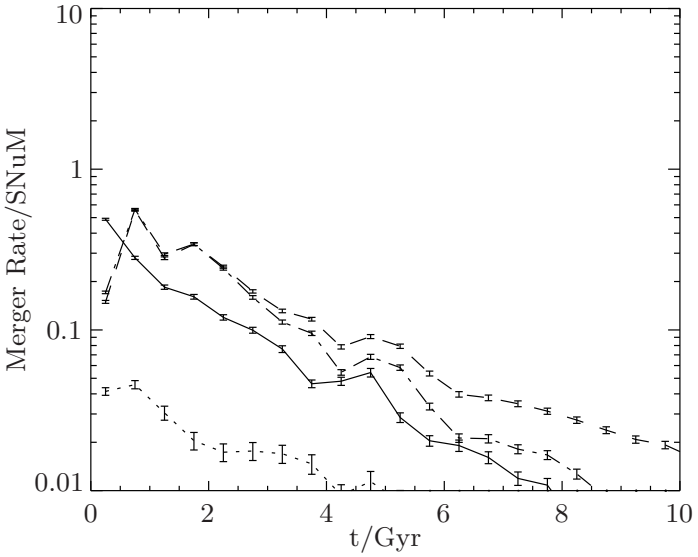

(a) Lines are the BSE code with $\alpha_{\rm CE}\lambda = 2$ (model i, solid line), the BSE code with $\alpha_{\rm CE}\lambda = 1$ (model ii, dotted line) the SeBa code using the $\gamma\alpha$ common envelope prescription (model iii, dashed line) and the SeBa code using the $\alpha\alpha$ prescription (model iv, dash-dot line).

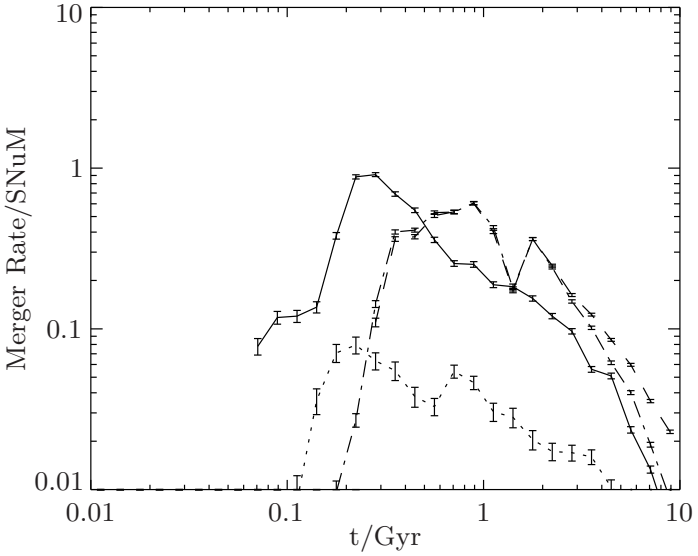

(b) As figure 2.15(a) with logarithmic time axis.

Figure 2.15 Merger rates of CO+CO WDs with sub-Chandrasekhar total mass following a burst of star formation. The error bars are purely statistical due to the finite size of the simulated binary grid. SNuM $\equiv 1/(100\,{\rm yr})\ /(10^{10}\,M_\odot)$.

2.5.4 Proportion of High-Mass White Dwarfs Formed in Mergers

To assess the possible proportion of high-mass white dwarfs that formed through mergers, the CO+CO merger products with $0.95\,M_\odot \leq M_1 + M_2 < 1.4\,M_\odot$ from the binary population synthesis, are subjected to the same process as the single population synthesis results, i.e., they are placed locally in the disk according to the method summarized in figure 2.7 and their observability in the SDSS and PG samples assessed according to figure 2.8.

We assume that no mass is ejected during the merger so that resultant white dwarf has mass $M_{\rm WD} = M_1 + M_2$. We also assume that the merger reheats the white dwarf sufficiently that the white dwarf has a cooling age of

$$t_{\rm WD} = t_{\rm form} - t_{\rm merge}$$

where $t_{\rm form}$ is the time prior to the present at which the binary initially formed, and $t_{\rm merge}$ is the length of time it took for the merger to occur, including the precursor lifetime. The resulting cumulative transverse velocity of $0.95\,M_\odot \leq M_1 + M_2 < 1.4\,M_\odot$ CO+CO merger products are shown in figure 2.16.

In figure 2.16 and the following we have combined the PG and SDSS samples to improve the statistics. We combine the Monte Carlo results by the empirical proportions of WDs in this sample, i.e., the observed PG-to-SDSS ratio of 5:9. Note however there is a possible discrepancy between the two samples in this high-mass bin. In particular the SDSS sample has few low velocity (< 14 km s^{-1}) white dwarfs (see the bottom right panel of figure 2.10), and this results in a 12% probability that they are drawn from the same distribution.

The distribution of transverse velocities in figure 2.16 shows that despite the uncertainties in binary evolution resulting in very different binary histories (figure 2.11) and overall merger rates (figure 2.15), the resultant velocity distributions are very similar. This is a result of the $\sim t^{-1}$ merger time distribution at late times discussed previously.

The results in figure 2.16 naturally lead the question of what fraction of mergers is consistent with the data to be addressed. We wish to assess the fraction of high-mass galactic white dwarfs formed by binary mergers (BSE) which we parameters by θ. This results in a fraction $1 - \theta$ from single-star evolution (SSE). To assess a value of θ for a given SSE and BSE Monte Carlo realization we first calculate the galactic formation rate of high-mass WDs from SSE and BSE in this realization, which we denote $\Gamma_{\rm SSE}$ and $\Gamma_{\rm BSE}$, respectively. Then, for both PG and SDSS we make α copies of the BSE objects simulated as observed, and β copies of objects simulated as observed from SSE. Assuming that equal numbers of objects were simulated in both the BSE and SSE realizations, then the two simulated samples combined have a galactic BSE fraction of

$$\theta = \frac{\beta\Gamma_{\rm BSE}}{\beta\Gamma_{\rm BSE} + \alpha\Gamma_{\rm SSE}}\,.$$

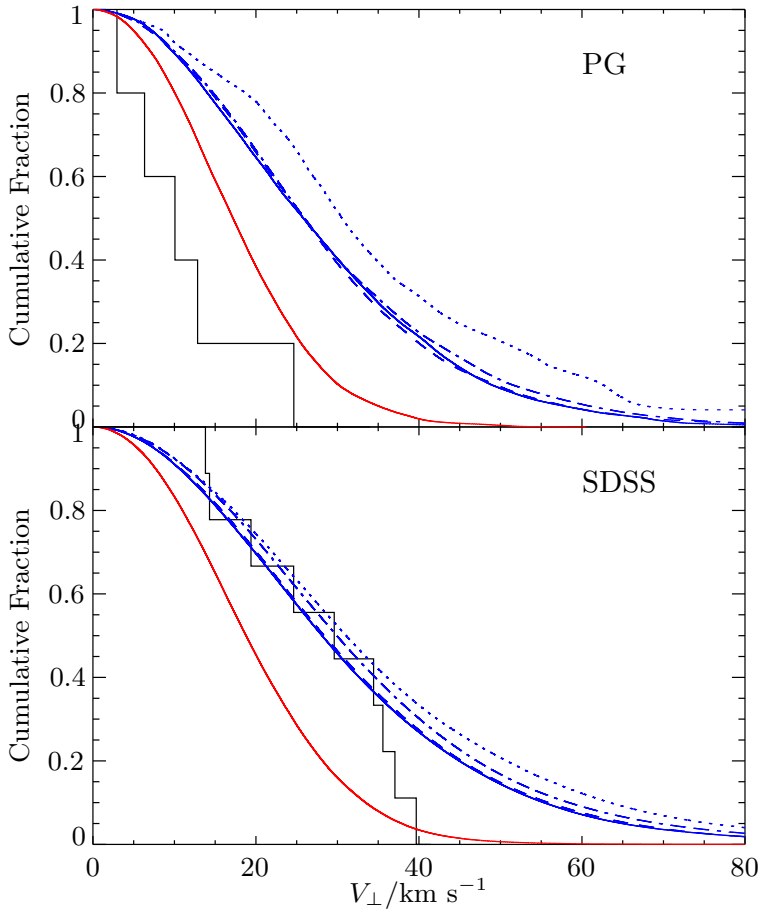

Figure 2.16 Predicted distribution of transverse velocities observed in SDSS and PG resulting from the merger of CO+CO WDs with $0.95 < M_1 + M_2/M_\odot < 1.4$. Lines are the BSE code with $\alpha_{\rm CE}\lambda = 2$ (solid blue line, model i), the BSE code with $\alpha_{\rm CE}\lambda = 1$ (dotted blue line, model ii) the SeBa code using the $\gamma\alpha$ common envelope prescription (dashed blue line, model iii) and the SeBa code using the $\alpha\alpha$ prescription (dash-dot blue line, model iv). Both SeBa models use $\alpha_{\rm CE}\lambda = 2$ and $\gamma = 1.5$. The red line is the predicted distribution of transverse velocities resulting from single-star evolution to a $0.95 < M/M_\odot < 1.4$ white dwarf according to model A in table 2.3, and the black line are the observed distributions. All BSE models use a constant SFR and the disk heating relation of model A in table 2.3.

To test whether the data is consistent with this realization, we use the two sample Anderson-Darling statistic (Pettitt, 1976). The Anderson-Darling test considers the difference between the samples across the entire distribution, and so is more statistically powerful that the more commonly used Kolmogorov-Smirnov test which depends only on the extremum. The number of simulated white dwarfs is always much larger, by at least a factor of ten, than the number observed.

The results for one particular choice of SSE and BSE model are shown in figure 2.17(a). In figure 2.17(b) we show the combined probability that the PG and SDSS samples are consistent with each value of θ. In table 2.5 we summarize the results of this procedure for the range of the BSE and SSE models described in tables 2.3 and 2.4.

The results in table 2.5 show that for the majority of models the fiducial numbers of white dwarfs formed via SSE and BSE are consistent with the data. The results taken at face value would also appear to show that, for most models, at the 1 per cent probability level, high-mass white dwarfs must come from a combination of single-star evolution and mergers of high-mass white dwarfs. This appears artificial however: From the right column of figure 2.17(a) the PG sample is consistent with all SSE, while the SDSS sample that has a low probability of arising purely from SSE.

This is a result of the lack of low velocity (< 14 km s^{-1}) white dwarfs in the SDSS sample. It may be that the lack of low velocity white dwarfs in SDSS is a statistical anomaly, since the number of objects is small. In theory this would be taken account of in the analysis described above, however young stellar objects can display prominent substructure in their kinematics as a result of moving groups (e.g., Dehnen, 1998). This would have the result of both reducing the effective sample size, and producing a very different velocity distribution than the Schwarzschild distribution assumed in the SSE Monte Carlo. There are indications that this is the case, since when the SDSS objects are plotted in the $U - V$ plane (assuming zero radial velocity) 7 of the 9 objects lie in the negative U, negative V quadrant. Depending on the unobserved radial velocity, many of these could have kinematics consistent with the Pleiades and Hyades moving groups. Indeed it has been shown that the the white dwarf GD 50, has a velocity and cooling age consistent with a Pleiades origin (Dobbie et al., 2006).

That the data rules out a white dwarf merger origin for the majority of high-mass white dwarfs appears more secure, despite the apparent consistency of the SDSS sample with the BSE simulations: The PG sample is entirely consistent with SSE, and neither sample contains a high-mass white dwarf traveling at > 50 km s^{-1} which would be convincing evidence of a BSE origin for some high-mass white dwarfs. This is not surprising, since the expected number of merger products observed in PG and SDSS ($N_{(\mathrm{BSE})}$ in table 2.5) is significantly smaller than the observed number of objects.

We note that a simpler empirical test for the origin of the high-mass white dwarfs is suggested by figure 2.4. The distribution of high-mass white dwarfs is consistent with the velocity distribution of the intermediate group that displays the kinematics of young objects at the 13 per cent level by

the Anderson-Darling test. This ignores the selection effects which the Monte Carlo simulation addresses, but does suggest that the entire combined group of high-mass white dwarfs is broadly consistent with SSE.

2.6 Scale Heights

One of the key results of this study is that hot white dwarfs of mass $\gtrsim 0.75\,M_{\odot}$ had much shorter main sequence lifetimes than their lower-mass counterparts, and hence their kinematics are characteristic of young stars. A direct result of this is that these higher-mass white dwarfs will have reduced scale height. This is vitally important to consider when calculating the formation rate as a function of mass using local samples such as in Liebert et al. (2005) or Kepler et al. (2007) or producing galactic white dwarf simulations such as Nelemans et al. (2001).

Unfortunately, neither the SDSS or PG sample allow accurate direct determination of the scale height of each white dwarf population, particularly the rare and less luminous high-mass groups. Instead, here we list the expected scale height by comparison with the SSE models that appear to accurately describe the kinematics. We do this to allow simple initial corrections without resorting to the simulations of the type performed in this work. The scale height, h, was defined through

$$\nu(z) = \nu_0 \,\mathrm{sech}^2\left(\frac{z}{2h}\right), \tag{2.15}$$

where $\nu(z)$ is the stellar number density in terms of the height above the plane of the galactic disk, z. The scale height, h, was estimated by constraining equation (2.15) to give both the correct overall number and central WD density, ν_0. We choose this method since the most common usage of the scale height is to calculate galactic birthrates from local densities. The results are give in table 2.6. Plots of the simulated vertical distributions in the solar neighborhood, together with their scale heights defined through equation (2.15) are shown in figure 2.18. Note that the higher-mass groups smaller scale height results in a local density enhanced by more than a factor of two over the more common low-mass group. In particular, the apparent excess of high-mass white dwarfs found in the PG survey (discussed in section 6 of Liebert et al., 2005) can be naturally explained by their lower scale height, which causes a high abundance in this relatively local survey. That the number of high-mass white dwarfs is consistent with single-star expectations in PG is confirmed by the number of expected white dwarfs from single-star evolution in table 2.5.

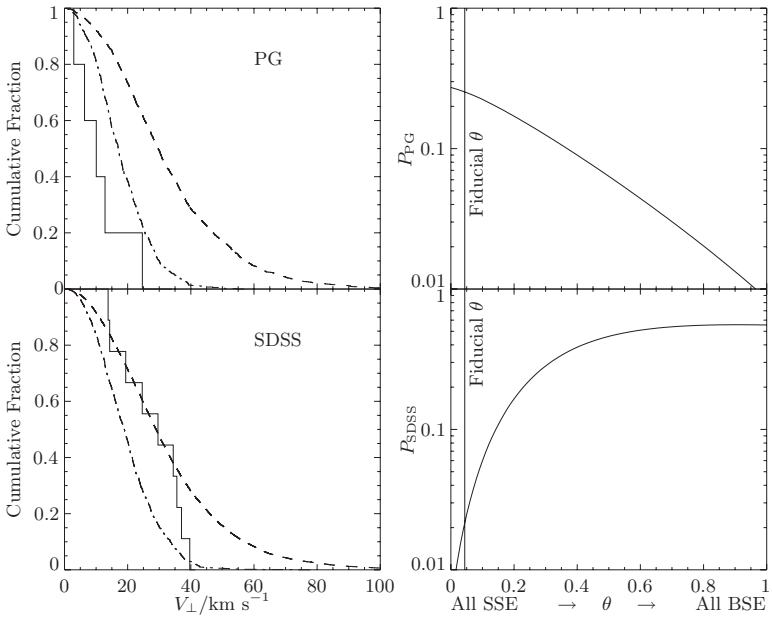

(a) The left column shows the cumulative distribution of transverse velocities of high-mass ($M > 0.95\,M_\odot$) white dwarfs in the SDSS and PG survey. The dashed-dot lines are the predictions of SSE model C and the dashed lines are the predictions of BSE model iv. The right column shows, for each fractional galactic formation fraction from BSE, θ, the probability that the velocity distribution is consistent with the data using the Anderson-Darling statistic for the PG sample, $P_{\rm PG}$, and the SDSS sample, $P_{\rm SDSS}$. The fiducial θ is the fiducial predicted galactic fraction from BSE model iii compared to SSE model C with 50 per cent binary fraction.

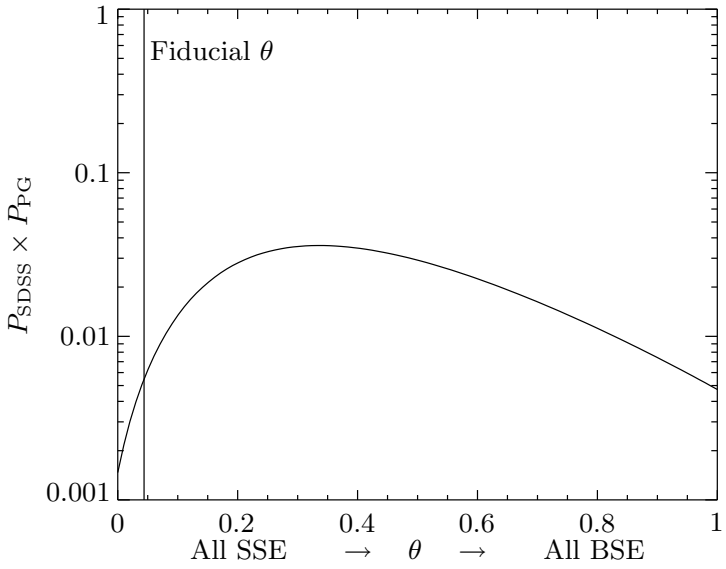

(b) The combined probability that each value θ is consistent with both the PG and SDSS samples. Calculated by the product of the probabilities in the right column of figure 2.17(a).

Figure 2.17 Plots showing the calculation of the galactic formation fraction of high-mass white dwarfs formed in mergers during binary-star evolution in model C compared to single-star evolution model iii.

SFR	SSE Model	BSE Model	$\Gamma_{\rm BSE}$	$\Gamma_{\rm SSE}$	$\theta_{\rm fid}$	PG		SDSS		$P(\theta_{\rm fid})$	$\theta(P > 0.01)$
						$N_{\rm SSE}$	$N_{\rm BSE}$	$N_{\rm SSE}$	$N_{\rm BSE}$		
Const	C	i	0.0006	0.03	0.02	7	0.1	17	0.9	0.02	0.09–0.9
	C	ii	0.0001	0.03	0.005	7	0.02	17	0.1	0.005	0.08–0.8
	C	iii	0.001	0.03	0.04	7	0.3	17	2.	0.04	0.08–0.8
	C	iv	0.001	0.03	0.04	7	0.3	17	2.	0.04	0.09–1.
Exp	D	i	0.0007	0.02	0.04	6	0.1	13	1.	0.04	0.1–0.9
	D	ii	0.0002	0.02	0.01	6	0.02	13	0.2	0.01	0.2–0.8
	D	iii	0.001	0.02	0.07	6	0.3	13	3.	0.07	0.1–0.9
	D	iv	0.001	0.02	0.06	6	0.3	13	2.	0.06	0.2–0.9

Table 2.5 Summary of the results of calculation of the fraction of high-mass white dwarfs formed in mergers compares to single-star evolution. The SSE models are described in table 2.3 and the BSE models are described in table 2.4. $\Gamma_{\rm BSE}$ is the galactic formation rate (in $\rm yr^{-1}$) from binary-star evolution assuming that the merger of two CO white dwarfs with combined mass between $0.95\,M_\odot$ and $1.4\,M_\odot$ results in a high-mass white dwarf. $\Gamma_{\rm SSE}$ is the galactic formation rate from single-star evolution. θ is the galactic fraction of high-mass white dwarfs formed from BSE so that the fiducial value is given by $\theta_{\rm fid} \equiv \frac{\Gamma_{\rm SSE}}{\Gamma_{\rm BSE}+\Gamma_{\rm SSE}}$. The numbers $N_{\rm SSE}$ and $N_{\rm BSE}$ are the predicted observed numbers from SSE and BSE evolution, respectively, in the PG and SDSS samples. $P(\theta_{\rm fid})$ is the probability that *both* the PG and SDSS velocity distributions are consistent with $\theta_{\rm fid}$ using the Anderson-Darling statistic. $\theta(P > 0.05)$ is the range of θ values which have a probability of being consistent with the data greater than 1 per cent. The fiducial value of θ is calculated assuming a 50 per cent binary fraction (i.e., two-thirds of all stars formed in binaries). Both SSE and BSE models use the same disk heating model and star formation history: model C of table 2.3 for the constant SFR models, and model D for the exponential.

Table 2.6 Scale heights, h, defined through equation (2.15) for three different mass groups. h is calculated by matching the central density and overall number to the simulations described in section 2.4.2.

$M_{\rm low}$ /$M_\odot$	$M_{\rm high}$ /$M_\odot$	h / pc
0.45	0.75	120
0.75	0.95	58
0.95	1.40	54

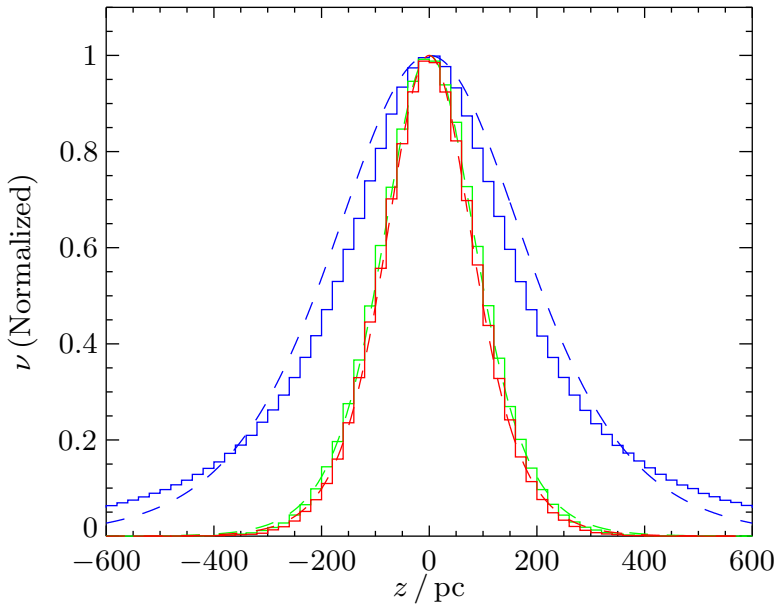

Figure 2.18 The vertical distribution of equation (2.15) with the scale heights from table 2.6 as dashed lines, compared to the simulations described in section 2.4.2 as solid lines. The three groups plotted are the low-mass ($0.45M_\odot < M \leq 0.75M_\odot$) in blue, the intermediate mass in green ($0.75M_\odot < M \leq 0.95M_\odot$) and high-mass ($> 0.95M_\odot$) in red.

2.7 Summary

We have analyzed the kinematics of young ($< 3 \times 10^8$ years) DA white dwarfs from both the PG and SDSS surveys and find a strong connection between their mass and kinematics: low-mass white dwarfs ($0.45\,M_\odot \leq M_1 + M_2 < 0.75\,M_\odot$) display the kinematics of old stars, with higher velocity dispersion ($\sim 46\,\mathrm{km\,s^{-1}}$) and asymmetric drift, while higher-mass white dwarfs ($0.75\,M_\odot \leq M_1 + M_2 < 0.95\,M_\odot$) display the kinematics of young stars with a velocity dispersion of only $\sim 19\,\mathrm{km\,s^{-1}}$. We have shown in section 2.4 that this is expected due to the shorter precursor lifetime of the more massive progenitors, and that there is agreement both on simple analytic grounds (section 2.4.1) and more quantitative Monte Carlo simulations of the PG and SDSS samples (section 2.4.2).

A further key conclusion is that the white dwarf scale height and its variation with age and mass is vitally important to consider when calculating birth rates based on local samples (section 2.6).

In addition, we have separately analyzed the highest-mass white dwarfs ($M > 0.95\,M_\odot$, section 2.5), since it has been suggested that many of these formed as a result of the merger of two lower-mass CO white dwarfs. We find at present a discrepancy in the SDSS velocity distribution where no high-mass white dwarfs with transverse velocity less than $14\,\mathrm{km\,s^{-1}}$ is detected. This results in a velocity distribution that within our statistical framework is inconsistent with purely single-star evolution. We argue this is likely to an anomaly, either be a statistical, or a result of a number of these white dwarfs being members of moving groups. We find that, even under the most optimistic binary evolution models, we would only expect to find 3 white dwarfs formed via white dwarf binary mergers and that the apparent excess of high-mass white dwarfs found in PG is caused by their reduced scale height. In addition, we note the kinematic 'smoking gun' of some fraction of high-mass white dwarfs coming from binary evolution would be high-mass white dwarfs traveling at $> 50\,\mathrm{km\,s^{-1}}$, of which none are found in PG or SDSS.

Appendix 2.A Likelihoods

Here we give our expressions for the proper motion likelihoods of an individual object. These largely follow Ratnatunga et al. (1989), modified to include errors in proper motion. We ignore errors in sky position (ℓ, b), which are small.

Assuming a Schwarzschild distribution function, then, in coordinates aligned with the principle axes of the velocity ellipsoid,

$$f(\mathbf{V}) = \frac{1}{\sqrt{8\pi^3}\sigma_1\sigma_2\sigma_3} \exp\left(-(\mathbf{V}-\mathbf{V_0})^{\mathrm{T}} \cdot \mathbf{\Gamma} \cdot (\mathbf{V}-\mathbf{V_0})\right) , \tag{2.16}$$

where $\mathbf{\Gamma} = \mathrm{diag}(1/2\sigma_1, 1/2\sigma_2, 1/2\sigma_3)$ and $\mathbf{V_0}$ is the mean velocity. Ignoring errors in distance, we

then rotate to axes aligned with the sky plane, and integrate over the unobserved radial velocity, which, in this case, is a nuisance parameter.

We define, $\mathbf{\Lambda}$, to be the dispersion tensor rotated into the coordinate system, (ℓ, b, d), aligned with the sky plane. This will be given by $\mathbf{\Lambda} = \mathbf{R} \cdot \mathbf{\Gamma}$, where $\mathbf{R}$ is a rotation matrix (given explicitly as equation A4 in Ratnatunga et al., 1989). The probability distribution, after integrating over the radial velocity as a nuisance parameter, is an ellipsoid in the sky plane

$$p(v_l, v_b) = C' \exp\Big[-\alpha(v_\ell - \bar{v}_\ell)^2 - \beta(v_b - \bar{v}_b)^2 - 2\gamma(v_\ell - \bar{v}_\ell)(v_b - \bar{v}_b)\Big], \tag{2.17}$$

where $\bar{v}_\ell$ and $\bar{v}_\ell$ are the components of $\mathbf{V_0}$ in the directions of l and b (which can be obtained via $(\bar{v}_\ell, \bar{v}_b, \bar{v}_d) = \mathbf{R} \cdot \mathbf{V_0}$) and α, β, γ, and C' are given by

$$\alpha = \Lambda_{22} - \Lambda_{12}^2/\Lambda_{11}\,, \tag{2.18}$$

$$\beta = \Lambda_{33} - \Lambda_{13}^2/\Lambda_{11}\,, \tag{2.19}$$

$$\gamma = \Lambda_{23} - \Lambda_{12}\Lambda_{13}/\Lambda_{11}\,, \tag{2.20}$$

$$C' = \sqrt{\alpha\beta - \gamma^2}/\pi\,. \tag{2.21}$$

For each object we have measurements of v_l and v_b, together with an associated velocity error σ. Integrating over the 'true' v_l and v_b gives the log likelihood used in equation (2.9) as

$$\begin{aligned}\log \mathcal{L}_i(v_\ell^{\rm obs}, v_b^{\rm obs}) &\equiv \log \int d\mathbf{V} f(\mathbf{V}) P(\mathbf{V}|v_\ell^{\rm obs}, v_b^{\rm obs}, \sigma) \\ &= \log C'' - \frac{\delta}{(\alpha+\delta)(\beta+\delta)-\gamma^2}\times \\ &\Big[(\Delta v_b^2 + \Delta v_\ell^2)(\alpha\beta - \gamma^2) + \\ &\delta(\beta\Delta v_b^2 + \alpha\Delta v_\ell^2 + 2\gamma\Delta v_\ell \Delta v_b)\Big],\end{aligned} \tag{2.22}$$

where

$$\delta = 1/2\sigma^2\,, \tag{2.23}$$

$$\Delta v_\ell = v_\ell^{\rm obs} - \bar{v}_\ell\,, \tag{2.24}$$

$$\Delta v_b = v_b^{\rm obs} - \bar{v}_b\,, \tag{2.25}$$

$$C'' = C' \frac{\delta}{\sqrt{\pi}\sqrt{(\alpha+\delta)(\beta+\delta)-\gamma^2}} \tag{2.26}$$

$$= \delta \sqrt{\frac{\alpha\beta - \gamma^2}{\pi^3[(\alpha+\delta)(\beta+\delta)-\gamma^2]}}\,. \tag{2.27}$$

Note that for small error, $\delta \to \infty$, and equation (2.22) reduces to the log of equation (2.17) as expected.

3

Photometric Identification and Spectroscopic Confirmation of Ultracool White Dwarfs[1]

Abstract

Ultracool white dwarfs display significant flux suppression red-wards of ~ 6000 Å due to collision-induced opacity (CIA). This which moves them out of the stellar locus. We show that their unique colors enable their identification purely photometrically. We applied cuts to SDSS photometry to produce targets and have observed and spectroscopically confirmed four new ultracool white dwarfs with a 100 per cent purity. One additional ultracool white dwarf was found in the SDSS data but did not pass the photometric quality cuts. These five new ultracool white dwarfs display disk kinematics and their density is consistent with previous estimates.

[1]This work will be submitted for publication in ApJ with authors: Christopher Wegg and Sterl Phinney in this order.

3.1 Introduction

Hot white dwarfs can easily be identified on the basis of their blue colors (e.g., Eisenstein et al., 2006; Liebert et al., 2005), however cool ($T_{\rm eff} \lesssim 8000\,K$) white dwarfs are more challenging to identify. In clusters they can readily be identified from their sub-luminous nature (e.g., Hansen et al., 2007), but in the field their colors are typically indistinguishable from the stellar locus. Instead the statistical technique of finding sub-luminous objects via their high proper motion and therefore faint reduced proper motion is used (e.g., Kilic et al., 2006; Vidrih et al., 2008). In this work we show that the coolest white dwarfs, those known as ultracool white dwarfs, can be identified via their unique colors, a prospect first suggested by Hansen (2001).

When white dwarfs cool below an effective temperature of $\sim$ 4000 K the hydrogen in their atmosphere forms neutral H_2 molecules. Since H_2 in its ground state has zero dipole moment, it usually absorbs photons only via higher-order transitions such as electric quadrupole transitions. This results in a dramatic lowering of the mean opacity of the atmosphere.

One result of this lowering of opacity is that the depth of the photosphere increases, and hence the pressure at the photosphere increases. This has the effect of increasing the rate of collisions between H_2 and other H_2 or He molecules. At these rates of collisions the dominant form of opacity becomes collision-induced absorption (CIA). CIA is the process whereby a H_2 molecule is sufficiently close to another species that a dipole is induced, resulting in electric dipole transitions being allowed. These CIA transitions are typically roto-vibrational and very broad. At the pressures found in white dwarfs at low temperature, they dominate the opacity at wavelengths longer than 1 μm (see Lenzuni et al., 1991, for opacity calculations and good explanations of the physics). As a result of this strong red-ward opacity there is a flux deficit, relative to a black body, at wavelengths longer than $>$ 1 μm.

A subset of these white dwarfs show stronger CIA. These are the white dwarfs termed ultracool white dwarfs by Gates et al. (2004) and Harris et al. (2008), which we search for and identify in this work. In these objects the flux deficit extends to 6000 Å. An example spectrum, that of SDSS J133739.40+0001428 (hereafter SDSS J1337, Harris et al., 2001), is compared to a 4000 K blackbody in figure 3.1.

Other examples of ultracool white dwarfs displaying significant CIA and flux suppression red-wards of 6000 Å are LHS 3250 (which was the first discovered, Harris et al., 1999), and those serendipitously targeted for spectroscopy by SDSS, such as the aforementioned SDSS J1337 and those found in Gates et al. (2004) and Harris et al. (2008). We summarize the known ultracool white dwarfs that lie in the SDSS DR7 footprint in table 3.1.

Table 3.1 Summary of the properties of the previously known, spectroscopically confirmed, ultracool white dwarfs which lie within the SDSS DR7 survey footprint. Three other ultracool white dwarfs showing strong optical CIA lie outside the survey footprint and are omitted: LHS 1402 (Oppenheimer et al., 2001; Salim et al., 2004), GD 392 (Farihi, 2004), and SSS J1556-0806 (Rowell et al., 2008).

Short Name	RA[a]	Dec[a]	Epoch[a] (MJD)	u	g	r	i	z	μ[b]	μ_α[b] (mas yr^{-1})	μ_δ[b]	H_g[c]	d[d] (pc)	$v_\perp$[d] (km s^{-1})	Discovery Paper	Strong Optical CIA?
J0947	09 47 23.0	+44 59 49	52283.4	20.74	19.45	18.85	18.93	19.44	85 ± 7	68 ± 5	51 ± 5	19.09	53	21	Gates et al. (2004)	Yes
J1001	10 01 03.4	+39 03 40	52639.5	21.42	20.04	19.58	19.99	20.55	353 ± 14	−302 ± 4	−181 ± 14	22.77	69	115	Gates et al. (2004)	Yes
J1220	12 20 48.7	+09 14 12	52345.3	22.43	20.35	19.31	19.45	19.88	501 ± 15	−320 ± 9	−385 ± 12	23.84	79	188	Gates et al. (2004)	Yes
J1251	12 51 06.1	+44 03 03	52724.3	21.44	20.17	20.39	20.69	20.86	170 ± 8	−167 ± 6	30 ± 6	21.32	73	59	Harris et al. (2008)	Yes
J1337	13 37 39.4	+00 01 43	51258.4	20.79	19.55	19.13	19.52	20.03	175 ± 7	−16 ± 5	−175 ± 5	20.77	55	46	Harris et al. (2001)	Yes
J1403	14 03 24.7	+45 33 33	52704.5	20.10	18.90	18.95	19.48	19.76	283 ± 10	−267 ± 7	−94 ± 7	21.15	41	55	Gates et al. (2004)	Yes
J1654[5]	16 54 01.2	+62 53 55	51638.4	19.68	18.39	17.86	18.07	18.55	570 ± 7	−548 ± 5	157 ± 5	22.17	32	87	Harris et al. (1999)	Yes
J0146	01 46 29.0	+14 04 38	51464.4	21.21	19.99	19.37	19.24	19.71	252 ± 7	251 ± 5	29 ± 5	22.00	67	81	Harris et al. (2008)	No
J0310	03 10 49.5	-01 10 35	52522.4	22.49	20.95	20.20	19.89	19.97	81 ± 8	−25 ± 6	−77 ± 6	20.50	105	40	Harris et al. (2008)	No
J0854	08 54 43.3	+35 03 53	52585.5	23.67	20.51	19.38	19.06	18.91	234 ± 8	−140 ± 6	−188 ± 6	22.36	86	95	Gates et al. (2004)	No
J1238	12 38 12.9	+35 02 49	53111.3	24.73	21.76	20.31	19.87	20.31	189 ± 9	−138 ± 6	−130 ± 6	23.14	152	136	Harris et al. (2008)	No
J1452	14 52 39.0	+45 22 38	52788.2	21.59	20.03	19.35	19.26	19.30	91 ± 7	−55 ± 5	72 ± 5	19.82	69	29	Harris et al. (2008)	No
J1632	16 32 42.2	+24 26 55	52811.3	21.33	19.60	18.72	18.49	18.47	349 ± 8	−16 ± 6	−349 ± 6	22.31	56	93	Harris et al. (2008)	No
J2239	22 39 54.1	+00 18 47	52197.3	21.51	20.16	19.53	19.47	20.09	120 ± 7	1 ± 5	120 ± 5	20.56	73	41	Harris et al. (2008)	No

[a] RA and Dec are given as equinox J2000 at the Julian date of SDSS observation in the Epoch column.
[b] Proper motions taken from the PPMXL catalog (Roeser et al., 2010).
[c] Reduced proper motion in g-band. See equation (1.2).
[d] Assuming the absolute magnitude in the g-band of LHS 3250.
[e] Originally discovered as LHS 3250.

Current model atmosphere fits to white dwarfs displaying strong CIA perform poorly. An example of this can be seen in the fits to ultracool white dwarfs in figure 16 of Kilic et al. (2010). It is especially useful therefore that LHS 3250 has a measured parallax of (33.04 ± 0.5) mas placing it at (30.3 ± 0.5) pc (Monet et al., 1992). This allows the absolute magnitude to be calculated directly, for example, in the V band it is M_v = (15.72 ± 0.04) (Harris et al., 1999). The close distances of these objects cause them to have very high proper motions[2]. For example, LHS 3250 has a proper motion of 565.7 ± 0.1 mas yr^{-1}, which is an order of magnitude larger than the typical proper motions displayed by the white dwarfs in chapter 2.

There are also a number of white dwarfs which display less significant CIA with only a mild optical flux suppression with more significant suppression in the IR. Examples of this class are LHS 1126 (Bergeron et al., 1994) and WD 0346 (Hambly et al., 1997), as well as several found in Harris et al. (2008). We do not attempt to exhaustively catalog this class in table 3.1, but when included they are marked as not having strong optical CIA.

The blue-ward evolution of the coolest white dwarfs is also illustrated as a blue-ward 'hook' in the cooling sequences of the globular cluster NGC 6397 shown in figure 1.2 (although the mass evolution along the cooling sequence may also contribute).

In this chapter we show that ultracool white dwarfs which display strong CIA can be detected by the unique colors alone. In section 3.2 we describe the cuts in color-color space that isolate CIA white dwarfs, in section 3.3 we describe our observations of four of these objects, all of which are confirmed to be ultracool white dwarfs, and in section 3.4 we discuss the implications and possible uses of this work.

3.2 Selection

The flux suppression red-ward of ∼ 6000 Å shown in figure 3.1 results in ultracool white dwarfs with strong CIA having reduced brightness in the i, z, and (to a lesser extent) the r-bands. This moves them out of the stellar locus into an extremely sparsely populated region of color space. By choosing cuts in color-color space that exclude the stellar locus but include the known CIA white

[2]This is why many ultracool white dwarfs have the object name prefix Luyten Half Second (LHS) — a catalog of objects with proper motions larger than 0.5" per year (Luyten, 1979).

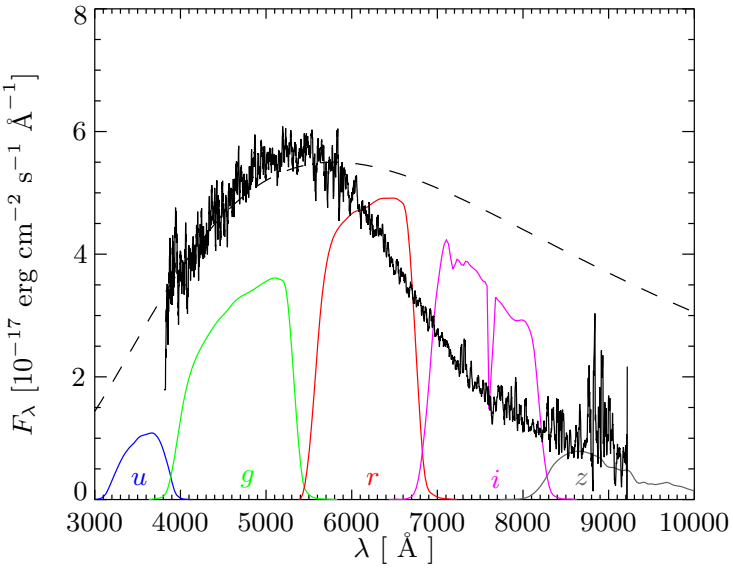

Figure 3.1 The spectrum of the white dwarf SDSS J1337 which displays significant CIA red-ward of 6000 Å (Harris et al., 2001). Also plotted is a 4000 K blackbody as the dashed line, and the SDSS response in filters u, g, r, i, z in blue, green, red, magenta, and gray, respectively.

dwarfs the number of targets is reduced to a manageable number. The cuts used were

$$\begin{aligned} r - i &< -0.3 + 0.5\,(g - r)\,, \\ r - z &< 0.95\,(g - r) - 0.7\,, \\ r - z &< -0.4\,, \\ u - g &> 1\,, \\ g - r &< 0.5\,(u - g) + 0.1\,. \end{aligned} \tag{3.1}$$

These cuts are illustrated in figure 3.2 together with the known ultracool white dwarfs from table table 3.1. Six of the seven previously known white dwarfs showing strong optical CIA pass these cuts.

These cuts were chosen empirically. However, in principle, it would be possible to make these cuts via atmospheric models. At present though the atmospheric models do not fit the spectra of ultracool white dwarfs sufficiently well to make this possible (Kilic et al., 2010).

Even a small number of the vast number[3] of objects in the stellar locus being scattered into this region of color-color space would be catastrophic. We therefore also require that the candidate objects have reliable photometry. We require in addition to the color-color cuts given in equation (3.1):

1. The object is classified by the SDSS photometry pipeline as a star.

[3]There are 357 million objects with measured photometry in SDSS DR7, from which we select $O(10)$ candidate objects.

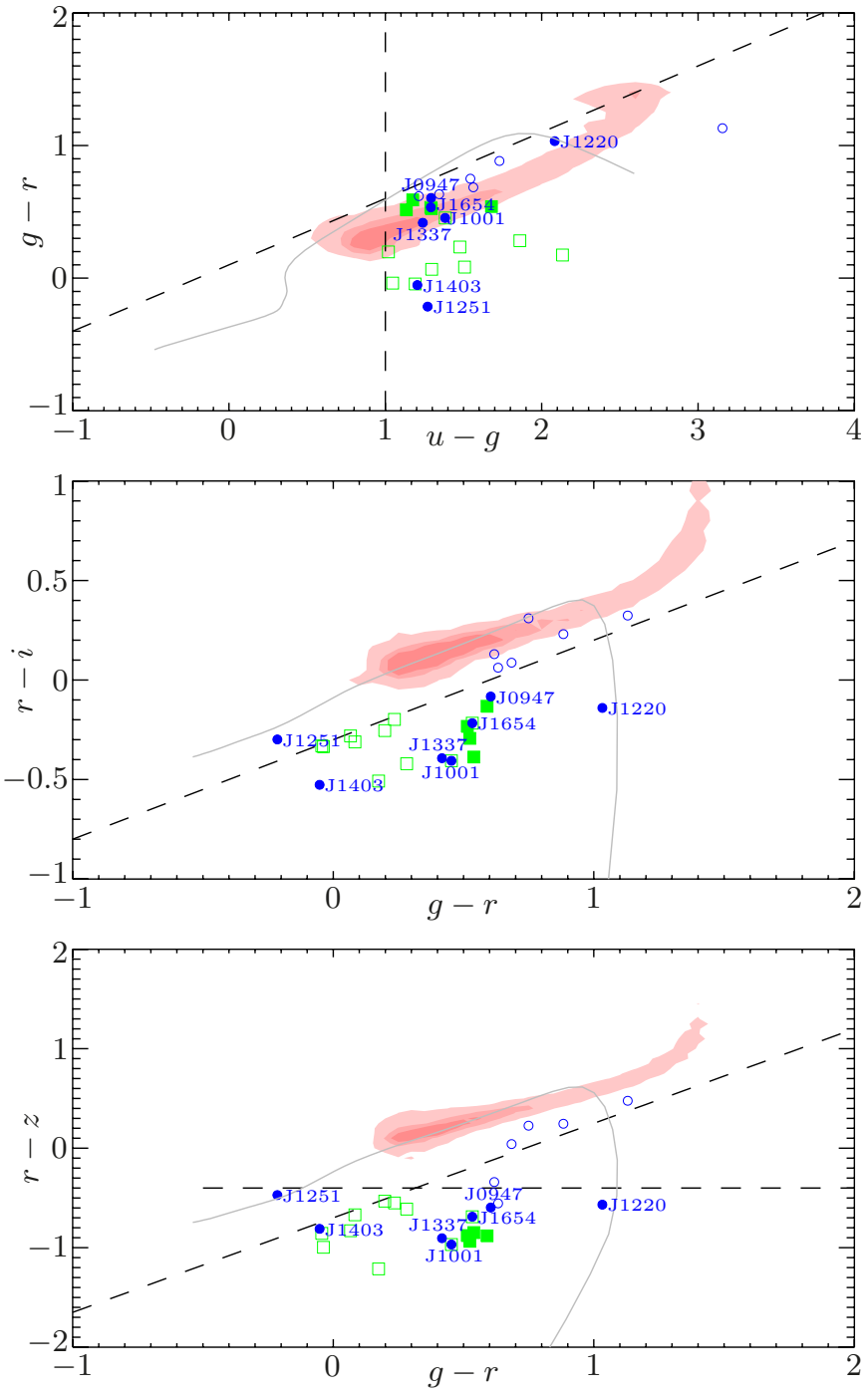

Figure 3.2 Known and candidate ultracool white dwarfs. The color-color cuts of equation (3.1) are shown as dashed lines. Known ultracool white dwarfs in table 3.1 are plotted in blue, those showing strong CIA absorption are plotted with filled circles and labeled. Candidate objects from table 3.2 are plotted in green, those observed in this work and shown to be ultracool white dwarfs are plotted as filled symbols. Contours of density of objects in color-color space are shown in pink and trace the stellar locus.

2. The object lies at galactic latitude higher than 30 deg. Accurate photometry in crowded fields is more difficult, and the SDSS photometry pipeline has occasional catastrophic failures in these fields that scatter objects from the stellar locus into the cuts described here.

3. The error in each band less than 0.21 mag. Errors larger than this often indicate unreliable photometry.

4. That none of the flags recommended by SDSS as indicating unreliable photometry are set in each band[4]: `EDGE`, `NOPROFILE`, `PEAKCENTER`, `NOTCHECKED`, `PSF_FLUX_INTERP`, `SATURATED`, or `BAD_COUNTS_ERROR`.

5. That the object was not deblended as a moving object (`DEBLENDED_AS_MOVING` flag).

6. If the object was deblended that the parent does not have the `DEBLEND_UNASSIGNED_FLUX` flag set. If this is the case the unassigned flux is assigned proportionally to its child objects, hence the child objects have unreliable photometry.

7. That there is no neighbor object within 6". Very close neighbors (<1") indicate spurious detections. Wider separations have PSFs where the wings may overlap making reliable photometry more difficult.

The resulting 14 objects which pass these selection criteria are shown in table 3.2 of which two were previously discovered as ultracool white dwarfs. Despite the efforts to isolate only genuine detections, five of these appear to be spurious since they are not detected in the Digitalized Sky Survey of second Palomar Observatory Sky Survey (POSS-II, Reid et al., 1991). A further three objects, despite passing the color-color selection cuts, had proper motion consistent with zero. If these objects were ultracool white dwarfs with the same absolute magnitude as LHS 3250 their transverse velocity would be less than 5 $\mathrm{km\,s^{-1}}$ and so are highly unlikely to be ultracool white dwarfs and were discounted. This leaves a sample of 4 candidate ultracool white dwarfs.

[4] http://www.sdss.org/dr7/tutorials/flags/index.html#clean

Table 3.2 White dwarfs that pass the candidate selection cuts described in section 3.2.

Short Name	RA[a]	Dec[a]	Epoch[a] (MJD)	u	g	r	i	z	μ[b]	μ_α[b] (mas yr^{-1})	μ_δ[b]	H_g[c]	d[d] (pc)	$v_\perp$[d] (km s^{-1})	Candidate?
J0805	08 05 21.7	+21 30 33	51638.4	20.65	19.60	19.64	19.97	20.64	-	-	-	-	56	-	No: Not detected in POSS II
J0821	08 21 47.4	+42 24 02	51987.4	20.89	19.42	19.18	19.38	19.73	14 ± 11	10 ± 8	−9 ± 8	15.08	52	3	No: Zero proper motion
J0826	08 26 38.7	+58 47 14	52754.4	21.53	20.51	20.31	20.56	20.84	6 ± 13	0 ± 9	−6 ± 9	14.44	85	2	No: Zero proper motion
J0957	09 57 43.4	+22 38 54	51962.2	21.89	19.75	19.58	20.09	20.79	10 ± 10	10 ± 7	1 ± 7	14.81	60	3	No: Zero proper motion
J1001	10 01 03.4	+39 03 40	51258.4	21.42	20.04	19.58	19.99	20.55	249 ± 10	127 ± 7	−215 ± 7	22.02	69	81	Yes: Found by Gates et al. (2004)
J1043	10 43 46.1	+32 12 38	52671.2	21.71	19.85	19.56	19.99	20.18	-	-	-	-	63	-	No: Not detected in POSS II
J1121	11 21 00.1	+14 17 29	52667.5	21.01	19.72	19.19	19.49	20.13	317 ± 7	94 ± 5	−303 ± 5	22.22	59	89	Yes: Observed. See figure 3.4
J1330	13 30 37.7	+00 29 01	53359.5	20.96	19.45	19.37	19.68	20.04	-	-	-	-	53	-	No: Not detected in POSS II
J1336	13 36 42.7	+07 48 27	53111.3	22.17	20.49	19.95	20.34	20.80	265 ± 9	−61 ± 7	258 ± 7	22.61	85	106	Yes: Observed. See figure 3.4
J1358	13 58 11.2	+04 30 02	52639.5	20.39	19.20	19.24	19.58	20.10	-	-	-	-	47	-	No: Not detected in POSS II
J1449	14 49 47.9	+09 08 40	52756.3	20.55	19.25	19.19	19.47	20.02	-	-	-	-	48	-	No: Not detected in POSS II
J1542	15 42 03.7	+27 50 22	52963.4	21.92	20.79	20.27	20.51	21.15	72 ± 10	−67 ± 7	−26 ± 7	20.07	97	33	Yes: Observed. See figure 3.4
J1602	16 02 44.9	+08 56 29	52812.2	21.68	20.51	19.92	20.05	20.80	56 ± 10	20 ± 7	−53 ± 7	19.26	86	23	Yes: Observed. See figure 3.4
J1654[e]	16 54 01.2	+62 53 55	52755.4	19.68	18.39	17.86	18.07	18.55	570 ± 7	−548 ± 5	157 ± 5	22.17	32	87	Yes: Found by Harris et al. (1999)

[a] RA and Dec are given as equinox J2000 at the Julian date of SDSS observation in the Epoch column.
[b] Proper motions taken from the PPMXL catalog (Roeser et al., 2010).
[c] Reduced proper motion in g-band. See equation (1.2).
[d] Assuming the absolute magnitude in the g-band of LHS 3250.
[e] Originally discovered as LHS 3250.

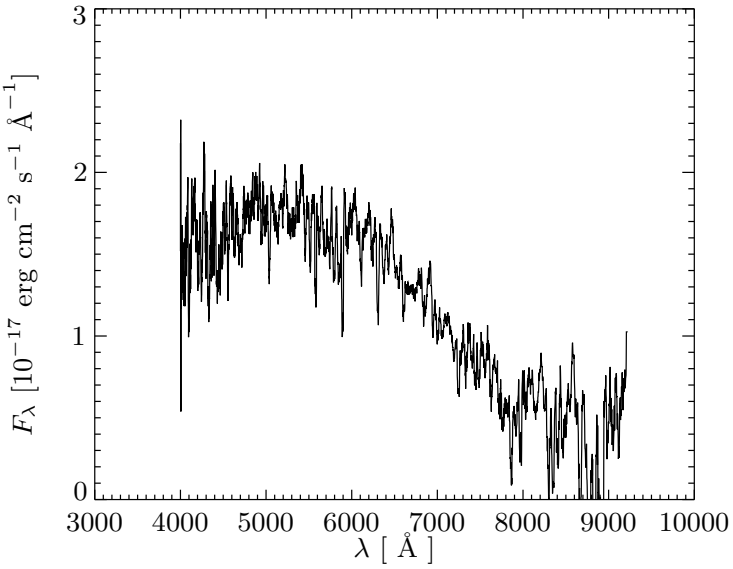

Figure 3.3 The spectrum, taken by SDSS, of SDSS J083511.55+184402.9: A white dwarf displaying CIA serendipitously found in the SDSS data which displays significant CIA red-ward of 6000 Å . This object did not pass the stringent cuts to be a candidate object, but instead the SDSS spectrum was serendipitously discovered while selecting those cuts.

While choosing the targets an ultracool WD already observed by SDSS was identified: SDSS J083511.55+184402.9, whose spectrum is shown in figure 3.3.

3.3 Observations

Four of the white dwarfs passing the cuts described above were observed using the Double Spectrograph (DBSP) on the 200-inch Hale telescope at Palomar observatory on the nights of 13 and 14 April 2007. The spectra were reducing using the standard procedure `doslit` in `iraf`.

The spectra are shown in figure 2.3. All four candidate objects are clearly white dwarfs demonstrating strong CIA.

Both nights were photometric and the spectra were flux calibrated using the standards HZ44, HD84937, BD+262606, and BD+284211. Since the observations were blind offset observation of objects with significant proper motions since the last epoch of observation, it possible that they were not well centered in the slit. However the observations were taken with the slit at the parallactic angle and, from figure 2.3 the results of the spectrophotometry are close to the SDSS photometry.

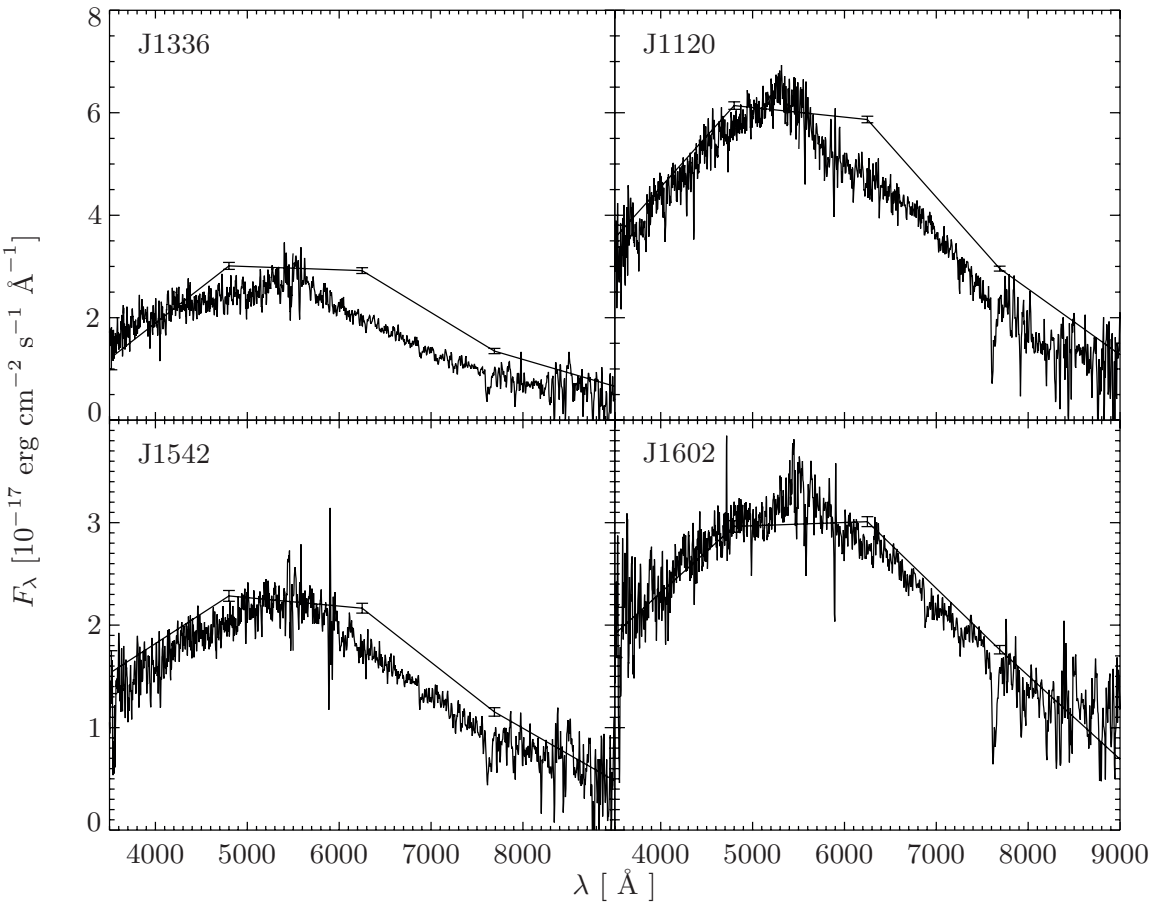

Figure 3.4 Spectra of ultracool white dwarfs observed using the double spectrograph on the 200-inch Hale telescope at the Palomar observatory. The SDSS photometry which led us to identify them is also plotted with each filter plotted at its $\lambda_{\rm eff}$.

3.4 Discussion

The density of ultracool white dwarfs can be estimated from the six found over the 8423 deg^2 legacy footprint of SDSS DR7 (which is the vast majority of SDSS imaging above 30 deg Galactic latitude). This gives an area density of ~ 0.0007 deg^{-2}. Only two of the seven white dwarfs previously known to display strong optical CIA pass the stringent selection cuts however. Correcting for this gives an area density of ~ 0.0025 deg^{-2}. This is larger than the ~ 0.0015 deg^{-2} found in SDSS spectra through April 2004 by Gates et al. (2004). The sample here is marginally deeper however, since that was based on those targeted as QSO candidates for which $i < 20.2$ is required.

The investigation of the kinematics of the white dwarfs in chapter 2 was complicated by the lack of radial velocity information. However in that work distances were calculable via fits to atmospheric models. The atmospheric models of ultracool white dwarfs however fit the observations poorly, and therefore are insufficient for this purpose. The ultracool white dwarfs are close enough however that the parallaxes should typically be 10 – 30 mas, and therefore be measurable in the near

future. Indeed GAIA could measure highly accurate parallaxes for many of the objects in this work (Lindegren, 2009), the primary difficultly being that the objects here are close to the faint magnitude limit.

Without either distances or radial velocities, detailed kinematic modeling of the type performed in chapter 2 is unwarranted. Instead we perform a qualitative check. In figure 3.5 we plot the velocities of the candidates in the Galactic plane i.e., the U-V plane, where U is towards the Galactic center, and V is directed in the direction of Galactic rotation. In making these plots we have assumed that all the ultracool white dwarfs have the same g-band absolute magnitude as LHS 3250. In addition in figure 3.5(a) we assume that the velocity out of the galactic plane is zero (i.e., $W = 0$), while in figure 3.5(b) we assume the unobserved radial velocity is zero.

While these are crude checks of the kinematics there are several points worth noting. None of the ultracool white dwarfs discovered in this work display halo kinematics. Indeed only one of the 19 ultracool white dwarfs displays halo kinematics: J1220 whose kinematics were noted by Gates et al. (2004). The other 18 white dwarfs in appear to have a dispersion and asymmetric drift (mean V velocity) consistent with membership of an old disk population, i.e., thick disk. This also indicates that on their absolute magnitudes are consistent with LHS 3250, at least on average, since this was assumed in the distance calculation.

3.4.1 Prospects

In the light of this work the upcoming Large Synoptic Survey Telescope (LSST) survey is especially promising for discovering ultracool white dwarfs. LSST is expected to have single-visit 5-σ depths in the u, g, r, i, z, and y-bands of 23.9, 25.0, 24.7, 24.0, 23.3, and 22.1, respectively (Ivezic et al., 2008). Each area of the sky is visited times 70, 100, 230, 230, 200, and 200, respectively, giving co-added depths of approximately 26.3, 27.5, 27.7, 27.0, 26.2, and 24.9. Assuming that all ultracool white dwarfs are similar to LHS 3250 and conservatively that they can be detected the single visit 5-σ depth then they would be detectable to ~ 210 pc, the limiting band being the u-band. This is a factor of 2.4 greater in distance than even the SDSS 2-σ limit of 22.0, and we therefore expect *at least* a factor of 10 increase in number. Less conservatively the single visit depth in the g and r-bands are ~ 650 pc and so, these images can be used to calculate the astrometric solution (i.e., position, proper motion, and parallax) of each object. The color-color cuts involving the u, i, and z-bands could be applied to the co-added image increasing the maximum detectable distance to ~ 650 pc. This would result in a 400-fold increase in number of ultracool white dwarf detections over SDSS, or of order 4000 ultracool white dwarfs.

This huge increase in number also highlights one of the important aspects of this work. LSST will identify vast numbers of many classes of objects, for example, in this thesis we predict both $O(1000)$ ultracool white dwarfs in this chapter, and $O(1000)$ tidal disruptions in chapter 4. It is

clearly unfeasible to follow up more than a small number of these objects. This work shows that ultracool white dwarfs will potentially require no follow up: they can unambiguously be identified photometrically.

In atmospheric fits to cool white dwarfs there is a degeneracy between distance and $\log g$. In the hotter white dwarfs in chapter 2, this degeneracy was broken by fits to the Balmer series. However, in cool white dwarfs this not possible. This degeneracy can is easily understood as a solid angle degeneracy: In cool white dwarfs the effect of increasing $\log g$ is to decrease the solid angle subtended, and therefore the white dwarf can also be fit by decreasing the distance (Mortlock et al., 2009).

Because the spectra of ultracool white dwarfs display broad absorption in their spectra, if the future, once the atmospheric models are of sufficient quality, it may be possible to fit the atmospheric parameters, $T_{\rm eff}$, $\log g$ and N(H)/N(He), purely from photometry. The greater difficulty may prove to be breaking the degeneracy between $\log g$ and N(H)/N(He), since both strongly affect the pressure at the photosphere. If the distance were known, then $T_{\rm eff}$ and N(H)/N(He) would be calculable. Unfortunately parallaxes are unlikely to be available for the majority of LSST objects. Instead it may be necessary to assume a mass, similar to the often used assumption $\log g = 8$. The validity of this assumption can be readily checked for those ultracool white dwarfs for which parallaxes will be measured by GAIA.

It should therefore be possible, purely from the photometry, to probe the $T_{\rm eff}$ and infer the ages of a large number of ultracool white dwarfs using LSST. If the models turn out to be non-degenerate in $\log g$ and N(H)/N(He), then the masses will also be estimable. These are tantalizing prospects since ultracool white dwarfs are the current end state of the majority of population II or halo stars with initial mass $0.9\,M_{\odot} \lesssim M \lesssim 8\,M_{\odot}$, and therefore tell us about the Galactic population of old stars, from parts of the initial mass function not probed by low mass main sequence stars. They therefore represent the local fossils with the most direct relation to the light from high redshift galaxies studied by missions such as Spitzer and the Hubble Space Telescope.

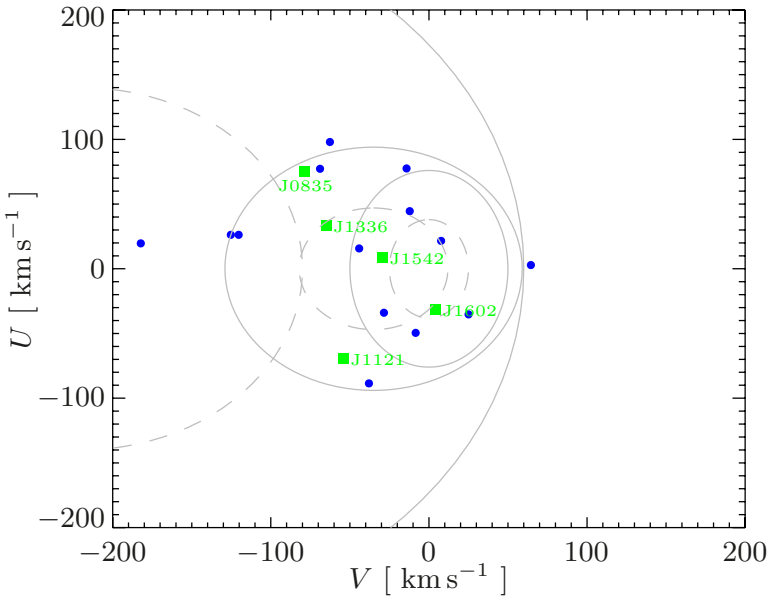

(a) Kinematics of ultracool white dwarfs assuming $W = 0$.

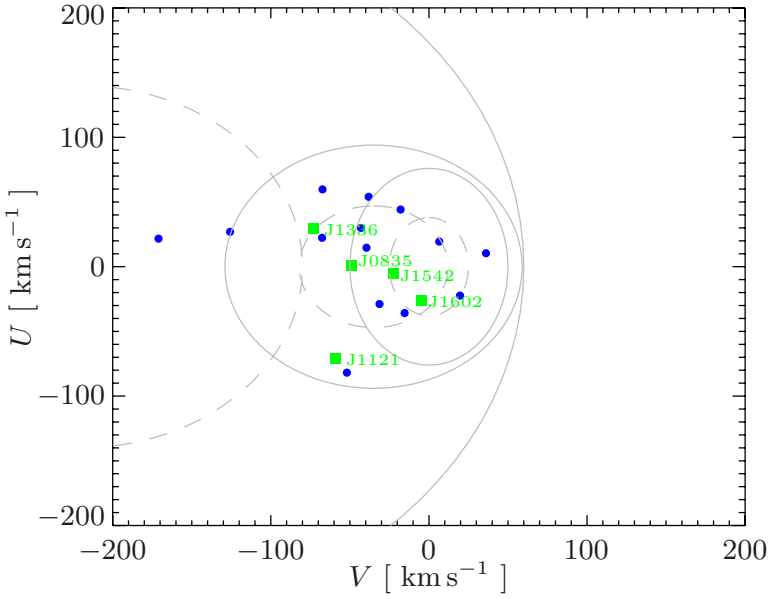

(b) Kinematics of ultracool white dwarfs assuming zero radial velocity.

Figure 3.5 Kinematics of ultracool white dwarfs assuming either that the velocity out of the galactic plane is zero in figure 3.5(a), or that the unobserved radial velocity is zero in figure 3.5(b). To calculate distances, and therefore transverse velocities, all white ultracool white dwarfs are assumed to have the same g-band absolute magnitude as LHS 3250. Previously known ultracool white dwarfs are shown in blue. Ultracool white dwarfs identified in this work are plotted in green and labeled. The gray ellipses are the galactic thin disk, thick disk, and halo, in order of increasing size. The dashed line is the 1-σ density contour (i.e., 68 per cent of objects should be enclosed), and solid line is the 2-σ density, assuming that the local velocity distribution is a Schwarzschild distribution.

4

Multiple Tidal Disruptions as an Indicator of Binary Supermassive Black Hole Systems[1]

Abstract

We find that the majority of systems hosting multiple tidal disruptions (TDs) are likely to contain hard binary SMBH systems, and also show that the rates of these repeated events are high enough to be detected by LSST over its lifetime. Therefore, these multiple TD events provide a novel method to identify supermassive black hole (SMBH) binary systems with parsec to sub-parsec separations. The rates of TDs are investigated using simulations of non-interacting stars initially orbiting a primary SMBH and the potential of the model stellar cusp. The stars are then evolved forward in time and perturbed by a secondary SMBH inspiraling from the edge of the cusp to its stalling radius. We find with conservative magnitude estimates that the next generation transient survey LSST should detect multiple TDs in approximately 3 galaxies over 5 years of observation, though less conservative estimates could increase this rate by an order of magnitude.

[1]This work was published as ApJL, 738, L8 (2011) , arXiv:1011.5874 with authors: Christopher Wegg and Nate Bode in this order (Wegg and Bode, 2011). Reproduced here by permission of the AAS, copyright © (2011).

4.1 Introduction

Stars with radius $R_\star$, and mass $M_\star$, which pass within the tidal disruption radius $r_t \sim R_\star(M_{\rm BH}/M_\star)^{1/3}$ of a supermassive black hole (SMBH) of mass $M_{\rm BH}$, will be ripped apart by tidal forces. In the case of sun-like stars,

$$r_t \approx 1.2 r_s M_8^{-2/3}\,, \tag{4.1}$$

where r_s is the Schwarzschild radius, and M_8 is $M_{\rm BH}/10^8 M_\odot$. Therefore, when $M_{\rm BH} \gtrsim 10^8 M_\odot$ the Schwarzschild radius lies outside r_t and any sun-sized star would be swallowed whole. Below this critical black hole mass the star's debris is launched on orbits which span an energy range $\Delta E \approx G M_{\rm BH} R_\star / r_t^2$ (Rees, 1988). This energy range is large compared to the energy of the highly elliptic initial orbit, and hence half the material will be initially unbound while half will begin to fall back onto the black hole. For main sequence stars the late time canonical fall-back rate declines as $t^{-5/3}$ (Phinney, 1989). This fall-back rate is initially super-Eddington for the canonical 10% accretion efficiency (Evans and Kochanek, 1989), but it is unclear whether a radiatively driven outflow results (Lodato and Rossi, 2011; Strubbe and Quataert, 2009), or the disk adjusts to lower its accretion rate.

Galaxies harboring an isolated SMBH at their center are expected to quickly clear a 'loss cone' of orbits whose angular momenta about the black hole are low enough that their peribothra lie inside r_t. At this point tidal disruptions (TDs) are predicted at a rate $\sim 10^{-4} - 10^{-5}\,{\rm yr}^{-1}$ as stars diffuse into the loss cone (Donley et al., 2002; Magorrian and Tremaine, 1999; Wang and Merritt, 2004). The majority of candidate TDs thus far have been found though x-ray (e.g., Donley et al., 2002) or UV surveys (e.g., Gezari et al., 2008). This is expected, as can be seen by modeling the TD as a thick disk emitting as a black body with luminosity $L_{\rm edd}$, temperature $T_{\rm eff}$, and initially extending to r_t. In reality the disk will expand outwards on a viscous timescale and the initial super-Eddington rate could launch an outflow. Ignoring these complications, however, gives (Ulmer, 1999)

$$T_{\rm eff} \sim 3.7 \times 10^5 M_8^{1/12} \left(\frac{M_\star}{M_\odot}\right)^{-1/6} \left(\frac{r_\star}{r_\odot}\right)^{-1/2} {\rm K}\,, \tag{4.2}$$

and the spectrum peaks in the extreme UV. Despite being in the Rayleigh-Jeans tail of this flux, optical transient surveys such as the Palomar Transient Factory (PTF), the Panoramic Survey Telescope and Rapid Response System (Pan-STARRS) and the Large Synoptic Survey Telescope (LSST) provide the prospect of finding many more TDs because of their unprecedented combination of high cadence and depth. It is expected that LSST will detect a striking $\sim 100 - 3000\,{\rm yr}^{-1}$ (Strubbe and Quataert, 2009).

In this chapter we calculate the rates of multiple TDs from a merging SMBH binary system, and show that the detection of multiple TDs from a single galaxy likely indicates the galaxy hosts a SMBH binary with a parsec to sub-parsec separation. Our results are summarized in table 4.1.

4.2 Simulations

We determine the rates of multiple TDs from a binary SMBH system using a simulation of 5×10^5 stars of radius $R_\odot$ orbiting the primary SMBH of mass M_1 in the test particle limit. The stars are initially chosen from a self-consistent isotropic stellar distribution centered on the primary SMBH (Dehnen, 1993; Tremaine et al., 1994). Given its initial conditions, each star is then integrated forward in time whilst, *at the same time,* the secondary, of mass qM_1, is moved inwards on a slightly eccentric inspiral until it reaches the stalling radius. During the integration, we ignore star-star interactions and, additionally, assume that the stellar potential does not change. If the star reaches r_t, it is counted as a TD, unless its angular momentum was initially within the TD loss cone.

Two mechanisms for enhanced rates of TDs in close SMBH binary systems have been considered in the literature: the Lidov-Kozai effect (Ivanov et al., 2005) and chaotic 3-body orbits (Chen et al., 2009). We have extended these works by including two additional aspects: the evolution of the binary, and the non-Keplerian stellar potential[2].

The initial conditions of our stars are drawn from an η-model cusp with stellar mass $2\,M_1$ (Dehnen, 1993; Tremaine et al., 1994) whose density is given by

$$\rho(r) = \frac{GM_1\eta}{2\pi r_c^3} \frac{1}{(r/r_c)^{3-\eta}(1 + r/r_c)^{1+\eta}} \,. \tag{4.3}$$

Here, r_c is the characteristic radius of the cusp and η parametrizes the cusp steepness. The advantage of this model is that it self-consistently describes a finite mass of isotropic stars distributed around a central black hole together with their stellar potential. A centrally relaxed Bahcall-Wolf cluster corresponds to $\eta = 1.25$ Bahcall and Wolf (1976). For the duration of the scattering experiments the stellar potential is assumed to be centered on the primary SMBH and is not allowed to vary with time. These assumptions are made for simplicity, and will be relaxed in future studies.

For a given η and SMBH mass ratio $q \leq 1$, our simulations depend only on the TD radius through r_t/r_c. The scaling of r_t/r_c to real galaxies is described later by equations (4.6) and (4.7).

The stars are initially on orbits consistent with the primary SMBH and the stellar potential, however their orbits are perturbed by the secondary SMBH. In a fully self-consistent simulation the orbit of the secondary would evolve due to this exchange of energy with the stars. However, for efficiency and simplicity the secondary SMBH's orbit follows an inspiral dominated by dynamical friction, halting at the stalling radius. Our approximation is checked in the lower panels of figure 4.1 where we plot the change in stellar and binary energies. If the secondary path had been chosen perfectly the two would lie on top of each other.

Specifically the secondary SMBH is, at time $t = 0$, given an eccentricity of 0.1 and an initial

[2]During the review process a further paper was published (Chen et al., 2011), which also considered the SMBH binary evolution and the stellar potential. Their disruption rates are consistent with ours.

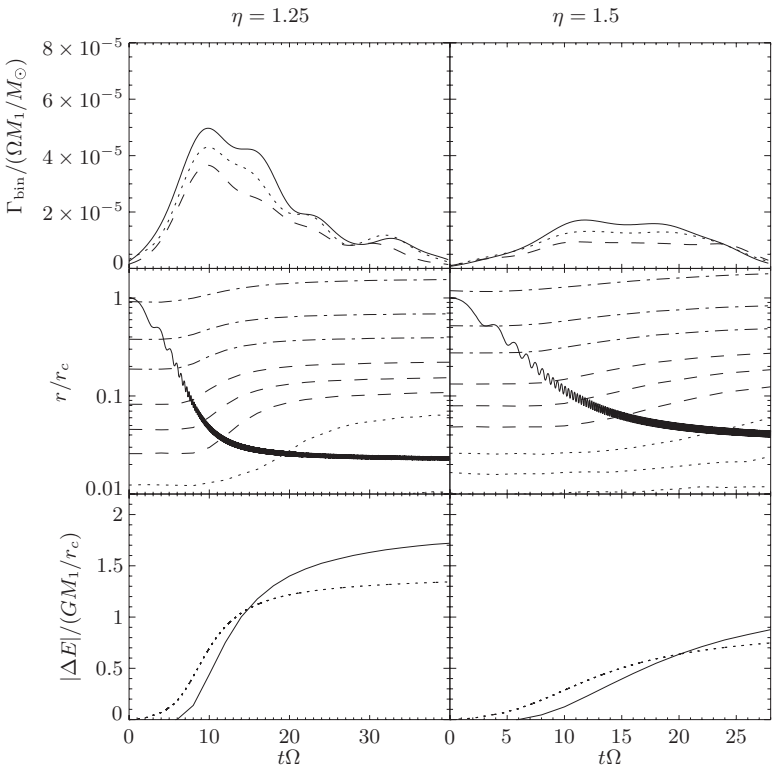

Figure 4.1 Results for mass ratio $q = 0.1$. The left-hand panels show an $\eta = 1.25$, Bahcall-Wolf cusp, the right-hand panels an $\eta = 1.5$ cusp. The upper panels shows TD rate, $\Gamma_{\rm bin}$, for TD to cusp radius ratios $r_t/r_c = (9, 7, 5) \times 10^{-7}$ in solid, dotted and dashed lines, respectively. The distribution of disruption times have been kernel smoothed with a Gaussian of width $\sigma = 2$. The middle panels shows the evolution of the binary separation as a solid line and radii enclosing 0.1, 0.2, 0.4% of the stellar mass in dotted, 1, 2, 4% in dashed and 10, 20, 40% in dash-dot lines. The lower panel shows the evolution of the energy of the binary as the solid line and the stars as the dotted. In a fully self-consistent evolution these would lie on top of each other. The simulations are scaled by $\Omega \equiv (2GM_1/r_c^3)^{1/2}$.

separation equal to the cusp radius, r_c. It is then migrated inwards on a path governed by

$$\frac{d\mathbf{v}}{dt} = -\frac{G\left[M_1(1+q) + M_\star(<r)\right]}{r^3}\mathbf{r} - \frac{\mathbf{v}}{t_{\rm df}} \tag{4.4}$$

where $M_\star(<r)$ is the stellar mass interior to r and

$$t_{\rm df} = \frac{v^3}{4\pi \log\Lambda\, q\, M_1\, \rho(<v)} \tag{4.5}$$

characterizes the dynamical friction (Binney and Tremaine, 2008). Here $\rho(<v)$ is the density of stars at r with velocity less than v. We have used a Coulomb logarithm that begins at $\log\Lambda \approx 4$, but which smoothly decreases to zero at the stalling radius calculated by Sesana et al. (2008). The functional form of the decrease was chosen to approximate the rate of shrinkage caused by the energy exchange with the stars during our simulations.

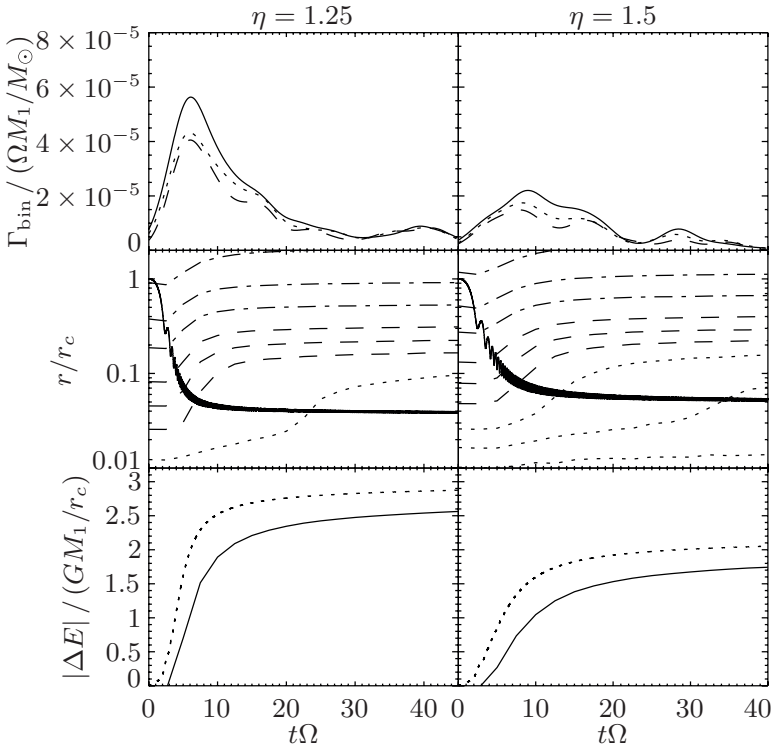

Figure 4.2 Results as described in figure 4.1 for $q = 0.3$.

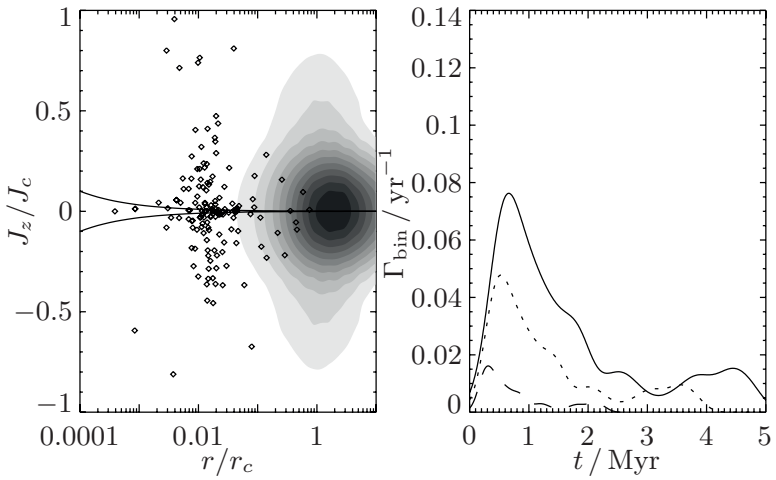

Figure 4.3 Plots of our $\eta = 1.25$, $q = 0.3$ simulation. Left panel shows the stars that are tidally disrupted for $r_t/r_c = 5 \times 10^{-7}$ as a function of their initial radius and z-component of angular momentum normalized to the circular angular momentum at that radius, J_z/J_c. The Kozai wedge is plotted together with the overall stellar density. A large fraction of the disrupted stars lie well outside the Kozai wedge indicating that these are chaotic orbits (cf. Chen et al., 2009). The contours show the initial stellar distribution, each is evenly spaced in density. The right-hand panel shows the rates from the same simulation scaled using the relations in equations (4.6) and (4.7) for $M_1 = 10^8 M_\odot$ in solid, $5 \times 10^7 M_\odot$ in dotted and $10^7 M_\odot$ dashed lines.

To perform our scattering experiments we implemented the adaptive symplectic integrator described in Preto and Tremaine (1999), with a timestep which varies as $\Delta t \sim U^{-1}$ where U is the potential energy. With this choice of timestep the integrator has the desirable property that it reproduces exactly Keplerian orbits independent of step size. Even for our mildly non-Keplerian orbits, this allows Kozai resonances to be correctly reproduced, since the spurious precession frequently found in other algorithms is absent. In addition, this integrator is well suited for this problem since it has been shown to correctly reproduce the highly eccentric orbits required for a star to be tidally disrupted (Peter, 2009).

The results of our scattering experiments and the resultant disruption rates, $\Gamma_{\rm td}$, are shown in figures 4.1 and 4.2 for $q = 0.1$ and $q = 0.3$, respectively. The plots are scaled by $\Omega \equiv (2GM_1/r_c^3)^{1/2}$.

The evolution of the rates can be understood qualitatively. Because we exclude stars initially in the loss cone, the rates are initially low. But, as the secondary inspirals, it enters denser regions and interacts with increasing numbers of stars, with a concomitant increase in the TD rate. The rate increases until the secondary reaches the stalling radius, where it clears a path and the rate begins to decline.

We find that the majority of TDs are due to the type of chaotic orbits described by Chen et al. (2009) as opposed to the Kozai effect discussed by Ivanov et al. (2005). This is demonstrated in the left-hand panel of figure 4.3. The primary reason for this is that apsidal precession in the non-Keplerian potential destroys the secular Kozai effect for the majority of orbits.

Our rates are lower than those discussed by Chen et al. (2009) largely because we have considered less steep cusps. This both reduces the number of stars that can be disrupted as the binary hardens, and increases the orbital timescale at the hardening radius. Both effects reduce the rate of disruptions. In addition we have considered the binary evolution which Chen et al. (2009) did not, although this has a smaller effect

To apply our simulations to physical galaxies, we use the fits from Merritt et al. (2009) to the inner regions of ACS Virgo Cluster galaxies (Côté et al., 2004). For power-law galaxies these give [3]

$$r_c = 22\,(M_1/10^8 M_\odot)^{0.55}\,\mathrm{pc}\,. \tag{4.6}$$

We assume the stars have radius $R_\odot$, thus giving

$$r_t/r_c = 4.9\times 10^{-7}(M_1/10^8 M_\odot)^{0.22}\,. \tag{4.7}$$

With these scalings, our simulations for $\eta = 1.25$ and $q = 0.3$ are shown in figure 4.3.

[3] D. Merritt personal communication. From fitting to figure 12 of Merritt et al. (2009).

4.3 Observable Tidal Disruptions

The absolute magnitude of an individual disruption has considerable modeling uncertainties and is likely to depend on many quantities such as the SMBH mass, the SMBH spin and the geometry of the disruption (Strubbe and Quataert, 2009).

We instead derive a simple empirical estimate of the volume accessible by comparison to Gezari et al. (2008). Two luminous optical events coincident with UV flares were discovered in $\sim 2.9\,\mathrm{deg}^2$. Their spectra and light curves were consistent with TD events, making this their most likely explanation. Their redshifts were $z = 0.33$ and $z = 0.37$, giving extinction corrected (but not K-corrected) absolute g-band magnitudes of -17.7 and -18.9 (Gezari, 2010). Requiring that these two cases be 2 mags brighter than the 25.0 g-band limit of LSST gives maximum redshifts of detection of $z = 0.27$ and $z = 0.43$, respectively. The 2 magnitude buffer better ensures a convincing light curve, which would display the characteristic fast rise and decay of a TD. Based on these numbers we choose $z = 0.35$ as the limit for LSST.

There is also only a small range of SMBH masses which needs to be considered. Because SMBHs of mass greater than $10^8\,M_\odot$ can't tidally disrupt stars (equation 4.1, ignoring SMBH spin), and SMBHs of mass less than $10^7\,M_\odot$ are significantly less luminous, (particularly if super-Eddington outflows are neglected), we restrict our analysis to SMBHs with masses between 10^7–$10^8\,M_\odot$.

4.4 Rates of Single Tidal Disruptions

We now calculate the rate of TDs observable by LSST both for systems with isolated SMBHs and systems with SMBH binaries.

In the case of isolated SMBHs, the rate of TDs observed by LSST will be approximately

$$\mathcal{R}^{(\mathrm{td})}_{\mathrm{single}} = f_{\mathrm{sky}} \int \frac{dN}{dM_{\mathrm{BH}}} V_{\mathrm{c}}(M_{\mathrm{BH}}) \Gamma_{\mathrm{td}}(M_{\mathrm{BH}})\, dM_{\mathrm{BH}} \tag{4.8}$$

where f_{sky} is the fraction of the sky covered by LSST, Γ_{td} is the rate of TDs per galaxy, V_c is the total co-moving volume over which a TD is observable and dN/dM_{BH} is the black hole mass function. We have used the black hole mass function (Aller and Richstone, 2002)

$$\frac{dN}{dM_{\mathrm{BH}}} = c \left(\frac{M_{\mathrm{BH}}}{M^{\star}_{\mathrm{BH}}} \right)^{-\alpha} e^{-M_{\mathrm{BH}}/M^{\star}_{\mathrm{BH}}}, \tag{4.9}$$

with the parameters $c = 3 \times 10^{-11} M_\odot^{-1}\,\mathrm{Mpc}^{-3}$, $M^{\star}_{\mathrm{BH}} = 1.1 \times 10^8 M_\odot$ and $\alpha = 0.95$ (values derived by Aller and Richstone, 2002, scaled to $H_0 = 71\,\mathrm{km\,s^{-1}\,Mpc^{-1}}$). The rate of TDs per galaxy is highly uncertain, and so we parametrize, $\Gamma_{\mathrm{td}} = \gamma \times 10^{-5}\,\mathrm{yr}^{-1}$, scaling to the observationally motivated constant rate per galaxy of (Donley et al., 2002) independent of M_{BH}. We also assume V_{c} is

independent of $M_{\rm BH}$ and is $10.7\,{\rm Gpc}^3$, corresponding to our redshift limit of $z = 0.35$ with the assumption that $H_0 = 71\ {\rm km\,s^{-1}\,Mpc^{-1}}$. Using these approximations and $f_{\rm sky} \approx 0.5$, the rate of TDs detected by LSST in galaxies containing isolated SMBHs is predicted to be

$$\begin{aligned}\mathcal{R}^{\rm (td)}_{\rm single} &\sim \Gamma_{\rm td} V_{\rm c} f_{\rm sky} \int_{10^7 M_\odot}^{10^8 M_\odot} \frac{dN}{dM_{\rm BH}}\, dM_{\rm BH} \\ &= \Gamma_{\rm td} \times 3 \cdot 10^7 \text{ Galaxies} \\ &= 300\gamma \text{ yr}^{-1}\,. \end{aligned} \tag{4.10}$$

Now consider systems hosting binary SMBHs. The rate of disruptions will be

$$\mathcal{R}^{\rm (td)}_{\rm bin} = f_{\rm sky} \int V_{\rm c} \Gamma_{\rm bin}(M_1, q, t) R_{\rm merge}(M_1, q)\, dq\, dM_1\, dt\,, \tag{4.11}$$

where $R_{\rm merge}(M_1, q)\, dq\, dM_1$ is the rate of mergers per unit co-moving volume for binary SMBHs with primary mass between M_1 and $M_1 + dM_1$ and with mass ratio between q and $q + dq$. The quantity $\int \Gamma_{\rm bin}(M_1, q, t)\, dt$ is the total number of TDs in a merger and was linearly interpolated/extrapolated from the simulations in figures 4.1 and 4.2 together with equations (4.6) and (4.7).

Over the narrow range of redshift and primary mass accessible we approximate

$$R_{\rm merge}(M_1, q) = C \frac{dN}{dM_1} F(q)\,, \tag{4.12}$$

where we have assumed the mass ratio distribution of SMBH binaries follows the local galaxy merger mass ratio distribution given by Stewart et al. (2009), $F(q) = q^{-0.25}(1-q)^{1.1}$. The normalization constant $C = 0.03\ {\rm Gyr}^{-1}$ was chosen to reproduce the simulated local merger rate[4] of SMBH binaries, with $10^7 M_\odot < M_1 < 10^8 M_\odot$ and $q > 0.05$, of approximately $9 \times 10^{-5}\,{\rm Mpc}^{-3}\,{\rm Gyr}^{-1}$.

Using these approximations, then, if all galaxies have an $\eta = 1.25$ cusp, we can expect LSST to detect

$$\begin{aligned}\mathcal{R}^{\rm (td)}_{\rm bin} \sim & V_{\rm c} f_{\rm sky} C \\ & \times \int_{10^7 M_\odot}^{10^8 M_\odot} dM_1 \int_{0.05}^{0.5} dq \int dt \frac{dN}{dM_1} F(q) \Gamma_{\rm bin}(M_1, q, t) \\ = & 8 \text{ yr}^{-1}\,, \end{aligned} \tag{4.13}$$

where we have limited the mass ratio to $q < 0.5$, since this is the limit of our simulations.

[4] M. Volonteri personal communication. From data in figure 2 of Volonteri et al. (2009).

Table 4.1 Summary of rates of tidal disruptions for three current and upcoming transient surveys. Symbols and calculation are described in the text. The numbers $N^{(\rm multi)}_{\rm single}$ and $N^{(\rm multi)}_{\rm bin}$ are for an observation time of $t_{\rm obs} = 5\,{\rm yr}$ and scale roughly as $t^2_{\rm obs}$.

Survey	mag limit (g-band)	$z_{\rm lim}$	$f_{\rm sky}$	$\mathcal{R}^{(\rm td)}_{\rm single}/\,{\rm yr}^{-1}$	$\mathcal{R}^{(\rm td)}_{\rm bin}/\,{\rm yr}^{-1}$	$N^{(\rm multi)}_{\rm single}$	$N^{(\rm multi)}_{\rm bin}$
PTF	21.0	0.06	0.2	$0.7\,\gamma$	0.02	$0.9\times10^{-4}\,\gamma^2$	0.008
Pan-STARRS[a]	25.0	0.35	10^{-3}	$0.7\,\gamma$	0.02	$0.8\times10^{-4}\,\gamma^2$	0.007
LSST	25.0	0.35	0.5	$300\,\gamma$	8	$0.03\,\gamma^2$	3

[a]Medium Deep Survey

Note that the number of galaxies in the enhanced state which occurs for

$$t_{\rm enh} \sim 10/\Omega \sim 1.5(M_1/10^8 M_\odot)^{0.33}\,{\rm Myr} \tag{4.14}$$

is

$$\begin{aligned} N_{\rm enh} \sim & V_{\rm c} f_{\rm sky} C \\ & \times \int_{10^7 M_\odot}^{10^8 M_\odot} dM_1 \int_{0.05}^{0.5} dq \left[\frac{dN}{dM_1} F(q) \times 10/\Omega(M_1)\right] \\ = & 400\,. \end{aligned} \tag{4.15}$$

4.5 Rates of Multiple Tidal Disruptions

We now calculate the rate of multiple TDs in systems containing both isolated and binary SMBHs.

In the case of isolated SMBHs, over a period of observing $t_{\rm obs}$ the total number of TDs will follow a Poisson distribution with mean $x \equiv t_{\rm obs}\Gamma_{\rm td}$. The probability of observing multiple TDs from a single galaxy is therefore, $P(x) = 1 - e^{-x} - xe^{-x}$.

Then the expected number of isolated SMBHs exhibiting multiple TDs during $t_{\rm obs}$ is

$$\begin{aligned} N^{(\rm multi)}_{\rm single} &= V_c f_{\rm sky} \int_{10^7 M_\odot}^{10^8 M_\odot} \frac{dN}{dM_{\rm BH}} P(t_{\rm obs}\Gamma_{\rm td})\, dM_{\rm BH} \\ &\sim 0.03\gamma^2\,(t_{\rm obs}/5\,{\rm yr})^2\,, \end{aligned} \tag{4.16}$$

where in the final relation we have expanded in the small parameter $x \equiv t_{\rm obs}\Gamma_{\rm td}$.

Similarly, the expected number of multiple TDs observed from binary SMBHs is

$$N^{(\rm multi)}_{\rm bin} = f_{\rm sky} V_{\rm c} \int P(\Gamma_{\rm bin} t_{\rm obs}) R_{\rm merge}\, dM_1\, dt\, dq\,. \tag{4.17}$$

Using the same approximations used in estimating equation (4.13) we find over an observation time, $t_{\rm obs} = 5\,{\rm yr}$, the expected number of close binary SMBHs exhibiting multiple TDs observable by LSST to be

$$\begin{aligned} N_{\rm bin}^{\rm (multi)} \sim & V_{\rm c} f_{\rm sky} C \int_{10^7 M_\odot}^{10^8 M_\odot} dM_1 \int_{0.05}^{0.5} dq \\ & \times \int dt \frac{dN}{dM_{\rm BH}} F(q) P(\Gamma_{\rm bin}(M_1, q, t) t_{\rm obs}) \\ = & 3\,, \end{aligned} \tag{4.18}$$

where $P(\Gamma_{\rm bin} t_{\rm obs})$ was calculated from our simulations together with equations (4.6) and (4.7).

Towards the upper end of the range 10^7–$10^8 M_\odot$, $\Gamma_{\rm bin} t_{\rm obs} \sim 0.5$ for major mergers. This indicates that the majority of close SMBH binaries with primaries in the upper end of this range could potentially be identified using multiple disruptions. Equation (4.18) broadly scales as $(t_{\rm obs}/5\,{\rm yrs})^2$, but this is only approximate because $x \equiv \Gamma_{\rm bin} t_{\rm obs} \sim 0.5$ for some systems.

4.6 Discussion

We have estimated the enhanced rate of tidal disruptions (TDs) from SMBH binaries, and shown that if a system exhibiting multiple TDs is observed then, in our fiducial model, it is $\sim 100/\gamma^2$ times more likely to be a close SMBH binary than an isolated SMBH system. It has also been shown that the upcoming transient survey LSST is likely to detect several systems with multiple disruptions during a 5 year observation period.

Once a double TD is detected these galaxies would be expected to have a steady TD rate, with further events on a human timescale. In the case that γ is larger, or it varies significantly between galaxies, other signatures will likely identify TDs that occurred in binaries. These include possible spectroscopic signatures, morphology or kinematics indicating a recent major merger, or interruption of the TD flare on a binary orbital timescale (Liu et al., 2009).

An ancillary conclusion is that, in our fiducial model, approximately 3% of all TDs occur in hardening binaries. Therefore, all systems containing a TD are potential binary hosts and should be monitored, either for a second TD or for other evidence of a SMBH binary.

Stone and Loeb (2011) suggested using multiple TDs due to the merged black holes recoil to identify host galaxies of SMBH mergers observed by LISA. Their period of enhancement is short enough to not affect our conclusions. Also since LISA will indicate where on the sky ($\approx 1\,{\rm deg}^2$) the merger takes place, the high rates discussed here do not effect their conclusions.

The TD rates are largely determined by the number of stars in the central regions of the galaxy, which, in turn, depends on the cusp profile and the size of the cusp. In this sense, multiple TDs are

also diagnostic of cusp profiles.

All our numbers scale by the uncertain detection volume, which could be significantly higher than we have conservatively assumed. Recently van Velzen et al. (2011) found two candidate disruptions with absolute g-band magnitudes -20.3 and -18.3. If the event with magnitude -20.3 was representative of the higher black hole mass disruptions where our binary-induced disruptions typically occur, then LSST could detect disruptions of this type to $z \sim 0.7$ increasing our predicted rates by approximately an order of magnitude.

5

The Increased Rate of Tidal Disruptions, Plunges, and EMRIs in Supermassive Black Hole Binaries[1]

Abstract

As discussed in chapter 4 the rate of tidal disruptions from a galactic nucleus would be greatly increased by the presence of close supermassive black hole (SMBH) binary. In this chapter we expand on that work.

The simulations, and their assumptions, are described in greater detail than the cursory description given in chapter 4. Additionally, relativistic corrections have been added which allow the simulation of extreme mass ratio inspirals (EMRIs). These corrections are described, and rates of EMRIs and plunges calculated. We also present an increased variety of simulation runs, primarily to encompass a greater range of SMBH binary mass ratios.

[1] This work in progress is as yet unpublished. A modified version of section 5.4 will be submitted in the coming weeks to MNRAS as part of a paper with authors: Nate Bode and Christopher Wegg in this order. Small sections of this work also appear in the thesis by Bode (2011), these sections are noted in the text.

5.1 Introduction

It is now well established that the majority of galaxies harbor a supermassive ($\gtrsim 10^6\,M_\odot$) black hole (SMBH) in their center (e.g., Ferrarese and Ford, 2005). In our current hierarchical formation scenario of galaxy formation, galaxy mergers are also frequent. Since observed galaxies contain only one SMBH, empirically the merger of galaxies must ultimately result in the merger of their central SMBHs, even if not all of the aspects of this process are understood (e.g., the 'final parsec problem', Milosavljević and Merritt, 2003).

In chapter 4 we showed that during the merger process, when the SMBHs form a close binary, separated by 0.1–1 pc, the rate of tidal disruptions is greatly increased. We also showed that this increased rate may allow close binary SMBHs to be detected via multiple tidal disruptions from a single galaxy.

The increased rate of tidal disruptions is due to the increased frequency of close encounters between stars and the SMBHs. In the case considered in chapter 4 these were main sequence stars encountering a SMBH with mass $\lesssim 10^8\,M_\odot$. In this case a close interaction results in a tidal disruption. However, if the star was a compact object[2], or the SMBH more massive than $10^8\,M_\odot$, a tidal disruption would not result. In this case the most likely outcome is a plunge, whereby the star crosses the event horizon of the SMBH without being torn apart by the tidal forces. Instead the mass of the SMBH is silently increased, without a transient flare. Less frequently the star may be captured in an elliptical orbit by the SMBH, and lose energy via the emission of gravitational radiation. This loss of gravitational radiation decreases the semi-major axis of the orbit, and increases the orbital frequency. Eventually the frequency is increased sufficiently that the emitted gravitational radiation lies in the band of potential low-frequency gravitational wave detection missions, such as the proposed Laser Interferometer Space Antenna (LISA), or its successors. These extreme mass ratio (typically $\gtrsim \frac{10^6 M_\odot}{10 M_\odot} \sim 10^5$) inspirals (EMRIs) are one of the primary sources for these low-frequency gravitational wave detectors. The typical formation scenario of EMRIs are that star-star scattering perturbs the orbit of an already eccentric star so that its periapsis is close to the SMBH. If sufficiently close then the timescale for gravitational wave losses is shorter than the timescale that perturbations due to star-star scattering can significantly change the periapsis. At this point an inspiral becomes likely and the star eventually forms an EMRI (e.g., the review by Amaro-Seoane, 2012).

An initial investigation of the rate of production of EMRIs by binaries was performed by Bode (2011), using extensions of the work in chapter 4. In this chapter we further extend those calculations by calculating a greater range of simulations. In particular we extend the range of SMBH mass ratios beyond the two ($q = 0.1$, $q = 0.3$) performed previously to encompass small mass ratios, and

[2]Throughout we use star to refer to either a compact object (i.e., neutron star, black hole, white dwarf), or conventional star (e.g., main sequence star).

mass ratios larger than one, i.e., we consider the cusp of stars around the secondary SMBH. To elucidate the dynamics, we also perform calculations of the relevant physical processes: The Kozai effect, precession due to General Relativity (GR) and the non-Keplerian stellar potential, and the fluctuations in angular momentum on shorter timescales than the secular Kozai effect. The resultant dynamics caused by the interplay of these processes can be rich and interesting.

This chapter is organized as follows: In section 5.2 we describe the numerical implementation and code in greater detail than the cursory explanation in chapter 4 or Bode (2011). In section 5.3 we show the results of our expanded parameter space, and apply them to EMRIs in section 5.5.1, plunges in section 5.5.2, and tidal disruptions in section 5.5.3. Finally we discuss the caveats and extensions of this work in section 5.6 and conclude in section 5.7.

5.2 Numerical Implementation

5.2.1 Physical Setup

In chapter 1 we discussed the processes that drive the evolution of pairs of SMBH in galactic nuclei, and briefly summarize the situation here. The aim of this work is to consider the cusp around a primary supermassive black hole (SMBH) together with a a second inspiraling SMBH and calculate the number of stars that have close approaches to either SMBH as a result. As described in section 1.4.1, depending on the nature and mass of the star and SMBH, these can result in a tidal disruption, an EMRI, or in the star silently plunging across the event horizon of the SMBH.

The parameter space of interest is not the final stages of merger where gravitational wave losses dominate, nor the widely separated pairs of SMBHs[3] found as AGN pairs. Of greater importance to stellar encounters are parsec-scale separations. The SMBH pairs are brought to these separations by exchanging energy with the neighboring stars, via a combination of dynamical friction (weak scatterings) and ejection (strong scatterings). For each factor of two reduction in the binary SMBH semi-major axis, the secondary SMBH must scatter a mass of stars approximately equal to its own mass. Hence when the stellar mass enclosed by the secondary SMBH is approximately equal to its mass, scatterings become inefficient, and inspiral slows. Under the simplest assumptions of a spherical galaxy, without gas, and a circular SMBH binary, the gravitational radiation timescale at this point is longer than a Hubble time, an issue known as the 'final parsec problem' (Milosavljević and Merritt, 2003).

As the SMBHs approach the stalling radius, the stellar density around the secondary increases and therefore the rate of close interactions resulting in tidal disruptions, EMRIs or plunges also increases, reaching a maximum just before the stalling radius, where the timescale for inspiral

[3]These are referred to a pairs as opposed to a binary since, being typically separated by ~ 1 kpc, the SMBHs are not directly gravitationally bound to each other.

rapidly increases from $O(\mathrm{Myr})$ to $O(\mathrm{Gyr})$ as the stars responsible for energy loss are ejected, and further shrinkage of the orbit becomes dependent on stellar relaxation. Since we are not interested in the slow, relaxation driven phase, we therefore neglect star-star scatterings. For the length of our simulations these are small perturbations compared to those from the secondary SMBH. This has the advantage that each star can be evolved separately making the computational problem embarrassingly parallel.

Both black holes are likely to be surrounded by a cusp of stars. The steepness of this cusp is an unsettled question. The equilibrium, equipartition, solution is of a steep Bahcall and Wolf (1976) cusp, whose stellar central density is $\rho \propto r^{-1.75}$. The best studied SMBH is that at the center of our galaxy surrounding Sgr A*. This cusp shows a profile closer to $\rho \propto r^{-1.5}$, and the timescale for reaching the Bahcall-Wolf cusp is approximately a Hubble time (e.g. Alexander, 2005; Phinney, 1989). It remains possible, however, that the stellar density cusp does have $\rho \propto r^{-1.75}$ since it is the visible stars that are observed, and the equilibrium solution would be mass segregated with the heaviest stars: $\sim 10\,M_\odot$ black holes, distributed as $\rho \propto r^{-1.75}$ in the center (Freitag et al., 2006).

To simulate the cusp of stars around the primary SMBH, and the resultant potential, we use the η-models described in Tremaine et al. (1994). The η-models are equivalent to the models of Dehnen (1993), but also contain a central SMBH. They are a spherical, isotropic, self-consistent, potential-density pair, for stars around an SMBH. The η-models contain a parameter, denoted μ, which represents the ratio between the SMBH mass and the total stellar mass. Throughout we use $\mu = 0.5$, i.e., the stellar mass in the cusp is twice the primary SMBH mass. The stellar density is

$$\rho(r) = \frac{GM_1\eta}{2\pi r_c^3}\frac{1}{(r/r_c)^{3-\eta}(1+r/r_c)^{1+\eta}}\,, \tag{5.1}$$

where M_1 is the mass of the primary SMBH, and r_c is the characteristic scale of the cusp. The stellar mass enclosed is by radius r is

$$M_\star(<r) = 4\pi\int_0^r r^2\rho(r)\,dr = \frac{2M_1 r^\eta}{(r_c+r)^\eta}\,. \tag{5.2}$$

Since the η-models are spherical and isotropic, the distribution function can be calculated using Eddington's formula (Binney and Tremaine, 2008). The process of assigning positions and velocities to stars such that they are drawn from this distribution function is described in appendix 5.A.

The secondary SMBH, of mass $M_2 \equiv qM_1$, inspirals towards the primary SMBH into this cusp. During this period, provided there is a cusp of stars around the primary, then the rate of inspiral is dominated by scattering of these stars (Sesana et al., 2008). In principle the path of the secondary SMBH could be calculated self-consistently, by requiring the total (stellar plus SMBH binary) energy and angular momentum be conserved. However, for computational efficiency, we instead pre-calculate the inspiral path adjusting it so that the instead the total energy is approximately

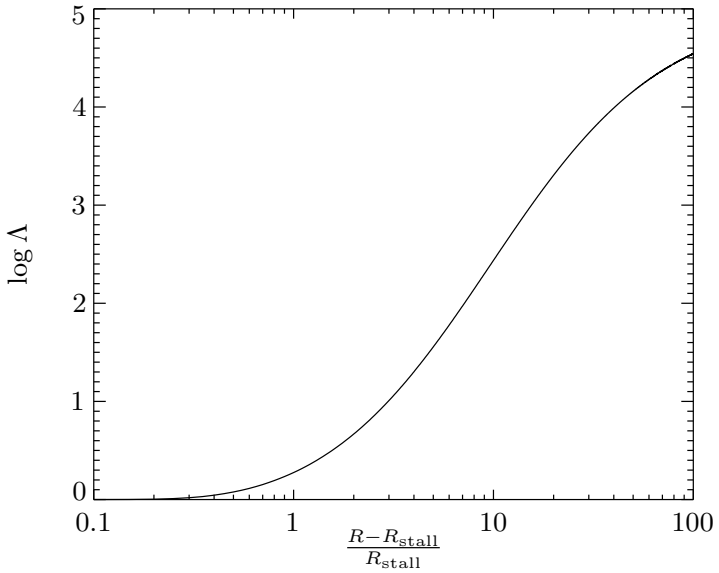

Figure 5.1 Functional form of the Coulomb logarithm, $\log\Lambda$, given in equation (5.5) as a function of the SMBH binary semi-major axis, R, and the stalling radius, $R_{\rm stall}$.

conserved in representative prior simulations. In this manner the computational problem remains embarrassingly parallel.

In particular, the SMBH inspiral path we choose is one governed by dynamical friction:

$$\frac{d\mathbf{v}}{dt} = -\frac{G\left[M_1(1+q) + M_\star(<r)\right]}{r^3}\mathbf{r} - \frac{\mathbf{v}}{t_{\rm df}}\,, \tag{5.3}$$

where

$$t_{\rm df} = \frac{v^3}{4\pi \log\Lambda\, q\, GM_1\, \rho(<v)}\,, \tag{5.4}$$

and $M_\star(<r)$ is the stellar mass interior to r, and $\rho(<v)$ is the stellar density at r with velocity less than v. The functional form of the Coulomb logarithm, $\log\Lambda$, was chosen to begin at $\log\Lambda = 5$, smoothly decreasing to zero at a stalling radii interpolated from those calculated by Sesana et al. (2008). The form was chosen so that the energy was approximately conserved in the lower panel of figures 4.1 and 4.2. Specifically we use

$$\log\Lambda = \frac{5}{10\exp\left[-R_{\rm stall}/(R_{\rm stall}-R)\right] - 9}\,, \tag{5.5}$$

where R is the semi-major axis of the SMBH binary and $R_{\rm stall}$, is the stalling radius. For reference we plot the functional form of the Coulomb logarithm given by equation (5.5) in figure 5.1.

It is important that the pre-calculated SMBH path is consistent with the integrated test particle equations of motion. If an inconsistency is present then a particle orbiting close to the primary

has a different acceleration towards the secondary. This represents an unphysical dipole-like perturbation, which would typically dwarf the smaller physical tidal quadrupole perturbation. An inconsistency of this type would arise if the stellar potential was chosen as the η-model potentials extending to infinity fixed to the primary, while the secondary orbit was calculated using equation (5.3) where only the stellar mass interior to the secondaries orbit appears.

This inconsistency could be resolved by forcing the secondary SMBH to effectively orbit a primary of mass $M_1 + M_{\star,\mathrm{tot}}$ where $M_{\star,\mathrm{tot}} = 2M_1$ is the total stellar mass. However, instead we choose a different approach: The stellar potential is truncated marginally inside the stalling radius. This has the result that the potential and stellar density are no longer self-consistent outside the stalling radius. However, stars outside the stalling radius that closely approach the SMBHs have typically undergone strong chaotic interactions with the binary. Therefore the stellar potential is less important in this region than for stars close to the primary which undergo secular interactions, for which having the correct potential, and therefore precession rate is important.

For reference therefore the potential used is

$$V(\mathbf{r}) = -\int_r^\infty \frac{M_\star(r)}{r^2}\,dr = \begin{cases} \frac{M_t}{r_t} + \frac{M_1}{2r_c(\eta-1)}\left[\left(\frac{r_t}{r_c+r_t}\right)^{\eta-1} - \left(\frac{r}{r_c+r}\right)^{\eta-1}\right] & \text{if } r < r_t \text{ and } \eta \neq 1 \\ \frac{M_t}{r_t} + \frac{M_1}{2r_c}\ln\left(\frac{1/r_c+1/r}{1/r_c+1/r_t}\right) & \text{if } r < r_t \text{ and } \eta = 1 \\ \frac{M_t}{r} & \text{if } r \geq r_t\,, \end{cases} \tag{5.6}$$

where M_t is the stellar mass inside the truncation radius, i.e., $M_t \equiv M_\star(r_t)$.

5.2.2 Symplectic Integrator Implementation

We require an integrator that is stable and accurate enough to produce interesting secular effects, such as the Lidov-Kozai effect. These effects of interest can occur on timescales much longer than the stellar orbital period. Naive integration schemes we tried, such as Runge-Kutta, were not sufficient. Instead, the integration scheme used is that described in Preto and Tremaine (1999). It is a symplectic integrator with an adaptive time step. The key features for the purposes of this work are that, with an appropriate choice of step size, the trajectories of orbits in Keplerian potentials are reproduced *exactly*, and that the time step can be adjusted to resolve periapsis for the highly eccentric orbits of interest, while remaining efficient elsewhere.

In this section, we outline our implementation of the symplectic integrator of Preto and Tremaine (1999) in the context of test particle integrations in the field of a supermassive black hole binary (SMBHB) plus the (truncated) stellar potential given of equation (5.6). We describe the integrator in our code units wherein $G = r_c = 1$, and the primary SMBH mass, $M_1 = \mu = 0.5$.

The Hamiltonian, H, is

$$H = T(\mathbf{v}) + U(\mathbf{r}, t) \tag{5.7}$$

where the kinetic energy, $T = \frac{1}{2}\mathbf{v}^2$, and U is the potential energy. In barycentric coordinates [4]

$$U(\mathbf{r}, t) = -\frac{\mu}{|\mathbf{r} - \mathbf{r}_1|} - \frac{q\mu}{|\mathbf{r} - \mathbf{r}_2|} - V(|\mathbf{r} - \mathbf{r}_1|)\,, \tag{5.8}$$

while in primary-centered coordinates (denoted with primes)

$$U(\mathbf{r}, t) = -\frac{\mu}{r'} - \frac{q\mu}{|\mathbf{r}' - \mathbf{r}_2'|} + \frac{q\mu \mathbf{r}'.\mathbf{r}_2'}{r_2^3} - V(r')\,, \tag{5.9}$$

where $\mathbf{r}_1 = \mathbf{r}_1(t)$ ($\mathbf{r}_2 = \mathbf{r}_2(t)$) is the position of the primary (secondary) at time t, $\mu(q\mu)$ is the masses of the primary (secondary). The third term in equation 5.9 is the indirect term which arises in the non-inertial primary centered frame as opposed to the center of mass frame. V is the stellar potential given in equation (5.6). Both primary centered and barycentric equations are implemented in the code. However, we use the barycentric frame throughout this work. Far from the primary the indirect term (i.e., center of mass motion) dominates, and in this region it is required to use the barycentric frame to avoid the barycentric motion dominating. While using primary centered frame close to the primary would be preferable, however switches between frames are non-symplectic, and thus we remain in the barycentric frame throughout.

Symplectic integrators typically require a fixed step size to preserve their symplectic properties. For the highly eccentric orbits considered in this work, this presents serious issues: To resolve periapsis a short time step is required making the points away from periapsis highly inefficient. The solution to this problem by Preto and Tremaine (1999) is to extend phase space through the introduction of a fictitious time variable τ defined through

$$dt \equiv g(\mathbf{q}, t) d\tau\,. \tag{5.10}$$

and then promoting t, and its conjugate variable, $p_0 = -H$, to be members of phase space. With a suitable g, fixed symplectic steps in τ, will resolve periapsis, while taking larger steps in t, and remaining computationally efficient elsewhere.

5.2.3 Equations of Motion

The easiest suitable choice of g is a function of the potential energy $g = g(U)$. Choosing this to be a power law:

$$g(U) = \epsilon U^{-\gamma}\,, \tag{5.11}$$

[4] Note that in the majority of simulations we modify the potential from $\propto 1/r$, as given in equations 5.8 and 5.9, to incorporate precession, for the reasons described in section 5.2.6. This is discussed in detail in chapter 6.

then the new Hamiltonian is (c.f. equation 35 of Preto and Tremaine, 1999):

$$\Gamma = \frac{\epsilon}{1-\gamma}\left([T_e(\mathbf{v},p_0)]^{1-\gamma} - [-U(\mathbf{r},t)]^{1-\gamma}\right), \qquad \gamma \neq 1, \tag{5.12}$$
$$= \epsilon\left(\log[T_e(\mathbf{v},p_0)] - \log[-U(\mathbf{r},t)]\right), \qquad \gamma = 1,$$

where $T_e(\mathbf{v},p_0) = v^2/2 + p_0$.

The equations of motion are:

$$\frac{d\mathbf{r}}{d\tau} = \frac{\epsilon\mathbf{v}}{(v^2/2+p_0)^\gamma}, \tag{5.13}$$
$$\frac{dt}{d\tau} = \frac{\epsilon}{(v^2/2+p_0)^\gamma}, \tag{5.14}$$
$$\frac{d\mathbf{v}}{d\tau} = -\frac{\epsilon}{U(\mathbf{r},t)^\gamma}\nabla U, \tag{5.15}$$
$$\frac{dp_0}{d\tau} = -\frac{\epsilon}{U(\mathbf{r},t)^\gamma}\frac{\partial U}{\partial t}, \tag{5.16}$$

where in barycentric coordinates,

$$\nabla U(\mathbf{r},t) = -\mathbf{F} = \left[\mu + \frac{r^\eta}{(1+r)^\eta}\right]\frac{\mathbf{r}-\mathbf{r}_1}{|\mathbf{r}-\mathbf{r}_1|^3} + q\mu\frac{\mathbf{r}-\mathbf{r}_2}{|\mathbf{r}-\mathbf{r}_2|^3} \tag{5.17}$$
$$\frac{\partial U(\mathbf{r},t)}{\partial t} = \left[\mu + \frac{r^\eta}{(1+r)^\eta}\right]\frac{\mathbf{v}_1.(\mathbf{r}-\mathbf{r}_1)}{|\mathbf{r}-\mathbf{r}_1|^3} + q\mu\frac{\mathbf{v}_2.(\mathbf{r}-\mathbf{r}_2)}{|\mathbf{r}-\mathbf{r}_2|^3} \tag{5.18}$$

and in primary centered coordinates

$$\nabla U(\mathbf{r},t) = -\mathbf{F} = \left[\mu + \frac{r^\eta}{(1+r)^\eta}\right]\frac{\mathbf{r}}{r^3} + q\mu\left[\frac{(\mathbf{r}-\mathbf{r}_2)}{|\mathbf{r}-\mathbf{r}_2|^3} + \frac{\mathbf{r}_2}{r_2^3}\right], \tag{5.19}$$
$$\frac{\partial U(\mathbf{r},t)}{\partial t} = q\mu\left[-\frac{(\mathbf{r}-\mathbf{r}_2).\mathbf{v}_2}{|\mathbf{r}-\mathbf{r}_2|^3} + \frac{\mathbf{r}.\mathbf{v}_2}{r_2^3} - 3\frac{\mathbf{r}.\mathbf{r}_2}{r_2^4}\frac{\partial r_2}{\partial t}\right]. \tag{5.20}$$

We choose to use $\gamma = 1$ for reasons motivated in section 5.2.4. The second-order drift-kick-drift leapfrog scheme for a constant step size of $\Delta\tau = 1$ in this case are (c.f. equation 37 of Preto and

Tremaine 1999, 3.21–3.26 of Peter 2008, or 14–19 of Peter 2009):

$$\mathbf{r}_{i+1/2} = \mathbf{r}_i + \frac{\epsilon \mathbf{v}_i}{v_i^2 + 2p_{0,i}} \tag{5.21}$$

$$t_{i+1/2} = t_i + \frac{\epsilon}{v_i^2 + 2p_{0,i}} \tag{5.22}$$

$$\mathbf{v}_{i+1} = \mathbf{v}_i + \frac{\epsilon}{U(\mathbf{r}_{i+1/2}, t_{i+1/2})} \nabla U(\mathbf{r}_{i+1/2}, t_{i+1/2}) \tag{5.23}$$

$$p_{0,i+1} = p_{0,i} + \frac{\epsilon}{U(\mathbf{r}_{1/2}, t_{1/2})} \frac{\partial U(\mathbf{r}_{i+1/2}, t_{i+1/2})}{\partial t} \tag{5.24}$$

$$\mathbf{r}_{i+1} = \mathbf{r}_{i+1/2} + \frac{\epsilon \mathbf{v}_{i+1}}{v_{i+1}^2 + 2p_{0,i+1}} \tag{5.25}$$

$$t_{i+1} = t_{i+1/2} + \frac{\epsilon}{v_{i+1}^2 + 2p_{0,i+1}} \tag{5.26}$$

which for faster computation can be written explicitly as a leapfrog scheme:

$$\mathbf{r}_{i+1/2} = \mathbf{r}_{i-1/2} + \frac{\epsilon \mathbf{v}_i}{v_i^2/2 + p_{0,i}} \tag{5.27}$$

$$t_{i+1/2} = t_{i-1/2} + \frac{\epsilon}{v_i^2/2 + p_{0,i}} \tag{5.28}$$

$$\mathbf{v}_{i+1} = \mathbf{v}_i + \frac{\epsilon}{U(\mathbf{r}_{i+1/2}, t_{i+1/2})} \nabla U(\mathbf{r}_{i+1/2}, t_{i+1/2}) \tag{5.29}$$

$$p_{0,i+1} = p_{0,i} + \frac{\epsilon}{U(\mathbf{r}_{1/2}, t_{1/2})} \frac{\partial U(\mathbf{r}_{i+1/2}, t_{i+1/2})}{\partial t} \tag{5.30}$$

5.2.4 Step Size

Preto and Tremaine (1999) show that for a Keplerian potential, $U = \mu/r$, then using $g = \mu/r$ for the step size, reproduces Keplerian orbits exactly, with only a phase error whose size is $O(N^{-2})$, where N is the number of steps per orbit. Close to either the primary or secondary our potential approaches Keplerian and this motivates the choice $\gamma = 1$, since the phase error is less important for our purposes.

Preto and Tremaine (1999) also show that the change in eccentric anomaly, Δu, per step, for $\gamma = 1$ in a Keplerian potential, is given by

$$\epsilon = 2\mu \frac{1 - \cos \Delta u}{na \sin \Delta u} \tag{5.31}$$

where $n = (\mu/a^3)^{1/2}$ and a is the semi-major axis. When many steps are taken per orbit Δu is small and this becomes

$$\epsilon \sim \mu \frac{\Delta u}{na} \,. \tag{5.32}$$

Since the number of steps per orbit is $N = 2\pi/\Delta u$ then

$$\epsilon = \frac{2\pi\mu}{Nna} = \frac{2\pi\mu}{N(\mu/a)^{1/2}} \,. \tag{5.33}$$

This motivates our choice of initial step size:

$$\epsilon = \frac{2\pi\mu}{N(2p_{0,0})^{1/2}} \,, \tag{5.34}$$

where $p_{0,0} \equiv p_0(t = 0)$. This will overestimate the points required close to the secondary whose mass is only $q\mu$, and will underestimate the number of points by μ far from the primary where the stellar potential is significant. We use equation (5.34) with a fiducial $N = 20000$ to estimate our initial step size.

While equation (5.34) is an appropriate initial choice for the step size, ϵ, orbits can undergo significant changes in their orbital timescale over their evolution, particularly the chaotic orbits in the 'outer problem' discussed by Chen et al. (2009). Our approach is to monitor whether the current choice of ϵ is appropriate by checking $\Delta r/r$ at each step for, both the primary and secondary. If this is larger than 1% then the entire integration is restarted with ϵ reduced by a factor of 4. Additionally, due to the finite lifespan of the authors, we limit the total number of steps taken to 2×10^{10}. These stars lie at smaller semi-major axis than those of interest, and are marked as crosses in figure 5.14.

5.2.5 General Relativistic Corrections

In addition to the Newtonian simulations described above, and performed in chapter 4 we have also incorporated general relativistic corrections. These have the additional advantage that they allow us to simulate the production of EMRIs in SMBH binaries.

While the ideal simulation method would be to integrate the Teukolsky equation, this is numerically challenging, and computationally intensive. Instead our approach was to integrate using the symplectic method described above, with general relativistic effects taken into account approximately. We ignore possible spins of the SMBHs. The two effects to be taken into account are precession of perihelia, and gravitational radiation. In this case, in the absence of perturbations due to the second SMBH, the the orbital plane remains constant. This provides two constants of motion (in the Keplerian limit the longitude of the ascending node, Ω, and the inclination , i), the gravitational radiation provides changes to two others (energy, E, and angular momentum, L), while the precession changes the argument of periapsis (ω). We do not consider relativistic corrections to the time of periapsis in this work, concentrating instead on the trajectories of the particles.

Note that recently (Naoz et al., 2012) studied the secular evolution of hierarchical triples in the secular limit to first post-Newtonian order (1PN). They reproduce the Lidov-Kozai effect (section

5.4.1, Lidov 1961, English translation Lidov 1962, Kozai 1962) but with additional terms in the Hamiltonian at 1PN. Our simulations are direct integrations, but should produce similar results, provided that higher order PN-terms, as included in our gravitational wave radiation and pseudo-Newtonian potential, do not significantly effect the orbit. We do not however include relativistic precession of the outer binary (which is included by Naoz et al. 2012), since it is negligible compared to precession in the stellar potential in our case. Similarly, the 1PN interaction term considered by Naoz et al. (2012) is also negligible, over the length of our simulations, because our outer SMBH binary orbit has low eccentricity as it stalls ($e \lesssim 0.05$).

5.2.6 General Relativistic Precession

Relativistic precession was taken into account by the use of a pseudo-Newtonian potential. Pseudo-Newtonian potentials are potentials in Newtonian physics which do not solve Poisson's equation (i.e., $\nabla^2 U \neq 4\pi\rho$). Instead they are chosen to better approximate some physical aspect of the of the problem at hand. In this case we choose the potential so that the precession of orbits perihelia matches the general relativistic precession for the nearly parabolic orbits that are typical in this work (stars of interest have typical eccentricities of $\gtrsim 10^{-5}$). The choice of potential is discussed in detail in chapter 6, and potential B from that chapter is used here. Potential C more accurately reproduces the precession for orbits close to the marginally bound orbit at specific angular momentum $L = 4\,GM/c$. However for those low angular momenta the neglected spin is likely to be important since there is evidence that at least some SMBHs have high spin (Brenneman and Reynolds, 2006). Therefore the accuracy is unwarranted, even for the marginal additional computational complexity. For reference this potential is

$$U(r) = -\frac{GM_1}{r_1}\left(\frac{1}{1-5r_{g1}/3r_1} + \frac{4r_{g1}}{3r_1}\right) - \frac{GM_2}{r_2}\left(\frac{1}{1-5r_{g2}/3r_2} + \frac{4r_{g2}}{3r_2}\right) \tag{5.35}$$

where $r_{gi} = GM_i/c^2$ and r_i is the distance to the i-th hole. In figure 5.2 we show the precession of an orbit produced by this potential and show that it matches the GR precession. In figure 5.3 we show a 'whirling' orbit with angular momentum just above the separatrix angular momentum, $L = 4GM/c$.

5.2.7 Gravitational Radiation [5]

When an object passes close to either hole, higher-order post-Newtonian effects become important. When the test particle passes within $100\,GM/c^2$ of each hole, we calculate an approximate change in specific energy and angular momentum, ΔE and ΔL.

[5] The text and equations from equation (5.36) to equation (5.39), as well as figure 5.4, also appear in the thesis by Bode (2011).

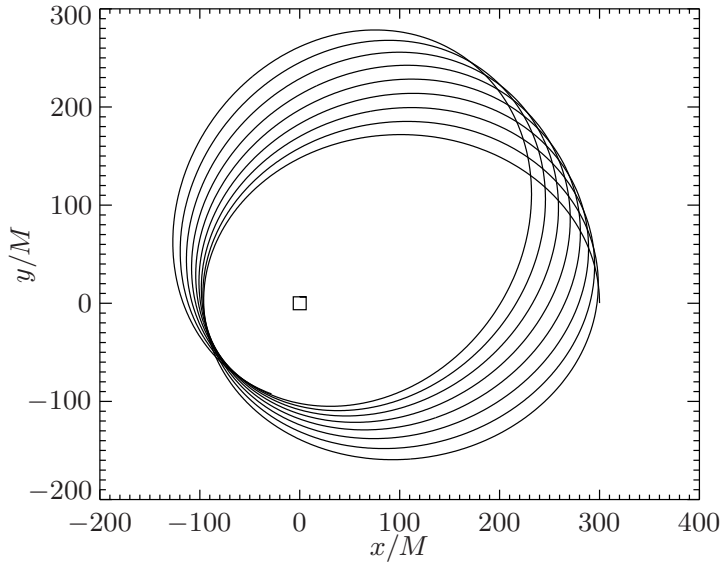

(a) Precession of an orbit in the pseudo-potential of equation (5.35) using the symplectic integrator described in section 5.2. The orbit is in the x-y plane, and the black hole is placed at $x = y = 0$. In this figure $G = c = 1$, however in the text we have retained these factors for clarity.

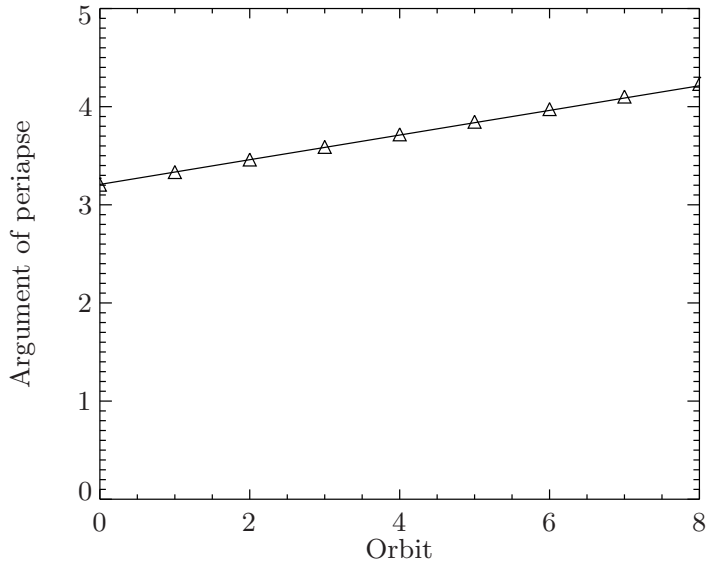

(b) Comparison of the argument of periapsis of figure 5.2(b) as triangles, with the far-field GR expression where the change in periapsis per orbit of $\Delta\phi = \frac{6\pi GM}{c^2 a(1-e^2)}$ (provided the periapsis is in the far-field, i.e., $\gg GM/c^2$) as the solid line.

Figure 5.2 Demonstration of an orbit precessing in the pseudo-Newtonian potential in equation (5.35) using the symplectic integrator described in section 5.2. The orbit has periapsis of $100\,GM/c^2$ and apoapsis $300\,GM/c^2$.

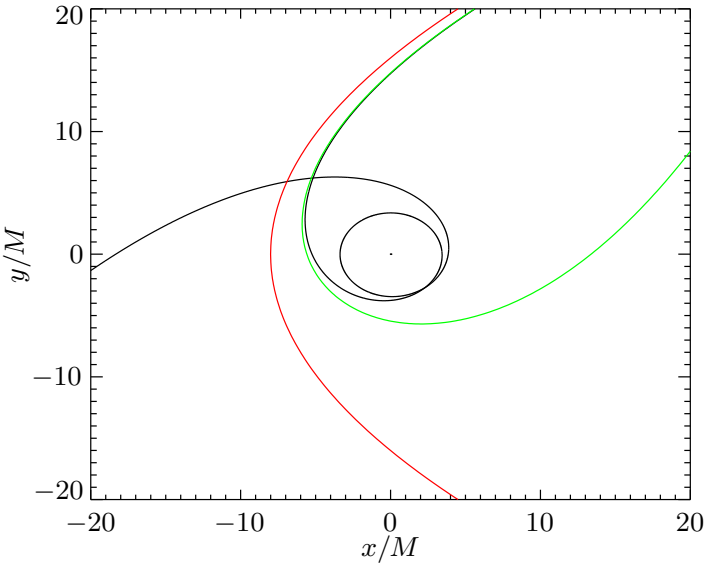

Figure 5.3 Demonstration of whirling orbit in the pseudo-Newtonian potential in equation (5.35) as the black line. The red line is the Newtonian GM/r potential. The green line is potential A from chapter 6 which matches the relativistic far-field precession, but does not diverge as $L \to 4\,Gm/c$. The particle has an angular momentum $L = 4.0001\,GM/c$.

We then subtract this energy and angular momentum loss at the step closest to periapsis. Since the changes typically occur slowly compared to the orbital timescale, the results are insensitive to point in the time at which the adjustment is made. However making the adjustment at the time step closest to periapsis is the best approximation, since close to periapsis is where the majority of the gravitational radiation losses occur.

Therefore, at the time step closest to periapsis we give the star a new velocity, $\vec{v'}$, calculated using the new specific energy, $E' = E + \Delta E$, and angular momentum, $L' = L + \Delta L$, where ΔE and ΔL are the change in specific energy and angular momentum calculated using methods A, B, C or D. Since the position is unchanged the potential energy is unchanged and therefore

$$v'^2 = v^2 + 2\Delta E\,. \tag{5.36}$$

The orbital plane is invariant for orbits around a Schwarzschild hole and therefore

$$\vec{L'} = \frac{L + \Delta L}{L}\vec{L} = \vec{r} \times \vec{v'}\,. \tag{5.37}$$

Taking the dot product of this with itself yields

$$\vec{r} \cdot \vec{v'} = \sqrt{L'^2 - r^2 v'^2} \tag{5.38}$$

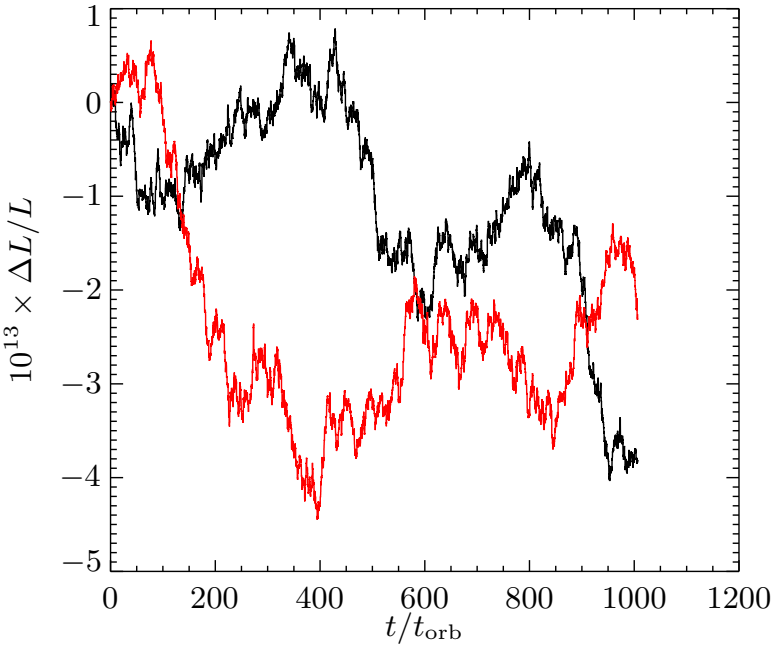

Figure 5.4 Plot showing the errors in conservation of reduced angular momentum, L over many orbital periods ($t_{\rm orb}$), of a high eccentricity ($e = 1 - 10^{-5}$) test particle. The red is without the procedure for calculating the change in $\vec{v}$ at periapsis, the black uses equation (5.39) but with $\Delta L = 0$. The secondary has zero mass. The errors are still at the level $\Delta h/h \sim 10^{-12}$.

where we take positive branch of $\vec{r}.\vec{v'}$ since this corresponds to the outgoing, post-periapsis solution. The cross-product $\vec{r} \times \vec{L'}$ yields

$$\vec{v'} = \frac{1}{r^2}\left[(\vec{r}\cdot\vec{v'})\vec{r} - \vec{r}\times\vec{L'}\right]. \tag{5.39}$$

Equation (5.39) together with (5.36), (5.37) and (5.38) are used to calculate the new velocity $\vec{v'}$ following a periapsis passage.

In figure 5.4 we show the numerical accuracy of this procedure by considering whether L remains constant over many orbits. The errors remain small over many orbital timescales.

We implemented four methods of calculating the gravitational wave loss, i.e., the change in specific energy and angular momentum, ΔE and ΔL, to be inserted to equations 5.36 and 5.37. As described below we adopted the fourth, the more accurate method D, as the method for the majority of simulations, varying it only to see the effect of the less accurate methods A, B, and C.

A) The approximation that the conic section of the orbit is unchanged and the losses on this path calculated using the quadrupole approximation (i.e., Peters and Mathews, 1963). The loss in specific energy E, and specific angular momentum $L = |\vec{L}| = |\vec{r}\times\vec{v}|$ over a conic section in the

quadrupole approximation is (Peters, 1964; Peters and Mathews, 1963):

$$\Delta E = -\frac{8\pi\sqrt{2}}{5}\frac{GM\epsilon}{p}\left(\frac{r_s}{p}\right)^{5/2}\left(1+\frac{73}{24}e^2+\frac{37}{96}e^4\right), \tag{5.40}$$

$$\Delta L = -\frac{16\pi}{5}\frac{GM\epsilon}{c}\left(\frac{r_s}{p}\right)^{2}\left(1+\frac{7}{8}e^2\right), \tag{5.41}$$

where $\epsilon = m_\star/m_1$ is the mass ratio between the test particle and the black hole, p is the semi-latus rectum given by

$$p = \frac{L^2}{GM}, \tag{5.42}$$

and e is the eccentricity given by

$$e = \sqrt{1-\frac{2p_0L^2}{G^2M^2}}. \tag{5.43}$$

For hyperbolic orbits there are corrections to equations (5.41) and (5.40) (these corrections are analogous to the errata Gair et al., 2006a). These corrections were calculated, but are not implemented in the code since they were found to be negligible for the orbits considered here. The majority of the loss occurs close to the hole and since the eccentricities are large this is a small correction. This is because the difference between hyperbolic, parabolic and eccentric close to periapsis of an $e \approx 1$ orbit is small.

B) The approximation that the orbit is a conic section close to the black hole, but where approximate orbital elements are calculated from the geodesic equation. This is Peters and Mathews (1963) with geodesic parameters in the vernacular of Gair et al. (2005). In particular we use equations (5.40) and (5.41) but replace equations (5.42) and (5.43) with equation (19) of Gair et al. (2005).

C) That the orbit follows the geodesic equation and the gravitational wave loss is calculated from the quadrupolar approximation. This is the semi-relativistic approximation of Gair et al. (2005). Equations (5.40) and (5.41) are replaced with equations (33) and (34) of Gair et al. (2005). For numerical speed the fitting functions were implemented.

D) The that the orbit is parabolic and the loss is calculated by fitting functions to integrations of the Teukolsky equation provided by Gair et al. (2006b). Equations (5.40) and (5.41) are replaced with with equations (13) and (15) of Gair et al. (2006b)

Either method A, or direct integration of the order 2.5 post-Newtonian approximation (2.5PN) are the most common approaches (e.g., Merritt et al., 2011a). However method D is the most accurate for the simulations considered here since the orbits are nearly parabolic. In addition methods D and C capture the divergent behavior as orbits approach the separatrix ($L \to 4GM/c^2$ for parabolic orbits). This behavior is analogous to the 'whirling' part of zoom-whirl orbits (e.g., Healy et al.,

2009; Pretorius and Khurana, 2007), and cannot be accurately simulated using PN expansions. Our simulations are unique in simulations of galactic dynamics in capturing this whirling behavior, using a combination of our pseudo-Newtonian potential, and gravitational radiation loss calculation.

We use D in this work as our fiducial method of calculating the gravitational radiation loss. A demonstration of the different timescales for EMRI formation for one particular star is shown in figure 5.5. The methods of gravitational wave loss are also compared in simulations S13–16, the results of which are given in table 5.2. As expected we find that D, which typically has the shortest EMRI timescale, produces the largest number of EMRIs, while A, which has the longest EMRI timescale, produces the least.

5.2.8 Implementation of Plunges, EMRIs and Tidal Disruptions

At each $< 100\,GM/c^2$ periapsis passage we also check for plunges directly into the black hole. The marginally bound orbit is the appropriate limit since the particles lie on highly eccentric orbits. This has a reduced angular momentum around a Schwarzschild black hole of $h = 4GM/c$. On periapsis passages if $h \leq 4\,GM/c$ a direct plunge is assumed to result and the integration is halted.

At each $< 100GM/c^2$ periapsis passage we additionally check whether the particles has entered the LISA frequency band, becoming an EMRI. We do this by checking if the semi-major axis is small enough that the test particles orbital period is below 10^4 s, i.e., for an EMRI produced by hole i:

$$p_0 \geq \frac{GM}{2a} = \frac{1}{2}\left(\frac{2\pi GM_i}{10^4\text{ s}}\right)^{2/3} \tag{5.44}$$

A demonstration of this is shown in figure 5.5.

We also keep track of the closest periapsis passage, and the time at which it occurred, as this allows the simulations to be applied to tidal disruptions. Given the adopted stellar mass and radius, the tidal disruption radius is calculated. For each star in the simulation we check if it crossed the tidal disruption radius during the simulation, and if it did, the time at which this occurred is calculated and recorded. This process is efficiently carried out following the simulation, using the recorded times and periapsis distances of close passages.

5.2.9 Code Tests and Checks

In this section we describe two of the tests performed to check that the code was reliable and accurate.

Stars picked from the η-model were evolved forwards in time with a negligible mass secondary in the full, non-truncated stellar potential. Since the η-model should be dynamically stable and not evolve with time under these conditions, this test checks both that the integration is correct and

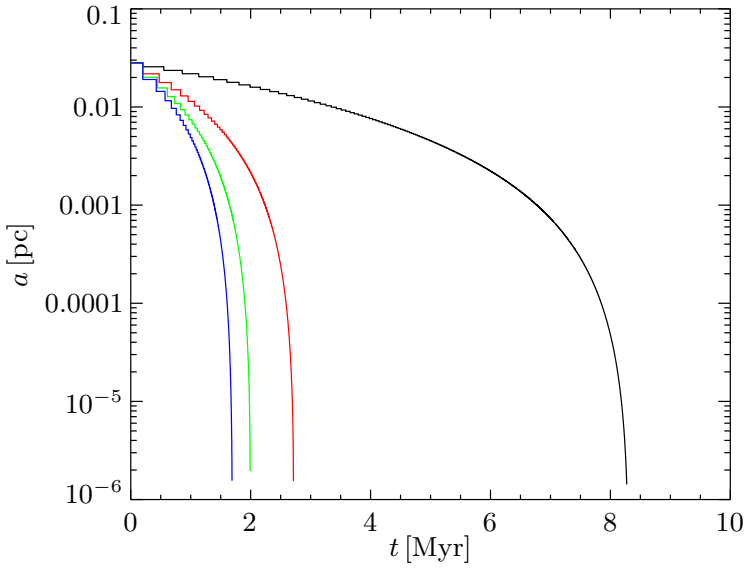

Figure 5.5 Demonstration of the four gravitational radiation approximations implemented for one star which becomes an EMRI. The SMBH has mass $10^6\,M_\odot$ and the star $10\,M_\odot$. The integration is terminated, and the star flagged as an EMRI, as it enters the LISA band. Method A is the black line, method B is red, method C is green, and method D blue. The initial angular momentum of the star is $L = 4.9\,GM/c$.

that the initial conditions of the stars are correctly being chosen from the η-model. One such test, showing that the stellar density is statistically constant, is shown in figure 5.6.

To check that we are accurately able to reproduce the Kozai effect and high eccentricities figure 1 from Ivanov et al. (2005) was reproduced. We compared the result of directly integrating a star with the result of integrating the secular Kozai equations. The result of this test is shown in figure 5.7. The oscillations seen in our simulations occur on the timescale of the binary SMBH orbit. They are real and are discussed in section 5.4.4.

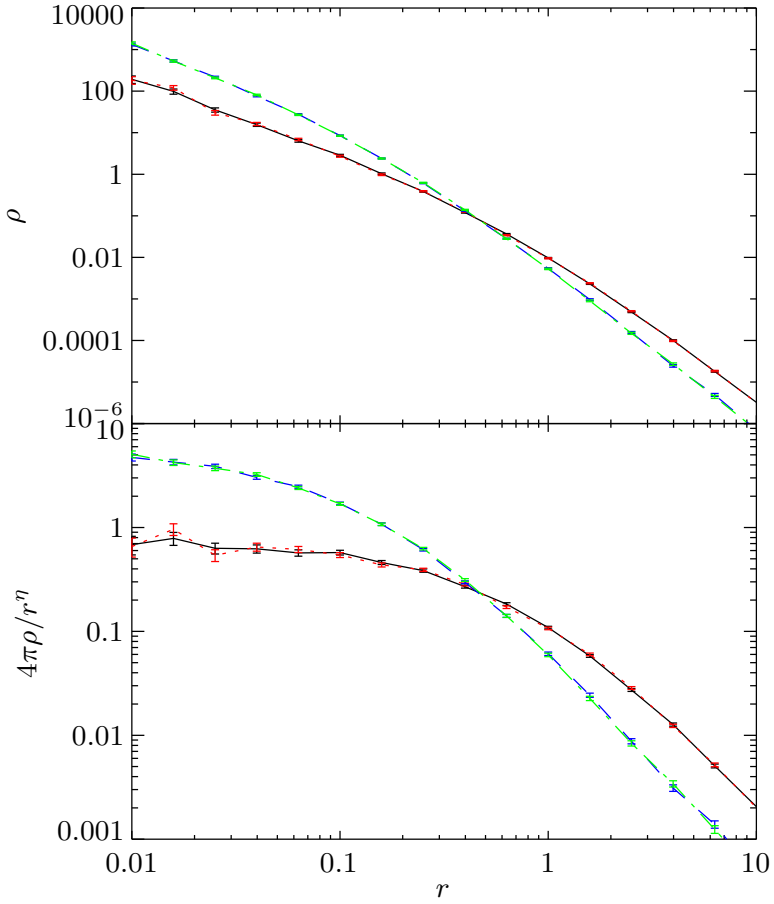

Figure 5.6 Demonstration that the stellar density for stars picked from η-model cusp is statistically constant when there is no secondary SMBH. Test shown is for 10,000 stars in an $\eta = 1.25$ cusp. The initial distribution is shown as the solid black line, the distribution after 5 dynamical times is shown as the red dotted line. Also shown is a cusp that has been rescaled to $r_c = 0.2$ initially (blue dashed line) and after 5 dynamical times (green dash-dot line). Typically we use code units where $r_c = 1$, however cusps with $r_c \neq 1$ are used for the simulations of $q > 1$. The error bars are the shot noise as a result of the number of stars in each radial bin.

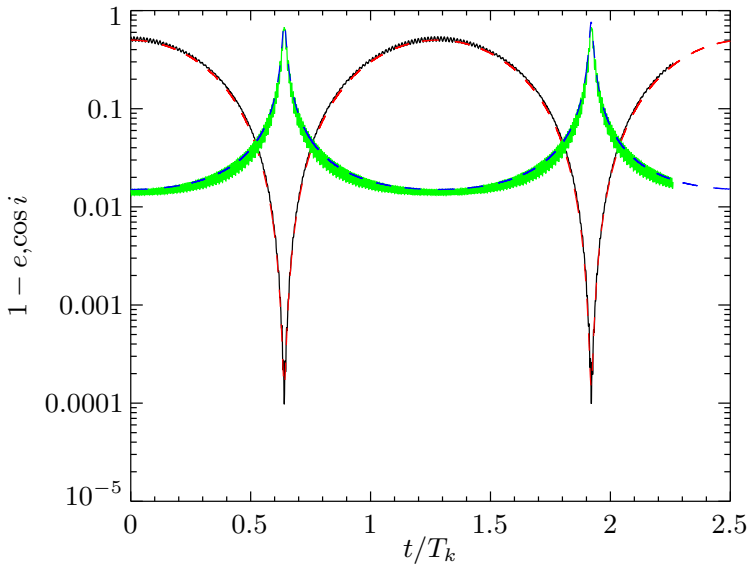

Figure 5.7 Demonstration that the code reproduces Kozai oscillations correctly. In the solid black and green lines we plot the eccentricity and $\cos i$ of a star integrated using our code. In the dashed red and blue lines we plot the eccentricity and $\cos i$ of integrations of the secular Kozai equations (e.g., Bode, 2011; Ivanov et al., 2005) for the same initial conditions. The SMBH mass ratio was $q = 0.1$ and had a circular orbit. The semi-major axis ratio between star and SMBH binary was 0.1. The initial conditions we chosen so as to reproduce figure 1 from Ivanov et al. (2005). The oscillations seen in our simulations occur on the timescale of the binary SMBH orbit. They not numerical artifacts and are discussed in section 5.4.4.

5.3 Simulations

For this work we have performed a wider range of simulations than either in chapter 4 or Bode (2011). They are summarized in table 5.1. For simulations with the same mass ratio, but different $M_\star$ or GW loss method, it was not necessary to repeat the integration of all stars. These parameters are only utilized when gravitational radiation losses are taken into account and therefore can be neglected for stars that never pass within $100GM/c^2$ of either hole. Therefore stars that pass within $100\,GM/c^2$ of either SMBH are noted, and only these stars are reintegrated.

Since each star is integrated independently the problem is embarrassingly parallel. The code was therefore written to utilize MPI, with one master node communicating the stars to be integrated to each worker node as they become available. The simulations were performed on the Northwestern Fugu cluster[6]. Each full 10^6 particle simulation typically requires 10 hours when distributed across ~ 150 cores.

Table 5.1 Summary of simulations performed.

Id[a]	q[b]	η[c]	$M_1/M_\odot$	$M_\star/M_\odot$[d]	r_c/ pc[e]	GW Loss Method	N[f]
S1[g]	0.3	1.25	10^6	10	1.7	D	10^6
S2	0.3	1.25	10^6	1	1.7	D	10^6
S3	0.1	1.25	10^6	10	1.7	D	10^6
S4	0.1	1.25	10^6	1	1.7	D	10^6
S5	0.03	1.25	10^6	10	1.7	D	10^6
S6	0.03	1.25	10^6	1	1.7	D	10^6
S7	0.6	1.25	10^6	10	1.7	D	10^6
S8	0.6	1.25	10^6	1	1.7	D	10^6
S9	10/3	1.25	10^6	10	1.7	D	10^6
S10	10/3	1.25	10^6	1	1.7	D	10^6
S11	10	1.25	10^6	10	1.7	D	10^6
S12	10	1.25	10^6	1	1.7	D	10^6
S13	0.3	1.25	10^6	10	1.7	None	10^6
S14	0.3	1.25	10^6	10	1.7	A	10^6
S15	0.3	1.25	10^6	10	1.7	B	10^6
S16	0.3	1.25	10^6	10	1.7	C	10^6
S17[h]	0.3	1.25	10^6	10	1.7	D	3×10^6

[a] Unique simulation identification used to cross reference throughout this chapter.
[b] SMBH mass ratio $q \equiv M_1/M_2$. The stellar cusp is placed around M_1 therefore for $q > 1$ the stellar cusp is around the secondary.
[c] Cusp profile, see equation (4.3) for definition. $\eta = 1.25$ corresponds to a Bahcall and Wolf (1976) cusp.
[d] Stellar mass, $M_\star$. All stars are assumed to have this mass.
[e] Radius of the stellar cusp,r_c, see equation (4.6).
[f] Number of stars simulated.
[g] Fiducial simulation.
[h] As simulation S1, but with increased number of stars and simulation length.

Simulations S9–12 have SMBH binary mass ratio, q, greater than 1. In this case the stellar cusp is effectively placed around the *secondary*. We do not follow the integration of the stars in the cusp

[6] Partially funded by NSF MRI grant PHY-0619274

around the more massive SMBH, although these dominate the rate of inspiral in our pre-calculated SMBH binary path. In simulations with mass ratio 10/3 (S11 and S12) we use the SMBH binary pre-calculated for the $q = 0.3$ simulations. In simulations with mass ratio 10 we utilize the the $q = 0.1$ binary inspiral. The stars must be integrated consistently with the binary evolution (for the reasons described in section 5.2). From equation (5.3), it follows that for a q^{-1} simulation, the binary separation and velocity from the q simulation must be increased by a factor

$$\left[\frac{\text{Total } q > 1 \text{ mass}}{\text{Total } q < 1 \text{ mass}}\right]^{1/3} = \left[\frac{0.5(q^{-1}+1) + M_{t,\text{new}}}{0.5(1+q) + M_{t,\text{old}}}\right]^{1/3} . \tag{5.45}$$

The new stellar mass in the truncated potential is given by $M_{t,\text{new}} = M_\star(r_{t,\text{new}})$ where the new truncation radius $r_{t,\text{new}}$ is chosen to lie at approximately the Hill radius.

5.4 Dynamics

The dynamics are surprisingly rich and interesting. We demonstrate some of the key aspects in this section with particular reference to our fiducial simulation S1. Where possible order-of-magnitude calculations that emphasize physical understanding are given.

To demonstrate that we have captured most of the EMRIs and plunges, in figure 5.8 the number of events as a function of time is plotted. Time is plotted in our code units of

$$\frac{1}{\Omega} = \sqrt{\frac{r_c^3}{2GM_1}} = 23 \times 10^3 \text{ yr } \frac{M_1}{10^6 M_\odot}\left(\frac{r_c}{1.7 \text{ pc}}\right)^3 . \tag{5.46}$$

It is clear from the longer period and larger simulation in figure 5.8(b) that, while the rate of events is not yet zero in figure 5.8(a), we have captured the peak in the rates of EMRIs and plunges. Note that our numbers of events are a lower limit because we only simulate the OMyr as the SMBH binary stalls. It is likely the rate of tidal disruptions, EMRIs, and plunges remains higher than the isolated SMBH rate throughout the possibly OGyr of the SMBH binary's existence. We outline the reasons for this in section 5.6.

5.4.1 Lidov-Kozai Effect

The key process in the formation of EMRIs, plunges, and (to a lesser extent) tidal disruptions is the secular Lidov-Kozai effect (Lidov 1961, English translation Lidov 1962, Kozai 1962). We do not give a mathematical treatment here [7] , instead referring the reader to the extensive literature on the subject (e.g., Innanen et al. 1997, or Ivanov et al. 2005).

[7] Appendix 5.B *does* derive the Kozai equations, but with the addition of relativistic precession. The orbital plane in appendix 5.B is different because we do not average over the SMBH binary orbit but, translating this, the Kozai equations are just equations (5.99)-(5.102) without the GR precession, ℓ^{-2}, term in (5.99).

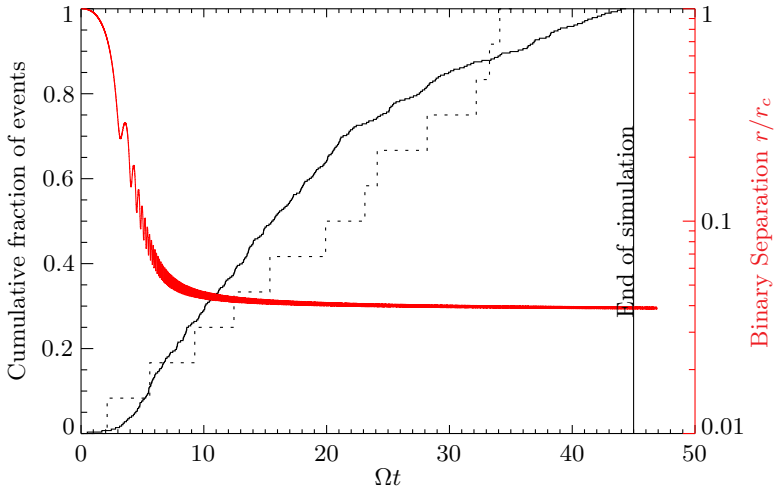

(a) The cumulative distribution of plunges and EMRIs as a function of time in simulation S1

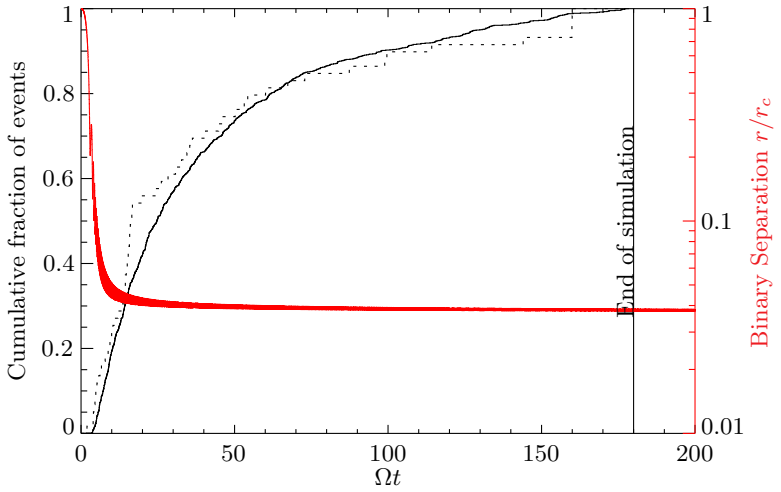

(b) The cumulative distribution of plunges and EMRIs as a function of time in simulation S17. This simulation is equivalent to simulation S1 but contains three times more stars, integrated for a longer period. It was performed to assuage fears that we had captured only a small fraction of the the total number of EMRIs.

Figure 5.8 The cumulative distribution of plunges (solid line) and EMRIs (dashed line) as a function of time are plotted on the left-hand axis. The binary separation during the pre-calculated inspiral path is plotted as the red line on the right-hand axis.

In the Lidov-Kozai process, stellar orbits around the primary SMBH are perturbed by the tidal quadrupole perturbation from the secondary SMBH. This process occurs on a long, secular, timescale and therefore both the stellar and secondary SMBH orbits are averaged over. We place the SMBH binary orbit in the x-y plane, and so symmetry about the z axis causes the z component of the stellar angular momentum, L_z, to be conserved. This holds to quadrupole order even in the case of an eccentric SMBH binary orbit in the restricted three body case (Naoz et al., 2011).

In figure 5.9 we plot the outcome of simulation S1 for each star as a function of its initial L_z. The majority of stars that form EMRIs (gold stars) do indeed have initially low L_z. Far from the secondary those that plunge (green dots), also have initially low L_z.

We also demonstrate in figure 5.10 that it is not that EMRIs and plunges all come from low angular momentum, and that L_z is 'special'. Low angular stars would naturally have a close pericenter distance so this is an important verification.

The timescale of the Lidov-Kozai process is to order unity given by (Chen et al., 2011)

$$\frac{1}{t_{\rm koz}} \sim \frac{1}{L}\frac{dL}{dt}\,, \tag{5.47}$$

where Keplerian specific angular momentum is given by $L^2 = GM_{\rm BH}a(1-e^2)$, and the torque due to the quadrupolar tidal force from the secondary is

$$\left|\frac{dL}{dt}\right| = \left|\vec{F}\times\vec{r}\right| \sim \frac{qGM_{\rm BH}a^2}{R^3}\,. \tag{5.48}$$

This gives a Kozai timescale of

$$t_{\rm koz} \sim \frac{\sqrt{1-e^2}}{2\pi q}\left(\frac{R}{a}\right)^3 P_\star \tag{5.49}$$

$$\sim \frac{\sqrt{1-e^2}}{2\pi q}\left(\frac{R}{a}\right)^{3/2} P_b\,. \tag{5.50}$$

where $P_\star$ is the orbital period of the star, and P_b is the orbital period of the SMBH binary. Except for the $\sqrt{1-e^2}$ and a 2/3 factor, this is just the conventional Kozai timescale (e.g., Ivanov et al., 2005).

$$T_k = \frac{2}{3\pi q}\left(\frac{R}{a}\right)^{3/2} P_b \tag{5.51}$$

We have retained the non-constant factor, $\sqrt{1-e^2}$, in equation (5.50) since it illustrates that the timescale for changes is shorter during high-eccentricity periods. We refer to $t_{\rm koz}$ as the instantaneous Kozai timescale to emphasize this difference.

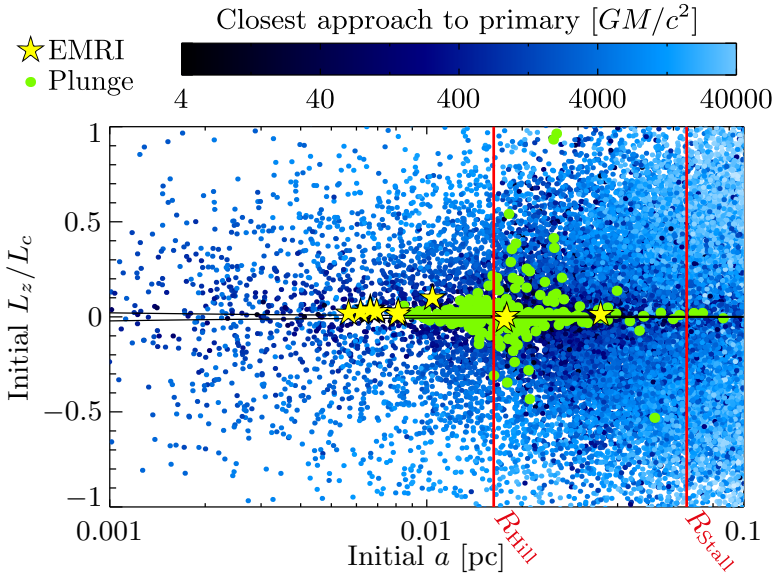

(a) Plot with L_z normalized to the circular angular momentum, $L_c \equiv \sqrt{GMa}$.

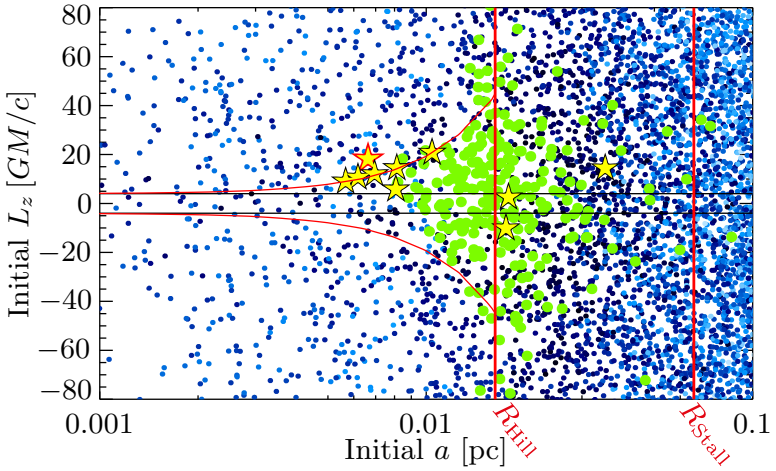

(b) Plot with L_z unnormalized. The additional red line marks, $|L_z| < 4\,GM/c + \Delta L_b$, the range of oscillations on the binary SMBH orbital period discussed in section 5.4.4.

Figure 5.9 Outcome for each star in simulation S1. EMRIs are gold stars, plunges green dots. Other stars are color coded by their distance of closest approach during the simulation. In the secular approximation L_z is conserved and therefore all plunges should come from the region with $|L_z| < 4\,GM/c$ which is plotted in black. This region is known as the Kozai wedge. A version of this figure also appears in Bode (2011).

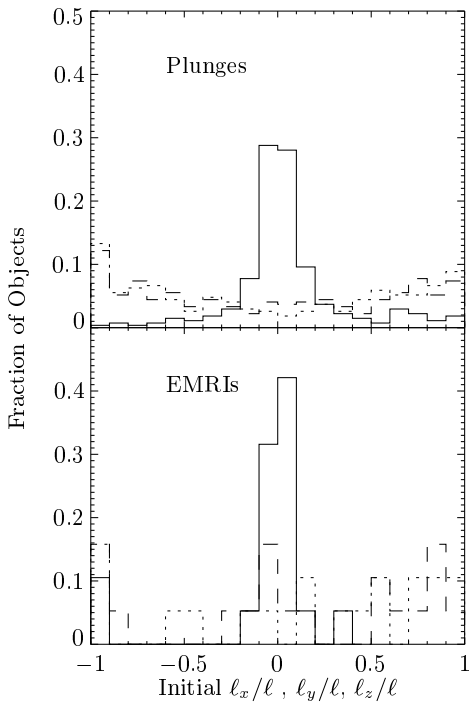

Figure 5.10 Distribution of EMRIs and plunges in angular momentum. While many of the plunges and EMRIs are outside the Kozai wedge where $L_z < 4\,GM/c$, they still predominantly come from low L_z.

5.4.2 Apsidal Precession

In the far-field limit general relativity causes the line of apsides to precess each orbit by an angle of (Weinberg, 1972)

$$\delta\omega_{\rm GR} = \frac{6\pi GM_{\rm BH}}{c^2 a(1-e^2)}\,. \tag{5.52}$$

The timescale to precess though π radians, upon which the torque due to the SMBH binary quadrupole, and hence the resultant evolution in L is reversed, is

$$t_{\phi,\rm GR} \equiv \frac{\pi}{\delta\omega_{\rm GR}} P_\star \sim \frac{c^2 a(1-e)}{3GM_{\rm BH}} P_\star\,. \tag{5.53}$$

There is also purely Newtonian precession due to the non-Keplerian stellar potential. This results in a precession per orbit of (e.g., Merritt et al., 2011b)

$$\delta\omega_{\rm SP} \sim -2\pi \frac{\sqrt{1-e^2}}{1+\sqrt{1-e^2}} \frac{M_\star(<a)}{M_{\rm BH}} \tag{5.54}$$

and hence orbits precess though π radians on a timescale

$$t_{\phi,\rm SP} \equiv \frac{\pi}{\omega_{\rm SP}} P_\star \sim \frac{1+\sqrt{1-e^2}}{\sqrt{1-e^2}} \frac{M_{\rm BH}}{M_\star(<a)} P_\star\,. \tag{5.55}$$

Note that $\delta\omega_{\rm GR}$ and $\delta\omega_{\rm SP}$ have opposite signs, i.e., GR and precession due to the stellar potentials are in opposite directions, and therefore competing effects. The GR precession however dominates for high eccentricities ($1-e \to 0$).

5.4.3 Extreme Apsidal Precession

When the timescales for apsidal precession (e.g., $t_{\phi,\rm GR}$ or $t_{\phi,\rm SP}$) are shorter than the Kozai timescale, then the size of the oscillations in L is reduced. This is sometimes referred to as 'detuning' the Kozai mechanism in the literature. In this case there are still oscillations, but their size is typically reduced by a fraction $\sim t_{\phi,\rm GR}/t_{\rm koz}$ (or $\sim t_{\phi,\rm SP}/t_{\rm koz}$). The mathematical details of this process when GR precession dominate are described in appendix 5.B. A result is that if a star is delivered to a high eccentricity, low angular momentum orbit, then the star's oscillations are damped and it will remain at high eccentricity. In this case the 'detuning' of the Kozai mechanism is an advantage in the formation of EMRIs.

5.4.4 Fluctuations on the orbital timescale of the SMBH binary

When averaged over the timescale of the binary the component of angular momentum perpendicular to the binary's orbit is conserved, however on shorter timescales this is not the case. The size of these fluctuations will be of order

$$\Delta L_b \sim \frac{dL}{dt}\frac{P_b}{4}\,, \tag{5.56}$$

where the factor 4 reflects, approximately, that this is a quadrupolar force, and hence there are 4 reverses in sign per P_b. Using the previously calculated torque

$$\Delta L_b \sim \frac{qGM_{\rm BH}a^2}{R^3}\frac{P_b}{4} = \frac{GM_{\rm BH}q}{4a}\left(\frac{a}{R}\right)^{3/2} P_\star\,, \tag{5.57}$$

or

$$\frac{\Delta L_b}{L_c} = \frac{\pi q}{2}\left(\frac{a}{R}\right)^{3/2}\,, \tag{5.58}$$

where $L_c = \sqrt{GM_{\rm BH}a}$ is the angular momentum of a circular orbit.

More rigorous calculations of this effect are given in appendix B of Ivanov et al. (2005). The result which differs only by an order unity factor from equation (5.57), is that, close to the peak in eccentricity,

$$\frac{\Delta L_b}{L_c} = \frac{15q}{8}\cos i_{\rm min}\left(\frac{a}{R}\right)^{3/2}\,, \tag{5.59}$$

where $i_{\rm min}$ is the minimum inclination, which for high eccentricity orbits will be small.

These oscillations, which result in oscillations in the otherwise conserved L_z, are particularly important in the case considered here because of the extreme eccentricities. However they are

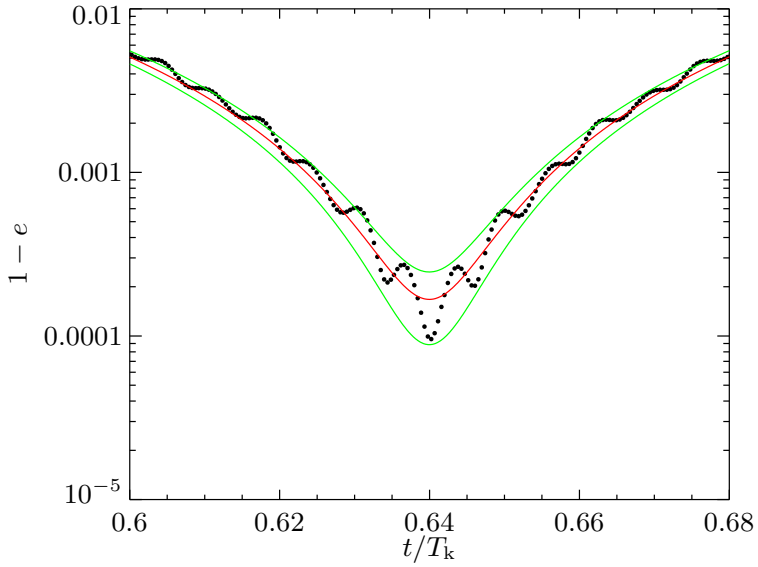

Figure 5.11 Zoom in on one of the peaks in eccentricity from figure 5.7. The black points are the simulated star, one point plotted at each periapsis passage. The red line is integration of the secular Kozai equations. The oscillations are due to the orbital period of the binary as the described in section 5.4.4. The green lines are the range of oscillations predicted by equation (5.59).

always present in the Kozai mechanism, and are often neglected because they do not appear in the secularly averaged equations. They are the reason for the oscillations seen in figure 5.7. In figure 5.11 we zoom in on one of the peaks in eccentricity to demonstrate these oscillations.

5.4.5 Stellar Orbital Timescale

The star has discrete periapsis passages. This make the stellar radial orbital period, $P_\star$, an important timescale because, for example, if the angular momentum falls below $L = 4\,GM/c$, a plunge does not immediately occur. Instead a plunge occurs only if the angular momentum remains below $L = 4\,GM/c$ at the next periapsis passage. Between periapsis passages the angular momentum of the star will undergo a change in angular momentum of typical size

$$\Delta L_\star \sim \frac{dL}{dt} P_\star \sim \frac{qGM_{\rm BH}a^2}{R^3} P_\star = \frac{GM_{\rm BH}q}{a}\left(\frac{a}{R}\right)^3 P_\star \tag{5.60}$$

or

$$\frac{\Delta L_\star}{L_c} = 2\pi q \left(\frac{a}{R}\right)^3 , \tag{5.61}$$

which is naturally of order $P_\star/P_b$ smaller than the oscillations on the binary timescale given by equation 5.57.

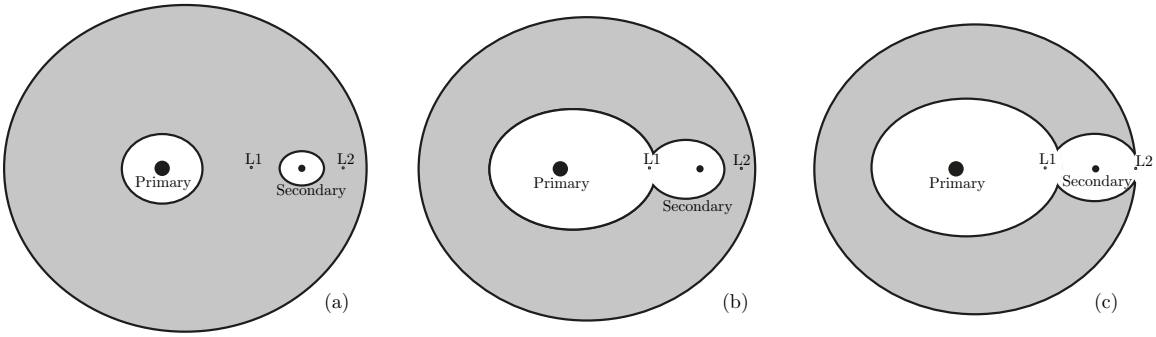

Figure 5.12 Schematic illustration of Hill stability in the x-y plane of the co-rotating frame. Each sub-figure (a)–(c) represents the allowed region of a star with decreasing Jacobi constant. Stars may not travel through the gray regions which have $2U < C_J$. In (a) $C_2 < C_1 < C_J$ and a star orbiting close to the primary must remain orbiting the primary. In (b) $C_2 < C_J < C_1$ and so the star may pass through the L1 Lagrange point to orbit the secondary, but cannot become unbound. In (c) $C_J < C_2 < C_1$ the star may also pass through the L2 Lagrange point to become unbound.

5.4.6 Unbound Stars

In the circular restricted three-body problem the only integral of motion is Jacobi's constant (e.g., Murray and Dermott, 2000). In the non-rotating, barycentric frame (which we work in throughout this section) this is given by

$$C_J = -2(E - nL_z) = 2U - v^2 + 2nL_z \,. \tag{5.62}$$

where E is the energy in the barycentric frame, and n is the mean motion of the massive bodies.

The case considered here is not the circular restricted three-body problem: The SMBH binary both inspirals, and is not circular. However, for the stars of interest, the inspiral is nearly adiabatic and so the adiabatic invariant semi-major axis of the stars remains nearly constant, and it is a semi-major axis limit we search for in this section. In addition the SMBH binary stalls with negligible eccentricity. The result is that the limit based on the Jacobi constant, C_J, in this section is remarkably accurate, despite its approximate nature.

At zero velocity $C_J = 2U$, which defines the zero-velocity surface (e.g., Murray and Dermott, 2000). This is a useful relation since a particle cannot travel through regions of space where $2U < C_J$. Define the value of the the Jacobi constant at Lagrange point L_i to be C_i. If $C_J < C_1$ then a particle initially orbiting the primary is able to cross L_1 and orbit the secondary. It will not however be ejected unless $C_J < C_2$ and it is able to exit the system across L_2. This is illustrated in figure 5.12.

In simulation S1, which has $q = 0.3$, the positions of L1 and L2 are $0.3791R$ and $0.4991R$ from the secondary, respectively. This gives $C_1 = 5.001GM_1/R$ and $C_2 = 4.627GM_1/R$.

The Hill stability criterion that $C_J > C_2$ can be translated to a criterion in semi-major axis, inside which all stars must remain bound. In the case under consideration, the most stringent stability

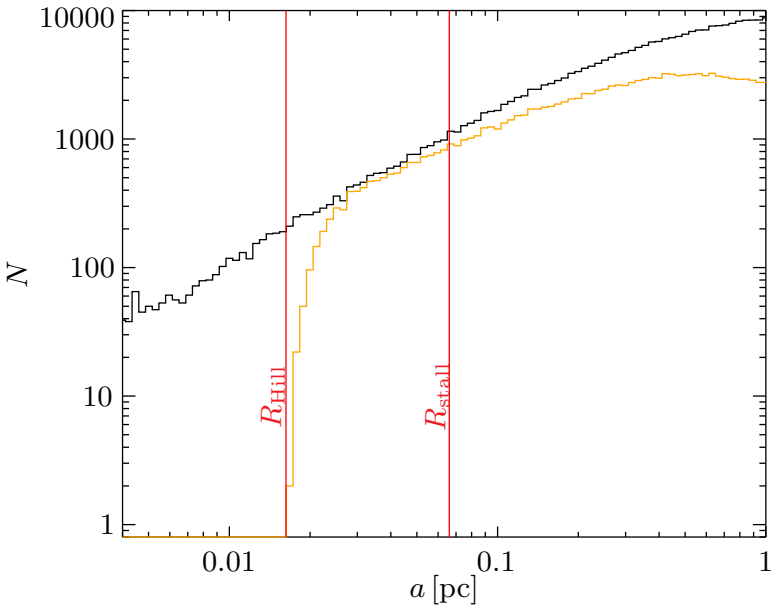

Figure 5.13 Demonstration of Hill stability criteria in simulation S1 ($q = 0.3$). A histogram of all stars is plotted in black. In orange are those stars that are unbound at the end of the simulation. In this case the criteria for stability ($C_J > C_2$) is $a < R_{\rm Hill} = 0.2462 R_{\rm stall}$.

criterion occurs at the SMBH stalling radius, $R_{\rm stall}$, at which point

$$n = \sqrt{\frac{GM_1(1+q)}{R_{\rm stall}^3}} \,. \tag{5.63}$$

At any semi-major axis the largest possible L_z is the circular orbit with $L_z = \sqrt{GMa}$. Therefore the largest possible C_J at semi-major axis a is

$$C_J = \frac{GM_1}{a} + GM_1 \sqrt{\frac{(1+q)a}{R_{\rm stall}^3}} \,. \tag{5.64}$$

Setting this equal to C_2 and solving for a, gives the radius inside which all orbits must remain bound:

$$R_{\rm Hill} = 0.2462 R_{\rm stall} \,. \tag{5.65}$$

In figure 5.13 we plot a histogram of the stars that become unbound for simulation S1. No stars with initial semi-major axis less that $R_{\rm Hill}$ are unbound at the conclusion of the simulation.

In figure 5.26 in appendix 5.D an example star that becomes unbound is shown. This star becomes unbound on a secular timescale after undergoing a Kozai oscillation.

5.4.7 Formation of EMRIs and Plunges

In figure 5.14 we plot the size of the oscillations in L on the star and binary orbital timescale given by equations (5.61) and (5.57), respectively, and the plunge angular momentum $L_{\rm Plunge} = 4\,GM/c$. We also plot lines when the Kozai timescale, $t_{\rm koz}$, and the apsidal precession timescales, $t_{\phi,\rm SP}$ and $t_{\phi,\rm GR}$, are equal. For smaller semi-major axis than these lines, the Kozai mechanism will be detuned. The results of the previous section allow the dynamics of the EMRI and plunge formation to be understood.

At the largest semi-major axes, from $\sim R_{\rm Hill}$ outwards, the majority of stars are ejected from the system, becoming unbound often after chaotic encounters with the secondary. A small fraction of these may be scattered close enough to either SMBH to plunge instead. A star scattered towards either SMBH has a larger cross section to plunge rather than form an EMRI, and therefore only a small fraction of the stars in this region form EMRIs.

Moving inwards from $R_{\rm Hill}$ all stars remain bound at the conclusion of the simulation. This is the region in which the secular Kozai oscillations become important. In this region if $L_z + \Delta L_b \lesssim L_{\rm Plunge}$ then the there is the possibility that the Kozai oscillations will drive the stars total angular momentum to $L_{\rm Plunge}$, and a EMRI or plunge will result.

In the region where $L_\star$ is a significant fraction of $L_{\rm Plunge}$, then stars are more likely to plunge than form an EMRI, because of the larger cross section for plunges.

However as $L_\star$ becomes small compared to $L_{\rm Plunge}$, stars are slowly perturbed towards the primary SMBH. Since the angular momenta for EMRI formation lie outside $L_{\rm Plunge}$, stars will be perturbed into this region first and an EMRI will result.

Finally to the left of the $t_{\rm Koz} = t_{\phi,\rm GR}$ line neither EMRIs nor plunges occur. This is because in this region, as a star is perturbed to smaller L, the GR precession rate increases precipitously, the star precesses reversing direction of the perturbing torque, and L increases again. This is referred to as the Schwarzschild barrier around isolated SMBHs by Merritt et al. (2011b). In that case the perturber was the torque due to the statistically aspherical stellar distribution, however this effect will occur when any sufficiently secular perturbation is combined with GR precession.

The result is that there is a 'sweet spot' for EMRI formation lying to the right of the $t_{\rm Koz} = t_{\phi,\rm GR}$ line, where $L_z \lesssim L_{\rm Plunge} + \Delta L_b$ and $\Delta L_b \ll L_{\rm Plunge}$. In this region the timescale for GR precession $t_{\phi,\rm GR}$ is also close to the orbital timescale of the SMBH binary, P_b, making the dynamics especially complex. The integration of an example star, the red outlined star in figure 5.14, from this region is shown in figure 5.27 in appendix 5.D.

In appendix 5.C we show equivalent plots for the other simulations in table 5.1.

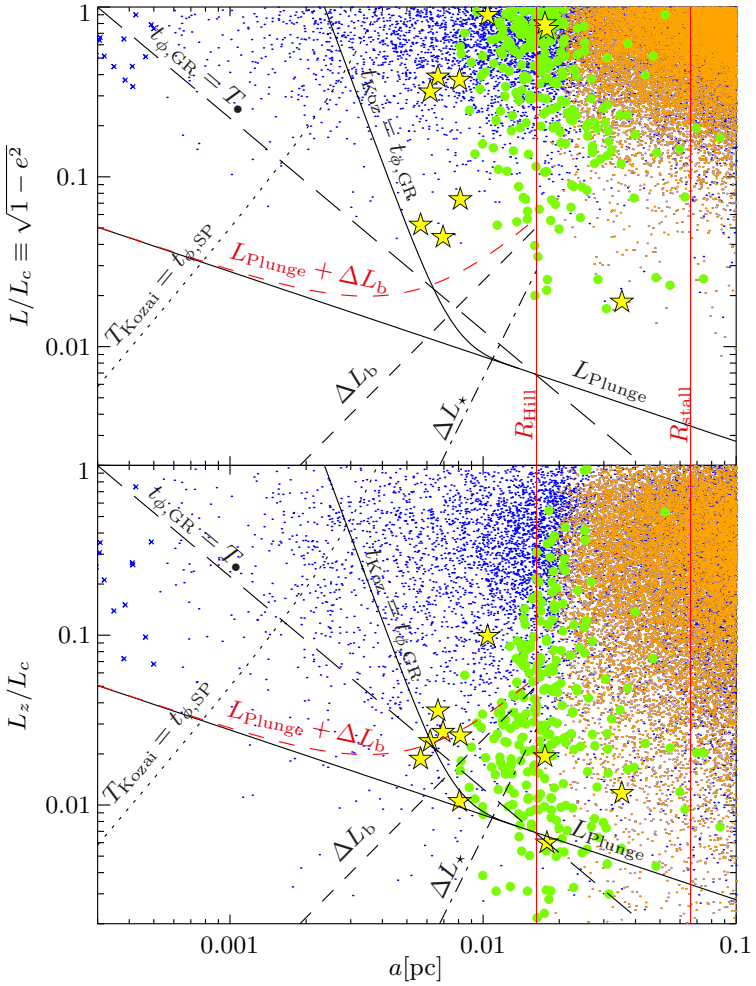

Figure 5.14 Results of S1 ($q = 0.3, M_\star = 10$) simulation as function of normalized angular momentum and semi-major axis. Outcomes are shown as function of normalized angular momentum and semi-major axis along with important delimiting lines (described in section 5.4). Initial L/L_c and L_z/L_c are plotted in the upper and lower panels, respectively. Each star is represented by its outcome: an EMRI (gold star), a plunge (green dot), becoming unbound (orange dot) or remaining in the cusp at the conclusion of our simulation (blue dot).

5.5 Results

A summary of the numbers of EMRIs, plunges and tidal disruptions produced from each simulation are shown in table 5.2.

Table 5.2 Summary of raw simulation results. Additional parameters for each simulation are described in table 5.1. These are the numbers of each event produced from our simulations with 10^6 stars. To scale to physical numbers produced from each merger, the number EMRIs or plunges should be multiplied by $2/M_\star$. I.e., We predict 2 EMRIs should arise during a SMBH merger with S1 parameters. To scale the TD numbers multiply by $2M_1/10^6 M_\odot$. Caveats regarding the scaling of TDs to primary masses other than $10^6 M_\odot$ are discussed in section 5.5.3.

Id[a]	q[b]	$M_\star/M_\odot$[c]	GW Loss Method	EMRIs	Plunges	TDs from primary of mass			TDs from secondary of mass		
						$10^6 M_\odot$	$10^7 M_\odot$	$10^8 M_\odot$	$q10^6 M_\odot$	$q10^7 M_\odot$	$q10^8 M_\odot$
S1[d]	0.3	10	D	10	287	427	341	301	4	3	3
S2	0.3	1	D	1	217	369	294	243	3	1	1
S3	0.1	10	D	13	277	451	351	298	3	3	3
S4	0.1	1	D	3	195	362	287	222	1	1	1
S5	0.03	10	D	9	417	695	530	446	4	2	0
S6	0.03	1	D	1	217	420	320	256	4	2	0
S7	0.6	10	D	39	390	605	488	415	16	10	6
S8	0.6	1	D	3	282	512	390	313	6	3	3
S9	10/3	10	D	13	577	856	718	598	61	52	44
S10	10/3	1	D	1	400	671	561	469	27	17	15
S11	10	10	D	35	600	1155	933	776	85	69	64
S12	10	1	D	1	482	859	701	581	35	30	30
S13	0.3	10	None	-	212	373	292	237	2	1	1
S14	0.3	10	A	2	203	363	275	231	2	1	1
S15	0.3	10	B	5	223	369	285	241	2	1	1
S16	0.3	10	C	3	238	377	294	249	2	1	1
S17[e]	0.3	10	D	58	1270	1629	1441	1300	27	24	15

[a] Unique simulation identification. See table 5.1

[b] SMBH mass ratio $q \equiv M_1/M_2$. The stellar cusp is placed around M_1 therefore for $q > 1$ the stellar cusp is around the secondary.

[c] Stellar mass, $M_\star$. All stars are assumed to have this mass.

[d] Fiducial simulation

[e] As S1 but with 3×10^6 stars and an increased simulation time.

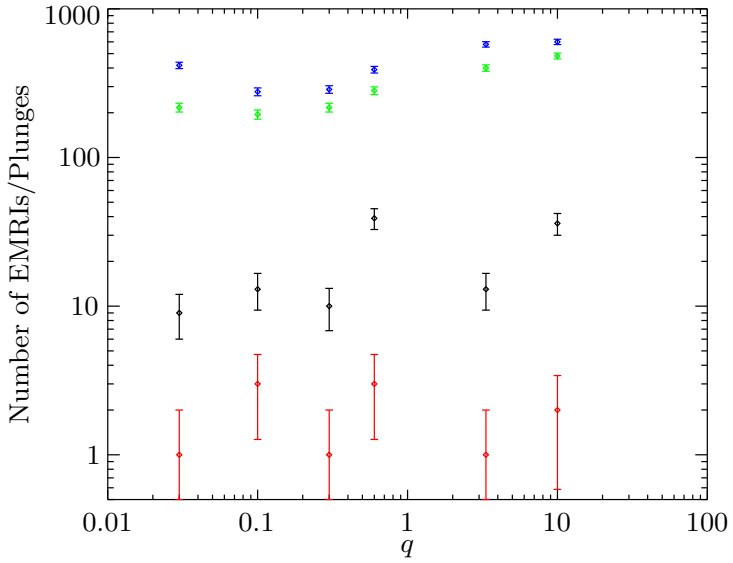

Figure 5.15 Number of EMRIs and plunges produced as a function of SMBH mass ratio, q, in simulations S1–S12. The number of EMRIs produced by the $M_\star = 10\,M_\odot$ and $M_\star = 1\,M_\odot$ simulations are plotted in black and red, respectively. The number of plunges produced by the $M_\star = 10\,M_\odot$ and $M_\star = 1\,M_\odot$ simulations are plotted in blue and green, respectively.

5.5.1 EMRIs

In figure 5.15 we plot the number of EMRIs produced by the various mass ratios simulated in S1–S12. Here we scale these numbers to estimate the number of EMRIs produced in close binary SMBHs to redshift $z = 1$. We first assume that all objects in the cusp are $10\,M_\odot$ black holes.

Simulations S7 ($q = 0.6$) and S11 ($q = 10$) produce a significantly higher number of EMRIs than the other simulations. The reason for this is unknown, especially considering the smaller number produced by S9 ($q = 10/3$), whose mass ratio lies between these. Instead we conservatively reject these simulations, assuming the results to be spurious, and will investigate the possibility that they are real in future work. The remainder of the simulations give a statistically constant number of EMRIs per simulation of 11 ± 2 (including S7 and S11 increases this number to 20 but a number independent of mass ratio would no longer be appropriate). Scaling this to the 2×10^5 objects in the cusp (i.e., dividing by $\frac{2\times10^6\,M_\odot \text{ cusp mass}}{10\,M_\odot \text{ mass objects}\times10^6 \text{ objects simulated}} = 5$) we predict 2.2 ± 0.4 EMRIs per merger.

We now wish to calculate an approximate rate of SMBH mergers with one component of mass $10^{5.5} - 10^{6.5}\,M_\odot$ up to redshift 1. We choose this mass range and redshift as appropriate for (optimistic), future space-based, low-frequency gravitational wave detectors.

Using the black hole mass function (Aller and Richstone, 2002)

$$\frac{dN}{dM_{\rm BH}} = c\left(\frac{M_{\rm BH}}{M^{\star}_{\rm BH}}\right)^{-\alpha} e^{-M_{\rm BH}/M^{\star}_{\rm BH}}, \tag{5.66}$$

with the parameters $c = 3\times10^{-11}M_{\odot}^{-1}$ Mpc^{-3}, $M^{\star}_{\rm BH} = 1.1\times10^{8}\,M_{\odot}$ and $\alpha = 0.95$ (values derived by Aller and Richstone, 2002, scaled to $H_0 = 71$ km s^{-1} Mpc^{-1}). Gives the number of SMBHs of mass $10^{5.5} - -10^{6.5}\,M_{\odot}$ to be 6×10^{-3} Mpc^{-3}.

Stewart et al. (2009) gives the number of merger rate of these galaxies with mass ratio $0.01 < q < 1$ to be $\sim 0.02\,{\rm Gyr}^{-1}(1+z)^{2.2}$ (which is consistent with observational constraints, e.g., Conselice, 2006). Assuming the density of black holes over this mass range to be constant, then integrating over co-moving volume, gives the rate of mergers to redshift 1 to be $0.06\,{\rm yr}^{-1}$.

We therefore predict $0.13\,{\rm yr}^{-1}$ EMRIs per year from SMBHs in the mass range $10^{5.5}$–$10^{6.5}M_{\odot}$ merging with less massive counterparts *if the cusp was entirely made of* $10\,M_{\odot}$ *black holes*. We have also begun simulations with mass ratios larger than 1, i.e., the less-massive SMBH in the frequency range to which the gravitational wave detector is sensitive. The results of these simulations (S9–12) are given in table 5.2, and it appears promising that a similar number will be produced through this channel.

Of course not all members of the cusp will be $10\,M_{\odot}$ black holes. However the EMRIs produced in our simulations originate from radii of ~ 0.01 pc (figure 5.14 and appendix 5.C). If the cusp is mass segregated, it is likely that the majority of objects at this radius will be stellar mass black holes **??**.

Interestingly, our simulations containing objects with $M_{\star} = 1\,M_{\odot}$ produce $O(1)$ object. Scaling this by the 2×10^{6} objects in the cusp in this case gives ~ 2 EMRIs per merger. Therefore, if the objects at ~ 0.01 pc are compact objects of mass $1\,M_{\odot}$, we also predict a similar rate.

If not all objects at ~ 0.01 pc are compact our results can be scaled to other densities by simply multiplying by the fraction of objects that are compact.

5.5.2 Plunges

The relatively large numbers of plunges produced from our simulations have little prospect of observation, since it is likely that for future low-frequency gravitational wave missions, they would be detectable only from the SMBH in our Galactic center (Hopman et al., 2007).

Instead they silently add only their mass to the SMBH. The mean number of plunges is 425 ± 8 from the $10\,M_{\odot}$ simulations, and 299 ± 7 from the $1\,M_{\odot}$ simulations. Scaling these to the number of objects in the cusp, we predict an increase in mass of $(6 - -8.5)\times10^{2}\,M_{\odot}$, or $0.06 - -0.085$ per cent of the SMBH mass.

Of more astrophysical interest is the resultant spin evolution. The change in the dimensionless

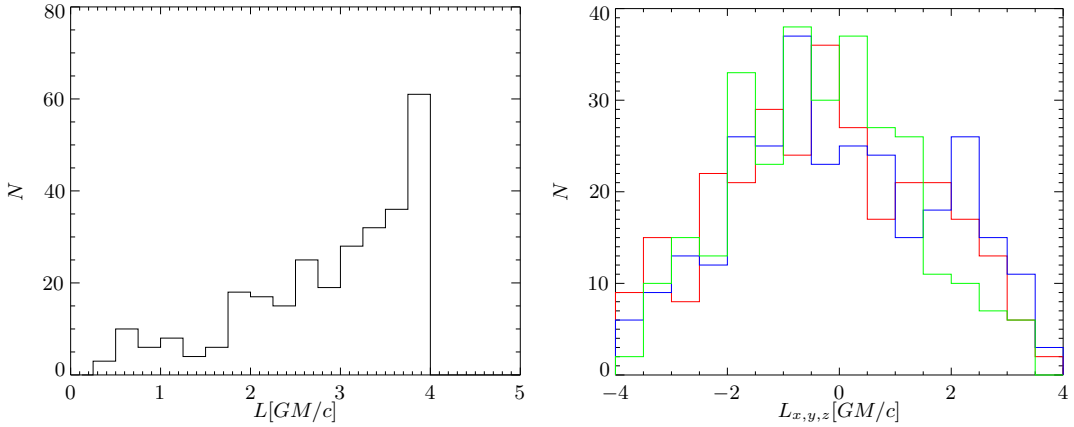

(a) Distribution of total angular momenta at plunge of the stars which plunge in simulation S1.

(b) Distribution of the components of angular momenta at plunge of the stars which plunge in simulation S1. Components L_x, L_y, and L_z are plotted in red, blue and green, respectively.

Figure 5.16 Distribution of reduced angular momenta of plunging stars from simulation S1.

spin of the black hole, a, will be given by (e.g., Kesden et al., 2010)

$$\Delta a = \Delta\left(\frac{S}{M^2}\right) \approx \frac{1}{M^2}\left(\Delta S - \frac{2S}{M}\Delta M\right) , \tag{5.67}$$

where S is the spin of the hole, and M its mass. A plunging orbit has close to zero energy and so ΔM is just the rest mass, $M_\star$, while ΔS is the angular momentum of the plunging star.

In figure 5.16 we plot the distribution of reduced angular momenta of plunging stars from simulation S1. From these distributions we see that the (assumed) initially zero spin will make a random walk as stars plunge. In simulation S1 we predict 58 plunges of stars with mass $10\,M_\odot$ and RMS plunge angular momentum $\sqrt{\langle L^2\rangle} = 3.0 M_1$. The RMS dimensionless spin at the conclusion of the simulation is therefore

$$\sqrt{\langle a^2\rangle} \sim \sqrt{N_{\rm plunge}} \times \frac{\sqrt{\langle L^2\rangle} M_\star}{M_1^2} = 2\times 10^{-4} . \tag{5.68}$$

This too small to be astrophysically interesting, however the situation changes if the SMBH was initially close to having maximum spin. Consider the spin to initially be $a_1 = 1-\delta_1$, with δ_1 possibly as small as 0.002, depending on the accretion and merger history of the SMBH (Kesden et al., 2010). Rewriting equation (5.67)

$$\frac{\Delta a}{a} = \left(\frac{\Delta S}{S} - 2\frac{\Delta M}{M}\right) . \tag{5.69}$$

If the distribution of plunge angular momenta was symmetric, as in simulation S1, then the first term would again make a small contribution. Neglecting this term and integrating equation (5.69)

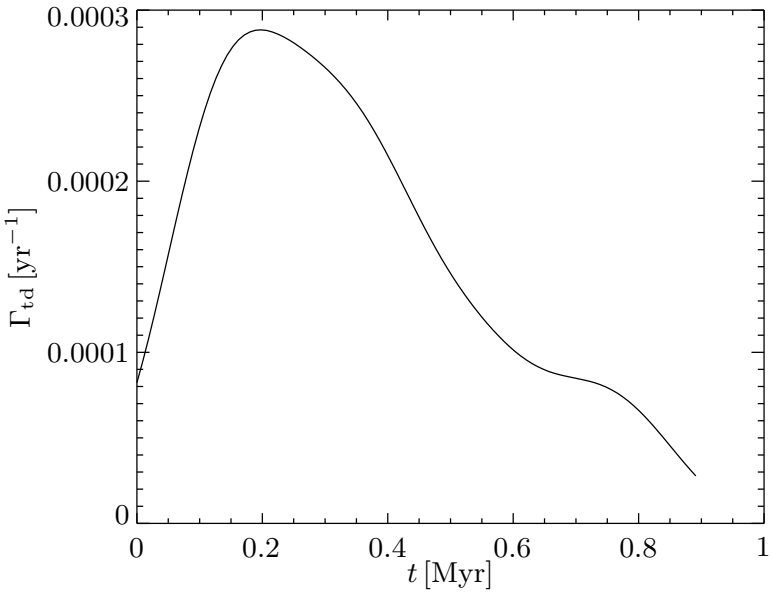

Figure 5.17 Tidal disruption rate as a function of time from simulation S1. The rate is not as significantly enhanced over the expected quiescent rate of $\sim 10^{-5}$ as the simulations in chapter 4. This is because of the relatively low-mass $10^6\,M_\odot$ primary SMBH, and the resultant low-mass stellar cusp.

then

$$\frac{a}{a_1} = \left(\frac{M}{M_1}\right)^{-2} . \tag{5.70}$$

The increase in mass of 0.6–0.85 per cent due to plunges in our simulations therefore, to first order in δ, causes the spin to be limited to $a < (0.9988\text{–}0.9983) - \delta_1$. In fact the first term in equation (5.69) will make this limit stricter, since retrograde, negative ΔS plunges, are likely to dominate due to their larger cross section and magnitude. We therefore predict that recently stalled SMBHs will not be maximally spinning. SMBHs at merger would also not be maximally spinning, without a subsequent period of spin evolution.

5.5.3 Tidal Disruptions

The tidal disruption rate from simulation S1 is shown in figure 5.17. The rate is not significantly enhanced, especially compared to the rates calculated in chapter 4. The reason is that in this chapter we have concentrated on simulations of lower-mass, $10^6\,M_\odot$, SMBHs than those considered in chapter 4. These naturally have cusps containing fewer stars which can be scattered and become tidal disruptions. We choose to focus on these as these lower mass SMBH's in this chapter because, if the stars are compact objects as opposed to main sequence stars which could be tidally disrupted, those are the black holes to which space-based, low-frequency gravitational wave detectors are expected to be sensitive.

Unlike the simulations in chapter 4 the simulations here cannot be directly scaled to other SMBH masses when calculating the tidal disruption rates. This is because the relativistic corrections introduced an additional scale to the problem: In essence the rate of GR precession at the tidal disruption radius cannot be varied without rerunning the simulation.

In table 5.2 however, we still scale the simulations in a similar manner to chapter 4 utilizing equation (4.7). This is because we have rerun the $q = 0.3$ simulation with a range of SMBH masses: $10^6 M_\odot$, $3 \times 10^6 M_\odot$, $10^7 M_\odot$ and $3 \times 10^7 M_\odot$ and with cusp sizes given by equation (4.7). We found estimates made in the manner of table 5.2 to be underestimates, in error by less than 35 per cent. We therefore provide numbers for $M_1 \neq 10^6 M_\odot$, but they should however be used with caution for this reason.

5.6 Caveats

Schwarzschild Black Holes: Throughout this work we ignore the effects of black hole spin on stellar dynamics. This is done for simplicity, since there is increasing evidence that at least some SMBHs have significant spin (Brenneman and Reynolds, 2006). Apart from very close passages, even in the presence of spin, the precession will be dominated by the Schwarzschild terms (Merritt, 2010). Instead the largest effect on the this work would be Lense-Thirring precession of the orbital plane since, if the BH spin is not aligned with the orbital plane, this would result in non-conservation of L_z. We expect this could therefore increase the rate of EMRIs and plunges since more stars can potentially undergo Kozai oscillations which result in close BH encounters, and we hope to investigate this possibility in the future.

Cusp Profile: One of the major factors in determining the rates is the stellar distribution. In our simulations we use an η-model (Tremaine et al., 1994) of a spherical stellar cusp with a central SMBH to establish the stellar distribution. This is the a self-consistent family of models of a stable spherical isotropic stellar cusp around an SMBH. In our simulations, we have chosen $\eta = 1.25$, the value appropriate for a relaxed stellar cusp. However, there is a complication: the galaxy where we can best resolve the inner parsec is our own Milky Way, and the visible cusp does not appear to be relaxed (Yusef-Zadeh et al., 2012). Of course, this raises the question of not only whether or not stellar cusps are generally relaxed. An alternative interpretation of the lack of a visible relaxed cusp is that a (Bahcall and Wolf, 1976) cusp is present in the Galactic center, but is 'dark' as a result of mass segregation causing the density to be dominated by stellar mass black holes (Freitag et al., 2006; Preto and Amaro-Seoane, 2010). In addition the cusps around M31 and M32 are also steep (Lauer et al., 1998), although the dynamics in the nucleus of M31 is complex (Tremaine, 1995). Our rates scale roughly linearly with the number density of stellar mass black holes at about $R_{\rm stall}/10 \sim 0.01\,{\rm pc}$, allowing them to easily be rescaled to other cusp profiles. This is also the reason

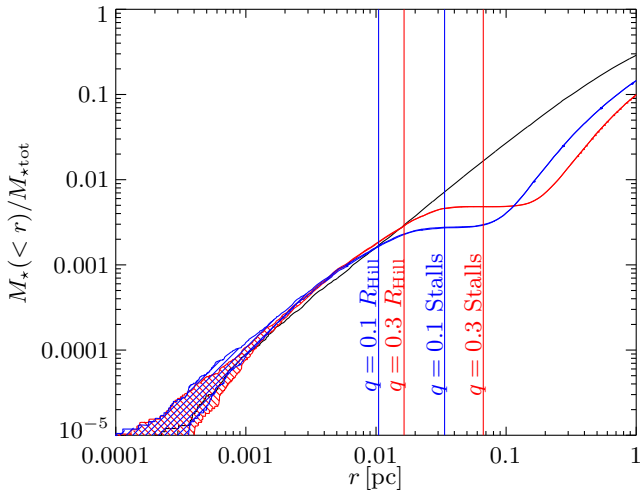

Figure 5.18 Stellar mass interior to a given radius normalized to the total stellar mass, $M_\star(<r)/M_{\star\mathrm{tot}}$. In black we plot the initial cumulative stellar mass, while in blue we plot the cumulative stellar mass at the end of the simulation for the $q = 0.1$, $M_\star = 10\,M_\odot$ run, and in red we plot the cumulative stellar mass at the end of the simulation for the $q = 0.3$, $M_\star = 10\,M_\odot$ run. Note that the initial conditions for all runs are the same. The only difference between the outcomes of the runs with the same q but different stellar masses is due to those stars which go within $100\,GM_1/c^2$, only a small fraction of all stars. Thus, the cumulative stellar mass for the runs with $M_\star = 1\,M_\odot$ are virtually the same as the $10\,M_\odot$ counterparts with the same q. The hatched regions are stars that had not completed the full simulation within the preset limit of 10^{10} steps. For reference we also plot the stalling radii of the secondary as vertical lines. A version of this figure also appears in Bode (2011).

that the assumption of the majority stars being $10\,M_\odot$ black holes is valid: While this would naively result in an unfeasible number of $10\,M_\odot$ black holes in the cusp, in reality all we are assuming is that the majority of stars at ~ 0.01 pc where the EMRIs form are $10\,M_\odot$ black holes.

Stellar Interactions: We have not considered relaxation processes such as that due to star-star scattering. The timescale for relaxation via star-star scattering is approximately 1 Gyr at r_c (Amaro-Seoane and Preto, 2011) and is not a strong function of r in the cusp (Alexander, 2005). Because this is much longer that out simulations we have neglected it. However, this approximation is not as accurate as might be assumed because the timescale to change angular momentum by of order itself will be reduced for high-eccentricity orbits to $\sim (1-e^2)t_r$ (Hopman and Alexander, 2005). Therefore for the highest eccentricity stars in our simulation relaxation could be beginning to become non-negligible. We expect the inclusion of star-star interactions to increase the numbers of EMRIs from SMBH binaries over that found in this work since any relaxation increases the number of stars that can potentially become EMRIs. In particular by the conclusion of our simulations the rate of EMRIs and plunges has dropped significantly since there are few low L_z stars remaining. Relaxation would refill this region of phase, a possibility we hope investigate in the future.

Invariant stellar potential: One inconsistency of our methodology is the assumption that the stellar potential does not evolve with time, though the stars' orbits do. To demonstrate the possible

effect of such an assumption we plot the mass interior to a given radius as a function of radius in figure 5.18. There the solid black line is the initial distribution given by equation (5.2), the red solid line is the curve for the $q = 0.3$ and $M_\star = 10\,M_\odot$ simulation, and the blue solid curve is for the $q = 0.1$ and $M_\star = 10\,M_\odot$ simulation. The mass of the star has little to no effect on these curves. The filled region represents stars that required more than 10^{10} steps to complete the simulation and were therefore terminated. Most EMRIs originate from $\approx 10^{-2}$ pc and at this radius the mass interior has not changed significantly, the plunges and EMRIs representing a small fraction of the stellar mass.

Simulation Length We have performed simulations only of length $\sim 1\,$Myr. Although the exact timescale is uncertain, the SMBH binary is expected to remain stalled for much longer than this. We expect that the rate of tidal disruptions, EMRIs, and plunges will remain enhanced over their rate from isolated SMBHs for this entire period. This is because it is only necessary for stars to be scattered to the $L_z + \Delta L_b \lesssim L_{\rm Plunge}$ 'loss wedge' in order to be secularly perturbed close to the SMBH, as opposed to the much smaller loss cone with $|L| < L_{\rm Plunge}$. Simulations of this would require prescriptions of relaxation to be incorporated to the code. However analytic estimates should be possible from our present simulations which provide the regions of parameter space from which tidal disruptions, EMRIs, and plunges result.

5.7 Conclusion

We have performed a range of simulations of the stellar dynamics around SMBH binaries, concentrating on calculating the number of EMRIs, plunges and tidal disruptions produced by each merger. In addition the code used to perform the simulations in chapter 4 and Bode (2011) was described in greater detail, and the modifications to incorporate general relativistic effects necessary to simulate the production of EMRIs.

We predict $0.13\,{\rm yr}^{-1}$ EMRIs per year from SMBHs in the mass range $10^{5.5} - -10^{6.5} M_\odot$ merging with less massive counterparts to redshift 1. This number must be scaled by the fraction of compact objects at 0.01 pc where the majority of the EMRIs in our simulations form. There is therefore reason to be optimistic that future, space-based, low-frequency, gravitational wave detectors could detect EMRIs from SMBH binaries. The stalled binary companion SMBH could potentially be inferred from the EMRI waveform Yunes et al. (2011). This prospect would be very unlikely without the greatly enhanced rates estimated here and, to date, no convincing SMBH binaries at this separation have been detected.

In addition we expect a much larger number of objects will plunge directly into the SMBHs. This will increase their mass by only $0.6 - -0.85$ per cent, but could have interesting consequences in reducing spin of an initially close to maximally spinning hole.

We have also calculated the numbers of tidal disruptions assuming the cusp was composed of

Sun-like main sequence star. We find for our simulations of $10^6 M_\odot$ SMBHs that the rates are only slightly enhanced over the isolated rates, but have provided rough scalings to other, higher-mass SMBHs.

Appendix 5.A Picking stars from the η-Models

Picking positions is straightforward. In code units (which are the same as the units in Tremaine et al., 1994) the total stellar mass is unity, and the mass interior to radius r is

$$M(<r) = 4\pi \int_0^r r^2 \rho_\eta(r)\, dr = \frac{r^\eta}{(1+r)^\eta}. \tag{5.71}$$

Therefore, given a uniform random number $u = U(0,1)$, stars drawn from this radial distribution can be generated via

$$r = \frac{u^{1/\eta}}{1-u^{1/\eta}}\,. \tag{5.72}$$

It is also necessary to pick a velocity for that star. Given a distribution function $f(\mathcal{E})$ the number of stars at r with velocities between v and $v+dv$ is

$$d\rho = 4\pi f(\mathcal{E}) v^2 dv = 4\pi f(\mathcal{E}) \sqrt{2(\Psi(r)-\mathcal{E})}\, d\mathcal{E} \tag{5.73}$$

where $\mathcal{E} = \Psi - \frac{1}{2}v^2$ is the relative energy. The relative potential $\Psi(r)$ is given by

$$\begin{aligned} \Psi(r) &= \frac{1}{\eta-1}\left[1 - \frac{r^{\eta-1}}{(1+r)^{\eta-1}}\right] + \frac{\mu}{r}, && \eta \neq 1, \\ &= \ln(1+1/r) + \frac{\mu}{r}, && \eta = 1, \end{aligned} \tag{5.74}$$

where μ is the SMBH mass.

The distribution function is calculated using Eddington's formula (Binney and Tremaine, 2008; Tremaine et al., 1994)

$$f(\mathcal{E}) = \frac{1}{2^{3/2}\pi^2} \frac{d}{d\mathcal{E}} \int_0^{\mathcal{E}} \frac{d\rho}{d\Psi} \frac{d\Psi}{\sqrt{\Psi - \mathcal{E}}} \tag{5.75}$$

$$= \frac{1}{2^{3/2}\pi^2} \int_0^{\mathcal{E}} \frac{d^2\rho}{d\Psi^2} \frac{d\Psi}{\sqrt{\Psi - \mathcal{E}}}\,. \tag{5.76}$$

We numerically calculated and tabulated the distribution function using equation (5.76). These tables were evenly distributed in $\log \mathcal{E}$ between -4 and 4 with 100 points per decade.

At the lowest energies (closest to unbound, $\mathcal{E} \to 0$) the distribution function becomes

$$f(\mathcal{E}) \to \frac{2^{5/2}}{5\pi^3(1+\mu)^4}\mathcal{E}^{5/2}\,. \tag{5.77}$$

At the highest energies (most bound to SMBH, $\mathcal{E} \to \infty$) the distribution function becomes

$$f(\mathcal{E}) \to \frac{\eta\Gamma(4-\eta)}{2^{7/2}\pi^{5/2}\mu^{3-\eta}\Gamma(\frac{5}{2}-\eta)}\mathcal{E}^{\eta-3/2}\,. \tag{5.78}$$

Beyond the extent of the tabulations the approximations in equations (5.77) and (5.78) were used.

A rejection method was used to pick velocities from these distributions (Press et al., 1992). Equation (5.73) can be written

$$\frac{d\rho}{d\mathcal{E}} = 4\pi f(\mathcal{E})\sqrt{2(\Psi(r)-\mathcal{E})} = 4\pi\sqrt{2}\Psi f(\mathcal{E})\sqrt{1-\mathcal{E}/\Psi} \tag{5.79}$$

and since $\mathcal{E}$ is always positive an upper limit is

$$\frac{d\rho_{\max}}{d\mathcal{E}} = 4\pi\sqrt{2}\Psi \max_{0\le\mathcal{E}\le\Psi} f(\mathcal{E})\,. \tag{5.80}$$

To pick velocities therefore first an energy is picked between 0 and Ψ and the ratio

$$\frac{d\rho}{d\rho_{\max}} = \frac{f(\mathcal{E})\sqrt{1-\mathcal{E}/\Psi}}{\max_{0\le\mathcal{E}\le\Psi} f(\mathcal{E})} \tag{5.81}$$

calculated. A uniform random number $U(0,1)$ is then picked and compared to this to the ratio. If less the energy is kept and converted to a velocity. If greater then the energy is rejected and the process is repeated.

In calculating $f(\mathcal{E})$, motivated by the power law form of equations (5.77) and (5.78), a power law distribution function over each interval in energy is assumed:

$$f(\mathcal{E}) = f_i(\mathcal{E}_i)\left(\frac{\mathcal{E}}{\mathcal{E}_i}\right)^{a_i} \qquad \mathcal{E}_i < \mathcal{E} < \mathcal{E}_{i+1}\,, \tag{5.82}$$

where the coefficients a_i are calculated from the tabulated data via

$$a_i = \frac{\log f_{i+1} - \log f_i}{\log \mathcal{E}_{i+1} - \log \mathcal{E}_i}\,. \tag{5.83}$$

Outside the range of the tabulated data the asymptotic equations (5.77) and (5.78) were used.

Examples of realizations of the resulting velocity distributions are shown in figure 5.19.

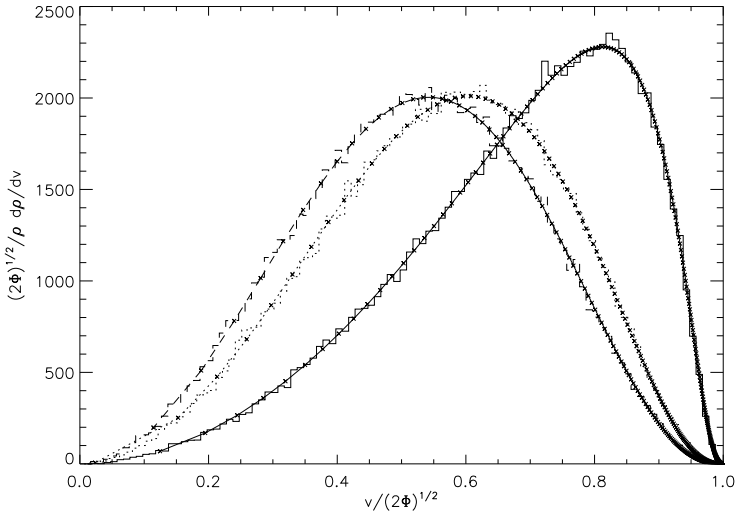

Figure 5.19 Comparison of Monte-Carlo stars within 10% of $r = 0.1$ (solid line), $r = 1$ (dotted) and $r = 10$ (dashed) for $\eta = 1.5$ and $\mu = 1$ to the expected distribution of velocities from the tabulated values of $f(E)$. A total of 10^6 stars were simulated.

.

Appendix 5.B The 'Reverse-Kozai Effect'

In section 5.4 we discussed the situation of 'extreme apsidal precession': The situation whereby the precession rate of the star is faster than the orbital period of the binary. In this case Kozai like oscillations still occur, with with reduced size. These can be thought of in the rotating frame where the stellar orbital apsis are fixed. In this case this frame it is clear that the Kozai effect remains, but the SMBH binary is effectively orbiting at the precession rate. We have termed this the 'reverse-Kozai effect'. In this section we derive the equations of motion for the star under these circumstances.

In the reverse-Kozai effect considered here the precessional period of the star orbiting the primary is much shorter than the binaries orbital period. In this case the secondary can be considered as a stationary perturber to the primaries orbit. The orbital period of the star, and hence its semi-major axis is also assumed to be much smaller than the secondaries.

Using purely Newtonian gravity the potential in the frame of the primary is

$$U(\mathbf{r}) = -\frac{GM}{r} - \frac{GMq}{|\mathbf{r} - \mathbf{r}_2|} + \frac{GMq\mathbf{r}.\mathbf{r}_2}{r_2^3} - V(r)\,, \tag{5.84}$$

where $\mathbf{r}_2$ is the position of the secondary which is assumed constant, $M(Mq)$ is the mass' of the primary (secondary). The third term in equation (5.84) is the indirect term which arises in the non-inertial primary centered frame as opposed to the center of mass frame. V is the stellar potential

for which we use (Tremaine et al., 1994)

$$V(r) = \frac{GM}{r_c(\eta-1)}\left[1 - \frac{r^{\eta-1}}{(r_c+r)^{\eta-1}}\right] \tag{5.85}$$

Expanding the second term in equation (5.84) in Legendre polynomials, $P_l(x)$ gives

$$\begin{aligned} U(\mathbf{r}) &= -\frac{GM}{r} - GMq\left[\sum_{l=0}^{\infty}\frac{r^l}{r_2^{l+1}}P_\ell(\cos\theta) - \frac{r}{r_2^2}\cos\theta\right] - V(r) \\ &= -\frac{GM}{r} - \frac{GMq}{r_2} - GMq\sum_{l=2}^{\infty}\frac{r^l}{r_2^{l+1}}P_\ell(\cos\theta) - V(r)\,, \end{aligned} \tag{5.86}$$

where θ is the angle between the secondary and the star. By assumption $r \ll r_2$ so retaining only the lowest order quadruple term leaves

$$U(\mathbf{r}) = -\frac{GM}{r} - \frac{GMq}{r_2} - \frac{GMqr^2(3\cos^2\theta - 1)}{2r_2^3} - V(r)\,. \tag{5.87}$$

Close to the primary the first term dominates producing nearly Keplerian orbits. By assumption the second term is an unimportant constant while the other terms cause a secular drift in the orbital elements. To calculate that drift we use perturbation theory following Merritt et al. (2011a). The perturbing Hamiltonian is therefore

$$\Delta H = H_{\rm Q} + H_{\rm M} + H_{\rm GR} \tag{5.88}$$

where

$$H_{\rm Q} = \frac{GMqr^2(3\cos^2\theta - 1)}{2r_2^3} \tag{5.89}$$

$$H_{\rm M} = V(r) \tag{5.90}$$

and $H_{\rm GR}$ represents GR precession.

Since $H_{\rm M}$ is a function of radius only it can only perturb the argument of periapsis. By assumption in the reverse-Kozai effect the precession due to GR dominates and so this term is unimportant and is ignored here.

Averaging the perturbational Hamiltonian over an orbit

$$\overline{\Delta H} = \overline{H_{\rm Q}} + \overline{H_{\rm M}} + \overline{H_{\rm GR}} \tag{5.91}$$

where

$$\overline{H_{\rm GR}} = -\frac{3G^2M^2}{c^2a^2}(1-e^2)^{-1/2}\,. \tag{5.92}$$

For simplicity GR precession has been included to first PN order. Aligning the z-axis with the secondary (and thus the orbital elements) then

$$\cos\theta = \sin i\,\sin(\psi+\omega) \tag{5.93}$$

where i is the inclination, ω the argument of periapsis, and ψ the true anomaly. Averaging over an unperturbed orbital period, $P = 2\pi\sqrt{\frac{a^3}{GM}}$,

$$\overline{H_{\rm Q}} = \frac{1}{P}\int_0^\tau dt\, H_{\rm Q} \tag{5.94}$$

changing variables using $\dot{\psi}r^2 = (GMa)^{1/2}\ell$ where $\ell^2 = 1-e^2$ gives

$$\begin{aligned}
\overline{H_{\rm Q}} &= \frac{GMq}{2P\ell r_2^3}\int_0^{2\pi} d\psi\, r^4\,(3\sin^2 i\sin^2(\psi+\omega)-1)\\
&= \frac{GMq}{2P(GMa)^{1/2}\ell r_2^3}\int_0^{2\pi} d\psi\,\frac{a^4(1-e^2)^4}{(1+e\cos\psi)^4}\left[3\sin^2 i\sin^2(\psi+\omega)-1\right]\\
&= \frac{GMqa^2}{8r_2^3}\left\{6\ell^2-10+3[5-3\ell^2+5(\ell^2-1)\cos(2\omega)]\sin^2 i\right\}\,.
\end{aligned} \tag{5.95}$$

Following Merritt et al. (2011a) we define the dimensionless time, $\tau = \nu_0 t$, where

$$\nu_0 = \nu_r\frac{3GM}{c^2a} \tag{5.96}$$

and ν_r is the radial frequency given by $\nu_r = \sqrt{GM/a^3}$. This gives the dimensionless perturbing Hamiltonian

$$\begin{aligned}
\overline{\Delta H'} &\equiv \frac{\overline{\Delta H}}{\nu_0(GMa)^{1/2}}\\
&= -(1-e^2)^{-1/2} + A_{\rm Q}\ell^2\left\{6\ell^2-10+3[5-3\ell^2+5(\ell^2-1)\cos(2\omega)]\sin^2 i\right\}\\
&= -\ell^{-1} + A_{\rm Q}\left\{6\ell^2-10+3[5-3\ell^2+5(\ell^2-1)\cos(2\omega)]\sin^2 i\right\}
\end{aligned} \tag{5.97}$$

where

$$A_{\rm Q} \equiv \frac{qc^2a^4}{24GMr_2^3}\,. \tag{5.98}$$

For our example star $A_{\rm Q}$ is approximately 10. Note that this is just the usual Kozai perturbing potential with the addition of a term due to GR precession (e.g., Innanen et al., 1997). There are two

key differences: *i)* In the case of Kozai oscillations the orbital reference plane is the orbital plane of the binary, while here the reference plane is perpendicular to the instantaneous position of the secondary. *ii)* There is an additional term due to GR precession which dominates the precession rate for high eccentricities.

Calculating the secular changes in the orbit using this potential gives

$$\begin{aligned}
\frac{\partial\omega}{\partial\tau} &= \frac{\partial(\overline{\Delta H'})}{\partial\ell} \\
&= \ell^{-2} + 6A_{\rm Q}\ell\left\{2 + [5\cos(2\omega) - 3]\sin^2 i\right\} && (5.99)\\
\frac{\partial\ell}{\partial\tau} &= -\frac{\partial(\overline{\Delta H'})}{\partial\omega} \\
&= -30A_{\rm Q}(\ell^2 - 1)\sin(2\omega)\sin^2 i && (5.100)\\
\frac{\partial\Omega}{\partial\tau} &= -\frac{\partial(\overline{\Delta H'})}{\partial\ell_z} \\
&= 6A_{\rm Q}[5 - 3\ell^2 + 5(\ell^2 - 1)\cos(2\omega)]\frac{\cos i}{\ell} && (5.101)\\
\frac{\partial\ell_z}{\partial\tau} &= -\frac{\partial(\overline{\Delta H'})}{\partial\Omega} = 0 && (5.102)
\end{aligned}$$

For small ℓ when the GR precession dominates then

$$\frac{\partial\omega}{\partial\tau} \approx \ell^{-2} \tag{5.103}$$

If we further assume that changes in ℓ are small then

$$\begin{aligned}
\omega &= \langle\ell\rangle^{-2}\,\tau && (5.104)\\
\ell &= \langle\ell\rangle - 15A_{\rm Q}\langle\ell\rangle^2\sin(2\tau/\langle\ell\rangle^2)\sin^2 i && (5.105)\\
\Omega &= \langle\Omega\rangle + 30A_{\rm Q}(1-e)^{1/2}\sin(2\tau/\langle\ell\rangle^2)\cos i && (5.106)
\end{aligned}$$

where $\langle\ell\rangle$ is the mean angular momentum over a cycle. The precise meaning of small changes in ℓ are that we have assumed $\langle\ell\rangle \gg \ell_+ - \ell_-$ where ℓ_+ and ℓ_- are the maximum and minimum angular momenta given by

$$\ell_+ - \ell_- = 15A_{\rm Q}\langle\ell\rangle^2\sin^2 i \tag{5.107}$$

Hence for our solution to be valid we require

$$\begin{aligned}
\langle\ell\rangle \gg \ell_+ - \ell_- &= 15A_{\rm Q}\langle\ell\rangle^2\sin^2 i && (5.108)\\
\rightarrow \langle\ell\rangle &\ll \left(15A_{\rm Q}\sin^2 i\right)^{-1} && (5.109)
\end{aligned}$$

which is satisfied when the GR precession dominates as shown by equation (5.99).

Finally we can rewrite the solution in terms of eccentricity

$$\omega = \frac{\nu_{\rm RK}}{2} t \tag{5.110}$$

$$1 - e = \langle 1 - e \rangle - (e_+ - e_-) \sin \nu_{\rm RK} t \tag{5.111}$$

where

$$\nu_{\rm RK} = \frac{6GM}{c^2 a(1-e^2)} \sqrt{\frac{a^3}{GM}} \tag{5.112}$$

$$\approx \frac{r_p}{3r_g} \sqrt{\frac{a^3}{GM}}\,, \tag{5.113}$$

$$e_+ - e_- = 15 A_{\rm Q} \langle \ell \rangle^3 \sin^2 i \tag{5.114}$$

$$\frac{e_+ - e_-}{1-e} \approx 30 A_{\rm Q} \langle \ell \rangle \sin^2 i \tag{5.115}$$

$$= \frac{5\sqrt{2}}{4} \frac{q c^2 a^4}{GM r_2^3} (1-e)^{1/2} \sin^2 i \tag{5.116}$$

The period of oscillation is

$$P_{\rm RK} = \frac{2\pi}{\nu_{RK}} \approx \frac{2\pi r_p}{3r_g} \sqrt{\frac{GM}{a^3}} = \frac{r_p}{3r_g} P_\star\,. \tag{5.117}$$

In figures 5.20 and 5.21 we show an artificial test designed to test the reverse-Kozai effect derived here, while in figure 5.22 we show an actual simulated star which is undergoing the reverse-Kozai effect.

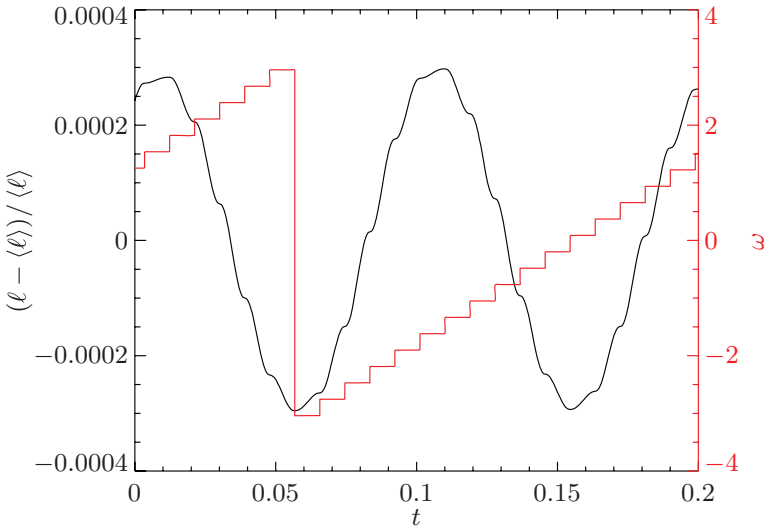

Figure 5.20 Simulation illustrating the reverse-Kozai effect. Parameters used are $q = 0.1$, $r_2 = 1$, $a = 0.01$, $\langle\ell\rangle = 0.001$. As expected there are two oscillations over each cycle in ω due to the quadrupole nature of the perturbation. Note the discrete nature of the precession of the argument of periapsis, ω, at each periapsis passage where GR becomes significant.

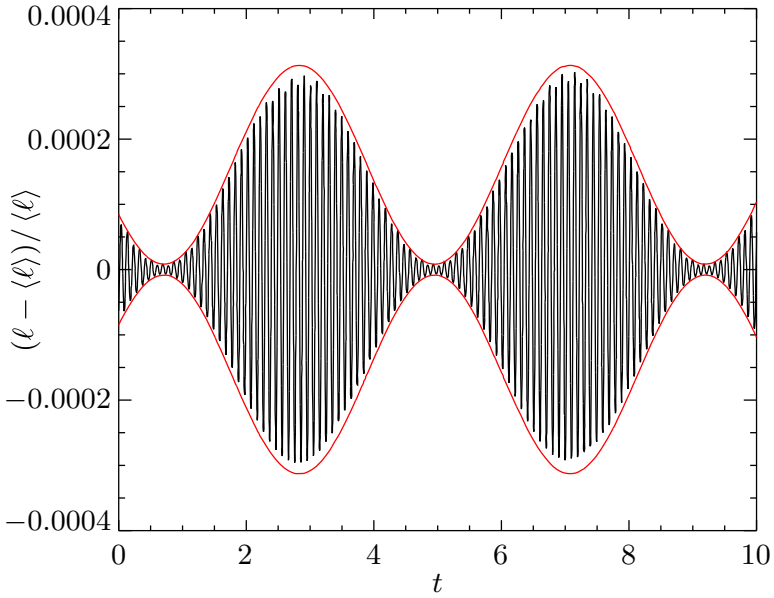

Figure 5.21 Simulation as figure 5.20 but over a longer period. As the secondary orbits the inclination of the test particle's orbit relative to it changes and this alters the amplitude of the oscillations. The envelope of the oscillations predicted by equation (5.107) is shown in red.

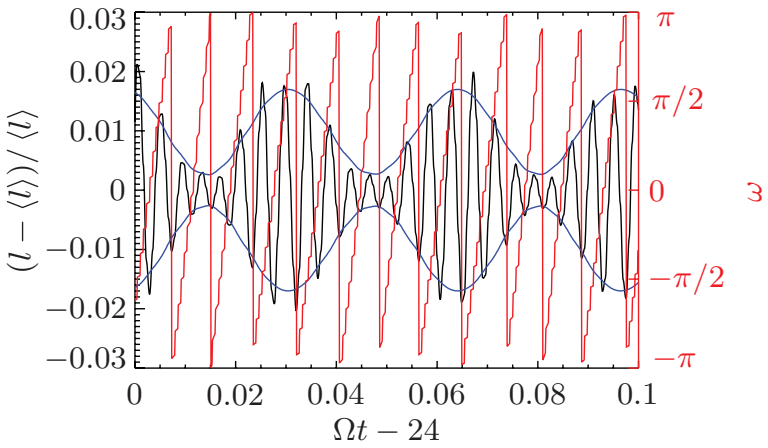

Figure 5.22 Star from simulation S1 simulation demonstrating the reverse-Kozai effect. Note the two oscillations over each cycle in ω due to the quadrupole nature of the perturbation. The envelope of the oscillation predicted by equation (5.107) is shown in blue.

Appendix 5.C Selected Parameter Space Plots

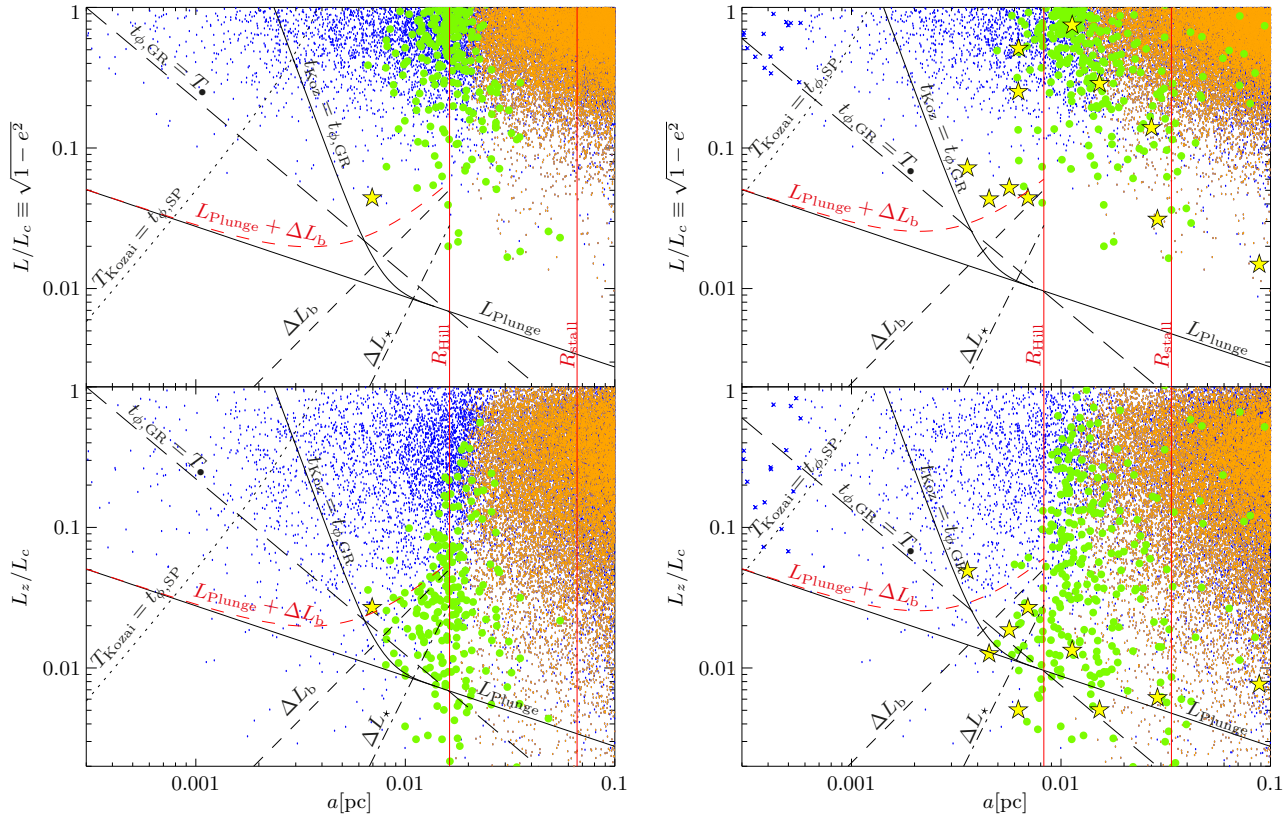

(a) Results of S2 ($q = 0.3$, $M_\star = 1$) simulation.

(b) Results of S3 ($q = 0.1$, $M_\star = 10$) simulation.

Figure 5.23 Parameter space plot showing outcomes as function of normalized angular momentum and semi-major axis along with important delimiting lines (described in section 5.4). Initial L/L_c and L_z/L_c are plotted in the upper and lower panels, respectively. Each star is represented by its outcome: an EMRI (gold star), a plunge (green dot), becoming unbound (orange dot), reaching the limit of 10^{10} steps (blue cross) or remaining in the cusp at the conclusion of our simulation (blue dot).

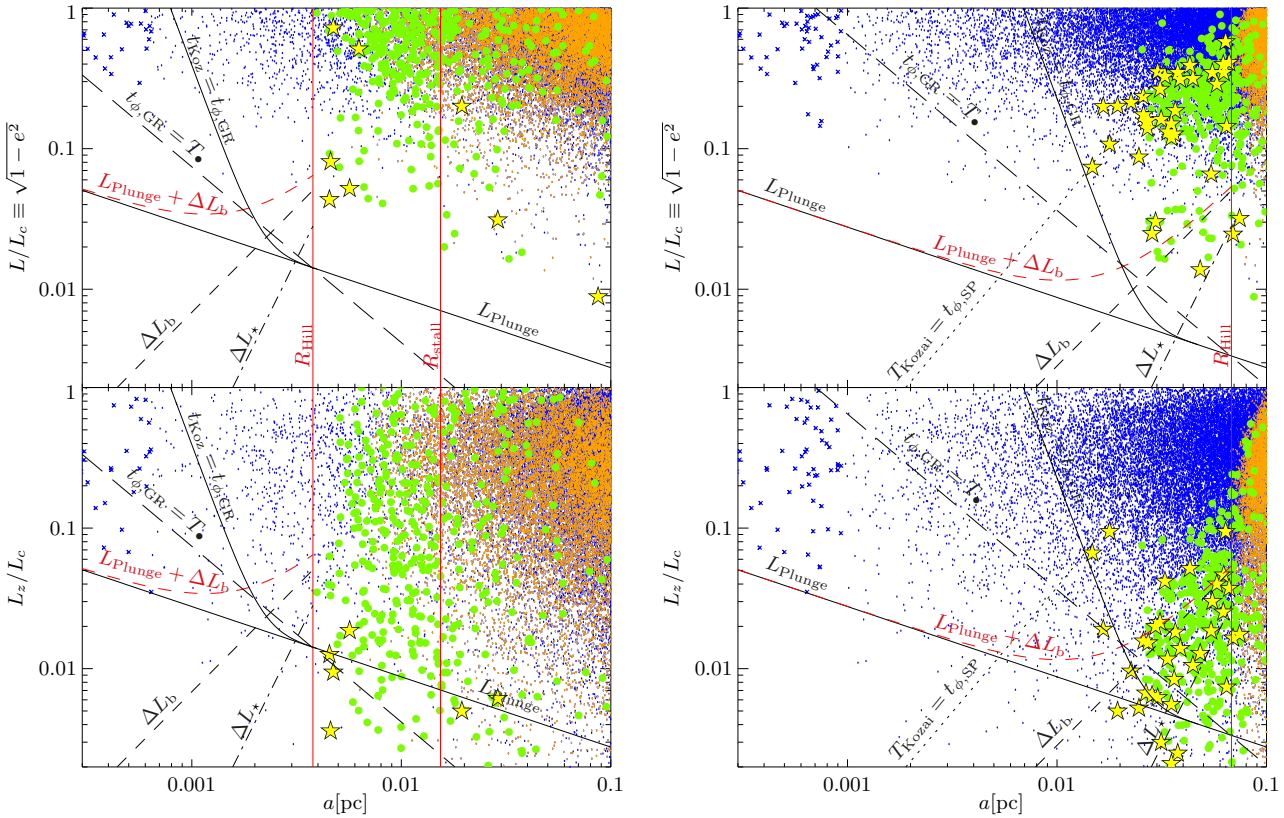

(a) Results of S5 ($q = 0.03$, $M_\star = 10$) simulation.

(b) Results of S7 ($q = 0.6$, $M_\star = 10$) simulation.

Figure 5.24 As figure 5.23 for simulations S5 and S7.

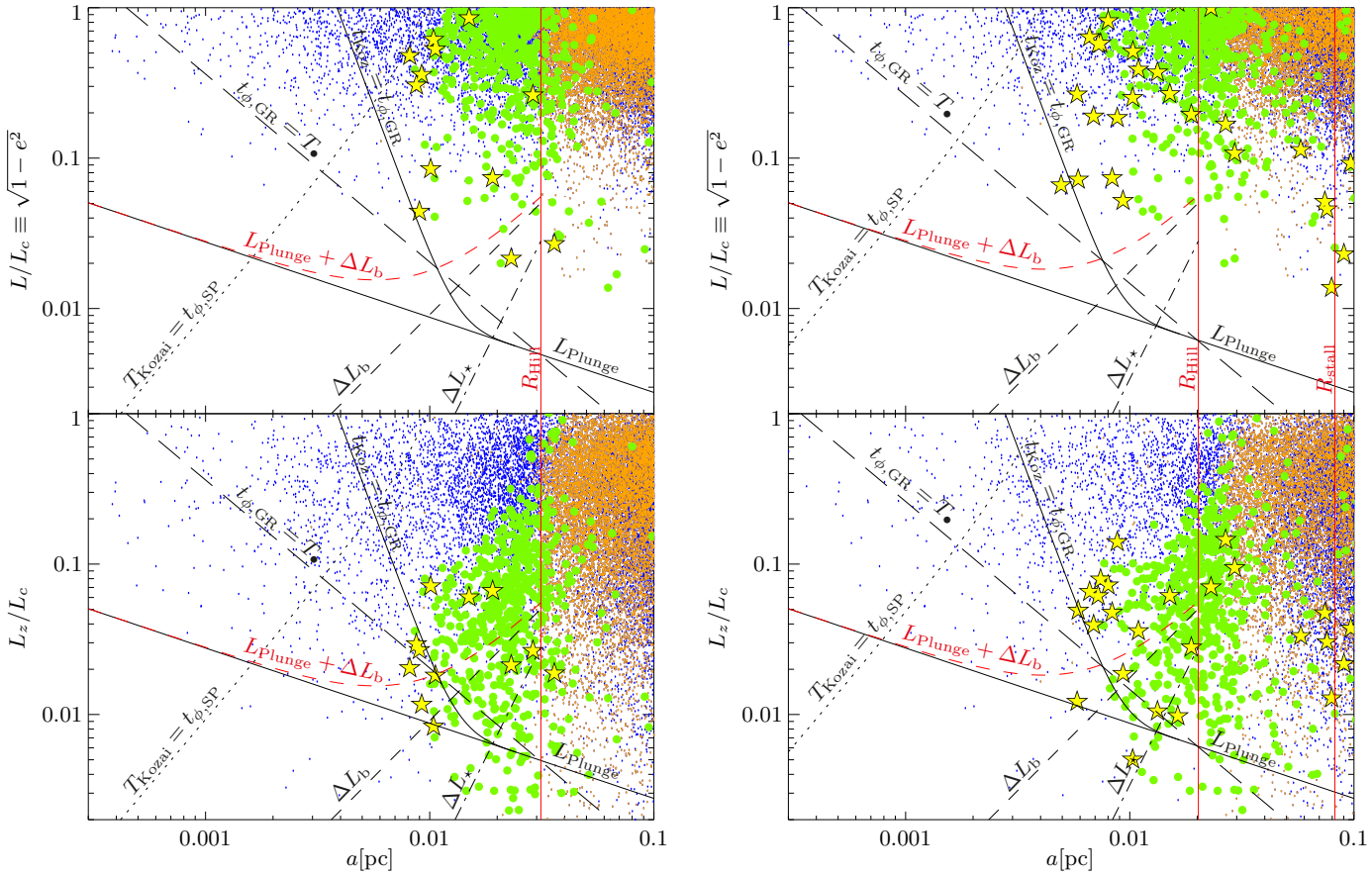

(a) Results of S9 ($q = 10/3$, $M_\star = 10$) simulation.

(b) Results of S11 ($q = 10$, $M_\star = 10$) simulation.

Figure 5.25 As figure 5.23 for simulations S9 and S11.

Appendix 5.D Example Integrations of 'Interesting Stars'

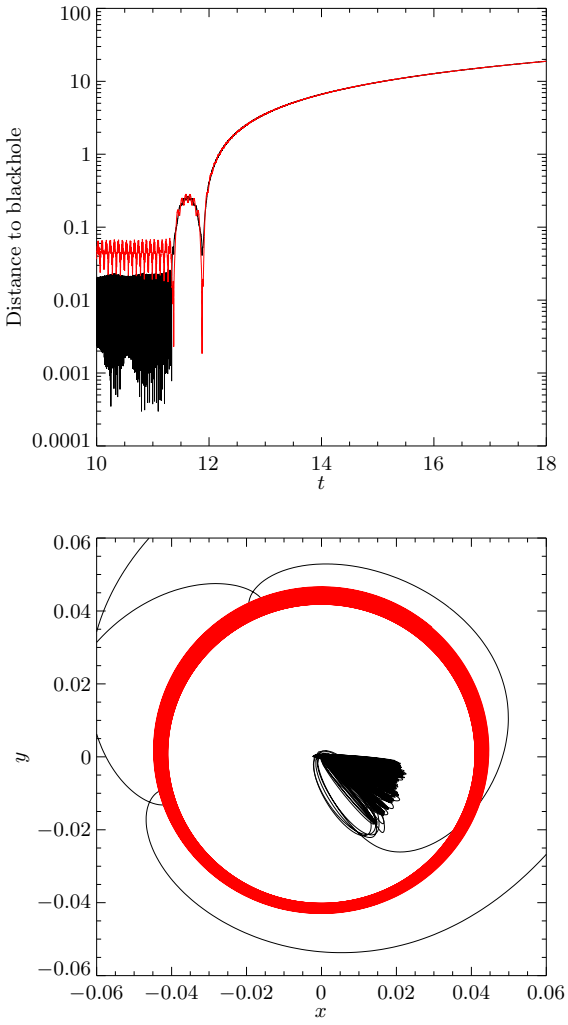

Figure 5.26 Illustration of a star becoming unbound after a Kozai oscillation. The upper plot shows the distance between the star and each hole, the primary SMBH in black, and secondary in red. The lower plot shows the projection onto the x-y plane, in primary centered coordinates, of the stellar orbit in black, and the secondary SMBH orbit in red. The star has small L_z and at peak eccentricity over a Kozai oscillation this star has an apoapsis which lies close to the secondary. It undergoes a strong interaction, and is ejected. The peak in eccentricity occurs when L_x and L_y are small and the orbit lies in the plane of the secondary, thus the chance of a close secondary encounter during this period is high.

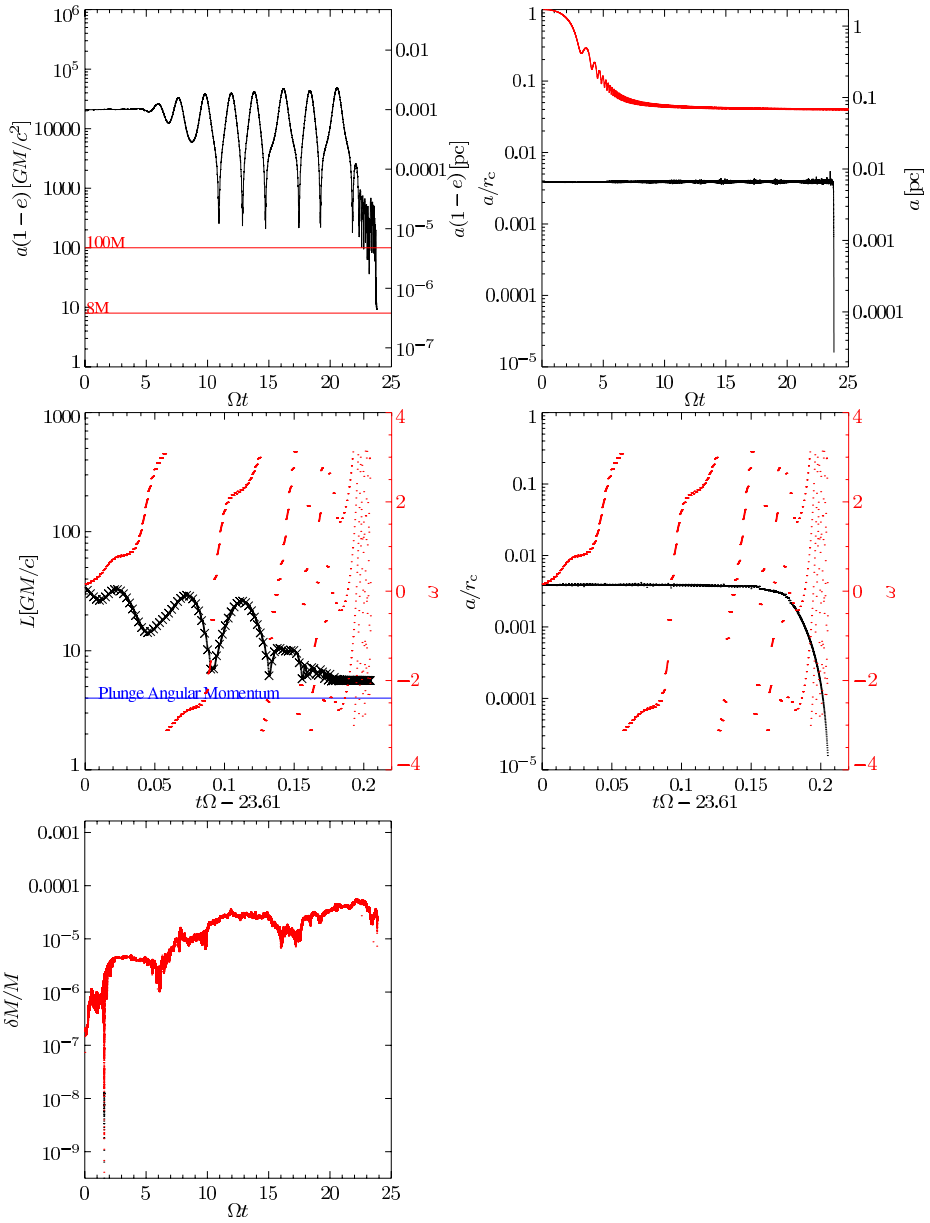

Figure 5.27 Example EMRI from simulation S1. In the upper-left we plot $a(1-e)$ which is a proxy for periapsis distance, in this plot the event horizon is at $8\,M$ and stars that pass inside $100\,M$ have the prescription for gravitational radiation losses applied. Kozai oscillations are clearly present in this plot, appearing as the binary inspirals. The upper-right panel shows the evolution of the semi-major axis (in black) and the binary separation (in red). Note the decreasing semi-major axis at the end of the integration as the star becomes an EMRI. The middle panels zoom in on this EMRI formation region. The left panel plots the stars angular momentum L in black, each periapsis passage is marked with a cross. In red is the argument of periapsis, plotted on the right axis. The right-hand middle plot shows the semi-major axis decreasing as an EMRI is formed. The lower-left panel shows the fractional integration error defined by $\frac{\delta M}{M} \equiv \frac{p_0+T+U}{p_0}$. We choose this representation of errors since with no integration error then $p_0 = -H = -T - U$. Peter (2009) shows that in Keplerian orbits errors in p_0 cause the equations of motion to still be Keplerian, but with increased mass $M + \delta M$.

6 Pseudo-Newtonian Potentials for Nearly Parabolic Orbits[1]

Abstract

We describe a pseudo-Newtonian potential which, to within 1% error at all angular momenta, reproduces the precession due to general relativity of particles whose specific orbital energy is small compared to c^2 in the Schwarzschild metric. For bound orbits the constraint of low energy is equivalent to requiring the apoapsis of a particle to be large compared to the Schwarzschild radius. Such low-energy orbits are ubiquitous close to supermassive black holes in galactic nuclei, but the potential is relevant in any context containing particles on low-energy orbits. Like the more complex post-Newtonian expressions, the potential correctly reproduces the precession in the far-field, but also correctly reproduces the position and magnitude of the logarithmic divergence in precession for low angular momentum orbits. An additional advantage lies in its simplicity, both in computation and implementation. We also provide two simpler, but less accurate potentials, for cases where orbits always remain at large angular momenta, or when the extra accuracy is not needed. In all of the presented cases the accuracy in precession in low-energy orbits exceeds that of the well known potential of Paczyński and Wiita (1980), which has $\sim 30\%$ error in the precession at all angular momenta.

[1]This work was published as ApJ, 749, 183 (2012) , arXiv:1202.5336 with Christopher Wegg as the sole author (Wegg, 2012). Reproduced here by permission of the AAS, copyright © (2012).

Table 6.1 Coefficients for the potentials $U(r) = -\alpha M/r - (1-\alpha)M/(r-R_x) - MR_y/r^2$ (equation 6.1) described in this work.

Potential	α	R_x/M	R_y/M	Precession error $r \gg M$	Precession error Maximum	Diverges at $h = 4M$?
A	1	—	3	0	No	100%[a]
B	0	5/3	4/3	0	Yes	$< 30\%$
C	$\frac{-4}{3}\left(2+\sqrt{6}\right)$	$\left(4\sqrt{6}-9\right)$	$\frac{-4}{3}\left(2\sqrt{6}-3\right)$	0	Yes	$< 1\%$
PW[b]	0	2	0	33%	Yes	33%

[a] Does not diverge at $h = 4M$
[b] Paczyński-Wiita

6.1 Introduction

Pseudo-Newtonian potentials that modify the Newtonian gravitational potential have a long history of use in astrophysics. While general relativity is now well understood in the astrophysics community, pseudo-Newtonian potentials are still useful in approximating relativistic effects in simpler and faster Newtonian simulations. The potential of Paczyński and Wiita (1980) is often used in the study of accretion onto relativistic objects. In this regime the Paczyński-Wiita potential often gives results close to those using full GR since it correctly reproduces the location of the inner most stable circular orbit (ISCO) and the marginally bound orbit as well as being a good approximation to the binding energy at the ISCO (for a review see Abramowicz, 2009).

Here we propose a series of Newtonian potentials with a different aim: to correctly reproduce the precession produced by general relativity in the Schwarzschild metric for test particles whose apoapsis lies far from the hole, i.e., in the nonrelativistic region. The Paczyński-Wiita potential has been used in this context multiple times (e.g., Chen et al., 2011), despite its key properties of closely reproducing the location and energy of the ISCO being unimportant in this regime. Instead, we propose alternative potentials that are more accurate and physically relevant for these orbits. We have used them to simulate galactic dynamics around supermassive black holes (SMBHs) in Bode and Wegg (2012). The primary concern in that context was to ensure that stars passing close to the black hole exited along the correct trajectories. These potentials are likely to be useful in other contexts, motivating the brief presentation here. Throughout this chapter we use geometrized units where $G = c = 1$.

6.2 Summary of Proposed Potentials

We present three new pseudo-Newtonian potentials in this paper. All of these potentials, and the potential of Paczyński and Wiita (1980), can be written in the form

$$U(r) = -\frac{\alpha M}{r} - \frac{(1-\alpha)M}{r-R_x} - \frac{MR_y}{r^2}\,. \tag{6.1}$$

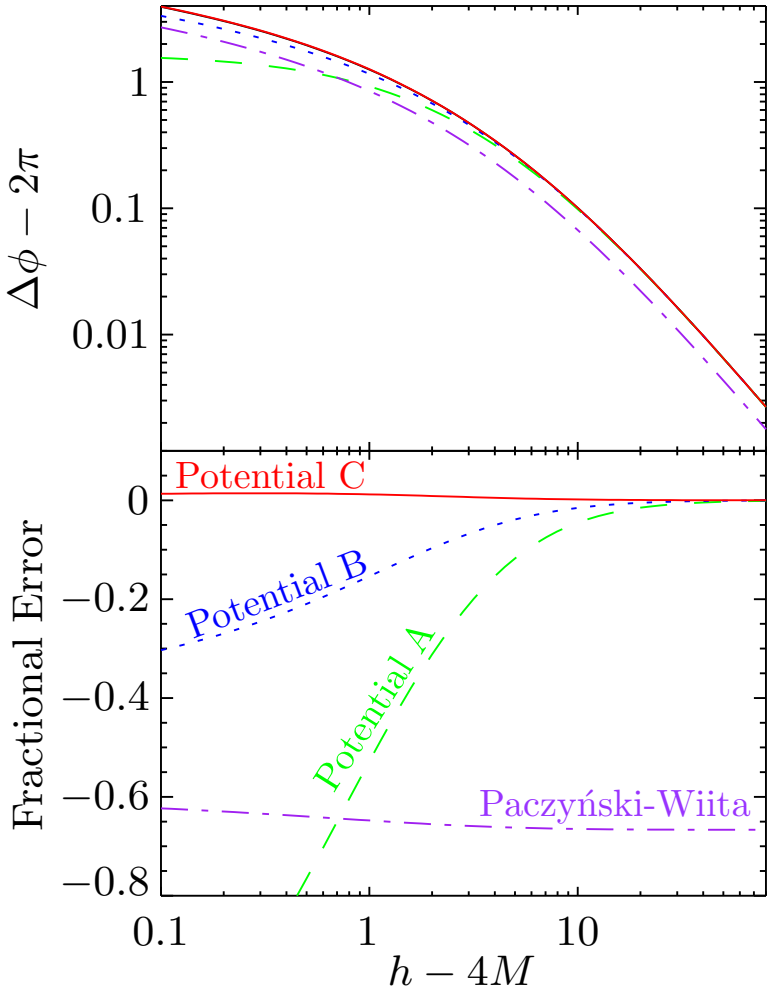

Figure 6.1 Comparison of the precession per orbit produced by the proposed potentials with the GR expression for parabolic orbits as a function of specific angular momentum, h. The labeled potentials are described in table 6.1. The GR precession is shown by a solid black line (in the upper panel the precession produced by potential C lies almost on top of the GR expression). In the lower panel we plot the fractional error relative to the relativistic precession, defined to be $(\Delta\phi - \Delta\phi_{\rm GR})/(\Delta\phi_{\rm GR} - 2\pi)$.

where the values of the coefficients α, R_x and R_y for the potentials are summarized in table 6.1. We choose potentials of this form since the presence of the $1/r^2$ term allows the far-field behavior to reproduced, while the $1/(r - R_x)$ term allows reproduction of the divergent behavior as the specific angular momentum approaches $4\,M$. The resultant precession per orbit is compared to the GR value in figure 6.1. In what follows we justify these choices.

6.3 Approach To Calculating Proposed Potentials

6.3.1 Precession Due to General Relativity

In general relativity the change in azimuthal angle of a test particle between two consecutive apoapsides on a geodesic in the Schwarzschild metric is given by (e.g., Equation 25.42 of Misner et al., 1973)

$$\Delta\phi_{\rm GR} = 2\int_{r_-}^{r_+}\left[\frac{(E+1)^2}{h^2} - \left(\frac{1}{h^2}+\frac{1}{r^2}\right)\left(1-\frac{2M}{r}\right)\right]^{-1/2}\frac{dr}{r^2}\,, \tag{6.2}$$

where E is the specific energy of the particle without rest mass energy (i.e., $E \equiv -p_0/\mu - 1$ where μ is the particles mass), h is the specific angular momentum (i.e., $h = p_\phi/\mu$), and $r_\pm$ are the radii of periapsis ($-$) and apoapsis ($+$) given by the two largest roots of the equation

$$(E+1)^2 - \left(1-\frac{2M}{r_\pm}\right)\left(1+\frac{h^2}{{r_\pm}^2}\right) = 0\,. \tag{6.3}$$

For our 'nearly parabolic orbits' ($E \ll 1$) the precession due to relativity is a function only of the angular momentum. Unless otherwise noted in this paper we work in the limit that $E = 0$.

6.3.2 Precession due to Newtonian Central Potential

By comparison, in classical mechanics the change in azimuthal angle for a test particle of any energy between two consecutive apoapsides in a central potential, $U(r)$, is given by (e.g., Landau and Lifshitz, 1969)

$$\Delta\phi_{\rm Newt.} = 2\int_{r_-}^{r_+}\left[\frac{E-U(r)}{h^2/2} - \frac{1}{r^2}\right]^{-1/2}\frac{dr}{r^2}\,, \tag{6.4}$$

where in this case $r_\pm$ are given by

$$2(E - U(r_\pm)) - \frac{h^2}{{r_\pm}^2} = 0\,. \tag{6.5}$$

6.3.3 Requirements of Proposed Pseudo-Newtonian Potentials

In principle it is possible to define a pseudo-Newtonian potential, $U(r)$, such that the precession angles given by equations (6.2) and (6.4) are equal in the limit $E \ll 1$, i.e.,

$$\Delta\phi_{\rm GR}(h) = \Delta\phi_{\rm Newt.}(h)\,. \tag{6.6}$$

This potential would have the property desired: on returning to large radii, test particles would have precessed through the correct angle, and be traveling along the correct path with only a time error. However, we also desire a simple potential for efficient calculation and so instead we seek potentials that minimize the precession error, $\delta\phi$, defined through

$$\delta\phi(h) = \Delta\phi_{\rm GR}(h) - \Delta\phi_{\rm Newt.}(h)\,. \tag{6.7}$$

We propose three potentials that, in order of complexity, minimize $\delta\phi$: *A*) in the far-field (large h) ; *B*) in the far-field *and* whose precession diverges logarithmically in the same location as GR ($h \to 4M$); and *C*) in the far-field, and whose precession diverges logarithmically as $h \to 4M$ *with the correct magnitude*.

6.4 Proposed Pseudo-Newtonian Potentials

6.4.1 Potential A: Matching The far-field Precession

In this section we consider the behavior of orbits with $h \gg 4M$, but we do not require $E = 0$, only that $E \ll 1$. In this case, inspection of equation (6.3) shows $r_\pm \gg M$ and the entire orbit lies in the far-field.

The change in angle in the far-field in GR can be calculated from equation (6.2) and is well known to be (e.g., Weinberg, 1972)

$$\Delta\phi_{\rm GR}(h) = 2\pi + \frac{6\pi M^2}{h^2} \quad \text{for} \quad h \gg 4M\,. \tag{6.8}$$

Note that all that is required is a sufficiently distant periapse. It is not required that the orbit have $E = 0$.

In the far-field we require potentials have the form

$$U(r) = -\frac{M}{r} - \frac{MR_y}{r^2} + O(r^{-3})\,. \tag{6.9}$$

Neglecting the terms $O(r^{-3})$ and higher, after some algebra, the precession calculated from equa-

tion (6.4) is

$$\Delta\phi_{\text{Newt.}}(h) = 2\int_{r_-}^{r_+}\left[\frac{2r_h a}{(r-r_-)(r_+-r)}\right]^{1/2}\frac{dr}{r}\,, \tag{6.10}$$

where $r_h \equiv h^2/2M$, $a \equiv -M/2E$, and

$$r_\pm = a\left[1 \pm \sqrt{1-\frac{2}{a}(R_y - r_h)}\right]. \tag{6.11}$$

Contour integration gives the integral

$$\begin{aligned}\Delta\phi_{\text{Newt.}}(h) &= 2\pi\left(1-\frac{R_y-a}{r_h}\right)^{-1/2}\\ &= 2\pi + \frac{2\pi M R_y}{h^2} + O(a/r_h)\,.\end{aligned} \tag{6.12}$$

Provided that $h \gg M$ and $E \ll 1$, then the final term can be dropped and matching the far-field precession given by equation (6.8) requires $R_y = 3M$.

When concerned with the far-field precession we therefore propose the pseudo-Newtonian potential

$$U(r) = -\frac{M}{r}\left(1+\frac{3M}{r}\right) \tag{6.13}$$

which requires only modest additional computation over the Newtonian expression. Note that this pseudo-Newtonian potential gives the correct precession for *all* orbits (parabolic, eccentric, or hyperbolic), provided that the periapse lies in the far-field. The resultant precession, labeled as potential A, is plotted in figure 6.1.

Since this potential does not reproduce the divergence as $h \to 4M$ this potential performs worse than the Paczyński-Wiita potential, even for parabolic orbits, when $h \lesssim 4.8M$ which corresponds to periapsis separation of $r \lesssim 8.5M$. For reference $h = 4M$ corresponds to periapsis separation $r = 5M$ for parabolic orbits in this potential.

6.4.2 Potential B: Logarithmic Divergence As $h \to 4M$

In this section we construct a potential that reproduces the logarithmic divergence of the general relativistic precession as $h \to 4M$.

First consider a potential of the form

$$U(r) = -\frac{M}{r-R_x}\,. \tag{6.14}$$

The precession in this potential for $E = 0$ is given by

$$\Delta\phi_{\text{Newt.}}(h) = 2\int_{r_-}^{\infty}\left[\frac{r^2}{r_h(r-R_x)} - 1\right]^{-1/2}\frac{dr}{r}\,. \tag{6.15}$$

The roots of the quadratic form in the integrand can be written as

$$r_{p,q} = \frac{r_h}{2}\left(1 \pm \sqrt{1 - \frac{4R_x}{r_h}}\right). \tag{6.16}$$

so that

$$\Delta\phi_{\text{Newt.}}(h) = 2\int_{r_p}^{\infty}\left[\frac{r_h(r-R_x)}{(r-r_p)(r-r_q)}\right]^{1/2}\frac{dr}{r}\,. \tag{6.17}$$

As $r_h \to 4R_x$, then $r_p \to r_q$ and the integral diverges logarithmically. $r_h \to 4R_x$ corresponds to $h \to \sqrt{8MR_x}$ and the leading order behavior of the integral is

$$\lim_{r_h \to 4R_x^+}\Delta\phi_{\text{Newt.}}(h) = -\log\left(h - \sqrt{8MR_x}\right). \tag{6.18}$$

A similar calculation using the GR expression gives a logarithmic divergence as $h \to 4M$ and the corresponding expression is

$$\lim_{h\to 4M^+}\Delta\phi_{\text{GR}}(h) = -\sqrt{2}\log\left(h - 4M\right). \tag{6.19}$$

For $\Delta\phi_{\text{Newt.}}$ to diverge at $h = 4M$, we must have $R_x = 2M$. This is exactly the potential of Paczyński and Wiita (1980), which therefore diverges at the correct angular momentum. However comparing equations (6.18) and (6.19), the potential of Paczyński and Wiita (1980) has the incorrect magnitude (by a factor of $\sqrt{2}$) as the angular momentum approaches $4M$, and as noted previously, has incorrect precession in the far-field.

To correct the far-field behavior consider the potential

$$U(r) = -\frac{M}{r - R_x} - \frac{MR_y}{r^2}\,. \tag{6.20}$$

The calculation of the precession proceeds in the same manner, but with the roots now given by

$$r_{p,q} = \frac{r_h - R_y}{2}\left(1 \pm \sqrt{1 - \frac{4R_x}{r_h - R_y}}\right). \tag{6.21}$$

Again, as the roots coincide the integral diverges logarithmically. Requiring that the divergence occurs as $h \to 4M$ and that the potential has the correct far-field limit (i.e., far from the hole the

expansion is given by equation (6.9) with $R_y = 3M$) gives $R_x = 5M/3$ and $R_y = 4M/3$. Our proposed potential which has the correct precession in the far-field and which also logarithmically diverges as $h \to 4M$ is therefore

$$U(r) = -\frac{M}{r}\left(\frac{1}{1 - 5M/3r} + \frac{4M}{3r}\right). \tag{6.22}$$

The resultant precession, labeled as potential B, is shown in figure 6.1. This is the potential used in Bode and Wegg (2012). For reference $h = 4M$ corresponds to periapsis separation $r = 10M/3$ for parabolic orbits in this potential.

6.4.3 Potential C: Correct Rate Of Logarithmic Divergence As $h \to 4M$

The potential proposed in equation equation (6.22), has the correct far-field behavior, and diverges logarithmically at the correct angular momentum. However, the rate of that divergence is incorrect: The behavior of the integral as $h \to 4M$ is

$$\lim_{h \to 4M^+} \Delta\phi_{\text{Newt.}}(h) = -\sqrt{\frac{6}{5}} \log\left(h - 4M\right), \tag{6.23}$$

which does not match the GR expression in equation equation (6.19).

An additional term in the potential allows this to rectified. Using a potential of the form

$$U(r) = -\frac{\alpha M}{r} - \frac{(1-\alpha)M}{r - R_x} - \frac{MR_y}{r^2}, \tag{6.24}$$

enables us to match the three constraints for the three coefficients α, R_x and R_y. The constraints on the coefficients are that: *1*) in the far-field the precession approaches equation (6.8) (i.e., equation 6.9 with $R_y = 3M$), *2*) the integral diverges logarithmically as $h \to 4M$, and *3*) the rate of divergence as $h \to 4M$ is given by equation equation (6.19). The values of α, R_x and R_y satisfying these constraints are

$$\begin{aligned} \alpha &= \frac{-4}{3}\left(2 + \sqrt{6}\right), \\ R_x &= \left(4\sqrt{6} - 9\right)M, \\ R_y &= \frac{-4}{3}\left(2\sqrt{6} - 3\right)M. \end{aligned} \tag{6.25}$$

The precession produced by this "potential C" is compared to the GR expression in figure 6.1. For reference $h = 4M$ corresponds to periapsis separation of $r = 2(\sqrt{6} - 1)M$ for parabolic orbits in this potential.

This potential produces precession which agrees with GR to within 1% for *all* orbits where $E \ll 1$, i.e., whose specific orbital energy is small compared to c^2 in the Schwarzschild metric. For

bound orbits this corresponds to requiring apoapsis be large compared to the Schwarzschild radius ($r_+ \gg M$).

6.5 Conclusions

We have proposed three pseudo-Newtonian potentials appropriate for 'nearly parabolic orbits' (orbital energy, $E \ll 1$) around a Schwarzschild black hole. These nearly parabolic orbits correspond to orbits with large apoapsis compared to the Schwarzschild radius of a central black hole, or mildly hyperbolic orbits.

For bodies which pass close to the black hole, these potentials accurately reproduce the changes in the "Newtonian" parts of the trajectories far from the black hole, differing from the exact GR expression only by a time error. In the far-field the time error as a fraction of the orbital period is of order $\delta P/P = O(E) \ll 1$ but diverges as $h \to 4M$ like $\delta P/P = O(E^{3/2} \log(h - 4M))$. Therefore, for $E \ll 1$, the fractional period error is small outside of an exponentially narrow region in h close to $4M$.

The potentials reproduce general relativistic precession with varying degrees of accuracy and simplicity. Namely, these potentials produce accurate relativistic precession: (Potential A) in the far-field (equation 6.13); (Potential B) in the far-field *and* with the logarithmic divergence as $h \to 4M$ (equation 6.22); and (Potential C) in the far-field *and with the correct magnitude* of logarithmic divergence as $h \to 4M$ (equation 6.24).

The potentials described do not include the effects of spin, or gravitational radiation, which can be astrophysically important for orbits passing close to the hole. Neither of these effects can be described by a pseudo-Newtonian potential without the presence of undesirable inseparable terms including both r and v, and so were not considered in this work. For objects whose mass ratio with the black hole is sufficiently close to the test particle limit, the effects of gravitational radiation can be included by subtracting energy and angular momentum at periapsis, for example, using the results of Gair et al. (2006b).

Close to the black hole these potentials should be interpreted with care since although they diverge at the correct angular momentum, the r at which this occurs does not correspond to the Schwarzschild radial coordinate.

7

An Analytic Solution to the Fokker Planck Equation in the Singular Isothermal Sphere[1]

Abstract

We consider the relaxation of stars using the Fokker-Planck equation in a background singular isothermal sphere. Dimensional arguments suggest that a self-similar solution should exist and we derive this solution analytically. We also present a simple general solution. Many astrophysical systems display properties approaching the singular isothermal sphere over some part of their profile, and we expect our solution to be used as a stepping stone between order of magnitude relaxation arguments and full N-body simulations. In addition we expect our solution to be of use in testing the relaxation properties of N-body codes. We discuss the applicability of the solution to the radial distribution of sub-populations in Galactic globular clusters.

[1] A shortened version of this work will be submitted for publication in MNRAS with the following authors: Christopher Wegg and Sterl Phinney in this order.

7.1 Introduction

The singular isothermal sphere is the simplest potential-density pair, i.e., the solution of *both* equations (1.21) and (1.22). The singular isothermal sphere is reviewed in section 7.3 however in order to understand the motivation for this work all that is required is that the density declines everywhere as $\propto r^{-2}$. The singular isothermal sphere is therefore scale-free, characterized only by the density at some fiducial radius (or equivalently the velocity dispersion). Consider then releasing a number of test stars into the singular isothermal sphere.

A priori we expect some properties from the manor in the which the stellar distribution evolves:

- That there is a characteristic relaxation time at each radius, $t_{\rm relax}$. This relaxation time can be estimated to be (e.g., equation 4-9 of Binney and Tremaine, 2008)

$$t_{\rm relax} \sim N_{\rm stars} \times t_{\rm cross} \sim \rho r^3 \times \frac{r}{\sigma} \sim \frac{\sigma r^2}{Gm} \, . \tag{7.1}$$

- Therefore, at a time t, inside of a radius $r_{\rm relax} = \sqrt{\frac{Gm}{\sigma}t}$, the relaxation time is such that the stars will have approximately reached equipartition. In the case of equal mass stars the density of test stars is therefore proportional to that of the field stars: $\rho \propto r^{-2}$.

- Since the problem is scale-free we expect a self-similar solution to exist in the variable

$$\Theta = \frac{\sigma^2}{Gm}\frac{r^2}{t} = \frac{t_{\rm relax}}{t} \, . \tag{7.2}$$

These properties are summarized graphically in figure 7.1.

While the problem may appear to be excessively contrived to be of practical use this is not the case. Globular clusters are well described by King profiles, which are a method of truncating the (non-singular) lowered isothermal sphere at zero energy and hence making them finite. Therefore when sufficiently outside the core of the isothermal sphere, and inside the truncation radius, then the density closely resembles the singular isothermal sphere.

The radial distribution of objects has been used to infer information about the progenitors of a number of types of objects. For example the radial distribution of blue stragglers has been investigated on numerous occasions (e.g., Ferraro et al., 2004; Lanzoni et al., 2007a,b; Mapelli et al., 2006; Salinas et al., 2012) in attempts to determine between the competing formation scenarios of collisions, or mass transfer in a close binary. In addition the lack of radial distribution of extreme horizontal branch (EHB) stars by Rich et al. (1997) to argue against a dynamical origin.

In addition we expect the solution, owing to the its simplicity, to be useful in checking the correctness and accuracy of both Fokker-Planck and N-body codes.

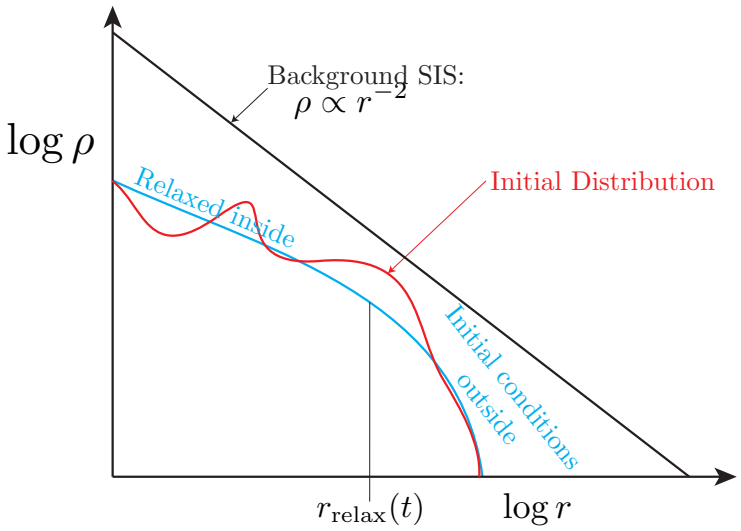

Figure 7.1 Illustration of the expected manor in which the stellar distribution evolves in a background of the singular isothermal sphere.

The work most closely related to that contained here is Merritt (2010) who considers 10 $M_\odot$ black holes as test particles that mass segregate in a background of lighter stars. The difference being that Merritt (2010) considers the distribution in the potential of a supermassive black hole surrounded by a Bahcall and Wolf (1976) cusp ($\rho \propto r^{-7/4}$), and is largely a numerical work.

7.2 Derivation of Energy Evolution Equation

Following King (1960) we first derive the evolution of the distribution function (i.e., the Fokker-Planck equation) in velocity space.

For the calculation of the diffusion coefficients in equations (1.26) and (1.27) we refer the reader to Rosenbluth et al. (1957). From equation (22) of Rosenbluth et al. (1957), equation (1.25) can be written in covariant form. Denoting the quantities relating to the field stars with a subscript b, and those relating to the test stars with subscript a, then

$$\Gamma^{-1}\partial_t f_a = -(f_a T^\mu)_{;\mu} + \frac{1}{2}(f_a S^{\mu\nu})_{;\mu\nu} \tag{7.3}$$

where $\Gamma = 4\pi G^2 m_b^2 \log\Lambda$ and

$$\begin{aligned} T_\mu &= h_{;\mu} \qquad S_{\mu\nu} = g_{;\mu\nu} \\ h(\vec{v}) &= \frac{m_a + m_b}{m_b} \int d\vec{v'} f_b(\vec{v'}) |\vec{v} - \vec{v'}|^{-1} \\ g(\vec{v}) &= \int d\vec{v'} f_b(\vec{v'}) |\vec{v} - \vec{v'}| \end{aligned}$$

Using spherical polar coordinates in velocity space, i.e., $ds^2 = dv^2 + v^2 d\theta^2 + v^2 \sin^2\theta d\phi^2$, and assuming isotropy in both the field star and background star distributions then, $f_a = f_a(v)$ and $f_b = f_b(v)$ so that the only non-vanishing derivatives of the Rosenbluth potentials, f and g, are those with respect to v. This gives

$$\begin{aligned} T^v &= \partial_v h, \qquad T^\theta = 0, \qquad T^\phi = 0 \\ (f_a T^\mu)_{;\mu} &= v^{-2} \partial_v (v^2 f \partial_v h) \\ S^{vv} &= \partial_v^2 g, \qquad S^{\theta\theta} = -v^{-3} \partial_v g, \qquad S^{\phi\phi} = -v^{-3} \sin^{-2}\theta \partial_v g \\ S^{v\theta} &= S^{\theta v} = S^{v\phi} = S^{\phi v} = S^{\theta\phi} = S^{\phi\theta} = 0 \\ (f_a S^{\mu\nu})_{;\mu\nu} &= -2v^{-2} \partial_v (f_a \partial_v g) + v^{-2} \partial_v (f_a v^2 \partial_v^2 g) \end{aligned} \tag{7.4}$$

then

$$\Gamma^{-1} \partial_t f_a = v^{-2} \partial_v \left[-f_a v^2 \partial_v h + \frac{1}{2} \partial_v \left(f_a v^2 \partial_v^2 g \right) - f_a \partial_v g \right] \tag{7.5}$$

where g and h can be evaluated through

$$\begin{aligned} h(\vec{v}) &= \frac{m_a + m_b}{m_b} \int d\vec{v'} f_b(\vec{v'}) |\vec{v} - \vec{v'}|^{-1} \\ &= 2\pi \frac{m_a + m_b}{m_b} \int_0^\infty v'^2 f(v') dv' \int_{-1}^1 \frac{d(\cos\theta)}{(v^2 + v'^2 - 2vv'\cos\theta)^{1/2}} \\ &= 4\pi \frac{m_a + m_b}{m_b} \left[\int_0^v dv' \frac{v'^2}{v} f_b(v') + \int_v^\infty dv' v' f_b(v') \right] \end{aligned} \tag{7.6}$$

$$\begin{aligned} g(\vec{v}) &= \int d\vec{v'} f_b(\vec{v'}) |\vec{v} - \vec{v'}| \\ &= 2\pi \int_0^\infty v'^2 f(v') dv' \int_{-1}^1 (v^2 + v'^2 - 2vv'\cos\theta)^{1/2} d(\cos\theta) \\ &= 4\pi \left[\int_0^v dv' f_b(v') \left(\frac{v'^4}{3v} + v'^2 v \right) + \int_v^\infty dv' f_b(v') \left(\frac{v' v^2}{3} + v'^3 \right) \right] \end{aligned} \tag{7.7}$$

Substituting equations (7.6) and (7.7) into (7.5) gives

$$\begin{aligned}(4\pi\Gamma)^{-1}\partial_t f_a &= v^{-2}\partial_v\left[\frac{m_a}{m_b}\left(\int_0^v v'^2 f_b(v')dv'\right)f_a\right. \\ &\left. + \frac{1}{3v}\left(\int_0^v v'^4 f_b(v')dv' + v^3\int_v^\infty v' f_b(v')dv'\right)\partial_v f_a\right] \end{aligned} \tag{7.8}$$

this equation agrees both with equation 2 of King (1960) and 2.10 of Hénon (1961). In the case of a spherically symmetric isotropic distribution of test stars then from Jeans theorem then the distribution function may be written as $f_b(\vec{x},\vec{v},t) = f_b(E,t)$. If we define $N(E)dE$ to be the number of stars with energies in the range E to $E+dE$ then (from equation 4-157 of Binney and Tremaine, 2008)

$$N(E) = 16\pi^2\int_0^{r_m(E)} r^2 dr v f(E) = 4\pi^2 p(E) f(E) \tag{7.9}$$

where $r_m(E)$ is the maximum radius a star with energy E can reach, i.e., $\Phi(r_m) = E$ and where

$$p(E) = 4\int_0^{r_m(E)} (2E - 2\Phi(r))^{1/2} r^2 dr \tag{7.10}$$

Taking the time derivative of equation (7.9) gives

$$\begin{aligned}\partial_t N(E) &= 4\pi^2 p(E)\partial_t f(E) \qquad (7.11)\\ &= (4\pi)^3\Gamma\int_0^{r_m(E)} r^2 dr v^{-1}\partial_v\left[\frac{m_a}{m_b}\left(\int_0^v v'^2 f_b(v')dv'\right)f_a\right. \\ &\left. + \frac{1}{3v}\left(\int_0^v v'^4 f_b(v')dv' + v^3\int_v^\infty v' f_b(v')dv'\right)\partial_v f_a\right] \\ &= (4\pi)^3\Gamma\int_0^{r_m(E)} r^2 dr\partial_E\left[\frac{m_a}{m_b}\left(\int_\Phi^E (2E' - 2\Phi)^{1/2} f_b(E')dE'\right)f_a\right. \\ &\left. + \frac{1}{3}\left(\int_\Phi^E (2E' - 2\Phi)'^{3/2} f_b(E')dE' + (2E - 2\Phi)^{3/2}\int_E^\infty f_b(E')dE'\right)\partial_E f_a\right]. \end{aligned}$$

Following Hénon (1961), since at $r = r_m$, v vanishes, then the integrand of this expression vanishes, and at r_m and we are free to swap the $\int_0^{r_m(E)} dr$ and ∂_E. Also, since f_a and f_b are functions of energy only, we may swap the integrations over r and E'. Defining

$$q(E) = \frac{4}{3}\int_0^{r_m(E)} (2E - 2\Phi(r))^{3/2} r^2 dr \tag{7.12}$$

then, following Cohn (1980), we may write the diffusion equation in flux conservative form [2]:

$$\partial_t N(E,t) = -\partial_E \mathcal{F}_E \tag{7.13}$$

[2]The total number is obviously conserved when written in this form: $\partial_t N_{\rm tot} = \int \partial_t N\, dE = \mathcal{F}_E|_{E_{\rm min}}^{E_{\rm max}}$, i.e., the change in number depends only on the flux $\mathcal{F}_E$ through the endpoints.

where

$$\mathcal{F}_E = -D_{EE}\partial_E f_a - D_E f_a \tag{7.14}$$

and

$$D_E = 16\pi^3\Gamma\frac{m_a}{m_b}\int_{\Phi(0)}^{E} p(E')f_b(E')dE' \tag{7.15}$$

$$D_{EE} = 16\pi^3\Gamma\left[\int_{\Phi(0)}^{E} q(E')f_b(E')dE' + q(E)\int_{E}^{\infty} f_b(E')dE'\right]. \tag{7.16}$$

In the case that $f_a = f_b$ (i.e., stars interact with themselves as opposed to a background distribution function) then this agrees with equations 6 through 8 in Cohn (1980) and 2.29 in Hénon (1961).

Note that the form of the diffusion equation in energy space given by equations (7.13) and (7.14) could easily be derived directly via the same procedure as the Fokker-Planck in velocity space (equation 1.25). Calculation of the diffusion coefficients however requires the treatment given above.

7.3 Singular Isothermal Sphere

We begin by reviewing the properties of the singular isothermal sphere. These properties are discussed more fully in Binney and Tremaine (2008).

Isothermal spheres have, by definition, a distribution function,

$$f_b(E) \equiv \frac{\nu_1}{(2\pi\sigma^2)^{3/2}}e^{-E/\sigma^2}\,. \tag{7.17}$$

Integrating the distribution function over the isotropic velocity gives the number density at position r:

$$\begin{aligned}\nu(r) &= \int f_b(E)d^3\,\boldsymbol{v} = 4\pi\int \frac{\nu_1}{(2\pi\sigma^2)^{3/2}}\exp\left(\frac{-\Phi(r)-\frac{1}{2}v^2}{\sigma^2}\right)v^2\,dv \\ &= \nu_1\exp\left(-\Phi(r)/\sigma^2\right). \end{aligned}\tag{7.18}$$

Utilizing Poisson's equation (1.22) then,

$$\nabla^2\Phi = 4\pi G\rho \tag{7.19}$$

$$\frac{1}{r^2}\frac{d}{dr}\left\{r^2\frac{d\Phi}{dr}\right\} = 4\pi G m_b\nu \tag{7.20}$$

$$\frac{1}{r^2}\frac{d}{dr}\left\{r^2\frac{d(-\sigma^2\log\nu/\nu_1)}{dr}\right\} = 4\pi G m_b\nu\,. \tag{7.21}$$

The singular isothermal sphere then results from the ansatz, $\nu = Cr^{-\gamma}$, which upon substitution gives

$$\gamma\sigma^2 r^{-2} = 4\pi G m_b C r^{-\gamma} \,. \tag{7.22}$$

Hence, an isothermal sphere of the form $\nu = Cr^{-\gamma}$ with $\gamma = 2$ and $C = 1/2\pi G m_b$ is self-consistent in the sense that it is a solution of Poisson's equation generating a potential-density pair:

$$\nu(r) = \frac{\sigma^2}{2\pi G m_b r^2} \tag{7.23}$$

$$\Phi(r) = 2\sigma^2 \log(r/r_1)\,, \tag{7.24}$$

where r_1 is position defined through $\nu(r_1) = \nu_1$. This solution is known as the singular isothermal sphere (SIS).

7.3.1 Calculation of Diffusion Coefficients

For the singular isothermal sphere the diffusion coefficients D_E and D_{EE} in equations (7.15) and (7.16) can be readily calculated.

Calculating first the 'density of states'[3] factor, $p(E)$, from $\Phi(r)$, using equation (7.24),

$$\begin{aligned} p(E) &= 4\int_0^{r_0 e^{E/2\sigma^2}} (2E - 4\frac{\sigma^2}{m_b}\log(r/r_0))^{1/2} r^2 dr \\ &= 8r_0^3\sigma \int_0^{e^{E/2\sigma^2}} \left(\frac{E}{2\sigma^2} - \log(r/r_0)\right)^{1/2} (r/r_0)^2\, d\,(r/r_0) \end{aligned} \tag{7.25}$$

substituting $x = r/r_0$ and $e^z = xe^{-E/2\sigma^2}$ reduces this to an elementary integral

$$\begin{aligned} p(E) &= 8r_0^3 y^3 \sigma \int_0^\infty e^{-3z} z^{1/2} dz \\ &= \frac{4}{3}\sqrt{\frac{\pi}{3}} r_0^3 \sigma e^{3E/2\sigma^2}. \end{aligned} \tag{7.26}$$

Making the same set of substitutions into equation (7.12) gives

$$q(E) = \frac{8}{9}\sqrt{\frac{\pi}{3}} r_0^3 \sigma^3 e^{3E/2\sigma^2}\,, \tag{7.27}$$

[3]The factor $p(E)$ is described as the density of states by analogy with solid-state and condensed matter physics since the number of stars in the interval E to $E + dE$ is $dN = 4\pi^2 p(E)\, dE$.

which gives the diffusion coefficients from equations (7.15) and (7.16) as

$$D_E = \frac{64}{3\sqrt{6}} \frac{m_a}{m_b} \pi^2 \Gamma \nu_1 r_0^3 e^{E/2\sigma^2} \tag{7.28}$$

$$D_{EE} = \frac{64}{3\sqrt{6}} \pi^2 \Gamma \nu_1 r_0^3 \sigma^2 e^{E/2\sigma^2} \,. \tag{7.29}$$

Note that $D_E = \frac{m_a}{m_b \sigma^2} D_{EE}$. This can be seen as a manifestation of the fluctuation dissipation theorem, relating the drift coefficient D_E, to the diffusion coefficient D_{EE}. It may be derived by the knowledge that the equilibrium solution in an isothermal sphere should have form $f_a = \exp\left(-\frac{m_a}{m_b}\frac{E}{\sigma^2}\right)$ at which point $\mathcal{F}_E = 0$ in equation (7.14).

7.3.2 Dimensionless Form of Evolution Equation

If we make the substitutions

$$x = e^{E/2\sigma^2} \,, \qquad T = \frac{t}{t_r} \,, \qquad t_r = \sqrt{2\pi} \frac{\sigma^3}{\Gamma \nu_1} \,,$$
$$R = \frac{m_a}{m_b} \,, \qquad f = \frac{w}{\sigma^3 r_1^3} e^{-ER/\sigma^2} \,, \tag{7.30}$$

then equation (7.13) becomes the dimensionless linear second-order PDE

$$\partial_T w = x^{2(R-1)} \partial_x (x^{2(1-R)} \partial_x w) \tag{7.31}$$

$$\partial_T w = \partial_x^2 w + \frac{2(1-R)}{x} \partial_x w \,. \tag{7.32}$$

This is just the diffusion equation with an additional first-order term. Note that the characteristic timescale,

$$t_r = \sqrt{2\pi} \frac{\sigma^3}{\Gamma \nu_1} = \frac{1}{\sqrt{2\pi} \log \Lambda} \frac{\sigma r_1^2}{G m_b} \,, \tag{7.33}$$

is the same, up to an order unity factor, as the relaxation time estimated in equation (7.1).

7.3.3 Steady-State Solution

The steady-state solution must satisfy

$$x^{2(1-R)} \partial_x w = \mathrm{C} \tag{7.34}$$

with solution

$$\begin{aligned} w &= \frac{C}{2(R-1)} x^{2(R-1)} + D \\ \rightarrow f &= \frac{C}{2(R-1)} e^{-E/\sigma^2} + D \exp\left(\frac{-E m_a}{\sigma^2 m_b}\right) \end{aligned} \tag{7.35}$$

So we see that the second term represents a Maxwellian distribution with velocity dispersion $\frac{m_b}{m_a}\sigma^2$ which is precisely equipartition.

The first term can be better understood by considering the rate of change of the total number of stars

$$\begin{aligned} \partial_T N_{\rm tot} &= 4\pi^2 \int dE p(E) \partial_T f(E,t) \\ &\sim \int_0^\infty \partial_T w(x,T) x^{2(1-R)} dx \\ &\sim \left[x^{2(1-R)} \partial_x w\right]_{x=0}^{\infty} \end{aligned} \tag{7.36}$$

so whilst the first term conserves stars, for positive C it corresponds to injecting them at infinite energy at a constant rate, whilst removing them at the same rate from zero energy. The steady state without injecting stars is therefore the equipartition solution, as expected and anticipated by the discussion on the fluctuation dissipation theorem in section 7.3.1.

7.3.4 Self-Similar Solution

7.3.4.1 Equal Mass Solution

When the mass ratio is equal ($R = m_a/m_b = 1$) then equation (7.32) becomes particularly simple:

$$\partial_T w = \partial_x^2 w \,. \tag{7.37}$$

Which in the context of the Fokker-Planck equation is known as a Weiner process (e.g., Risken, 1989), or in other situations as the heat equation. The self-similar solution to this equation is well known since it is the classic application of the method of Green's functions. Because the substitution $x = \exp(E/2\sigma^2)$ was used then equation (7.37) is only valid for $x > 0$. We use Neumann boundary conditions at this boundary $\partial_x w(x = 0, t) = 0$, as well as at $x = \infty$. This choice is motivated by number conservation: With this choice then the flux through the boundary is zero and the number of stars is conserved. Consider then initial condition $w(x, T = 0) = \delta(x)$. The solution is then,

$$w(x,T) = \frac{1}{\sqrt{4\pi T}} \exp\left[-\frac{x^2}{4T}\right], \tag{7.38}$$

which is self-similar since it may be written in the form,

$$w(x,T) = h(T)g\left[\frac{x^2}{4T}\right]. \tag{7.39}$$

Equation (7.39) also gives a self-similar solution in density. The density, $\rho(r)$, is given by:

$$\rho(r,t) = 4\pi \int_0^\infty f v^2\, dv \tag{7.40}$$

$$= 4\pi \int_{\Phi(r)}^\infty f(E)\sqrt{2E - 2\Phi(r)}\, dE\,. \tag{7.41}$$

Then using the self-similar solution equation (7.39) (and for a general mass ratio R)

$$\rho(r,t) = 4\pi\sigma^{-3} r_1^{-3} \int e^{-ER/\sigma^2} w\left(e^{E/2\sigma^2}, \frac{t}{t_r}\right)\sqrt{2E - 4\sigma^2 \log r/r_1}\, dE \tag{7.42}$$

$$= \sqrt{\frac{4\pi t_r}{t}}\sigma^{-3} r_1^{-3} \int e^{-ER/\sigma^2} g\left[\frac{e^{E/\sigma^2} t_r}{4t}\right]\sqrt{2E - 4\sigma^2 \log r/r_1}\, dE\,. \tag{7.43}$$

Substituting $\zeta = e^{E/\sigma^2}\frac{t_r}{4t}$ gives

$$\rho(r,t) = \sqrt{\frac{8\pi t_r}{t}}\left(\frac{t_r}{4t}\right)^R r_1^{-3} \int_{\frac{t_r}{4t}\left(\frac{r}{r_1}\right)^2}^\infty g\left[\zeta\right]\sqrt{\log\frac{4tr_1^2\zeta}{r^2}}\,\frac{d\zeta}{\zeta^{R+1}} \tag{7.44}$$

$$= \sqrt{\frac{8\pi t_r}{t}}\left(\frac{t_r}{4t}\right)^R r_1^{-3} u\left[\frac{t_r}{4t}\left(\frac{r}{r_1}\right)^2\right] \tag{7.45}$$

where

$$u\left[\theta\right] = \int_\theta^\infty g\left[\zeta\right]\sqrt{\log\frac{\zeta}{\theta}}\,\frac{d\zeta}{\zeta^{R+1}}\,. \tag{7.46}$$

Equation (7.45) gives the self-similar solution in density space, given a self-similar solution in the form of equation (7.39). In figure 7.2(a) we plot the self-similar solution in density space for the equal mass case ($R = 1$).

Note that the similarity variable may be written as

$$\theta = \frac{t_r}{4t}\left(\frac{r}{r_1}\right)^2 = \frac{\sigma}{4\sqrt{2\pi}Gm_b\log\Lambda}\frac{r^2}{t}\,, \tag{7.47}$$

which is proportional to the similarity variable in equation (7.2), which we argued must exist via dimensional arguments.

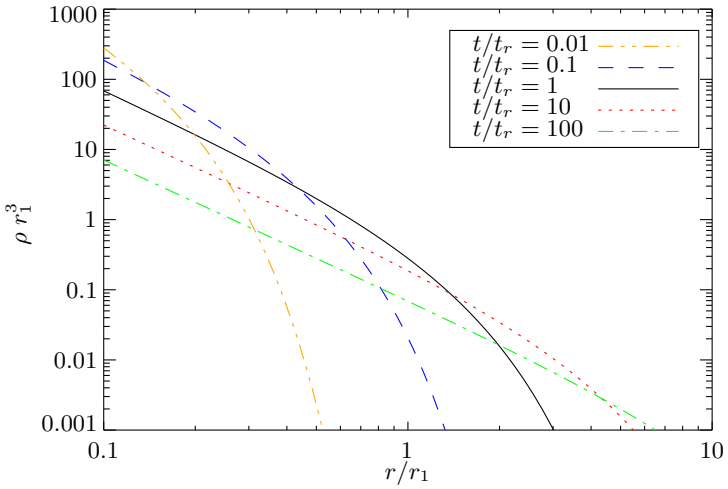

(a) Mass ratio $R = m_a/m_b = 1$. The equipartition solution is $\nu \propto \exp(-E)$ which gives $\rho \propto r^{-2}$. This is the asymptotic solution for $r \ll r_1\sqrt{t/t_r}$ and is the asymptotic slope of the solution.

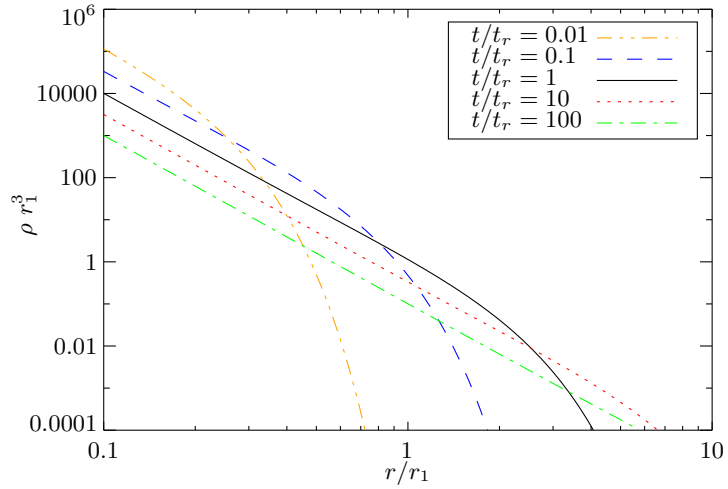

(b) Mass ratio $R = m_a/m_b = 2$. In this case the equipartition solution is $\nu \propto \exp(-2E)$ which gives $\rho \propto r^{-4}$ for $r \ll r_1\sqrt{t/t_r}$.

Figure 7.2 Self-similar solution in density space of stars diffusing in a background of equal mass stars in a singular isothermal sphere.

7.3.4.2 Unequal Mass Solution

Substituting equation (7.39) into equation (7.32) gives

$$\frac{h'}{h}T = \frac{1}{g}\left\{\zeta g'' + \left[\zeta - \left(\frac{3}{2} - R\right)\right]g'\right\}\,, \tag{7.48}$$

where $\zeta = x^2/4T$. The left-hand function is a function of only T, while the right is a function only of ζ, and so both must separately be equal to a constant. The total number of stars is given by

$$\begin{aligned} N_{\text{tot}} &= 4\pi^2 \int p(E) f(E)\, dE \\ &\propto \int x^{2(1-R)} w\, dx = \sqrt{T} h(T) \int g(\zeta)\, d\zeta\,. \end{aligned} \tag{7.49}$$

For the total number of stars to be conserved by the self-similar solution we therefore require $h(T) = 1/\sqrt{T}$. As a result both sides of equation (7.48) are equal to $-\frac{1}{2}$. The right-hand side of equation (7.48) results in a differential equation for g:

$$\zeta g'' + \left[\zeta + \left(\frac{3}{2} - R\right)\right]g' + \frac{1}{2}g = 0\,. \tag{7.50}$$

This is a second-order ODE known as the confluent hypergeometric differential equation. It has solution

$$g(\zeta) = A\ {}_1F_1\left(\frac{1}{2}; \frac{3}{2} - R; -\zeta\right) + B\ U\left(\frac{1}{2}, \frac{3}{2} - R, -\zeta\right) \tag{7.51}$$

where ${}_1F_1\left(\cdot;\cdot;\cdot\right)$ and $U\left(\cdot,\cdot,\cdot\right)$ are the confluent hypergeometric function of the first and second kinds, respectively. The self-similar solution is plotted in density space in figure 7.2(b). We choose $B = 0$ since this term results in an divergent number of stars.

7.3.5 Eigenfunction Expansion

Although we have calculated the self-similar solution which was the motivation for this work, we also give the solution in terms of an eigenfunction expansion. We provide these since they are easier to use: One may decompose an initial distribution function into its eigenfunctions which can then be separately evolved forwards in time.

Using separation of variables on equation (7.32):

$$w(x, T) = \xi(x)\tau(T) \tag{7.52}$$

gives for $\tau(T)$, using $-\beta^2$ as the separation constant,

$$\tau' = -\beta\tau \quad \rightarrow \quad \tau \sim \exp(-\beta^2 T)\,. \tag{7.53}$$

Equation (7.32) therefore becomes,

$$-\beta^2\xi = \mathcal{L}\xi\,, \tag{7.54}$$

where $\mathcal{L}$ is the differential operator,

$$\mathcal{L} = \partial_x^2 + \frac{2(1-R)}{x}\partial_x\,. \tag{7.55}$$

Written in this form it is clear that $\xi(x)$ are the eigenfunctions of $\mathcal{L}$.

$\mathcal{L}$ is not a Hermitian operator, however the problem can be transformed to one (e.g., Risken, 1989). Consider,

$$\psi(x) = x^{1-R}\xi(x) \quad , \quad \mathcal{L}' = x^{1-R}\mathcal{L}x^{R-1}\,. \tag{7.56}$$

Then it can be shown $\mathcal{L}'$ is a Hermitian operator and equation (7.54) becomes the eigenfunction equation,

$$\mathcal{L}'\psi = -\beta^2\psi \tag{7.57}$$

$$\rightarrow x^2\psi'' + [R(1-R) + (\beta x)^2]\psi = 0\,. \tag{7.58}$$

For equal mass ($R = 1$) the solution is trivially $\psi = A\sin\beta x + B\cos\beta x$. For $R \neq 1$ equation (7.58) this may be written

$$0 = x^2\partial_x^2(x^{-1/2}\psi) + 2x\partial_x(x^{-1/2}\psi) + (\beta^2x^2 - (R-1/2)^2)(x^{-1/2}\psi)\,. \tag{7.59}$$

which is Bessel's equation with solution

$$\psi(x) = x^{1/2}\left(AJ_{R-1/2}(\beta x) + BY_{R-1/2}(\beta x)\right)\,. \tag{7.60}$$

The solutions are orthogonal as expected for a Hermitian operator via the closure equation of Bessel functions:

$$\int_0^\infty xJ_a(\beta x)J_a(\beta' x)\,dx = \frac{1}{\beta}\delta(\beta-\beta')\,. \tag{7.61}$$

Summarizing the solutions:

$$\xi(x) = \begin{cases} x^{R-1/2}\left(AJ_{1/2-R}(\beta x) + BY_{1/2-R}(\beta x)\right) & R < 3/2 \\ A\cos\beta x + B\sin\beta x & R = 1 \\ x^{R-1/2}\left(AJ_{R-1/2}(\beta x) + BY_{R-1/2}(\beta x)\right) & R > 3/2 \end{cases} \tag{7.62}$$

where J_ν and Y_ν are the Bessel and Neumann functions of order ν, respectively.

The most general solution is therefore

$$w(x,T) = \int_0^\infty d\beta \begin{cases} x^{R-1/2}\left[A(\beta)J_{1/2-R}(\beta x) + B(\beta)Y_{1/2-R}(\beta x)\right]\exp(-\beta^2 T) & R \leq 3/2 \\ \left[A(\beta)\cos\beta x + B(\beta)\sin\beta x\right]\exp(-\beta^2 T) & R = 1 \\ x^{R-1/2}\left[A(\beta)J_{R-1/2}(\beta x) + B(\beta)Y_{R-1/2}(\beta x)\right]\exp(-\beta^2 T) & R > 3/2 \end{cases} \tag{7.63}$$

As with the equipartition solution we must calculate the flux at the boundaries in order to choose the physically relevant solution for the case at hand. We give an example of this for $R = 2$ below. The boundary conditions, together with the initial distribution, determine $A(\beta)$ and $B(\beta)$.

7.3.6 Example for $R = 2$

Motivated by possible application to blue stragglers we show here an example the use of the eigenfunction solution for mass ratio $R = \frac{m_a}{m_b} = 2$. In this case the solution is

$$w(x,T) = \int_0^\infty d\beta\, x^{3/2}\left[A(\beta)J_{3/2}(\beta x) + B(\beta)Y_{3/2}(\beta x)\right]\exp(-\beta^2 T)\,. \tag{7.64}$$

We also require boundary conditions. We use that the distribution function be zero at some large x which we denote $x_{\max}$. While we do this to eliminate divergences, but it is physically motivated by the cluster being truncated at the energy corresponding to $x_{\max}$. We use $w(x \geq x_{\max}, T) = 0$ as opposed to the (number conserving) boundary condition that the flux go to zero. The physical reason is that stars may diffuse outwards across $x_{\max}$, and then be unbound. This is the same boundary condition used by the lowered isothermal, or King models (Binney and Tremaine, 2008). We also require that the flux be zero at some small x which we denote $x_{\min}$. Again this is motivated by lowered isothermal, or King models (Binney and Tremaine, 2008), where the center of the cluster has a finite potential. Away from the core however this cut-off should not affect the solution beyond a normalization. This boundary condition is $\partial_x w(x = x_{\min}, T) = 0$, and corresponds to a Robin (or third type) boundary condition in ξ. For $R = 2$ this is

$$\partial_x \xi + \frac{3}{2}\frac{\xi}{x} = 0\,. \tag{7.65}$$

Consider the function

$$u(\lambda_n x) = Y_{3/2}(\lambda_n x_{\max})J_{3/2}(\lambda_n x) - J_{3/2}(\lambda_n x_{\max})Y_{3/2}(\lambda_n x)\,. \tag{7.66}$$

As $x \to x_{\max}$ then $u \to 0$, so the outer boundary condition is naturally satisfied. Choosing λ_n to be

the n-th largest root of

$$0 = \partial_x u(\lambda_n x_{\rm min}) + \frac{3}{2}\frac{u}{\lambda_n x_{\rm min}}\,, \tag{7.67}$$

then the inner boundary condition is also satisfied. The solution consistent with the boundary conditions is therefore

$$w(x,T) = \sum_{n=1}^{\infty} A_n x^{3/2} u(\lambda_n x)\exp[-(\lambda_n/x_{\rm max})^2 T]\,. \tag{7.68}$$

To calculate the coefficients A_n multiply by $x^{-1/2}u(\lambda_m x)$, and integrate from $x_{\rm min}$ to $x_{\rm max}$. For the boundary conditions considered here then (proved in Appendix 7.A)

$$\int_{x_{\rm min}}^{x_{\rm max}} x u(\lambda_m x) v(\lambda_n x)\,dx = \delta_{m,n}\Big\{\frac{{x_{\rm max}}^2}{2}u'(\lambda_n x_{\rm max})^2 + \frac{{x_{\rm min}}^2}{2}\Big[u(\lambda_n x_{\rm min})u''(\lambda_n x_{\rm min}) - \Big(\frac{9}{4}+\frac{3}{2\lambda_n x_{\rm min}}\Big)u(\lambda_n x_{\rm min})^2\Big]\Big\}\,, \tag{7.69}$$

where $\delta_{m,n}$ is the Kronecker delta. Therefore

$$A_n = \frac{2}{C_n}\int_{x_{\rm min}}^{x_{\rm max}} dx\, x^{-1/2} u(\lambda_n x) w(x, T=0) \tag{7.70}$$

where

$$C_n = {x_{\rm max}}^2 u'(\lambda_n x_{\rm max})^2 + {x_{\rm min}}^2\Big[u(\lambda_n x_{\rm min})u''(\lambda_n x_{\rm min}) - \Big(\frac{9}{4}+\frac{3}{2\lambda_n x_{\rm min}}\Big)u(\lambda_n x_{\rm min})^2\Big]\,. \tag{7.71}$$

Again anticipating possible application to blue stragglers we choose the initial conditions to be $\rho_a \propto \rho_b$, i.e., $f \propto \exp(-E/\sigma^2)$ and $w(x, T=0) = Cx^2$ with C a normalization constant. We show the evolution of these initial conditions, calculated via equations (7.68) and (7.70) in figures 7.3 and 7.4.

Because of the choice of boundary condition the equipartition solution is never completely reached. The equilibrium equipartition solution corresponds to constant w, which due to the boundary condition $w(x = x_{\rm max}, T) = 0$ results in $w \to 0$ as $T \to \infty$, i.e., given sufficient time all the stars diffuse out of the cluster.

7.4 Numerical Solution

In order to check the analytic solution in the previous section we have also written a code to numerically solve the spherical isotropic Fokker-Planck equation. Equation (7.13) can be written

$$\partial_t f = \frac{1}{4\pi^2 p(E)}\partial_E(D_{EE}(E)\partial_E f + D_E(E) f)\,. \tag{7.72}$$

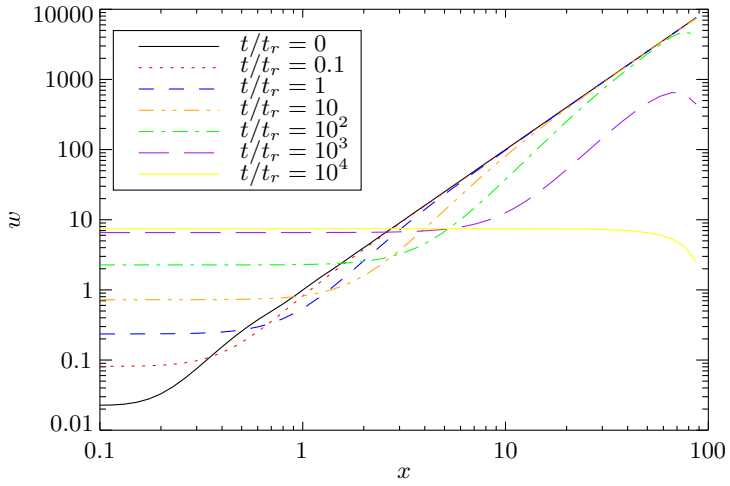

(a) Evolution of the distribution function. As time increases the radius to which the stars are in equipartition (w constant) increases.

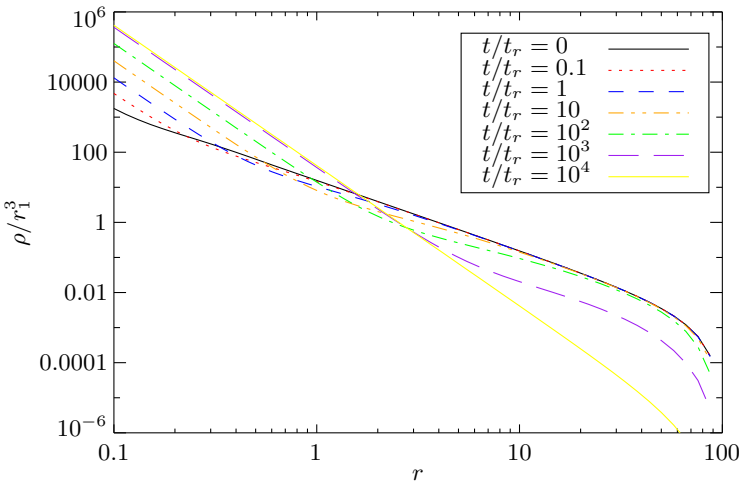

(b) Evolution of the density. As time increases the radius to which the stars are in equipartition ($\rho \propto r^2$) increases.

Figure 7.3 Evolution of test stars against a background of stars distributed as a singular isothermal sphere. The mass ratio of test stars to background stars is $R = \frac{m_a}{m_b} = 2$. The initial conditions are that the test stars are distributed proportionally to the isothermal sphere, i.e., both are $\rho \propto r^{-2}$. The boundary conditions are that flux is conserved at the inner edge, and that the distribution function is zero at the outer edge. These boundary conditions are introduced to eliminate divergences, and are physically motivated by the King model.

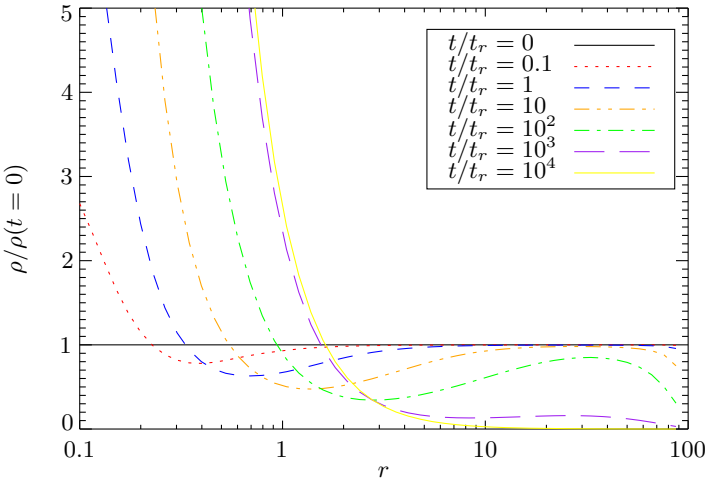

(a) Evolution of the density normalized to the initial density, logarithmic scale.

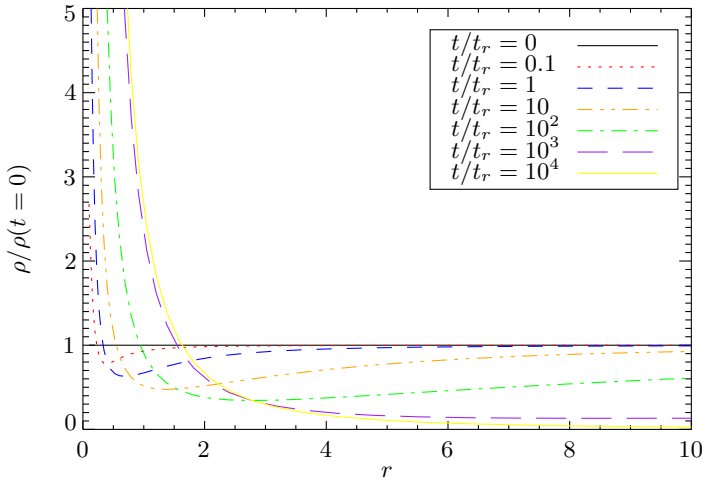

(b) Evolution of the density normalized to the initial density, linear scale.

Figure 7.4 As figure 7.3 but with the density normalized to the initial conditions, which are also the distribution of background stars i.e., $\rho(t=0) \propto \rho_b \propto r^{-2}$.

We choose to make the substitution

$$w(E) = f \exp\left(-\int \frac{D_E}{D_{EE}} dE\right) , \tag{7.73}$$

since $\exp\left(-\int \frac{D_E}{D_{EE}} dE\right)$ is the equilibrium solution, and therefore the evolved variable, $w(E)$, does not contain the large variations present in $f(E)$. Using equation (7.73) the diffusion equation becomes

$$\begin{aligned} \partial_t w &= \frac{e^{\int \frac{D_E}{D_{EE}} dE}}{4\pi^2 p(E)} \partial_E (D_{EE} e^{-\int \frac{D_E}{D_{EE}} dE} \partial_E w) \\ &= \frac{1}{A(E)} \partial_E (B(E) \partial_E w) \end{aligned} \tag{7.74}$$

There are many possible methods of numerically finding solutions to this equation, but the method of Chang and Cooper (1970) has the desirable feature that the number of stars is conserved, and is more elegant than naive differencing schemes. For the properties of this differencing scheme, and proof that the number of stars is conserved, we refer the reader to Chang and Cooper (1970), and only outline its implementation here.

Denote $w(E,t) = w_j^n$ where j and n are indices defined through $E = E_0 + j\Delta E$, $t = n\Delta t$. Writing the flux in energy space as $F = B\partial_E w$ and representing the time derivative as a forward difference, and the derivative in energy space as a centered difference gives

$$\frac{1}{\Delta t}(w_j^{n+1} - w_j^n) = \frac{1}{A_j \Delta E}(\tilde{F}_{j+1/2} - \tilde{F}_{j-1/2}) , \tag{7.75}$$

where $\tilde{F} = \theta F^{n+1} + (1-\theta)F^n$. Therefore, $\theta = 0$ represents an explicit differencing scheme, $\theta = 1$ is the totally implicit scheme, and $\theta = 1/2$ is the Crank-Nicolson scheme. The boundary conditions used at the edge of the computation domain are $F_{-1/2} = 0$ and $F_{J_{MAX}+1/2} = 0$ which corresponds to zero flux of stars through the edge of the computational domain.

The energy derivative contained within the flux is represented as a centered difference, for example,

$$\tilde{F}_{j+1/2} = \frac{B_{j+1/2}}{\Delta E}(\tilde{w}_{j+1} - \tilde{w}_j) \tag{7.76}$$

then

$$w_j^{n+1} - w_j^n = C_{j+1/2}\tilde{w}_{j+1} - (C_{j+1/2} + C_{j-1/2})\tilde{w}_j + C_{j-1/2}\tilde{w}_{j-1} \tag{7.77}$$

where $C = \frac{\Delta t}{\Delta E^2} B$.

The fully implicit method was implemented since it is guaranteed to be stable, while its analysis tends to be simpler that the general or even Crank-Nicolson case. The equation to be solved at each step is

$$C_{j+1/2} w_{j+1}^{n+1} + \left[1 - (C_{j+1/2} + C_{j-1/2})\right] w_j^{n+1} + C_{j-1/2} w_{j-1}^{n+1} = w_j^n , \tag{7.78}$$

together with the corresponding equations at the boundaries

$$C_{1/2} w_1^{n+1} + \left[1 - C_{1/2}\right] w_0^{n+1} = w_0^n$$
$$\left[1 - C_{J_{\rm MAX}-1/2}\right] w_{J_{\rm MAX}}^{n+1} + C_{J_{\rm MAX}-1/2} w_{J_{\rm MAX}-1}^{n+1} = w_{J_{\rm MAX}}^n \ . \tag{7.79}$$

This set of implicit equations can be written as

$$\mathbf{D}.\mathbf{w}^{n+1} = \mathbf{w}^n \ , \tag{7.80}$$

where $\mathbf{w}$ is the solution and $\mathbf{D}$ is a tridiagonal matrix.

The tridiagonal form of $\mathbf{D}$ allows the set of implicit J_{MAX} equations to be solved in $O(J_{MAX})$ operations provided that $\mathbf{D}$ is diagonally dominant (see, e.g., 2.4 of Press et al., 1992). Since C will be greater than zero for physical diffusion equations then for diagonal dominance it is sufficient to require

$$1/2 > C_{j+1/2} + C_{j-1/2} \ . \tag{7.81}$$

For most problems this simply sets a limit on the step size for a given number of grid points. For especially pathological diffusion coefficients then, if this condition is violated, it is possible to fall back to a less efficient method for the solution of the implicit equations, and as a last resort the direct inversion of $\mathbf{D}$.

In figure 7.5 we plot the evolution of a initially narrow distribution in energy, for the equal mass case ($R = 1$), using this code. We also evolve the analytic Eigenfunction solution provided by equation (7.63) and show that they agree.

7.5 Source Terms

Equation (7.13) can be easily be modified to include a source term:

$$\partial_t N(E,t) = -\partial_E F_E + S(E) \ , \tag{7.82}$$

where $S(E)$ is the rate of production of test stars between E and $E + dE$.

The source term in energy space can be calculated from the production rate in position space by using a slight variation on Eddington's formula (Binney and Tremaine, 2008)

$$S(E) = \sqrt{2} p(E) \frac{d}{dE} \left[\int_E^\infty \frac{d\Gamma}{d\Phi} \frac{d\Phi}{\sqrt{\Phi - E}} \right] , \tag{7.83}$$

where Γ is considered to be a function of Φ through $\Phi(r)$.

As an example, in the case of collisions in position space the production rate per unit volume is

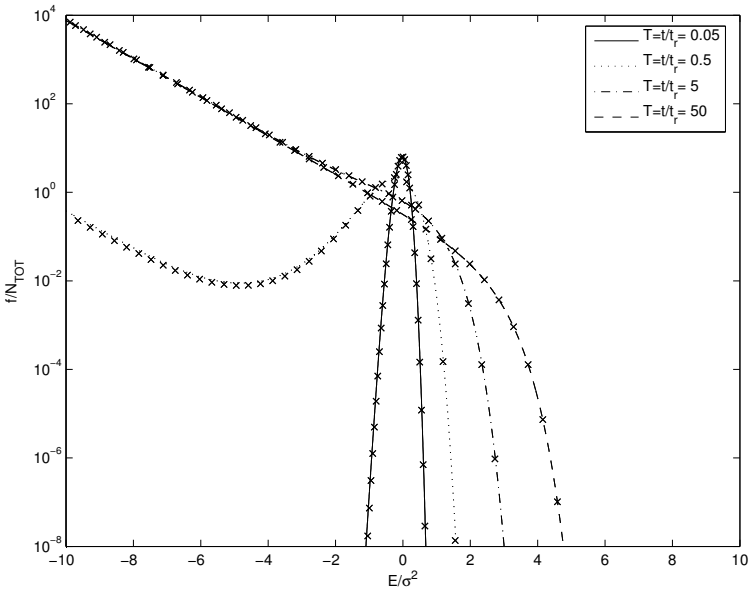

(a) Evolution in energy space.

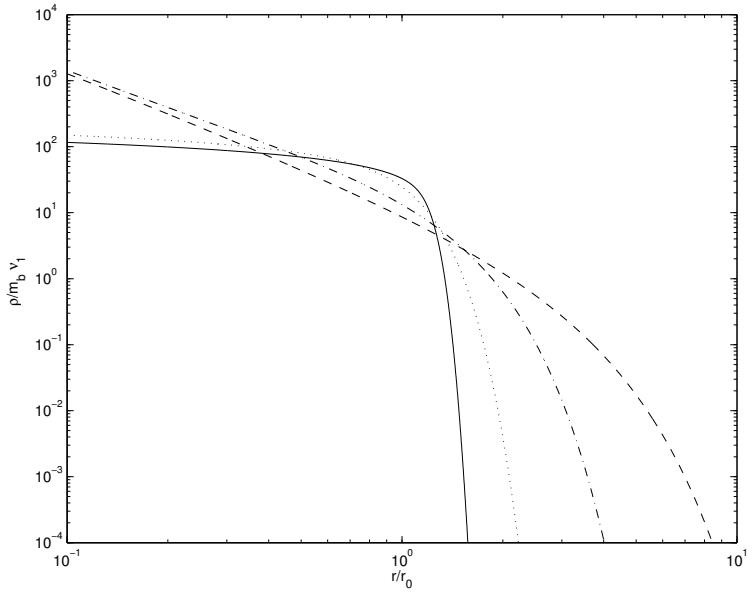

(b) Evolution in radial coordinates.

Figure 7.5 Comparison of analytic and numerical solution. The plots show the evolution of an initially narrow distribution in energy in an equal mass (i.e., $R = \frac{m_a}{m_b} = 1$) background of stars distributed as the singular isothermal sphere. The solid, dotted, dash-dot, and dashed lines are the numerical solutions provided the code described in section 7.4 at times $t/t_r = 0.05$, 0.5, 5 and 50, respectively. The crosses are the analytic eigenfunction solution described in section 7.3.5.

given by Binney and Tremaine (2008)

$$\Gamma_{\rm coll}(r) = 16\sqrt{\pi}\nu(r)^2\sigma R_\star^2\left(1+\frac{Gm}{2\sigma^2 R_\star}\right), \tag{7.84}$$

where $R_\star$ is the radius at which a merger occurs.

For the isothermal sphere then the density varies as $\nu = \nu_0 e^{-\Phi/\sigma^2}$ and so the collision rate is proportional to $\nu^2 = \nu_0^2 e^{-2\Phi/\sigma^2}$. This can be converted to energy space easily since this is just proportional to the original isothermal density with $\sigma \to \sigma/\sqrt{2}$ and so the result of equation (7.83) must be

$$S(E) = \frac{16\sqrt{2}}{\pi}\frac{R_\star^2\nu_0^2}{\sigma^2}\left(1+\frac{Gm}{2\sigma^2 R_\star}\right)p(E)e^{-2E/\sigma^2}. \tag{7.85}$$

In this case the resultant distribution is already in equilibrium. This is because the merger products of collisions in a relaxed isotropic population are also relaxed. This also holds for multimass systems, unequal mass mergers, and non-singular solutions. The only requirement is a Maxwellian distribution function, and complete merger (i.e., no mass loss).

7.6 Applications

7.6.1 Radial Distribution of Blue Stragglers

Blue stragglers (BSS) are stars that lie on the main sequence in a globular cluster, but beyond the main sequence turn off. There are two main theories for the origin of blue stragglers: That they formed via collisions (sometimes denoted COL-BSS), or via mass transfer in a close binary (MT-BSS).

The radial distribution of blue stragglers has been investigated on numerous occasions (e.g., Ferraro et al., 2004; Lanzoni et al., 2007a,b; Mapelli et al., 2006; Salinas et al., 2012). These often show a 'zone of avoidance' at roughly the radius to which the cluster is relaxed. An example of this is shown in distribution of blue stragglers shown in figure 7.6. If formed by collisions then it is difficult for the BSS fraction to rise towards the edge of the cluster. However the distribution is very suggestive of the $R = 2$ analytic solution in figure 7.4(a).

Unfortunately the solution here is not directly applicable to any of the previously calculated BSS distributions. For this solution we require that the density distribution be close to $\propto r^{-2}$ for a significant range of radii. Globular clusters tend to be well fit by a lower isothermal sphere (or King model). These models do approach $\propto r^{-2}$, but only when they have a high concentration parameter. The best fitting King model for 47 Tuc is plotted in figure 7.7. As can be seen in figure 7.7(b) there is no radial range where the singular isothermal sphere is approached.

Instead for accurate application of this solution the cluster should have a high central concentration, $c \equiv \log r_t/r_0$. These are clusters that have undergone core-collapse (e.g., Binney and

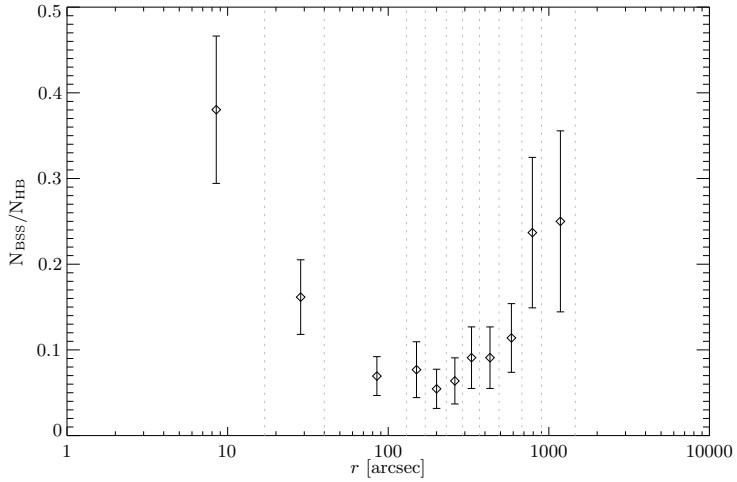

Figure 7.6 Blue straggler radial distribution, normalized to the number of horizontal branch stars for the globular cluster 47 Tuc. From data published in Ferraro et al. (2004).

Tremaine, 2008). Unfortunately it appears none of the globular clusters for which there is radial BSS distribution data has undergone core collapse.

7.6.2 Application to NGC 6397

The globular cluster NGC 6397 is one of the closest globular clusters at only 2.2 kpc. It is fit by King models with high concentration ($c \approx 2.47$, Meylan and Mayor 1991) indicating that it has undergone core collapse, and as a result its radial profile closely approximates the singular isothermal sphere.

The central region of NGC6397 was imaged by the Advanced Camera for Surveys Wide Field Camera (ACS/WFC) camera on the Hubble Space Telescope (HST) over ten visits during 2004 and 2005 (Proposal ID: 10257, PI: Anderson). During each visit four long, ~ 390 s exposures were taken using the F658N (H_α) filter, and two exposures in either F435W ($\sim B$) or F625W ($\sim r$)— one long (340 s) and one short (~ 10 s). The result is a data-set consisting of 40 long exposures in H_α, and five long and five short exposure in both B and r filters. Despite the changing roll angle of the observations over the year the central 80" of the cluster are imaged in all exposures.

This data set was searched for He core white dwarfs by Strickler et al. (2009) and 24 strong candidates identified. Since the primary aim here is to demonstrate the usefulness of the solution described in this chapter, we do not attempt to produce the exquisite photometry of Strickler et al. (2009). In that work models were fit to the spatial variation of the PSF in each image separately. Instead the data consisting of the individual `_flt.fits` exposures in each filter were aligned, cleaned of cosmic rays and bad pixels, and stacked using the `Multidrizzle` algorithm (Koekemoer et al., 2003). All images were aligned with sub-pixel precision to the long R-band

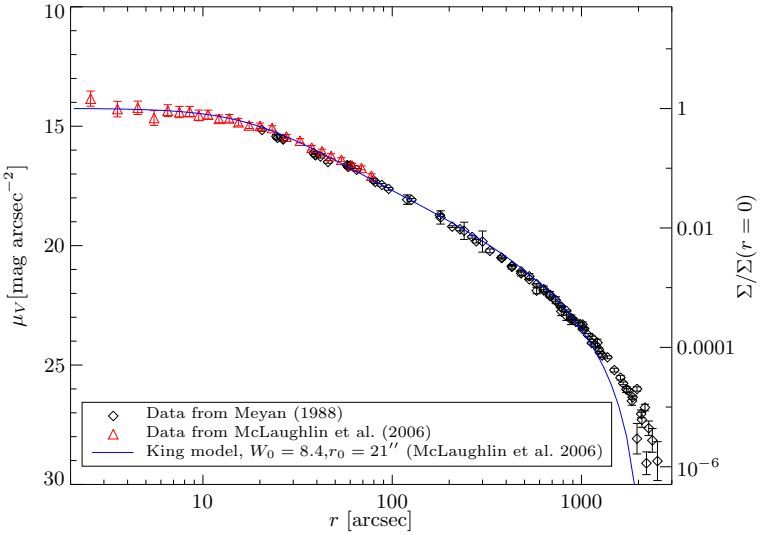

(a) Surface brightness of 47 Tuc plotted on the left-hand axis. Central red data is taken from Mclaughlin et al. (2005), black data is taken from Meylan (1988). In blue and plotted on the right axis is the best-fitting single-mass King model from Mclaughlin et al. (2005) which has $W = \Phi(0)/\sigma^2 = 8.4$ and core radius $r_0 = 21''$.

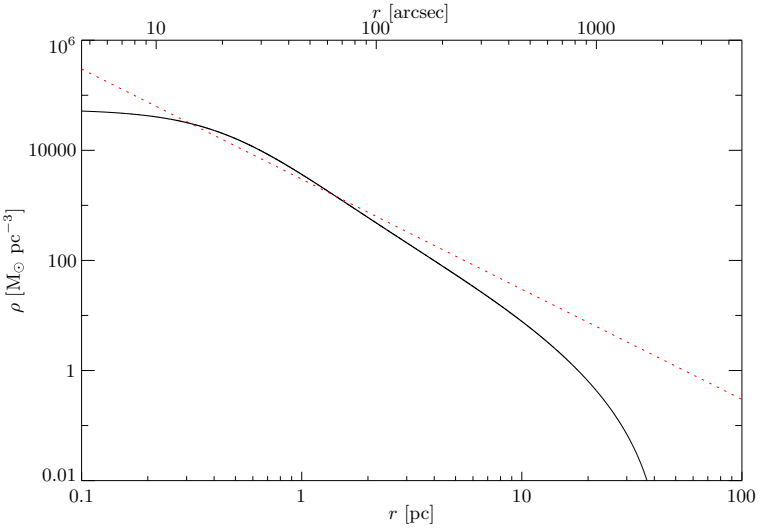

(b) Density of best fitting King model taken from Mclaughlin et al. (2005) compared to a singular isothermal sphere with $\sigma = 9$ km s^{-1}.

Figure 7.7 Observational data, best-fitting King model, and singular isothermal sphere profile for the globular cluster 47 Tuc.

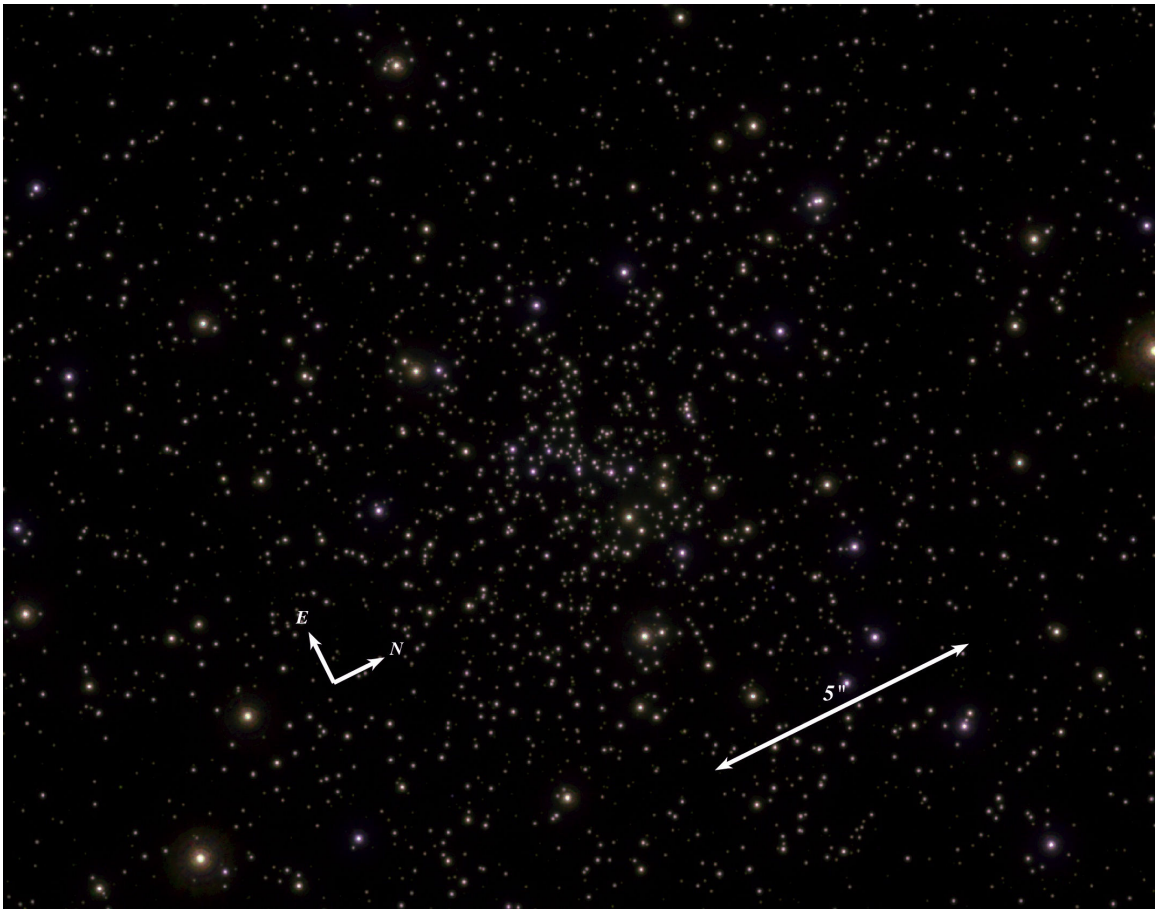

Figure 7.8 False color image of the core of NGC 6397. The red channel is the stacked 5×300s exposures in the *r*-band, the green channel is the stacked 40×300s exposures in the H_α-band, and the blue channel is the stacked $5 \times 300s$ exposures B-band. All channels are logarithmically scaled.

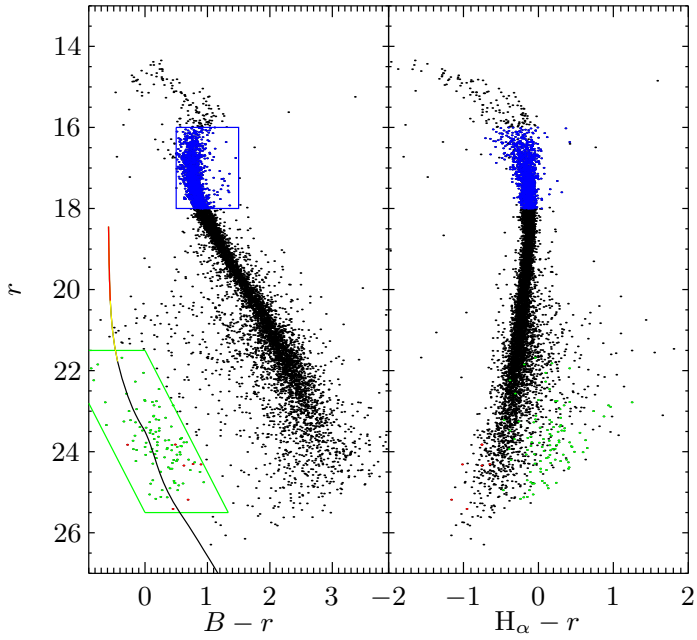

Figure 7.9 Color-magnitude diagrams of the core of NGC 6397. All objects lie in the central 80" and are well fit by the PSF ($\chi^2/DOF < 2$). Objects defined to be white dwarfs are the green points in the green box in the left-hand panel. Only those showing significant H_α absorption in the right panel are included, which removes the red dots. Also plotted is the cooling model for a $0.6\,M_\odot$ white dwarf[a] at a distance 2.2 kpc. The yellow region are white dwarfs with age $< 10^7$ yr, and red $< 10^6$ yr. Objects in the blue box are those defined as main sequence turn off stars. The *r*-band begins to saturate at $r \sim 17$.

[a] Available from http://www.astro.umontreal.ca/~bergeron/CoolingModels/, uses results from from Holberg and Bergeron (2006), Kowalski and Saumon (2006), Tremblay et al. (2011) and Bergeron et al. (2011).

image, `j92801ckq_flt.fits`, before stacking. The images were stacked into five separate stacks composed of the H_α images, and the long and short *B* and *r*-band images. The resultant image of the center of the cluster is shown in figure 7.8.

Photometry was performed using the crowded field PSF fitting package `DAOPHOT` (Stetson, 1987). The initial source list provided for the fitting in all bands was taken from running `DAOFIND` on the stacked H_α exposure as it was generally deepest, its length (40×390s) overcoming the narrowness of the filter. The resultant color-magnitude diagram is show in figure 7.9. Photometric zero points are taken from Sirianni et al. (2005).

The radial distribution of white dwarfs identified from their position in this diagram are shown in figure 7.10.

The velocity dispersion in the inner arcmin is $(4.5 \pm 0.6)\,\mathrm{km\,s^{-1}}$ (Meylan and Mayor, 1991).

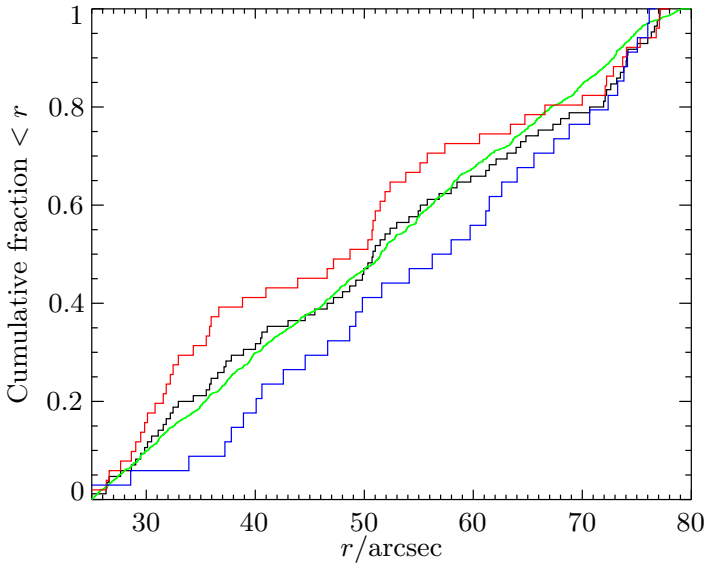

Figure 7.10 Cumulative distribution of white dwarfs in the center of NGC 6397 are plotted as the black line. Faint white dwarfs ($R > 24$) are in blue, bright in ($R < 24$) red. The distribution of main sequence turnoff stars are plotted as the green line. The center is assumed to be at 17 : 40 : 42.049″, −53 : 40 : 28.72″ (Strickler et al., 2009). We only plot from 25" outwards since crowding inside this severely limits the detection of faint white dwarfs.

Outside the core equation (7.33) gives the relaxation time to be,

$$t_r = 4 \times 10^5 \,\mathrm{yr} \frac{10}{\log \Lambda} \frac{\sigma}{4.5 \,\mathrm{km\,s^{-1}}} \frac{1 M_\odot}{m_b} \frac{r^2}{(0.1 \,\mathrm{pc})^2} \,. \tag{7.86}$$

At a distance of 2.2 kpc the fiducial radius of 0.1 pc corresponds to 1 arcmin. Even at the at the edge of the 80" field of figure 7.10 the relaxation time is only 1.8×10^6 yr. Therefore only the red region of the white dwarf model plotted in figure 7.10 will the solution here be useful. The older white dwarfs will be relaxed. This is why the radial white dwarf distribution in figure 7.10 is so similar to the main sequence turn off distribution.

If sufficient young unrelaxed white dwarfs were available it would have been possible to test the presence of the 3–6 $\mathrm{km\,s^{-1}}$ kick at the white dwarf birth suggested by Davis et al. (2008).

Unfortunately equation (7.86) also suggests the solution presented here cannot readily be applied to *any* population in the observed NGC9397. Inside 80" there are only ~ 10 horizontal branch stars (Strickler et al., 2009), which have a lifetime of $\sim 10^8$ yr. Therefore there will not be sufficient stars to test this solution for any group of objects sufficiently young or short lived to not be relaxed.

From the attempted application to two clusters here the requirements for the applicability of the solution to be presented can be formed.

First from section 7.6.1 the cluster should be have a high concentration, i.e., core collapsed with

$c \gtrsim 2.5$. Consider then a population with a lifetime or age T_0. For the solution here to be useful, then the radius to which that population is relaxed should lie in the region where the solution is applicable. For the stars not be relaxed at the outer edge of the region of applicability we require

$$T_0 < t_r(r_a) = 2 \times 10^8 \,\mathrm{yr} \frac{10}{\log \Lambda} \frac{\sigma}{5 \,\mathrm{km\,s^{-1}}} \frac{1 M_\odot}{m_b} \frac{r_a^2}{(2\,\mathrm{pc})^2} \tag{7.87}$$

where the outer edge of the region of applicability is $r_a = \min(r_h, r_{\mathrm{fov}})$, the minimum of the observed field of view, and the half mass radius (beyond which King models no longer closely approach the singular isothermal sphere). For the population to be relaxed at the inner edge of applicability we require

$$T_0 > t_r(r_c) = 5 \times 10^5 \,\mathrm{yr} \frac{10}{\log \Lambda} \frac{\sigma}{5 \,\mathrm{km\,s^{-1}}} \frac{1 M_\odot}{m_b} \frac{r_c^2}{(0.1\,\mathrm{pc})^2} \tag{7.88}$$

where r_c is the core radius.

From these relations we see the reason that the solution could not be applied to NGC 6397 was that the observed field of view, and therefore r_a, was too small. NGC 6397 was selected on the basis of its nearby distance, however this in fact hampered attempts to apply the solution there. Based on the requirements, the cluster M15 appears a more promising candidate for the application of this solution, and there is already data on UV bright objects available (Dieball et al., 2007; Haurberg et al., 2010). We plan to investigate application of the solution to M15 in the near future.

Appendix 7.A Orthogonality Relation

The derivation in this appendix broadly follows (4.31) of Tranter (1968) but with mixed Neumann and Robin boundary conditions as opposed to purely Neumann.

The function

$$u = Y_\nu(\lambda_n x_{\max}) J_\nu(\lambda_n x) - J_\nu(\lambda_n x_{\max}) Y_\nu(\lambda_n x) \tag{7.89}$$

satisfies Bessel's equation

$$x^2 \partial_x^2 u + x \partial_x u + (\lambda_n^2 x^2 - \nu^2) u = 0 \,. \tag{7.90}$$

Consider the function

$$v = Y_\nu(\lambda_m x_{\max}) J_\nu(\lambda_m x) - J_\nu(\lambda_m x_{\max}) Y_\nu(\lambda_m x) \tag{7.91}$$

which satisfies

$$x^2 \partial_x^2 v + x \partial_x v + (\lambda_m^2 x^2 - \nu^2) v = 0 \,. \tag{7.92}$$

Multiplying equation (7.90) by v/x, equation (7.92) by u/x and subtracting gives

$$\begin{aligned}(\lambda_m^2 - \lambda_n^2)xuv &= x(u\partial_x^2 v - v\partial_x^2 v) + (u\partial_x v - v\partial_x u) \\ &= \partial_x[x(u\partial_x v - v\partial_x u)]\,. \end{aligned} \tag{7.93}$$

Integrating from $x_{\min}$ to $x_{\max}$

$$(\lambda_m^2 - \lambda_n^2)\int_{x_{\min}}^{x_{\max}} xuv\,dx = x(u\partial_x v - v\partial_x u)|_{x_{\min}}^{x_{\max}}\,. \tag{7.94}$$

We are considering the boundary conditions $u(x = x_{\max}) = v(x = x_{\max}) = 0$ and $\partial_x(x^{R-1/2}u) = \partial_x(x^{R-1/2}u) = 0$. Note that $\partial_x(x^{R-1/2}u)|_{x=xmin} = 0$ is the Robin boundary condition

$$\partial_x u(x = x_{\min}) + \left(R - \frac{1}{2}\right)\frac{u(x = x_{\min})}{x_{\min}} = 0\,. \tag{7.95}$$

Substituting these into the right-hand side of equation (7.94) gives zero. Therefore provided $\lambda_m \neq \lambda_n$ then $\int_{x_{\min}}^{x_{\max}} xuv = 0$. When $\lambda_m \neq \lambda_n$ then $u = v$ and using L'Hospital's rule

$$\begin{aligned}\int xu^2\,dx &= \lim_{\lambda_m\to\lambda_n} x\left\{\frac{u(\lambda_n x)\partial_x u(\lambda_m x) - u(\lambda_m x)\partial_x(\lambda_n x)}{\lambda_m^2 - \lambda_n^2}\right\} \\ &= \lim_{\lambda_m\to\lambda_n} x\left\{\frac{\lambda_m u(\lambda_n x)u'(\lambda_m x) - \lambda_n u(\lambda_m x)u'(\lambda_n x)}{\lambda_m^2 - \lambda_n^2}\right\} \\ &= \lim_{\lambda_m\to\lambda_n}\left[-\frac{x}{2\lambda_m}\frac{\partial}{\partial\lambda_m}\left\{\lambda_m u(\lambda_n x)u'(\lambda_m x) - \lambda_n u(\lambda_m x)u'(\lambda_n x)\right\}\right] \\ &= -\frac{x}{2\lambda_n}\lim_{\lambda_m\to\lambda_n}\left[u(\lambda_n x)u'(\lambda_m x) + x\lambda_m u(\lambda_n x)u''(\lambda_m x)\right. \\ &\qquad\qquad \left. -\lambda_n x u'(\lambda_m x)u'(\lambda_n x)\right] \\ &= \frac{x^2}{2}\left[u'(\lambda_n x)^2 - u(\lambda_n x)u''(\lambda_n x) - \frac{u(\lambda_n x)u'(\lambda_n x)}{x\lambda_n}\right]\,. \end{aligned} \tag{7.96}$$

Using the boundary conditions $u(x = x_{\max}) = \partial_x u(x = x_{\min}) + (R - 1/2)u(x = x_{\min})/x_{\min} = 0$ we find

$$\begin{aligned}\int_{x_{\min}}^{x_{\max}} xu^2\,dx = \frac{{x_{\max}}^2}{2}u'(\lambda_n x_{\max})^2 + \frac{{x_{\min}}^2}{2}\Big[u(\lambda_n x_{\min})u''(\lambda_n x_{\min}) - \\ \left((R-1/2)^2 + \frac{R-1/2}{\lambda_n x_{\min}}\right)u(\lambda_n x_{\min})^2\Big]\,. \end{aligned} \tag{7.97}$$

Summarizing these results

$$\begin{aligned}\int_{x_{\min}}^{x_{\max}} xu(\lambda_m x)v(\lambda_n x)\,dx = \delta_{m,n}\Big\{\frac{{x_{\max}}^2}{2}u'(\lambda_n x_{\max})^2 + \\ \frac{{x_{\min}}^2}{2}\Big[u(\lambda_n x_{\min})u''(\lambda_n x_{\min}) - \left((R-1/2)^2 + \frac{R-1/2}{\lambda_n x_{\min}}\right)u(\lambda_n x_{\min})^2\Big]\Big\} \end{aligned} \tag{7.98}$$

where $\delta_{m,n}$ is the Kronecker delta.

Bibliography

G. Abell. PASP **67**, 258 (1955). Bibcode: 1955PASP...67..258A. Cited on 21.

M. Abramowicz. A&A **500**, 213 (2009). Bibcode: 2009A&A...500..213A. Cited on 133.

T. Alexander. Physics Reports **419**, 65 (2005). Bibcode: 2005PhR...419...65A. Cited on 80, 115.

T. Alexander and C. Hopman. ApJ **697**, 1861 (2009). Bibcode: 2009ApJ...697.1861A. Cited on 10, 15.

M. C. Aller and D. O. Richstone. AJ **124**, 3035 (2002). Bibcode: 2002AJ....124.3035A. Cited on 72, 111.

P. Amaro-Seoane. arXiv (2012). Bibcode: 2012arXiv1205.5240A. Cited on 78.

P. Amaro-Seoane and M. Preto. Classical and Quantum Gravity **28**, 9, 4017 (2011). Bibcode: 2011CQGra..28i4017A. Cited on 115.

T. Anselowitz, R. Wasatonic, K. Matthews, E. M. Sion, and G. P. McCook. PASP **111**, 702 (1999). Bibcode: 1999PASP..111..702A. Cited on 18.

P. Armitage and P. Natarajan. ApJ **567**, L9 (2002). Bibcode: 2002ApJ...567L...9A. Cited on 14.

J. Bahcall and R. Wolf. ApJ **216**, 883 (1977). Bibcode: 1977ApJ...216..883B. Cited on 10.

J. N. Bahcall and R. Wolf. ApJ **209**, 214 (1976). Bibcode: 1976ApJ...209..214B. Cited on 10, 13, 68, 80, 96, 114, 143.

M. C. Begelman, R. D. Blandford, and M. J. Rees. Nature **287**, 307 (1980). Bibcode: 1980Natur.287..307B. Cited on 12.

A. Beloborodov, A. Illarionov, P. Ivanov, and A. Polnarev. MNRAS **259**, 209 (1992). Bibcode: 1992MNRAS.259..209B. Cited on 9.

P. Bergeron, M.-T. Ruiz, S. K. Leggett, D. Saumon, and F. Wesemael. ApJ **423**, 456 (1994). Bibcode: 1994ApJ...423..456B. Cited on 56.

P. Bergeron, F. Wesemael, P. Dufour, A. Beauchamp, C. Hunter, R. A. Saffer, A. Gianninas, M. T. Ruiz, et al. ApJ **737**, 28 (2011). Bibcode: 2011ApJ...737...28B. Cited on 4, 20, 165.

J. Binney and S. Tremaine. *Galactic Dynamics: Second Edition* (Princeton University Press, 2008). Bibcode: 2008gady.book.....B. Cited on 7, 10, 12, 69, 80, 117, 142, 145, 146, 154, 159, 161.

O. Blaes, M. H. Lee, and A. Socrates. ApJ **578**, 775 (2002). Bibcode: 2002ApJ...578..775B. Cited on 14.

J. N. Bode. *Black Hole Mergers and Their Electromagnetic Counterparts*. Ph.D. thesis, California Institute of Technology, Pasadena, California (2011). Cited on 77, 78, 79, 87, 95, 96, 100, 115, 116.

J. N. Bode and C. Wegg. Production of EMRIs in Supermassive Black Hole Binaries (2012). In Prep. Cited on 133, 139.

L. Brenneman and C. Reynolds. ApJ **652**, 1028 (2006). Bibcode: 2006ApJ...652.1028B. Cited on 87, 114.

W. Brown, M. Geller, S. Kenyon, M. Kurtz, and B. Bromley. ApJ **671**, 1708 (2007). Bibcode: 2007ApJ...671.1708B. Cited on 8.

S. Catalán, J. Isern, E. García-Berro, and I. Ribas. MNRAS **387**, 1693 (2008). Bibcode: 2008MNRAS.387.1693C. Cited on 27.

J. Chang and G. Cooper. Journal of Computational Physics **6**, 1 (1970). Bibcode: 1970JCoPh...6....1C. Cited on 158.

P. Chatterjee, L. Hernquist, and A. Loeb. ApJ **592**, 32 (2003). Bibcode: 2003ApJ...592...32C. Cited on 14.

X. Chen, P. Madau, A. Sesana, and F. K. Liu. ApJL **697**, L149 (2009). Bibcode: 2009ApJ...697L.149C. Cited on 68, 70, 71, 86.

X. Chen, A. Sesana, P. Madau, and F. K. Liu. ApJ **729**, 13 (2011). Bibcode: 2011ApJ...729...13C. Cited on 68, 99, 133.

H. Cohn. ApJ **234**, 1036 (1979). Bibcode: 1979ApJ...234.1036C. Cited on 15.

H. Cohn. ApJ **242**, 765 (1980). Bibcode: 1980ApJ...242..765C. Cited on 145, 146.

H. Cohn and R. Kulsrud. ApJ **226**, 1087 (1978). Bibcode: 1978ApJ...226.1087C. Cited on 15.

C. Conselice. ApJ **638**, 686 (2006). Bibcode: 2006ApJ...638..686C. Cited on 111.

P. Côté, J. Blakeslee, L. Ferrarese, A. Jordán, S. Mei, D. Merritt, M. Milosavljević, E. Peng, et al. ApJS **153**, 223 (2004). Bibcode: 2004ApJS..153..223C. Cited on 11, 71.

C. Cutler, D. J. Kennefick, and E. Poisson. Phys. Rev. D **50**, 6, 3816 (1994). URL http://dx.doi.org/10.1103/PhysRevD.50.3816. Cited on 11.

D. Davis, H. Richer, I. King, J. Anderson, J. Coffey, G. Fahlman, J. Hurley, and J. Kalirai. MNRAS **383**, L20 (2008). Bibcode: 2008MNRAS.383L..20D. Cited on 166.

W. Dehnen. MNRAS **265**, 250 (1993). Bibcode: 1993MNRAS.265..250D. Cited on 68, 80.

W. Dehnen. AJ **115**, 2384 (1998). Bibcode: 1998AJ....115.2384D. Cited on 45.

W. Dehnen and J. Binney. MNRAS **298**, 387 (1998). Bibcode: 1998MNRAS.298..387D. Cited on 6, 7, 18, 22, 23, 24, 26, 30.

A. Dieball, C. Knigge, D. Zurek, M. Shara, K. Long, P. Charles, and D. Hannikainen. ApJ **670**, 379 (2007). Bibcode: 2007ApJ...670..379D. Cited on 167.

P. Dobbie, R. Napiwotzki, N. Lodieu, M. Burleigh, M. Barstow, and R. Jameson. MNRAS **373**, L45 (2006). Bibcode: 2006MNRAS.373L..45D. Cited on 45.

S. Doeleman, J. Weintroub, A. Rogers, R. Plambeck, R. Freund, R. Tilanus, P. Friberg, L. Ziurys, et al. Nature **455**, 78 (2008). Bibcode: 2008Natur.455...78D. Cited on 7.

J. L. Donley, W. N. Brandt, M. Eracleous, and T. Boller. AJ **124**, 1308 (2002). Bibcode: 2002AJ....124.1308D. Cited on 67, 72.

D. J. Eisenstein, J. Liebert, H. C. Harris, S. J. Kleinman, A. Nitta, N. M. Silvestri, S. A. Anderson, J. C. Barentine, et al. ApJS **167**, 40 (2006). Bibcode: 2006ApJS..167...40E. Cited on 4, 17, 19, 20, 54.

C. R. Evans and C. S. Kochanek. ApJ **346**, L13 (1989). Bibcode: 1989ApJ...346L..13E. Cited on 67.

J. Farihi. ApJ **610**, 1013 (2004). Bibcode: 2004ApJ...610.1013F. Cited on 55.

M. Feast and P. Whitelock. MNRAS **291**, 683 (1997). Bibcode: 1997MNRAS.291..683F. Cited on 22.

L. Ferrarese and H. Ford. Space Sci. Rev. **116**, 523 (2005). Bibcode: 2005SSRv..116..523F. Cited on 7, 8, 78.

F. Ferraro, G. Beccari, R. Rood, M. Bellazzini, A. Sills, and E. Sabbi. ApJ **603**, 127 (2004). Bibcode: 2004ApJ...603..127F. Cited on 142, 161, 162.

G. Fontaine, P. Brassard, and P. Bergeron. PASP **113**, 409 (2001). Bibcode: 2001PASP..113..409F. Cited on 19.

M. Freitag. ApJ **583**, L21 (2003). Bibcode: 2003ApJ...583L..21F. Cited on 12.

M. Freitag, P. Amaro-Seoane, and V. Kalogera. ApJ **649**, 91 (2006). Bibcode: 2006ApJ...649...91F. Cited on 10, 80, 114.

M. Freitag and W. Benz. A&A **375**, 711 (2001). Bibcode: 2001A&A...375..711F. Cited on 15.

J. R. Gair, D. J. Kennefick, and S. L. Larson. Phys. Rev. D **72**, 84009 (2005). Bibcode: 2005PhRvD..72h4009G. Cited on 11, 91.

J. R. Gair, D. J. Kennefick, and S. L. Larson. Phys. Rev. D **74**, 109901 (2006a). Bibcode: 2006PhRvD..74j9901G. Cited on 91.

J. R. Gair, D. J. Kennefick, and S. L. Larson. ApJ **639**, 999 (2006b). Bibcode: 2006ApJ...639..999G. Cited on 12, 91, 140.

E. Gates, G. Gyuk, H. C. Harris, M. Subbarao, S. Anderson, S. J. Kleinman, J. Liebert, H. Brewington, et al. ApJ **612**, L129 (2004). Bibcode: 2004ApJ...612L.129G. Cited on 54, 55, 60, 62, 63.

K. Gebhardt, T. Lauer, J. Kormendy, J. Pinkney, G. Bower, R. Green, T. Gull, J. Hutchings, et al. AJ **122**, 2469 (2001). Bibcode: 2001AJ....122.2469G. Cited on 7.

K. Gebhardt, D. Richstone, S. Tremaine, T. Lauer, R. Bender, G. Bower, A. Dressler, S. Faber, et al. ApJ **583**, 92 (2003). Bibcode: 2003ApJ...583...92G. Cited on 8.

R. Genzel, R. Schödel, T. Ott, F. Eisenhauer, R. Hofmann, M. Lehnert, A. Eckart, T. Alexander, et al. ApJ **594**, 812 (2003). Bibcode: 2003ApJ...594..812G. Cited on 10.

S. Gezari. Co-Evolution of Central Black Holes and Galaxies **267**, 319 (2010). Bibcode: 2010IAUS..267..319G. Cited on 72.

S. Gezari, S. Basa, D. C. Martin, G. Bazin, K. Forster, B. Milliard, J. P. Halpern, P. G. Friedman, et al. ApJ **676**, 944 (2008). Bibcode: 2008ApJ...676..944G. Cited on 67, 72.

A. Ghez, S. Salim, S. Hornstein, A. Tanner, J. Lu, M. Morris, E. Becklin, and G. Duchêne. ApJ **620**, 744 (2005). Bibcode: 2005ApJ...620..744G. Cited on 7.

O. K. Guseinov, K. I. Novruzova, and I. S. Rustamov. Ap&SS **97**, 305 (1983). Bibcode: 1983Ap&SS..97..305G. Cited on 18.

N. C. Hambly, S. J. Smartt, and S. T. Hodgkin. ApJL **489**, L157 (1997). Bibcode: 1997ApJ...489L.157H. Cited on 56.

Z. Han. MNRAS **296**, 1019 (1998). Bibcode: 1998MNRAS.296.1019H. Cited on 38.

B. Hansen. Microlensing 2000: A New Era of Microlensing Astrophysics **239**, 82 (2001). Bibcode: 2001ASPC..239...82H. Cited on 54.

B. M. S. Hansen, J. Anderson, J. Brewer, A. Dotter, G. G. Fahlman, J. R. Hurley, J. S. Kalirai, I. King, et al. ApJ **671**, 380 (2007). Bibcode: 2007ApJ...671..380H. Cited on 3, 54.

H. C. Harris, C. Dahn, F. Vrba, A. Henden, J. Liebert, G. Schmidt, and I. N. Reid. ApJ **524**, 1000 (1999). Bibcode: 1999ApJ...524.1000H. Cited on 54, 55, 56, 60.

H. C. Harris, E. Gates, G. Gyuk, M. Subbarao, S. F. Anderson, P. B. Hall, J. A. Munn, J. Liebert, et al. ApJ **679**, 697 (2008). Bibcode: 2008ApJ...679..697H. Cited on 54, 55, 56.

H. C. Harris, B. Hansen, J. Liebert, D. V. Berk, S. Anderson, G. R. Knapp, X. Fan, B. Margon, et al. ApJ **549**, L109 (2001). Bibcode: 2001ApJ...549L.109H. Cited on 54, 55, 57.

N. Haurberg, G. Lubell, H. Cohn, P. Lugger, J. Anderson, A. Cool, and A. Serenelli. ApJ **722**, 158 (2010). Bibcode: 2010ApJ...722..158H. Cited on 167.

J. Healy, J. Levin, and D. Shoemaker. Physical Review Letters **103**, 13, 131101 (2009). Bibcode: 2009PhRvL.103m1101H. Cited on 91.

M. Hénon. Annales d'Astrophysique **24**, 369 (1961). Bibcode: 1961AnAp...24..369H. Cited on 145, 146.

J. B. Holberg and P. Bergeron. AJ **132**, 1221 (2006). Bibcode: 2006AJ....132.1221H. Cited on 4, 20, 31, 165.

J. Holmberg and C. Flynn. MNRAS **313**, 209 (2000). Bibcode: 2000MNRAS.313..209H. Cited on 31.

J. Holmberg, B. Nordstrom, and J. Andersen. A&A **475**, 519 (2007). Bibcode: 2007A&A...475..519H. Cited on 6.

C. Hopman. ApJ **700**, 1933 (2009). Bibcode: 2009ApJ...700.1933H. Cited on 15.

C. Hopman and T. Alexander. ApJ **629**, 362 (2005). Bibcode: 2005ApJ...629..362H. Cited on 15, 115.

C. Hopman, M. Freitag, and S. Larson. MNRAS **378**, 129 (2007). Bibcode: 2007MNRAS.378..129H. Cited on 111.

J. R. Hurley, O. R. Pols, and C. A. Tout. MNRAS **315**, 543 (2000). Bibcode: 2000MNRAS.315..543H. Cited on 29, 35, 40.

K. Innanen, J. Zheng, S. Mikkola, and M. Valtonen. AJ **113**, 1915 (1997). Bibcode: 1997AJ....113.1915I. Cited on 97, 121.

P. Ivanov, J. Papaloizou, and A. Polnarev. MNRAS **307**, 79 (1999). Bibcode: 1999MNRAS.307...79I. Cited on 14.

P. B. Ivanov, A. G. Polnarev, and P. Saha. MNRAS **358**, 1361 (2005). Bibcode: 2005MNRAS.358.1361I. Cited on 68, 71, 93, 95, 97, 99, 102.

Z. Ivezic, J. A. Tyson, R. Allsman, J. Andrew, R. Angel, and for the LSST Collaboration. arXiv **astro-ph** (2008). URL http://arxiv.org/abs/0805.2366v1. Cited on 63.

M. Iwasawa, S. An, T. Matsubayashi, Y. Funato, and J. Makino. ApJ **731**, L9 (2011). Bibcode: 2011ApJ...731L...9I. Cited on 14.

F. Jenet, A. Lommen, S. Larson, and L. Wen. ApJ **606**, 799 (2004). Bibcode: 2004ApJ...606..799J. Cited on 14.

K. Joshi, F. Rasio, and S. P. Zwart. ApJ **540**, 969 (2000). Bibcode: 2000ApJ...540..969J. Cited on 15.

A. Just and H. Jahreiß. MNRAS **402**, 461 (2010). Bibcode: 2010MNRAS.402..461J. Cited on 28, 29.

J. S. Kalirai, B. M. S. Hansen, D. D. Kelson, D. B. Reitzel, R. M. Rich, and H. B. Richer. ApJ **676**, 594 (2008). Bibcode: 2008ApJ...676..594K. Cited on 29.

S. O. Kepler, S. J. Kleinman, A. Nitta, D. Koester, B. G. Castanheira, O. Giovannini, A. F. M. Costa, and L. G. Althaus. MNRAS **375**, 1315 (2007). Bibcode: 2007MNRAS.375.1315K. Cited on 18, 20, 46.

M. Kesden. Phys. Rev. D **85**, 2, 24037 (2012). Bibcode: 2012PhRvD..85b4037K. Cited on 9.

M. Kesden, G. Lockhart, and E. Phinney. Phys. Rev. D **82**, 12, 124045 (2010). Bibcode: 2010PhRvD..82l4045K. Cited on 112.

U. Keshet, C. Hopman, and T. Alexander. ApJ **698**, L64 (2009). Bibcode: 2009ApJ...698L..64K. Cited on 10, 15.

F. Khan, A. Just, and D. Merritt. ApJ **732**, 89 (2011). Bibcode: 2011ApJ...732...89K. Cited on 14.

M. Kilic, S. Leggett, P. Tremblay, T. von Hippel, P. Bergeron, H. Harris, J. Munn, K. Williams, et al. ApJS **190**, 77 (2010). Bibcode: 2010ApJS..190...77K. Cited on 56, 57.

M. Kilic, J. Munn, H. Harris, J. Liebert, T. von Hippel, K. Williams, T. Metcalfe, D. Winget, et al. AJ **131**, 582 (2006). Bibcode: 2006AJ....131..582K. Cited on 5, 54.

M. Kilic, D. Winget, T. von Hippel, and C. Claver. AJ **128**, 1825 (2004). Bibcode: 2004AJ....128.1825K. Cited on 5.

I. King. AJ **65**, 122 (1960). Bibcode: 1960AJ.....65..122K. Cited on 143, 145.

S. J. Kleinman, H. C. Harris, D. J. Eisenstein, J. Liebert, A. Nitta, J. Krzesinski, J. A. Munn, C. C. Dahn, et al. ApJ **607**, 426 (2004). Bibcode: 2004ApJ...607..426K. Cited on 20, 31.

A. M. Koekemoer, A. S. Fruchter, R. N. Hook, and W. Hack. In S. Arribas, A. Koekemoer, and B. Whitmore, editors, *The 2002 HST Calibration Workshop : Hubble after the Installation of the ACS and the NICMOS Cooling System, Proceedings of a Workshop held at the Space Telescope Science Institute, Baltimore, Maryland, October 17 and 18, 2002. Edited by Santiago Arribas, Anton Koekemoer, and Brad Whitmore. Baltimore, MD: Space Telescope Science Institute, 2003., p.337*, page 337 (2003). Cited on 162.

S. Komossa. The Astrophysics of Gravitational Wave Sources **686**, 161 (2003). Bibcode: 2003AIPC..686..161K. Cited on 14.

P. Kowalski and D. Saumon. ApJ **651**, L137 (2006). Bibcode: 2006ApJ...651L.137K. Cited on 4, 20, 165.

Y. Kozai. AJ **67**, 591 (1962). Bibcode: 1962AJ.....67..591K. Cited on 87, 97.

P. Kroupa. MNRAS **322**, 231 (2001). Bibcode: 2001MNRAS.322..231K. Cited on 38.

L. D. Landau and E. M. Lifshitz. *Mechanics* (Course of Theoretical Physics, Oxford: Pergamon Press, 2nd ed., 1969). Bibcode: 1969mech.book.....L. Cited on 135.

B. Lanzoni, E. Dalessandro, F. Ferraro, C. Mancini, G. Beccari, R. Rood, M. Mapelli, and S. Sigurdsson. ApJ **663**, 267 (2007a). Bibcode: 2007ApJ...663..267L. Cited on 142, 161.

B. Lanzoni, E. Dalessandro, S. Perina, F. Ferraro, R. Rood, and A. Sollima. ApJ **670**, 1065 (2007b). Bibcode: 2007ApJ...670.1065L. Cited on 142, 161.

T. Lauer, S. Faber, E. Ajhar, C. Grillmair, and P. Scowen. AJ **116**, 2263 (1998). Bibcode: 1998AJ....116.2263L. Cited on 114.

S. Leggett, M. Ruiz, and P. Bergeron. ApJ **497**, 294 (1998). Bibcode: 1998ApJ...497..294L. Cited on 5.

P. Lenzuni, D. Chernoff, and E. Salpeter. ApJS **76**, 759 (1991). Bibcode: 1991ApJS...76..759L. Cited on 54.

M. L. Lidov. Iskusstv Sputn Zemli **8**, 5 (1961). Cited on 87, 97.

M. L. Lidov. Planetary and Space Science **9**, 719 (1962). Bibcode: 1962P&SS....9..719L. Cited on 87, 97.

J. Liebert, P. Bergeron, and J. B. Holberg. ApJS **156**, 47 (2005). Bibcode: 2005ApJS..156...47L. Cited on 17, 18, 19, 20, 22, 31, 35, 46, 54.

A. P. Lightman and S. L. Shapiro. ApJ **211**, 244 (1977). Bibcode: 1977ApJ...211..244L. Cited on 15.

L. Lindegren. IAU Symposium **261**, 296 (2009). Bibcode: 2010IAUS..261..296L. Cited on 63.

F. K. Liu, S. Li, and X. Chen. ApJL **706**, L133 (2009). Bibcode: 2009ApJ...706L.133L. Cited on 75.

G. Lodato, S. Nayakshin, A. King, and J. Pringle. MNRAS **398**, 1392 (2009). Bibcode: 2009MNRAS.398.1392L. Cited on 14.

G. Lodato and E. Rossi. MNRAS **410**, 359 (2011). Bibcode: 2011MNRAS.410..359L. Cited on 67.

J. Lotz, P. Jonsson, T. Cox, D. Croton, J. Primack, R. Somerville, and K. Stewart. ApJ **742**, 103 (2011). Bibcode: 2011ApJ...742..103L. Cited on 12.

W. J. Luyten. *A catalogue of stars with proper motions exceeding 0.5" annually* (Minneapolis: University of Minnesota, 2nd ed., 1979). Bibcode: 1979lccs.book.....L. Cited on 56.

J. Magorrian and S. Tremaine. MNRAS **309**, 447 (1999). Bibcode: 1999MNRAS.309..447M. Cited on 15, 67.

D. Maoz, K. Sharon, and A. Gal-Yam. ApJ **722**, 1879 (2010). Bibcode: 2010ApJ...722.1879M. Cited on 40.

M. Mapelli, S. Sigurdsson, F. Ferraro, M. Colpi, A. Possenti, and B. Lanzoni. MNRAS **373**, 361 (2006). Bibcode: 2006MNRAS.373..361M. Cited on 142, 161.

D. Mclaughlin, J. Anderson, G. Meylan, K. Gebhardt, C. Pryor, D. Minniti, and S. Phinney. ApJS **166**, 249 (2005). Bibcode: 2006ApJS..166..249M. Cited on 163.

D. Merritt. ApJ **718**, 739 (2010). Bibcode: 2010ApJ...718..739M. Cited on 114, 143.

D. Merritt, T. Alexander, S. Mikkola, and C. Will. Phys. Rev. D **84**, 4, 44024 (2011a). Bibcode: 2011PhRvD..84d4024M. Cited on 91, 120, 121.

D. Merritt, T. Alexander, S. Mikkola, and C. Will. Phys. Rev. D **81**, 6, 62002 (2011b). Bibcode: 2010PhRvD..81f2002M. Cited on 101, 106.

D. Merritt, J. D. Schnittman, and S. Komossa. ApJ **699**, 1690 (2009). Bibcode: 2009ApJ...699.1690M. Cited on 11, 71.

G. Meylan. A&A **191**, 215 (1988). Bibcode: 1988A&A...191..215M. Cited on 163.

G. Meylan and M. Mayor. A&A **250**, 113 (1991). Bibcode: 1991A&A...250..113M. Cited on 162, 165.

G. E. Miller and J. M. Scalo. ApJS **41**, 513 (1979). Bibcode: 1979ApJS...41..513M. Cited on 38.

M. Milosavljević and D. Merritt. The Astrophyics Of Gravitational Wave Sources AIP Conference Proceedings **686**, 201 (2003). Bibcode: 2003AIPC..686..201M. Cited on 14, 78, 79.

C. W. Misner, K. S. Thorne, and J. A. Wheeler. *Gravitation* (San Francisco: W.H. Freeman and Co., 1973). Bibcode: 1973grav.book.....M. Cited on 11, 135.

M. Miyoshi, J. Moran, J. Herrnstein, L. Greenhill, N. Nakai, P. Diamond, and M. Inoue. Nature **373**, 127 (1995). Bibcode: 1995Natur.373..127M. Cited on 8.

D. Monet, C. Dahn, F. Vrba, H. Harris, J. Pier, C. Luginbuhl, and H. Ables. AJ **103**, 638 (1992). Bibcode: 1992AJ....103..638M. Cited on 56.

D. Mortlock, H. Peiris, and Ž. Ivezić. MNRAS **399**, 699 (2009). Bibcode: 2009MNRAS.399..699M. Cited on 64.

D. Mortlock, R. Webster, and P. Francis. MNRAS **309**, 836 (1999). Bibcode: 1999MNRAS.309..836M. Cited on 14.

J. A. Munn, D. G. Monet, S. E. Levine, B. Canzian, J. R. Pier, H. C. Harris, R. H. Lupton, Z. Ivezic, et al. AJ **127**, 3034 (2004). Bibcode: 2004AJ....127.3034M. Cited on 20.

J. A. Munn, D. G. Monet, S. E. Levine, B. Canzian, J. R. Pier, H. C. Harris, R. H. Lupton, Z. Ivezic, et al. AJ **136**, 895 (2008). Bibcode: 2008AJ....136..895M. Cited on 20, 21, 22.

C. D. Murray and S. F. Dermott. *Solar System Dynamics* (Cambridge University Press, 2000). Bibcode: 2000ssd..book.....M. Cited on 104.

S. Naoz, W. Farr, Y. Lithwick, F. Rasio, and J. Teyssandier. Nature **473**, 187 (2011). Bibcode: 2011Natur.473..187N. Cited on 99.

S. Naoz, B. Kocsis, A. Loeb, and N. Yunes. eprint arXiv:12064316 (2012). Bibcode: 2012arXiv1206.4316N. Cited on 86, 87.

G. Nelemans, L. R. Yungelson, S. F. P. Zwart, and F. Verbunt. A&A **365**, 491 (2001). Bibcode: 2001A&A...365..491N. Cited on 35, 38, 40, 46.

B. Nordstrom, M. Mayor, J. Andersen, J. Holmberg, F. Pont, B. R. Jørgensen, E. H. Olsen, S. Udry, et al. A&A **418**, 989 (2004). Bibcode: 2004A&A...418..989N. Cited on 6, 18, 28.

B. R. Oppenheimer, N. C. Hambly, A. P. Digby, S. T. Hodgkin, and D. Saumon. Sci **292**, 698 (2001). Bibcode: 2001Sci...292..6980. Cited on 5, 18, 55.

B. Paczyński and P. Wiita. A&A **88**, 23 (1980). Bibcode: 1980A&A....88...23P. Cited on 8, 132, 133, 138.

P. Padovani and F. Matteucci. ApJ **416**, 26 (1993). Bibcode: 1993ApJ...416...26P. Cited on 29.

E.-M. Pauli, R. Napiwotzki, U. Heber, M. Altmann, and M. Odenkirchen. A&A **447**, 173 (2006). Bibcode: 2006A&A...447..173P. Cited on 18.

A. H. G. Peter. Proquest Dissertations And Theses 2008 Section 0181 page 1 (2008). Bibcode: 2008PhDT.....1P. Cited on 85.

A. H. G. Peter. Phys. Rev. D **79**, 103531 (2009). Bibcode: 2009PhRvD..79j3531P. Cited on 71, 85, 131.

P. Peters. Phys. Rev. D **136**, 1224 (1964). Bibcode: 1964PhRv..136.1224P. Cited on 11, 12, 13, 91.

P. Peters and J. Mathews. Phys. Rev. D **131**, 1, 435 (1963). Cited on 90, 91.

A. Pettitt. Biometrika **63**, 1, 161 (1976). Cited on 45.

E. S. Phinney. The Center of the Galaxy: Proceedings of the 136th Symposium of the International Astronomical Union **136**, 543 (1989). Bibcode: 1989IAUS..136..543P. Cited on 67, 80.

W. H. Press, S. A. Teukolsky, W. T. Vetterling, and B. P. Flannery. Cambridge: University Press (1992). Bibcode: 1992nrca.book.....P. Cited on 118.

W. H. Press, S. A. Teukolsky, W. T. Vetterling, and B. P. Flannery. *Numerical recipes in C. The art of scientific computing* (Cambridge: University Press., 1992). Bibcode: 1992nrca.book.....P. Cited on 159.

M. Preto and P. Amaro-Seoane. ApJL **708**, L42 (2010). URL http://iopscience.iop.org/2041-8205/708/1/L42. Cited on 15, 114.

M. Preto and S. Tremaine. AJ **118**, 2532 (1999). Bibcode: 1999AJ....118.2532P. Cited on 9, 71, 82, 83, 84, 85.

F. Pretorius and D. Khurana. Classical and Quantum Gravity **24**, 83 (2007). Bibcode: 2007CQGra..24S..83P. Cited on 92.

G. Quinlan. New Astronomy **1**, 255 (1996). Bibcode: 1996NewA....1..255Q. Cited on 15.

K. U. Ratnatunga, J. N. Bahcall, and S. Casertano. ApJ **339**, 106 (1989). Bibcode: 1989ApJ...339..106R. Cited on 50, 51.

M. J. Rees. Nature **333**, 523 (1988). Bibcode: 1988Natur.333..523R. Cited on 67.

I. Reid, C. Brewer, R. Brucato, W. Mckinley, A. Maury, D. Mendenhall, J. Mould, J. Mueller, et al. PASP **103**, 661 (1991). Bibcode: 1991PASP..103..661R. Cited on 59.

I. N. Reid. ARA&A **43**, 247 (2005). Bibcode: 2005ARA&A..43..247R. Cited on 18.

R. Rich, C. Sosin, S. Djorgovski, G. Piotto, I. King, A. Renzini, E. Phinney, B. Dorman, et al. ApJ **484**, L25 (1997). Bibcode: 1997ApJ...484L..25R. Cited on 142.

H. Richer, A. Dotter, J. Hurley, J. Anderson, I. King, S. Davis, G. Fahlman, B. Hansen, et al. AJ **135**, 2141 (2007). Bibcode: 2008AJ....135.2141R. Cited on 3.

H. Risken. *The Fokker-Planck equation. Methods of solution and applications* (Springer Series in Synergetics., 1989). Bibcode: 1989fpem.book.....R. Cited on 16, 149, 153.

C. Rodriguez, G. Taylor, R. Zavala, A. Peck, L. Pollack, and R. Romani. ApJ **646**, 49 (2006). Bibcode: 2006ApJ...646...49R. Cited on 14.

C. Rodriguez, G. Taylor, R. Zavala, Y. Pihlström, and A. Peck. ApJ **697**, 37 (2009). Bibcode: 2009ApJ...697...37R. Cited on 14.

S. Roeser, M. Demleitner, and E. Schilbach. AJ **139**, 2440 (2010). Cited on 21, 55, 60.

M. Rosenbluth, W. Macdonald, and D. Judd. Physical Review **107**, 1 (1957). Bibcode: 1957PhRv..107....1R. Cited on 143.

N. Rowell, M. Kilic, and N. Hambly. MNRAS **385**, L23 (2008). Bibcode: 2008MNRAS.385L..23R. Cited on 55.

S. Salim, R. Rich, B. Hansen, L. Koopmans, B. Oppenheimer, and R. Blandford. ApJ **601**, 1075 (2004). Bibcode: 2004ApJ...601.1075S. Cited on 55.

R. Salinas, L. Jílková, G. Carraro, M. Catelan, and P. Amigo. MNRAS **421**, 960 (2012). Bibcode: 2012MNRAS.421..960S. Cited on 142, 161.

W. Sargent, P. Young, C. Lynds, A. Boksenberg, K. Shortridge, and F. Hartwick. ApJ **221**, 731 (1978). Bibcode: 1978ApJ...221..731S. Cited on 8.

D. J. Schlegel, D. P. Finkbeiner, and M. Davis. ApJ **500**, 525 (1998). Bibcode: 1998ApJ...500..525S. Cited on 20.

R. Schödel, T. Ott, R. Genzel, R. Hofmann, M. Lehnert, A. Eckart, N. Mouawad, T. Alexander, et al. Nature **419**, 694 (2002). Bibcode: 2002Natur.419..694S. Cited on 7.

G. M. Seabroke and G. Gilmore. MNRAS **380**, 1348 (2007). Bibcode: 2007MNRAS.380.1348S. Cited on 28.

A. M. Serenelli, L. G. Althaus, R. D. Rohrmann, and O. G. Benvenuto. MNRAS **325**, 607 (2001). Bibcode: 2001MNRAS.325..607S. Cited on 19.

A. Sesana, F. Haardt, and P. Madau. ApJ **686**, 432 (2008). Bibcode: 2008ApJ...686..432S. Cited on 13, 69, 80, 81.

E. M. Sion, M. L. Fritz, J. P. McMullin, and M. D. Lallo. AJ **96**, 251 (1988). Bibcode: 1988AJ.....96..251S. Cited on 18.

M. Sirianni, M. Jee, N. Benítez, J. Blakeslee, A. Martel, G. Meurer, M. Clampin, G. D. Marchi, et al. Publications of the Astronomical Society of the Pacific **117**, 1049 (2005). Bibcode: 2005PASP..117.1049S. Cited on 165.

P. Stetson. Publications of the Astronomical Society of the Pacific **99**, 191 (1987). Bibcode: 1987PASP...99..191S. Cited on 165.

K. R. Stewart, J. S. Bullock, E. J. Barton, and R. H. Wechsler. ApJ **702**, 1005 (2009). Bibcode: 2009ApJ...702.1005S. Cited on 12, 73, 111.

N. Stone and A. Loeb. MNRAS **412**, 75 (2011). Bibcode: 2011MNRAS.412...75S. Cited on 75.

R. Strickler, A. Cool, J. Anderson, H. Cohn, P. Lugger, and A. Serenelli. ApJ **699**, 40 (2009). Bibcode: 2009ApJ...699...40S. Cited on 162, 166.

L. E. Strubbe and E. Quataert. MNRAS **400**, 2070 (2009). Bibcode: 2009MNRAS.400.2070S. Cited on 67, 72.

H. Sudou, S. Iguchi, Y. Murata, and Y. Taniguchi. Sci **300**, 1263 (2003). Bibcode: 2003Sci...300.1263S. Cited on 14.

C. Tranter. *Bessel Functions with Some Physical Applications*. Applied Mathematics Series (English Universities Press, 1968). Cited on 167.

S. Tremaine. AJ **110**, 628 (1995). Bibcode: 1995AJ....110..628T. Cited on 114.

S. Tremaine, D. O. Richstone, Y.-I. Byun, A. Dressler, S. M. Faber, C. Grillmair, J. Kormendy, and T. R. Lauer. AJ **107**, 634 (1994). Bibcode: 1994AJ....107..634T. Cited on 68, 80, 114, 117, 120.

P.-E. Tremblay, P. Bergeron, and A. Gianninas. ApJ **730**, 128 (2011). Bibcode: 2011ApJ...730..128T. Cited on 4, 20, 165.

A. Ulmer. ApJ **514**, 180 (1999). Bibcode: 1999ApJ...514..180U. Cited on 67.

M. Valtonen, H. Lehto, K. Nilsson, J. Heidt, L. Takalo, A. Sillanpää, C. Villforth, M. Kidger, et al. Nature **452**, 851 (2008). Bibcode: 2008Natur.452..851V. Cited on 14.

M. Valtonen, S. Mikkola, D. Merritt, A. Gopakumar, H. Lehto, T. Hyvönen, H. Rampadarath, R. Saunders, et al. ApJ **709**, 725 (2010). Bibcode: 2010ApJ...709..725V. Cited on 14.

S. van Velzen, G. Farrar, S. Gezari, N. Morrell, D. Zaritsky, L. Östman, M. Smith, J. Gelfand, et al. ApJ **741**, 73 (2011). Bibcode: 2011ApJ...741...73V. Cited on 76.

S. Vennes. ApJ **525**, 995 (1999). Bibcode: 1999ApJ...525..995V. Cited on 18, 35.

S. Vidrih, D. Bramich, P. Hewett, N. Evans, G. Gilmore, S. T. Hodgkin, M. Smith, L. Wyrzykowski, et al. MNRAS **382**, 515 (2008). Bibcode: 2007MNRAS.382..515V. Cited on 54.

M. Volonteri, J. M. Miller, and M. Dotti. ApJL **703**, L86 (2009). Bibcode: 2009ApJ...703L..86V. Cited on 73.

J. Wang and D. Merritt. ApJ **600**, 149 (2004). Bibcode: 2004ApJ...600..149W. Cited on 67.

C. Wegg. ApJ **749**, 183 (2012). Bibcode: 2012ApJ...749..183W. Cited on 132.

C. Wegg and J. N. Bode. ApJ **738**, L8 (2011). Bibcode: 2011ApJ...738L...8W. Cited on 66.

C. Wegg and E. Phinney. eprint arXiv:12061056 (2012). Bibcode: 2012arXiv1206.1056W. Cited on 17.

S. Weinberg. *Gravitation and Cosmology: Principles and Applications of the General Theory of Relativity* (Wiley-VCH., 1972). Bibcode: 1972gcpa.book.....W. Cited on 101, 136.

R. Wielen. A&A **60**, 263 (1977). Bibcode: 1977A&A....60..263W. Cited on 18.

M. A. Wood. In D. Koester and K. Werner, editors, *White Dwarfs*, volume 443 of *Lecture Notes in Physics, Berlin Springer Verlag*, page 41 (1995). Cited on 19, 30.

Q. Yu. MNRAS **331**, 935 (2002). Bibcode: 2002MNRAS.331..935Y. Cited on 14.

Q. Yu and S. Tremaine. ApJ **599**, 1129 (2003). Bibcode: 2003ApJ...599.1129Y. Cited on 8.

N. Yunes, M. C. Miller, and J. Thornburg. Phys. Rev. D **83**, 4, 44030 (2011). Bibcode: 2011PhRvD..83d4030Y. Cited on 15, 116.

F. Yusef-Zadeh, H. Bushouse, and M. Wardle. ApJ **744**, 24 (2012). Bibcode: 2012ApJ...744...24Y. Cited on 114.